EVOLUTION OF GLOBULARISATION IN TI-6AL-4V ALLOY DURING SECONDARY COGGING OPERATIONS UNDER INDUSTRIAL SCALE CONDITIONS

MATHIEU FABRIS

SUBMITTED IN FULFILMENT OF THE REQUIREMENTS FOR THE DEGREE OF
Doctor of Engineering

DESIGN, MANUFACTURING AND ENGINEERING MANAGEMENT

UNIVERSITY OF STRATHCLYDE

JANUARY 2022

Declaration of Authenticity and Author's Rights

This thesis is the result of the author's original research. It has been composed by the author and has not been previously submitted for examination which has led to the award of a degree.

The copyright of this thesis belongs to the author under the terms of the United Kingdom Copyright Acts as qualified by University of Strathclyde Regulation 3.50. Due acknowledgement must always be made of the use of any material contained in, or derived from, this thesis.

Signed: Mathieu Fabris

Date: 28/06/2021

Abstract

Understanding the relationship between process parameters and microstructural evolution during thermo-mechanical processing of Titanium alloys is essential to ensure that the desired mechanical properties are achieved in the final component and to reduce production costs. This thesis particularly focuses on the evolution of globularisation in Ti-6Al-4V alloy during secondary cogging operations, with an attempt to model the phenomenon based on the dominant mechanisms.

A methodology has been developed to evaluate the effect of processing parameters such as forging temperature, strain and strain path on the evolution of microstructure during open die forging operations. It replicates industrial conditions of cogging process using large cubic samples and a 500T hydraulic press.

The methodology was benchmarked against the literature and validated using uniaxial forging trials. The main mechanisms of globularisation were found to be the creation of α/α boundaries separating laths into smaller grains, termination migration and edge spheroidisation. The kinetics of globularisation increases with strain and annealing duration, and is unaffected by the interruption of the deformation and intermediate annealing. During multiaxial forging with orthogonal compressions, a range of behaviours were observed with some α laths that retained their hard orientation with regard to the compression direction and resisted deformation. On the other hand, laths with favourable orientations further deformed during additional forging steps, resulting in heterogeneous deformation and a lower level of globularisation than those that underwent uniaxial compression. For the range of conditions tested in this work, the process route and the deformation increment had limited effect on the kinetics of globularisation during cogging; whereas the forging temperature affected the main deformation mechanisms with the lower temperature (viz.900°C) producing more heterogeneous deformation and lower kinetics of globularisation.

A novel empirical model was developed to predict globularisation during cogging operations based on the classic Avrami equation. It includes modifications to the existing models by taking into consideration the effects of strain path and inter-step annealing for the prediction of the kinetics of globularisation. This newly developed empirical model has been successfully implemented into a finite element framework, using DEFORM software package, as a user subroutine that can help industries investigate new processing routes to optimise the existing manufacturing routes and to explore new methodologies.

Acknowledgements

Firstly, I would like to express my greatest thanks to my supervisor Dr. Salaheddin Rahimi for his help and guidance throughout this project. I am particularly grateful for his valuable scientific input and his crucial contribution to this thesis. His support during this EngD has been truly appreciated. A special thanks also to Dr. Andrzej Rosochowski for his supervision during this project.

I would like to acknowledge Aubert&Duval, especially Christian Dumont for offering his expertise, and supplying Ti-6Al-4V material for this project, and Sebastien Nouveau for all the technical and emotional support he provided through these years. I would also like to thank the people from Timet (both UK and Europe) for sharing their incredible knowledge, and I am particulary thankful to Yvon Millet for his valued input and for making time and welcoming me to the site of Timet Savoie, making it a very rewarding trip. The expert guidance received from these two forging companies has been an essential driver for this project.

Many thanks to all people at the Advanced Forming Research Centre who helped me during the different stages of this project, Dorothy Evans for always checking up on me and helping with all the administrative side of this EngD, the team in the Hot Workshop for making the forging trials possible, the team in the material characterisation lab for their help with sample preparation and microscopy, and the materials team for their overall support.

I would like to thank all my friends, for their support and encouragements, the group of EngD students for the countless cups of tea and for making this time memorable, and I am especially grateful to Claire for helping me push this project over the finish line. Lastly, I would like to thank my parents and my sister for their patience and loving support throughout this long journey.

Table of contents

Declaration of Authenticity and Authors Rights *i*

Abstract *ii*

Acknowledgements *iv*

Table of contents *v*

List of figures *viii*

List of tables *xv*

1 Introduction **1**

2 Literature review **4**

2.1 Titanium and its alloys 4
2.1.1 Physical properties of titanium 4
2.1.2 Crystal structure 5
2.1.3 Effect of alloying elements 6
2.1.4 Classification of titanium alloys 8
2.2 Microstructure of α+ β alloys 10
2.3 Thermomechanical processing of alpha/beta alloys 13
2.3.1 Deformation mode 13
2.3.2 Manufacturing process 16
2.4 Microstructural evolution during final α/β working 18
2.4.1 Mechanisms of globularisation 18
2.4.2 Kinetics of globularisation 20
2.4.2.1 Effect of initial microstructure 21
2.4.2.2 Effect of strain 23

2.4.2.3 Effect of strain rate 24
2.4.2.4 Effect of deformation temperature 25
2.4.2.5 Effect of post-deformation annealing 27
2.4.2.6 Effect of strain path 28
2.4.2.7 Effect of cooling rate 34
2.4.3 Prediction of globularisation 35
2.5 Summary 38

3 Experimental methodologies 40
3.1 Overview 40
3.2 Material 42
3.3 Forging trials 43
3.3.1 Uniaxial compression 45
3.3.2 Effect of strain path 45
3.3.3 Effect of forging temperature 47
3.3.4 Effect of post-deformation annealing duration 47
3.3.5 Forging trials 48
3.4 Process modelling of the forging trials 50
3.5 Metallographic Inspection 52
3.5.1 Sample preparation 52
3.5.2 Material characterisation 53
3.5.3 Texture characterisation 56
3.6 Summary 60

4 Results 61
4.1 Preliminary FE simulation 61
4.2 Initial microstructure 65
4.3 Effect of uniaxial compression on globularisation 67
4.4 Effect of strain path on globularisation 74
4.5 Effect of forging temperature on globularisation 88
4.6 Effect of post-forging annealing duration on globularisation 92
4.7 Texture evolution 96
4.8 Summary 100

5 Microstructure modelling 101
5.1 Application of existing models 101

5.1.1 Avrami based model 101
5.1.2 Boundary splitting model 102
5.1.3 Termination migration model 104
5.1.4 Empirical models 106
5.2 A new model for globularisation 107
5.2.1 Dynamic globularisation 108
5.2.2 Static globularisation 109
5.2.3 Effect of changes in strain path 111
5.2.4 Creation of the new model for globularisation 113
5.3 Summary 117

6 Discussion 118

6.1 Globularisation during forging and annealing 118
6.2 Microstructural modelling 129
6.3 Summary and outcome for the forging industry 133

7 Conclusions and further work 136

7.1 Conclusions 136
7.2 Further work 138

References 140

Appendix A 153

Appendix B 162

List of figures

2.1 Specific strength as a function of temperature for various structural materials [41]. 5
2.2 crystal structure of α and β phase [41]. 6
2.3 Schematic illustration of the effect of alloying elements on titanium's phase diagram [41]. 7
2.4 Schematic representation of titanium phase diagram as function of chemical compositions (i.e. α and β stabilising elements) and temperature, with the domain of stability of five different classes of titanium alloys highlighted [21]. 8
2.5 Appearances of the lamellar structure with different cooling rates: water quenched (a), air cooled (b) and furnace cooled (c) [75]. 12
2.6 An example of a fully equiaxed structure [50]. 12
2.7 An example of a bi-modal structure [82]. 13
2.8 Slip systems in hexagonal structure [5]. 14
2.9 Schematic diagram showing slip mechanism in a single crystal under compressive loading [53]. 15
2.10 Temperature dependence of CRSS for different slip systems in single crystals of Ti-6.6Al [104]. 15
2.11 Schematic plot of primary working for titanium alloys. 18
2.12 Schematic of the steps of globularisation [85]. 19
2.13 Schematic illustrations of intra-phase boundaries splitting (a and b), and the grooving process (c) [95]. 20
2.14 Progression of termination migration process [89]. 20
2.15 Microstructures after multi-step forging for (a) a fine structure and (b) a coarse structure [36]. 21
2.16 Illustration of the kinking of laths during hot deformation of a Ti-6Al-4V specimen[90]. 23

2.17 Fraction of dynamic globularisation in BT25 titanium alloy as functions of strain and strain rate at 940°C (a), 960°C (b), 980°C (c), 1000°C (d)[51]. 24
2.18 Influence of temperature on active deformation mechanisms of α laths partitioning, (a) illustration of shear band formation, (b) illustration of lammela buckling, and (c) competition mechanism between the stress required for shear band formation and lamella buckling [113]. 26
2.19 Effect of annealing time and temperature on the fraction of globularised α [96]. 27
2.20 Effect of annealing time and pre-strain on the fraction of globularised α [95]. 28
2.21 Microstructures achieved after applying a strain of 0.5 in torsion (a) and reversed torsion (b) [56]. 29
2.22 Fractions of equiaxed particles vs accumulated strain for different strain paths [37]. 29
2.23 Fraction of equiaxed grains as a function of accumulated strain for different strain path in torsion: monotonic (M), reversed (R), and double-reversed (DR) [67]. 32

3.1 A flow chart depicting the general approach to this work. 41
3.2 Machining of the cubic samples out of billet sections and marking of the billet axis. 43
3.3 Schematic representation of a multi-axial forging represented by screen shots from the FE simulation carried out in DEFORM. 44
3.4 Schematic plot of thermo-mechanical trials carried out throughout the course of this study. 44
3.5 Hydraulic press used for the forging experiments. 49
3.6 Impact of the strain increment on the forgeability of cubic samples: strain increment of 0.4 (a) and 0.25 (b). 50
3.7 FE simulation of the forging trials (a), predicted strain distribution (b), and predicted temperature distribution(c). 52
3.8 Sample extraction for material characterization. 53
3.9 The various strain zones investigated in sample '1_0.5U_WQ' (a) and '4_0.25M_WQ' (b). 54

3.10 Microstructure with superimposed grid for point count procedure with a measurement highlighted. 55
3.11 Schematic highlighting the measurements of the aspect ratio of α grains. 55
3.12 Schematic highlighting the representation of globularisation volume fraction with respect to strain for various process conditions. 56
3.13 An example of an acquired EBSD map displaying the grain boundaries and the grain crystallographic orientation using inverse pole figure (IPF) colouring with respect to the loading direction. . . . 57
3.14 An example of pole figure for a uniaxially compressed sample (i.e., '1-0.5U-WQ'). 58

4.1 Photographs of one of the samples in the as forged conditions, (a) side view, and (b) top-view with the sides used for dimensional measurements highlighted. 62
4.2 Simulated strain distributions predicted under different conditions: (a) HTC 500 - COF 0.08, (b) HTC 2500 - COF 0.3, (c) HTC 8000 - COF 0.6. The scale is between 0 and 2. 63
4.3 Simulated temperature distributions predicted under different conditions: (a) HTC 500 - COF 0.08, (b) HTC 2500 - COF 0.3, (c) HTC 8000 - COF 0.6. The scale is between 700°C and 980°C. 64
4.4 Plot of temperature evolution as a function of time for the solution heat treatment. 65
4.5 Optical microscopy appearance of the initial microstructure that was heat treated at 1050°C for 1 hour followed by furnace cooling at 5°C/min. 66
4.6 Optical microscopy appearance of the initial microstructure that was heat treated at 950°C for 1 hour followed by water quenching. 66
4.7 Optical micrographs of the sample '1-0.5U-WQ' in the low strain zone (ε= 0.8). Arrows point at buckled α laths. 68
4.8 Optical micrographs of the sample '1-0.5U-WQ' in the high strain zone (ε= 1.7). Arrows indicates remnants of grain boundary α layer. 68
4.9 Plots of α lath aspect ratio distributions for the uniaxially forged samples, (a) '1-0.5U-WQ', (b) '1-0.5U-1h-WQ', (c) '1-0.5U-1h-FC', (d) '1-0.5U-4h-FC'. 69
4.10 Optical micrographs of the sample '1-0.5U-WQ' in the high strain zone (ε= 1.7) after: (left) 1 hour annealing, and (right) 4 hours annealing). . 70

4.11 Plots of globularised fraction as a function of local strain for the uniaxially forged samples followed by various annealing. 70
4.12 Predicted strain distribution for the test ’2-(0.25U-1h)-WQ’. 70
4.13 Optical micrographs of the sample: (left) ’2-(0.25U-1h)-WQ’, and (right) ’2-(0.25U-1h)-FC’ in the high strain zone (ε= 1.3). 71
4.14 Plots of α lath aspect ratio distributions for the uniaxially forged samples, (a) ’2-(0.25U-1h)-WQ’, and (b) ’2-(0.25U-1h)-FC’. 71
4.15 Plots of the thickness of α laths of samples forged uniaxially and annealed under different conditions. 72
4.16 Optical micrographs of the sample ’5-(0.1U-1h)-FC’ in the high strain zone (ε= 0.85): a) 100x magnification, and b) 200x magnification. . . 73
4.17 Optical micrographs of the sample: a) ’5-(0.1U-1h)-FC’ in the high strain zone (ε= 0.85), and b)’1-0.5U-4h-FC’ in the low strain zone (ε= 0.8). 73
4.18 Optical micrographs of the high strain zone (ε= 1.4) of the samples: a) ’2-(0.25M-1h)-WQ’ , and b) ’2-(0.25M-1h)-FC’. 75
4.19 Optical micrographs of the sample ’2-(0.25M-1h)-FC’ highlighting unaffected α colonies (solid circle), fragmented α laths (dashed circle), and remnant of Prior-β grain boundaries (arrows). 75
4.20 Plots of α lath aspect ratio distributions for the biaxially forged samples, (a) ’2-(0.25M-1h)-WQ’, (b) ’2-(0.25M-1h)-FC’, and (c) ’2-0.25M-1h-FC’. 76
4.21 Optical micrographs of the sample forged biaxially with no annealing between the two steps ’2-0.25M-1h-FC’. 77
4.22 Optical micrographs of the high strain zone (ε= 1.5) of ’5-(0.1M-1h)-FC’ sample. 78
4.23 Optical micrographs of the high strain zone (ε= 1.7) of ’5-0.1M-5h-FC’ sample. 79
4.24 Optical micrographs of ’3-0.1M-3h-2-0.1M-2h-FC’ sample in two different strain zones: (a) ε= 1.5, and (b) ε= 0.7 79
4.25 Plots of α lath aspect ratio distributions for samples: (a) ’5-(0.1M-1h)-FC’, (b) ’5-0.1M-5h-FC’, and (c) ’3-0.1M-3h-2-0.1M-2h-FC’. 80
4.26 Plots of globularised fraction as a function of local strain for the multi-axially forged samples followed by various annealing. 80

4.27 Optical micrographs of the samples ’3-0.1M-1h-WQ’ (left) and ’3-0.1M-1h-3-0.1M-1h-WQ’ (right). 82
4.28 Plots of α lath aspect ratio distributions for samples: (a) ’3-0.1M-1h-WQ’, and (b) ’3-0.1M-1h-3-0.1M-1h-WQ’. 82
4.29 Optical microscopy appearance of the interrupted test: ε= 3*0.1 - 3h annealing - WQ. 83
4.30 Plots of α lath aspect ratio distributions for ’3-0.1M-3h-WQ’ sample. . 83
4.31 Optical micrographs of sample ’4-0.25M-WQ’ in the zone: (a) ε= 3.1, and (b) ε= 1.5 84
4.32 Optical micrographs of sample ’10-0.1M-WQ’in the strain zone: (a) ε= 3.1, and (b) ε= 1.5 85
4.33 Plots of α lath aspect ratio distributions for samples: (a) ’4-0.25M-WQ’, and (b) ’10-0.1M-WQ’. 85
4.34 Plots of globularised fraction as a function of local strain for tests ’upset’ and ’45 $degree$’ as well as for tests ’3-0.1M-1h-WQ’ and ’1-0.5U-WQ’ for comparison. 87
4.35 Optical micrographs of samples: (a) ’upset’, and (b) ’45°’. 87
4.36 Plots of α lath aspect ratio distributions for samples: (a) ’upset’, and (b) ’45°’. 88
4.37 Optical micrographs of sample ’1-0.5U(900°C)-WQ’: (a-b) as forged, (c) after 1 hr annealing, and (d-e) after 4 hrs annealing. 90
4.38 Plots of α lath aspect ratio distributions for sample ’1-0.5U(900°C)-WQ’: (a) as forged, (b) after 1 hr annealing, and (c) after 4 hrs annealing. 91
4.39 An optical micrograph of sample ’3-0.1M(900°C)-3h(950°C)-WQ’. . 91
4.40 Plots of α lath aspect ratio distributions for sample ’3-0.1M(900°C)-3h(950°C)-WQ’. 92
4.41 Optical micrographs of sample ’4-0.25M-WQ’: (a) as forged, (b) after 1 hr annealing, and (c) after 4 hrs annealing. 93
4.42 Plots of α lath aspect ratio distributions for sample ’4-0.25M-WQ’: (a) as forged, (b) after 1 hr annealing, and (c) after 4 hrs annealing. 94
4.43 Plots of globularised fraction as a function of local strain for uniaxially and multiaxially forged samples followed by various annealing. 94
4.44 Optical micrograph of sample ’4-0.25M-1h-WQ’ displaying different mechanisms of globularisation. 95

4.45 Optical micrographs of sample '1-0.5U-1h-WQ' in the low strain zone ($\varepsilon = 0.8$): (a) as forged, and (b) after 4 hrs annealing. 95

4.46 Plot of α laths thickness for uniaxially and multiaxially forged samples followed by various annealings. 96

4.47 $\{0001\}$, $\{11\bar{2}0\}$, $\{10\bar{1}0\}$ pole figures of the material: (a) after initial heat treatment and (b) 'SA+1h'. 97

4.48 $\{0001\}$, $\{11\bar{2}0\}$, $\{10\bar{1}0\}$ pole figures of the material after uniaxial compression test: (a) water quenched (b) annealed for 1hr then water quenched and (c) annealed for 4hrs then slow cooled. 98

4.49 $\{0001\}$, $\{11\bar{2}0\}$, $\{10\bar{1}0\}$ pole figures of the material after test '2_0.25M _1h_FC'. 99

4.50 $\{0001\}$, $\{11\bar{2}0\}$, $\{10\bar{1}0\}$ pole figures of the material from tests including an annealing between compressions: (a) uniaxial and (b) orthogonal compressions. 99

4.51 $\{0001\}$, $\{11\bar{2}0\}$, $\{10\bar{1}0\}$ pole figures of the material from test '4_0.25M_WQ'. 99

4.52 $\{0001\}$, $\{11\bar{2}0\}$, $\{10\bar{1}0\}$ pole figures of the material from test '1_0.5U_WQ(900°C)_WQ'. 100

5.1 Plot of the globularised fractions as a function of local strain; predicted using Avrami model from literature and experimentally determined in this study. 102

5.2 Predicted time for boundary splitting mechanism in Ti-6Al-4V subjected to different deformation conditions. 104

5.3 Comparison between the experimentally measured fractions of globularisations with the results of predictions using empirical model in Eq.2.3. 107

5.4 Predicted globularised fraction by JMAK model and asymptotic model for different deformation conditions [18]. 110

5.5 Plot of the strain as a function of time for test '4_0.25M_WQ'. 112

5.6 Effect of different factors on the accuracy of the global model. 114

5.7 Plot of the globularised fraction as a function of strain for test "5_0.1M_5h_FC" along with the predicted values from the new model. 114

5.8 Two methods fo of subroutine implementation in DEFORM FE package (a)post-processor subroutine, and (b) embedded FEM subroutine. 116
5.9 Distribution of globularised fraction obtained with the subroutine for test '5_0.1M_5h_FC'. 117
5.10 Distribution of globularised fraction obtained with the subroutine for test '4_0.25M_4h_AC'. 117

6.1 Plots of globularised fraction as a function of local strain for interrupted tests with 2 steps of deformation. 119
6.2 Plots of globularised fraction as a function of local strain for uniaxial compressions tests with and without interruption of deformation. . . . 120
6.3 Locations in samples where the strain tensors is evaluated for the conditions: (a) uniaxial compression to 50% reduction, (b) two orthogonal compressions of 25% reduction each, and (c) four orthogonal compressions of 25% reduction each. 121
6.4 Optical microscopy appearance of a region in the high strain zone (ε= 1.7) taken from sample '1-0.5U-WQ'. Arrows show the α laths fragmentation by different mechanisms. 123
6.5 Optical microscopy appearance of the high strain level (ie., ε= 1.7) zone from sample '1-0.5U-WQ' after 1hr annealing. Arrows indicate α laths fragmented by β phase penetration. 124
6.6 Plots of globularised fraction as a function of local strain for interrupted tests with 2 steps of deformation. 126
6.7 Plots of globularised fraction as a function of local strain for interrupted tests with 5 steps of deformation. 127
6.8 Plots of globularised fraction as a function of local strain for trials to a strain of 1 with annealing of 1 hr (left) and 4 hrs (right). 128
6.9 Plot of β phase volume fraction as a function of temperature [52]. . . . 128
6.10 Plot of globularised fraction as a function of local strain for the uniaxially forged samples at 900°C and 950°C followed by various annealing. 129
6.11 Predictions of static globularisation fraction as a function of annealing time with JMAK model for different values of exponent *n*. 132

List of tables

2.1 Effect of cumulative strain for monotonic and multiaxial deformation process on the fraction of different types of boundaries [72]. 30

3.1 Thermo-mechanical conditions investigated throughout this study. . . 46
3.2 Thermo-mechanical conditions investigated throughout this study. . . 47
3.3 Heat treatment conditions studied in this work. 48
3.4 Settings used to generate the pole figures. 57
3.5 Thermo-mechanical conditions investigated by EBSD. 59

4.1 Summary of the measured dimensions and the results of prediction models with different heat transfer coefficient (HTC) and coefficient of friction (COF). 63

5.1 List of constants for boundary splitting model. 103
5.2 Comparison between the experimentally measured globularised fractions and the results of model prediction based on the termination migration mechanism. 104
5.3 List of constants from the empirical model predicting globularised fraction. 106
5.4 Combinations of options for the new model. 113

Chapter 1

Introduction

Titanium alloys due to their low density, high strength and toughness, excellent corrosion resistance, and crack propagation resistance are often among selected engineering materials for manufacturing of high value components. These combined with high temperature mechanical properties (i.e. up to 600°C) make them very attractive for applications where both mechanical properties and light weighting are required. These mainly include applications in aviation and aerospace industry where more than half of the worlds titanium production is used. These are for the production of fan blades and low pressure compressor components in jet engines, and critical structural parts such as landing gear that require high strength to weight ratio and thus a reduction in fuel consumption which is one of the main concerns of the aviation industry. Additionally, titanium alloys are also used in chemical industry for containers, heat exchangers and pressure reactors because of their high corrosion resistance. Other applications of titanium alloys include medical applications such as joint replacements and medical tools, due to their good biocompatibility and corrosion resistance; in the automotive industry and in manufacture of components for sport applications such as golf club heads and cycle frames, although they are less common due to the high cost which is about 20 times higher than steel in weight.

The continuous demand for reductions in fuel consumption and CO_2 emissions put the aerospace industry under pressure to enhance the efficiency of jet engines and optimise manufacturing processes. This in turn results in components and structures in which the materials are used to the limits of their thermal and mechanical capabilities. For example, blades and discs are critical components in jet engines as they determine the operation conditions and thus the efficiency of the engine. These challenging conditions have driven significant level of research projects on titanium metallurgy in order to optimise its manufacturing processes. Despite significant number of excellent research outputs in this field (e.g. [9, 41, 66, 77]), there are still gaps in the existing knowledge related to titanium production and processing. The extraction process of titanium from ore, the refining operations and thermo-mechanical processing (i.e. forging) are extremely expensive (i.e. between 5-10 times more than those of aluminium) and investigations are carried out on new procedures to reduce cost and improve efficacy. One of the gaps in the existing knowledge is related to the forging and cogging operations and the understanding of the effect of process parameters on microstructure evolution and the properties of the final product. More specifically and related to the topic of this EngD project, the primary hot working of Ti-6Al-4V alloy and the microstructural evolution occurring during these processes at industrial scale are not fully understood.

The required thermo-mechanical processing to transform as cast ingots of titanium into intermediate products such as billets, involves complex operations comprising sequential hot working and heat treatments. Each step of these processes is designed for a specific purpose to tailor microstructure to fulfil a specific goal. Control of the microstructure is key to yield the mechanical properties of the material and consequently the performance of the produced component in service. Hence, understanding the inter-relationships between processing conditions, microstructure evolution and the materials final properties are essential for the optimisation of the forging process of titanium alloys. One stage of the thermo-mechanical processing of titanium alloys aims to transform the lamellar structure to a globular/equiaxed microstructure. This is known as globularisation, which is essential for good ductility during later forging and forming operations as well as for enhancing the performance of the material in service (i.e., resistance to fatigue crack). This has been the subject of a large volume of research studies. Some focused on the effect of process parameters on microstructural evolution [61, 79] while others looked at the underlying microstructure evolution mechanisms [23, 95, 102]. Several models have been proposed to predict microstructure evolutions [94, 100], however these models are proposed based on data obtained from small scale samples, and often do not consider all the process parameters. For examples, the effect of strain path and inter-pass annealing on kinetics of globularisation during industrial forging are not fully understood and hence not considered in these models.

Globularisation is known to be fairly heterogeneous, meaning that there is often an inhomogeneous distribution of globularised fraction at a microstructural level. This heterogeneous deformation can lead to non-globularised areas and regions where grains display close crystallographic orientations in industrial products. This is undesirable as these features could act as sites for crack initiation during further forming or in service. To prevent this, forging industries often carry out large amount of redundant work in their processing routes. Understanding the mechanisms behind heterogeneous globularisation and how this evolves during cogging operations depending on the process parameters is a crucial step towards the optimization of the industrial processing routes for $\alpha+\beta$ titanium alloys.

This EngD project is designed to evaluate the effect of processing parameters on the evolution of microstructure and globularisation in Ti-6Al-4V alloy during multiaxial forging at a scale comparable to industrial cogging, using large scale samples. The aims are, (1) to generate knowledge on the kinetics of globularisation during industrial cogging operations by conducting a series of trials on large samples, (2) to understand the underlying mechanisms of the globularisation process, and (3) to develop an empirical model to predict microstructural evolution during cogging in Ti-6Al-4V alloy that can be applied to industrial scale forging.

Chapter 2

Literature review

This chapter provides an overview of relevant previous research works on titanium and its alloys to shed a light on the inter-relationship between thermo-mechanical processing and microstructural evolution, and attempts to highlight the deficiencies in the existing knowledge, with particular focus on forging of Ti-6Al-4V. For this purpose, fundamentals of titanium alloys, their microstructures and their manufacturing processes are covered. Emphasis has been made on the microstructural evolution during processing in dual phase $\alpha + \beta$ temperature range, and the proposed models for most likely mechanisms and their kinetics are reviewed.

2.1 Titanium and its alloys

2.1.1 Physical properties of titanium

Titanium is the ninth most commonly used element and the fourth most abundant metal on the planet Earth constituting about 0.63% of its crust. Due to high reactivity with oxygen it is always found in oxide form, rather than pure. The two major sources of titanium are: titanic iron ore known as ilmenite ($FeTiO_3$) and a titanium dioxide known as rutile (TiO_2). It was first discovered in 1791 by Reverend Gregor in England; though rediscovered in 1795 by a German scientist, Klaproth, who named it titanium, originating from Titans in Greek mythology [50].

Titanium is one of the lightest non-ferrous metals with a density of 4.5 g.cm^{-3} [13]. Titanium alloys exhibit several unique mechanical properties such as high strength and toughness to weight ratio, great resistance to fatigue and superior resistance to corrosion [66]. Figure 2.1 shows the strength-to-weight ratio as a function of temperature for titanium alloys in comparison to other common structural materials. Also the high melting point of 1678°C makes titanium alloys ideal for applications at high temperature (i.e. up to 600°C [6]) compared to aluminium counterparts that can only be used up to a maximum of about 250°C [32]. Furthermore, due to its high reactivity with oxygen, titanium is able to form a thin passive oxide surface layer that enhances its resistance to corrosion and environmentally assisted degradations. Titanium alloys are mainly used in demanding environments where this particular set of properties is required. These justify the higher production cost for titanium alloys compared to other structural materials used for engineering applications [41].

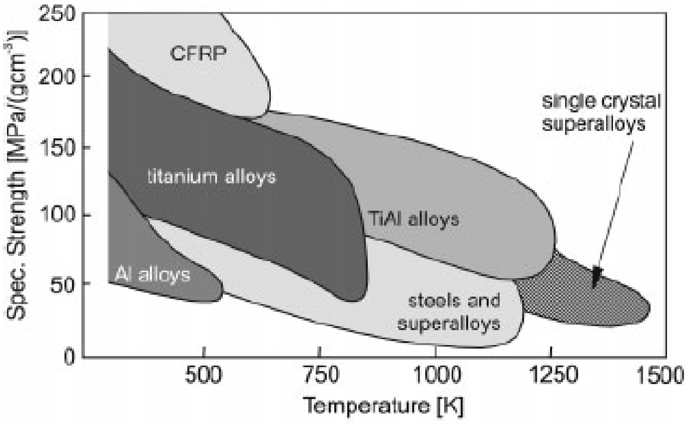

Figure 2.1: Specific strength as a function of temperature for various structural materials [41].

2.1.2 Crystal structure

Similar to other allotropic metals such as iron, cobalt or zirconium, titanium also has two crystal structures depending on temperature. At temperatures in excess of 882°C, pure titanium adopts a body-centered cubic (bcc) crystal structure known as β phase with a lattice parameter of a = 0.332 nm. At lower temperatures (i.e. below 882°C) its crystal structure transforms into hexagonal close packed (hcp) known as the α phase with lattice parameters of a = 0.295 nm and c = 0.468 nm as is shown in Figure 2.2. The allotropic transformation from β phase to α phase occurs on cooling at 882°C which is known as the β-transus temperature. The β phase is stable at temperatures above the β-transus up to the melting point that is 1678°C for pure titanium. Similarly to steels, the feasibility of designing a microstructure based on phase transformation and controlling volume fractions and morphologies of different phases is the basis for obtaining a large spectrum of desired properties [41].

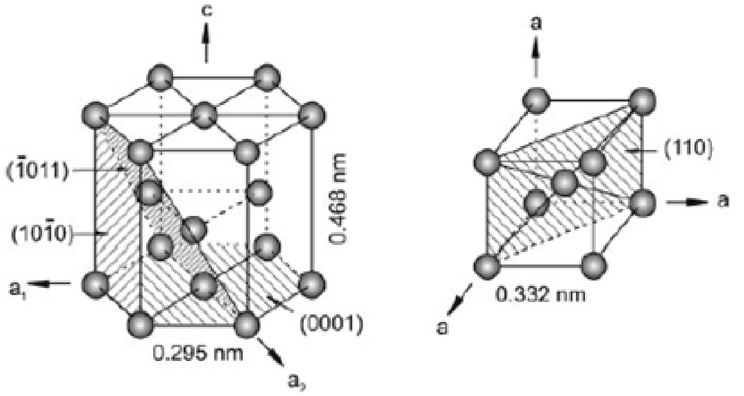

Figure 2.2: crystal structure of α and β phase [41].

2.1.3 Effect of alloying elements

In order to achieve desired properties for certain applications, alloying elements are added to the composition of titanium alloys. These elements have different impacts on the alloy's final properties, depending on their inherent properties and their effects on the stability of the constituent phases [41, 103]. On this basis, three categories of alloying elements including α-stabilisers, β-stabilisers and neutral are distinguished. Their effects on the phase diagram of titanium is shown schematically in Figure 2.3.

α-stabilising elements extend the stability of α phase towards higher temperatures (i.e. increase the β- transus). Among these, aluminium is the most commonly used element due to its substantial solid solution strengthening that improves the tensile and creep resistance of the alloy while lowering its density. Other elements such as oxygen, nitrogen and carbon are also considered as α-stabilisers. These elements in titanium are interstitial in solid solution that enhance the strength of the material, and have particularly been used to produce several grades of commercially pure (CP) titanium with a range of strength and ductility. Boron, Gallium and some rare earth elements can also be used as α-stabilisers, but their usage due to their lower solubility level compared to that of aluminium is seldom. However, the amount of α-stabilisers has to be controlled carefully as these elements tend to increase susceptibility to embrittlement by forming an ordered phase α_2 (Ti_3Al) [66].

β-stabilisers enhance the stability domain of β phase towards lower temperatures and decrease the β-transus temperature. They also increase the amount of β phase retained at room temperature. β-stabilisers are divided into two main groups of (i) the isomorphous, and (ii) the eutectoids. The former comprises elements such as vanadium, molybdenum and niobium. These have relatively high solubility in titanium and improve solid solution hardenability of the β phase. The latter includes elements like iron, silicon and chromium. Due to their lower solubility in the β phase these elements tend to form inter-metallic compounds. The precipitation of such compounds often improves mechanical properties of the alloy; for instance, silicon particles were found to increase creep resistance [63].

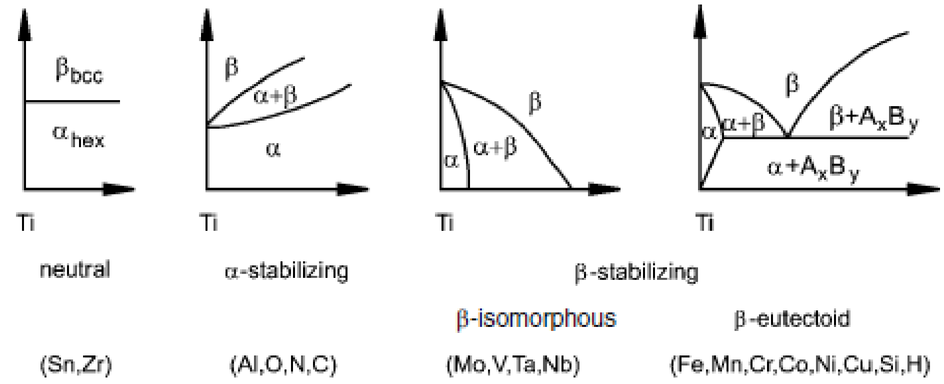

Figure 2.3: Schematic illustration of the effect of alloying elements on titanium's phase diagram [41].

Some elements such as tin and zirconium, barely affect the α/ β stability, and hence are considered as neutral alloying elements [41]. They are used in titanium alloys due to their substantial influence on improving the ultimate tensile strength [59].

2.1.4 Classification of titanium alloys

Depending on microstructure, titanium alloys are divided into five categories, including (i) α, (ii) near-α, (iii) $\alpha + \beta$, (iv) metastable β, and (v) β alloys. The domains of stability of these phases are schematically shown on a pseudo phase diagram, including the start and termination of martensite formation (i.e. line M_S/M_f in Figure 2.4. During cooling from elevated temperatures, passing through the β-transus will initiate $\beta \rightarrow \alpha$ transformation either by nucleation and growth of α phase or by diffusionless martensitic transformation, depending on cooling rate. If the cooling rate is fast enough to overcome the M_S/M_f threshold then a certain amount of β phase can be retained at room temperature while a cooling beyond the M_S/M_f line leads to a complete retention of β phase.

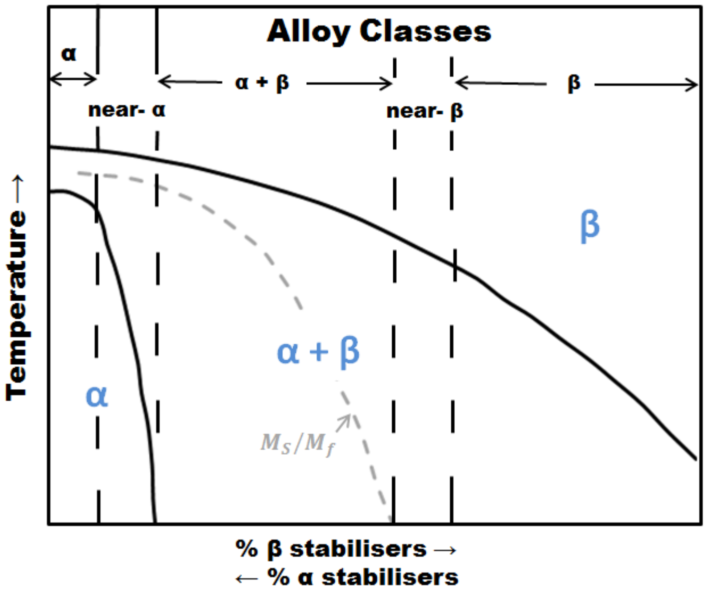

Figure 2.4: Schematic representation of titanium phase diagram as function of chemical compositions (i.e. α and β stabilising elements) and temperature, with the domain of stability of five different classes of titanium alloys highlighted [21].

In α alloys, β phase cannot be retained at room temperature, and thus these alloys contain a single phase α hcp crystal structure. As such, this class of alloys is not suitable for heat treatment to achieve desired properties, instead the strengthening is typically achieved through solid solution hardening, predominantly by oxygen. These alloys exhibit a relatively low strength, however, their toughness and resistance to creep are very high. Furthermore, they show a good corrosion resistance, weldability and thermal stability. α alloys are thus used for applications that require these specific properties; for example, Ti-5Al-2.5Sn is used in hydrogen fuel vessel due to its high toughness and ductility at cryogenic temperatures [9], and Grade 2 CP-Ti is used for skin panels and fire walls in aircraft, and tubing in heat exchangers [66].

Near-α alloys contain up to 2% of β-stabilisers which broaden the range of α+ β temperature, enabling the feasibility of hot working in this class of alloys for microstructure modification purposes. Even though a small amount of β phase is present in the material, they behave more like α alloys than α + β alloys. These alloys can be heat-treated and hot worked to improve their strength and creep resistance, and present the best properties at elevated temperatures. For example, Timetal 834 is used for blades, discs and rotors in the medium and high pressure compressor of jet engines where the working temperatures reach 600°C [9]. Ti-3Al-2.5V-Ru alloy was invented specially to produce pipes for geothermal brine wells and oil and gas production where severe conditions of temperature associated with corrosive environments are encountered. The addition of Ruthenium improves the resistance to crevice corrosion and stress corrosion cracking [74].

α+β alloys contain a certain fraction of both α and β stabilisers, with the latter being typically between 4 and 6% [31]. This broadens the domain of α+β field such that a certain fraction of β phase is retained at room temperature. As a result, dependant on the nature of thermo-mechanical processing, a wide spectrum of microstructures is achievable in this class of alloys that leads to a broad range of desired mechanical properties. α+β alloys show good combinations of mechanical properties and resistance to degradation. For instance, they possess medium to high strength, good toughness and high resistance to fatigue and creep fracture [50]. Ti-6Al-4V is the most commonly used α + β alloy with applications such as fan discs, low pressure compressor discs and blades in jet engines [9]. They are also used for medical applications such as orthodontic appliances, and in-joint replacements [66].

Near-β alloys contain up to 10-15% of β stabilisers thus reaching beyond the M_S/M_f limit in the phase diagram (see Figure 2.4) at room temperature. This implies that martensitic transformation may be avoided, allowing retention of β phase at room temperature. This retained β phase is metastable as fine particles of α phase starts to precipitate in the matrix through heat treatment. This age hardening is a particularly important mechanism in these alloys as it allows really high strength to be reached [21]. The most used metastable β alloy is Ti-10V-2Fe-3Al. It has high strength, toughness and fatigue resistance, and is used for landing gears for example [9].

β alloys contain 10-30% of β stabilisers; this leads to the presence of stable β phase at room temperature [21]. Due to dominance of bcc crystal structure, these alloys show high forgeability and cold workability. They also exhibit high strength, toughness and resistance to high cycle fatigue, however, due to the higher density of the alloying elements, these alloys exhibit higher density than α or α + β alloys. Manufacturing of β alloys typically involves solution treatment and/or hot working followed by ageing for precipitation of α particles to improve mechanical properties (e.g. yield strength). These alloys have various applications; for example, Ti-15-3 is used as replacement for steel in nut clips in airplane for weight-saving purpose, and Beta-C alloy is used for spring applications [50].

2.2 Microstructure of α+ β alloys

The mechanical properties and resistance to degradations in titanium alloys depend strongly on microstructure characters distributions [49]. The microstructure of titanium alloys is influenced mostly by their chemical composition and the thermo-mechanical process history of the material. The microstructure constituents are distinguished on the bases of their crystallographic structure, size and morphology. The $\beta \rightarrow \alpha$ transformation can occur through a diffusion-controlled mechanism or a diffusionless shear process, each resulting in different forms of α phase.

Primary α is not generated from β phase through nucleation and growth on cooling, but it is rather the non-transformed α phase during heating of the alloy to the α + β temperature range. The fraction of primary α decreases as the temperature increases to reach the β-transus. Sufficient exposure time to temperatures in dual phase α=β field results in an equilibrium in the fractions of α and β phases through a diffusion-controlled $\beta \leftrightarrow \alpha$ transformations [41]. The leftover non-transformed α is known as the primary α. The shape of primary α grains depends on whether the material has been subjected to thermo-mechanical processing or not. In a non-deformed material, primary α grains have a plate or lath shape, while in a deformed material curved lath with various degrees of spheroidisation are observed [42]. In a recrystallised material a fully globular structure can be achieved [88].

Secondary α or transformed β is a phase that is generated during cooling of β phase through the β-transus. α phase nucleates and grows quickly at the β grain boundaries and triple junctions. A slower diffusion transformation occurs within β grains leading to the formation of α lamellae separated by the β phase retained by the partitioning of the β stabilising elements. Clusters of α and retained β lamellae can form a so-called colony of individual plates that acts as a larger microstructural unit. The cooling rate from elevated temperatures is a critical parameter in the process of producing lamellar structure. A slow cooling rate favours the growth of laths and a coarse structure is thus generated, whereas a faster cooling rate favours the nucleation of thin laths resulting in a finer structure [41]. Under faster cooling rates, colonies nucleate not only near beta grain boundaries, but also within the beta grains, leading to a ”basketweave” structure also known as Widmanstatten structure [22].

α' (alpha prime) phase originates from martensitic (i.e. diffusionless shear) transformation of β phase on rapid cooling. For this transformation to occur, a fast cooling (i.e. water or oil quenching) is required along with a relatively lower concentration of β stabilisers [50]. α' phase has the same hcp structure as the α phase. However, it is in a form of fine acicular (i.e. needle-shaped) structure containing a high density of dislocation and stacking faults [103].

α'' (alpha double prime) phase is another form of martensitic structure that can be generated during quenching of titanium alloys with higher concentrations of β stabilisers, from lower temperatures. When a titanium alloy is quenched from lower temperatures, a higher fraction of β-stabilisers is retained which results in reducing the M_S/M_f temperature leading to the formation of α'' martensite. This phase has an orthorhombic crystal structure and is softer than α' martensite [103].

Dual phase α/β alloys typically contain three main microstructures including lamellar, equiaxed and bi-modal. Fully lamellar structure also called β-annealed structure that can be obtained during the last stage of processing route through annealing above β-transus. This structure consists of colonies of α and β plates within prior β grains along with α phase present at the prior β grain boundaries. The most important parameter in the formation of such a microstructure is the cooling rate from above β-transus temperatures (i.e. β phase field). Indeed, the plates size, colonies size and the thickness of α layer at the β grain boundaries decrease with increasing cooling rate from above β-transus[50], as shown in Figure 2.5.

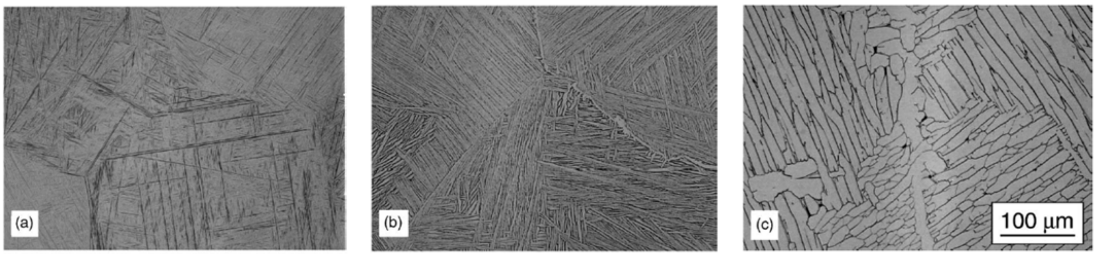

Figure 2.5: Appearances of the lamellar structure with different cooling rates: water quenched (a), air cooled (b) and furnace cooled (c) [75].

To generate a fully equiaxed structure, a considerable level of plastic deformation (i.e. strain) needs to be introduced into a lamellar structure in the α+β dual phase field. This leads to the break up of the lamellar structure into globular alpha grains. Further heat treatment at dual phase α+β temperature range followed by slow cooling is usually required to complete the spheroidization of the entire structure. An increase in the annealing time leads to an increase in the size of the equiaxed grains; thus this has to be controlled carefully to avoid grain coarsening [41]. Such globular structure is shown in Figure 2.6.

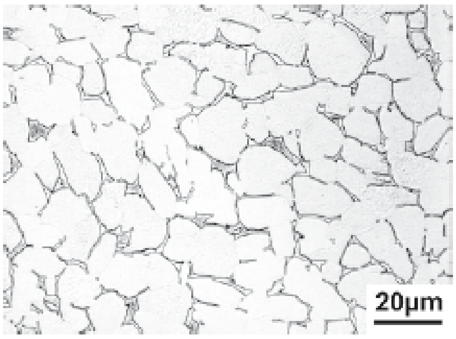

Figure 2.6: An example of a fully equiaxed structure [50].

A bi-modal structure is also achievable in α + β titanium alloys that consists of primary α grains and lamellar structure of interspersing α laths within β plates (see Figure 2.7). The process route to create such a structure is similar to that used to develop an equiaxed microstructure, with the only difference being a faster cooling rate from α + β temperature range during the final annealing stage. Several process parameters are critical in the formation of a bi-modal structure. The cooling rate in the first steps of thermo-mechanical processing impacts the thickness of the lamellar structure, and at later stage the size of primary alpha particles. The temperature of the final annealing heat treatment affects the percentage of primary alpha in the final microstructure, whereas the cooling rate from that annealing temperature affects the width of alpha laths in beta grains. An example of a bi-modal structure is displayed in Figure 2.7.

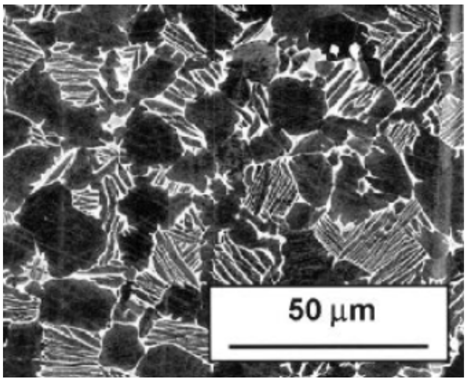

Figure 2.7: An example of a bi-modal structure [82].

2.3 Thermomechanical processing of alpha/beta alloys

2.3.1 Deformation mode

One of the prominent mechanisms of plastic deformation is slip by dislocations motion. In hcp metals they are not as symmetrically distributed as in metals with a cubic crystal structure. Primary slip systems are also fewer and their action is limited to slip of dislocation along the $\langle a \rangle$ direction. Secondary mechanisms such as twinning and pyramidal $\langle c + a \rangle$ slip are thus essential to the ductility of titanium alloys. Also, the critical resolved shear stress (CRSS) for these different systems can vary significantly from one system to another. These various factors result in an important heterogeneity of deformation and formation of strong texture in hcp metals [112].

In metallic alloys with a hexagonal crystal structure, slip can occur on 4 planes (prismatic, basal, pyramidal of 1^{st} and 2^{nd} order) and along 2 directions of $\langle a \rangle$ and $\langle c + a \rangle$ (see figure 2.8). The main slip directions are the close-packed ones of the type $\langle 11\overline{2}0 \rangle$. The planes indicated in Figure 2.8 together with the possible slip directions, suggest there are a total of 12 slip systems. However, this is not the case due to two slip systems combined action duplicating the action of other slip systems. Taking this into account there are only 4 independent slip systems [41].

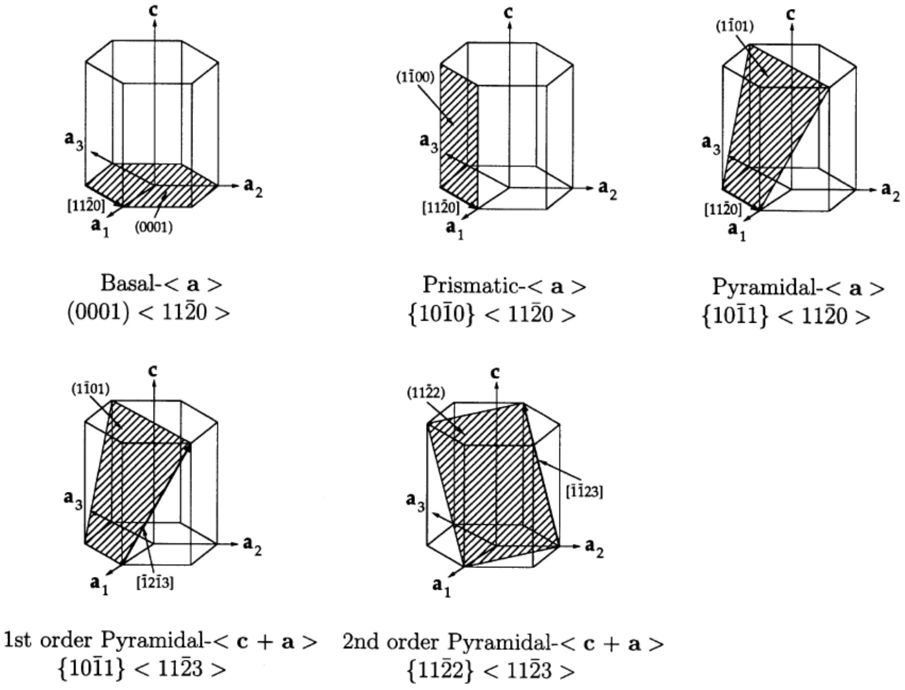

Basal-$< \mathbf{a} >$ $(0001) < 11\bar{2}0 >$

Prismatic-$< \mathbf{a} >$ $\{10\bar{1}0\} < 11\bar{2}0 >$

Pyramidal-$< \mathbf{a} >$ $\{10\bar{1}1\} < 11\bar{2}0 >$

1st order Pyramidal-$< \mathbf{c} + \mathbf{a} >$ $\{10\bar{1}1\} < 11\bar{2}3 >$

2nd order Pyramidal-$< \mathbf{c} + \mathbf{a} >$ $\{11\bar{2}2\} < 11\bar{2}3 >$

Figure 2.8: Slip systems in hexagonal structure [5].

The Von Mises criterion stating that at least five independent slip systems are required for homogeneous plastic deformation in metals is thus not met for titanium alloys, making the α phase difficult to deform. The restricted ductility exhibited by α phase is mostly due to the activation of other mechanisms such as twinning and secondary slip systems including pyramidal $\langle c + a \rangle$ [111]. However, twinning was found to be suppressed at elevated temperatures in titanium alloys with an aluminium content greater than 5% [104], such as Ti-6Al-4V.

The activation of each slip system is controlled by Schmid's law (eq.2.1) which describes the critical resolved shear stress for activation of slip systems as functions of the grain $\langle c \rangle$ orientation, the loading direction and the yield stress.

$$\tau_c = \sigma_y cos(\phi) cos(\lambda) \tag{2.1}$$

where τ_c is the critical resolved shear stress, σ_y is the yield stress, ϕ is the angle between the slip plane's normal and the direction of the load, and λ is the angle between the glide direction and the loading direction as shown in Figure 2.9.

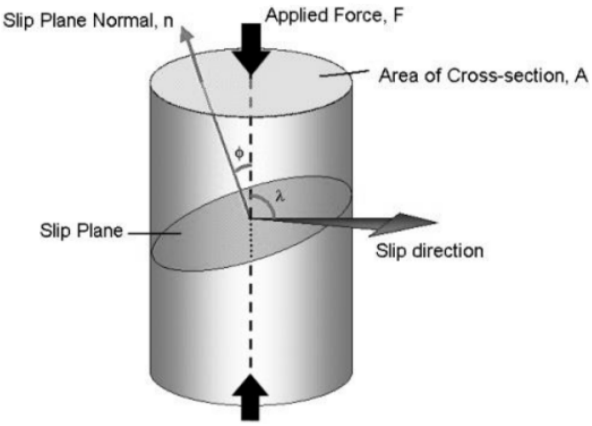

Figure 2.9: Schematic diagram showing slip mechanism in a single crystal under compressive loading [53].

With an increase in the applied load, the resolved shear stress for each slip system progressively rises until τ_c is reached. Plastic deformation then starts to occur in the form of activated slip system (i.e. dislocation motion), which is known as the primary slip. Further increase in load leads to the activation of other slip systems as their critical resolved shear stress is achieved [53].

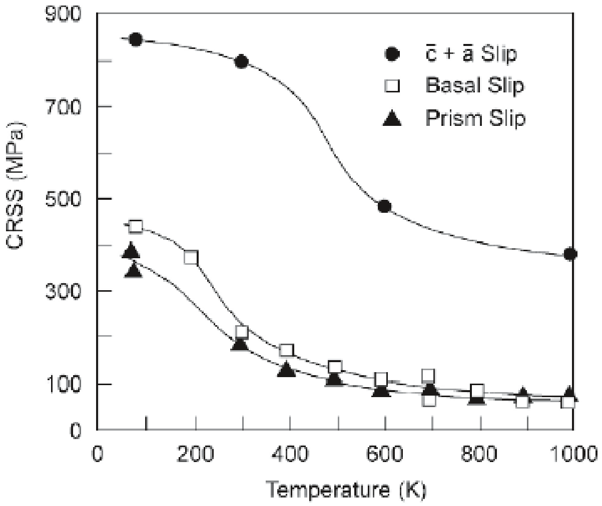

Figure 2.10: Temperature dependence of CRSS for different slip systems in single crystals of Ti-6.6Al [104].

Plastic deformation in titanium has been studied extensively to understand its heterogeneous mechanical behaviours [10, 71]. Critical resolved shear stress was found to be different for each slip system with the pyramidal one being almost twice as high as the basal and prismatic ones [104] (see Figure 2.10). The fraction of grains deformed by $\langle c + a \rangle$ slip is low in α titanium as activation of $\langle a \rangle$ slip is easier. Thus, some grains deform more easily than others, depending upon their orientation compared to the loading direction.

2.3.2 Manufacturing process

Extraction of pure titanium from its oxide forms (i.e. ilmenite, rutile) is the first stage in the production of titanium alloys. The first commercially attractive process for titanium extraction was developed in 1937 by Kroll. In this process titanium ore is initially carbo-chlorinated to remove elements such as oxygen and iron, and produce a vapour of $TiCl_4$. It is then reduced at high temperature by vapour of molten magnesium to produce metallic titanium sponge, then the impurities are removed by leaching or vacuum distillation [11]. Currently, the Kroll method remains the principal process for titanium production despite being considerably time and energy consuming making titanium a very expensive metal to produce with a price five to ten times higher than aluminium [13]. Other processes such as the FFC Cambridge, which involves electrolysis of titanium dioxide by electrolysis in molten calcium salts, and plasma and vapour phase process are investigated to reduce production costs [27], however more research is required to make them matured enough to be implemented them at industrial scales.

Titanium alloys are created at this point by crushing titanium sponge and adding alloying elements. At least two melting steps are necessary to obtain an alloy with a satisfying homogeneity in the final ingot. These operations require to be carefully controlled to achieve a high quality ingot and avoid segregations of alloying elements and formation of defects such as high density inclusions, beta flecks and voids [15].

Thermo-mechanical processing (TMP) refers to a set of sequential hot working and heat treatment stages that are performed to transform the as-cast ingots into final shape products. It also aims to achieve desired mechanical properties to meet certain in-service requirements through design and control of microstructure. Two major steps are distinguished during TMP including (i) primary working to convert ingot into mill products such as billets, flat rolled products or bars [50], and (ii) secondary working that involves forging and heat treatments during which a desired shape for the final product is obtained. An example of primary working process route is shown in Figure 2.11.

The ingot breakdown is performed through preheating with subsequent cogging at β phase temperatures, approximatively 100-150°C above the β-transus. This high temperature allows significant level of plastic deformation to be achieved without a requirement for high forces. The main aim of this operation is to homogenise the microstructure and reduce the as-cast β grain size.

Then, forging at α+β dual phase temperature range followed by an annealing above the β-transus, with a subsequent cooling to room temperature is performed. This is designed to obtain lamellar α inside the recrystallised β structure. This operation has been investigated extensively to develop a robust understanding of static recrystallization and texture development in β phase, as well as the evolution of the transformed microstructure on cooling (e.g. α variant selection, and platelet thickness) [77].

Finally, a set of hot working and annealing in the dual phase α + β temperature range is completed to break the lamellar structure into equiaxed grains, which are more ductile and desirable for further forming operations. Extensive research has been carried out to identify the mechanisms underpinning plastic flow and deformation during this forging stage, to characterise the kinetics of globularisation of α phase and the evolution of microstructure and crystallographic texture in the material [77]. The mill products are then shaped into final parts through processes like ring rolling, extrusion or closed-die forging.

Forged parts are usually subjected to a heat treatment after the forming stage. Various heat treatments are developed for different applications. Each specific heat treatment can form special microstructures to tailor desired mechanical properties. It can also be used to relieve residual stresses in the material. Ageing can occur as well in certain conditions to improve the strength of the alloy by precipitation of particles like secondary α or Ti_3Al.

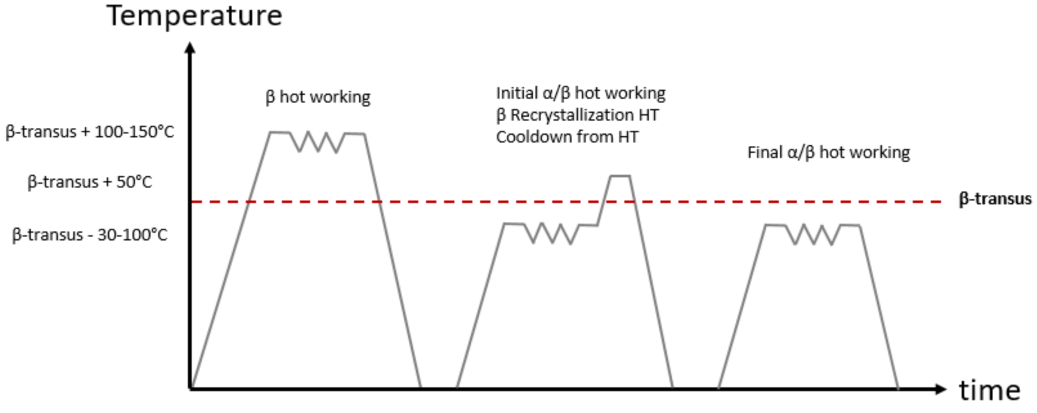

Figure 2.11: Schematic plot of primary working for titanium alloys.

2.4 Microstructural evolution during final α/β working

Globularisation or spheroidisation is the process through which a lamellar structure is transformed into a microstructure with equiaxed grains. This is crucial in tailoring microstructures in the mill products. This section summarises the outcome of previous research carried out in this area. with a particular attention to the mechanisms involved and the kinetics of the process. The modelling aspect of globularisation is also briefly discussed.

2.4.1 Mechanisms of globularisation

During hot deformation, the breakage in α lamellae occurs via the formation of α/α boundaries within the laths [102]. In zones where laths are unfavourably orientated with regards to the direction of loading, viz. lamellae that are either parallel or perpendicular to the applied force, shear bands can develop inside the laths due to stress localisation that may be caused by heterogeneities in the local microstructure. In laths favourably orientated to the loading direction, local deformation takes place through the activation of slip systems that lead to buckling, kinking or bending of the laths [42, 54]. Under large levels of strains, this leads to the fracture and complete fragmentation of the laths.

Likewise, extended dynamic recovery, also known as continuous dynamic recrystallisation, may lead to the formation of α/α boundaries [23, 73]. Dislocations introduced during hot working may be annihilated or rearranged into low angle boundaries via dislocation climb, slip or glide [29]. The misorientation angles of these low angle boundaries then increase progressively with increased strain magnitude (i.e. deformation), to a point where they turn into high-angle boundaries and recrystallised equiaxed α grains (see Figure 2.12). High temperatures and low strain rates favour such continuous dynamic recrystallisation mechanism [76]. Geometric dynamic recrystallisation is also thought to be involved in the globularisation process. This mechanism explains the serration of original high angle boundaries, as strain elongates α grains, that eventually leads to pinching of the high angle boundaries, separating laths into smaller grains [7].

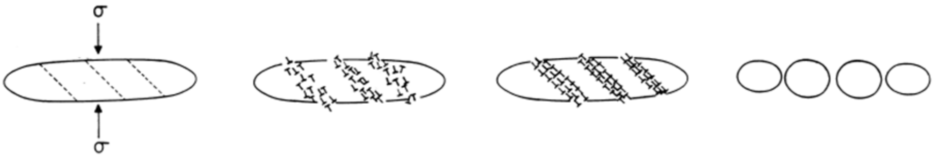

Figure 2.12: Schematic of the steps of globularisation [85].

Boundaries formed either by recrystallisation or localised shear, create unstable 90° dihedral angle with both α/β and α/α interface boundaries. Driven by interfacial tensions, diffusion of β phase occurs along α/α boundaries known as thermal grooving. This process is known as boundary splitting and happens during deformations followed by short annealing times at temperatures below the β-transus. The rate of penetration of β phase depends on diffusion kinetics and the ratio of the interfacial energies of α/α boundaries and the α/β interfaces. The diffusion of β phase along α/α boundaries ultimately leads to a pinch-off (i.e. fragmentation) of laths [95, 116]. The boundary splitting process is schematically visualised in Figure 2.13.

Under annealing times, microstructure coarsening takes place and further reduces the aspect ratio of α grains [95]. This mainly occurs through termination migration, edge spheroidisation and Ostwald ripening. Termination migration describes the movement of atoms from the curved to the flat surface of a particle. This mechanism is driven by a chemical potential gradient that results from the curvature difference between the termination and flat interface [89]. This dissolution of termination and mass transfer to the flat surface leads to shorter but thicker α grains (see Figure 2.14). Ostwald ripening characterises the mass transfer from small to

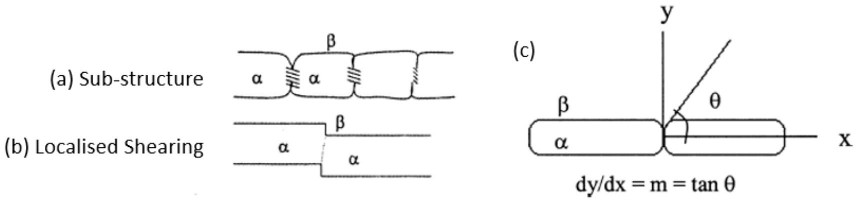

Figure 2.13: Schematic illustrations of intra-phase boundaries splitting (a and b), and the grooving process (c) [95].

large particles. The small particles gradually shrink and eventually disappear while the larger ones become coarser. This is to reduce the energy associated with α/β interface [18]. Edge spheroidisation process happens via capillary forces due to curvature difference; that leads to the formations and growth of ridges which eventually decompose the edges into spheres [89].

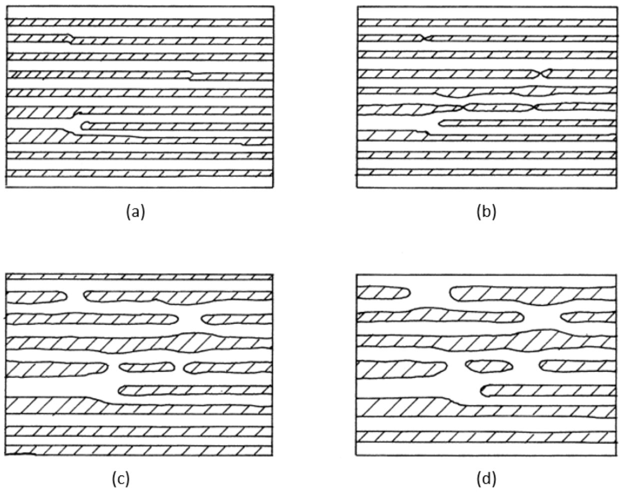

Figure 2.14: Progression of termination migration process [89].

2.4.2 Kinetics of globularisation

The kinetics of globularisation in titanium alloys and the influence of different parameters on globularisation have thoroughly been investigated to improve practices of industrial production [12, 35, 58, 93, 99, 105]. The effects of some of these parameters have been reviewed in this literature survey, despite the fact that they are not completely independent of one another during processing.

2.4.2.1 Effect of initial microstructure

Thermo-mechanical processing prior to final forging at α + β temperature range can produce a wide range of microstructures from fine acicular to coarse lamellar grains. These microstructures then behave differently during hot working stage of the manufacturing. For instance, the α lath thickness is an important parameter for globularisation kinetics such that it is easier to break the thinner laths into an equiaxed structure [35, 110]. Figure 2.15 illustrates this difference for the spheroidisation kinetics between a fine and a coarse initial structure. The thin structure has a much higher globularised fraction than the coarse structure. Shell and Semiatin [91] found that a certain level of strain is required to generate α/β interfaces within the laths which is lower for thinner structures. Furthermore, the faster kinetics of globularisation in the fine structure was attributed to the ease of β phase penetration along the generated boundaries. However, the fine microstructure was found more sensitive to coarsening during preheating step of the hot compression tests, where the kinetics of globularisation was decreased with an increase in temperature for the fine martensitic structure.

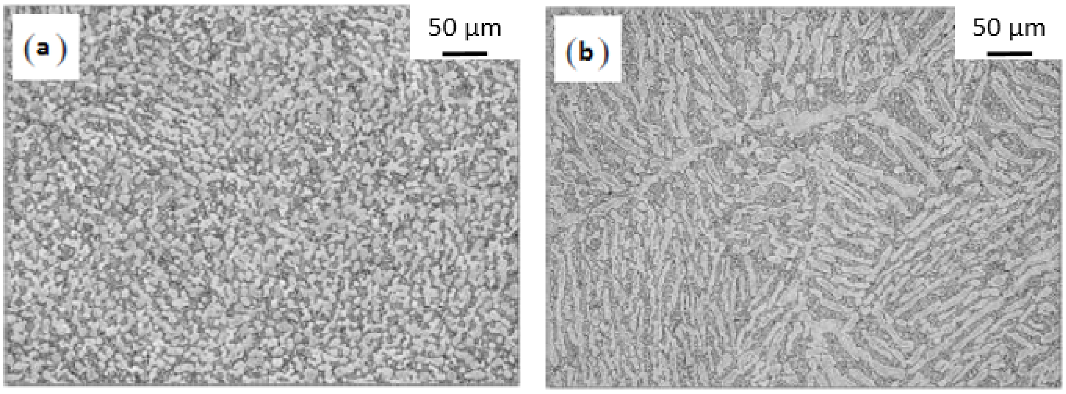

Figure 2.15: Microstructures after multi-step forging for (a) a fine structure and (b) a coarse structure [36].

The impact of prior-β grain size on spheroidisation kinetics in Ti-6Al-4V alloy was also investigated and two trends were identified depending on the grain size. Prasad et al. [68] for instance has found that Ti-6Al-4V alloy with prior-β grain sizes of 0.5-1 mm and 2-3 mm have a similar behviour, implying that the kinetics of globularisation would not be influenced by grain size for prior-β grain size larger than 500 μm due to the intragranular nature of spheroidisation mechanism. On the other hand, work reported in [78] showed that for material with prior-β grain size lower than 500 μm spheroidisation rate increases with decreasing grain size. Zhao et al. [114] observed a similar trend in their study on TA15 alloy. The faster rate of spheroidisation observed in the material with smaller grain size has been explained by the higher density of grain boundaries which provides nucleation sites for spheroidisation [91]. Also, shorter laths are nucleated in smaller grains which promotes faster spheroidisation.

The orientation of lamellae with respect to the direction of loading and its crystallographic orientation are also critical parameters affecting the spheroidisation process. They are observed to be responsible for the heterogeneous behaviour of α colonies during deformation [8]. Owing to intrinsic heterogeneity in the lamellar structure, some colonies undergo higher levels of deformation than the others. Since local shear strain in the α laths is a driving force for the initiation of globularisation, it appears that even within localised microstructural regions, there is significant variation in the rate of dynamic globularisation and/or accumulation of stored energy for subsequent static globularisation [57]. Bieler and Semiatin [8] studied the effect of initial grain orientation on the globularisation kinetics during upsetting of Ti-64 alloy. It was found that laths with the c-axis within 15° of the compression direction were stable even after large levels of applied strain. This was because neither prismatic or basal slip systems were available in that particular orientation and the lamellar structure thus remained intact. When the c-axis was nearly perpendicular to the compression direction, the prismatic slip system was partially activated, but it was found inefficient due to the occurrence of concurrent recovery. When the orientation included the c-axis between 15° and 75° inclination from the compression direction, both basal and prismatic slips occurred and globularisation rate was substantially high with the highest efficiency for a condition where the c-axis was orientated at 55° to the loading direction. It was observed that in some regions, shear bands may develop, which led to kinking of lamellae [8]. These bands led to easy flow of material around hard zones (i.e. with α laths that are unfavourably orientated to the loading direction) that survive after deformation. A similar impact of the α lath orientation was observed by Mironov et al. [54] during warm working of Ti-64 alloy. Both reached a similar conclusion whereby a change in loading direction could be beneficial to the microstructural evolution at warm temperature.

2.4.2.2 Effect of strain

Strain plays a pivotal role in the spheroidisation of lamellar structures and its impact during both dynamic and static spheroidisation has been investigated extensively. It has been observed that a minimum level of deformation is needed to trigger the spheroidisation mechanisms in a material. This level of strain serves to kink, buckle or bend lamellae orientated favourably to the loading direction while the other laths rotate to accommodate further kinking [61] (see Figure 2.16). The strain also serves to form intraphase boundaries within the α laths before boundary splitting mechanism starts to occur. At later stages, the globularised fraction expands with an increase in strain, following a sigmoid curve trend until completion, for a certain level of deformation. The levels of strains at the initiation and completion of spheroidisation vary with parameters such as the alloying elements, strain rate and temperature. For example, Wu et al. [105] found the initiation and completion strain values of 0.34-0.59 and 3.40-6.80, respectively, in a study on TA15 alloy, whereas Semiatin et al. [79] found strain levels of 0.75-1 and 2-2.5 for Ti-6Al-4V alloy. An example of the evolution of the globularised fraction with strain is shown in Figure 2.17.

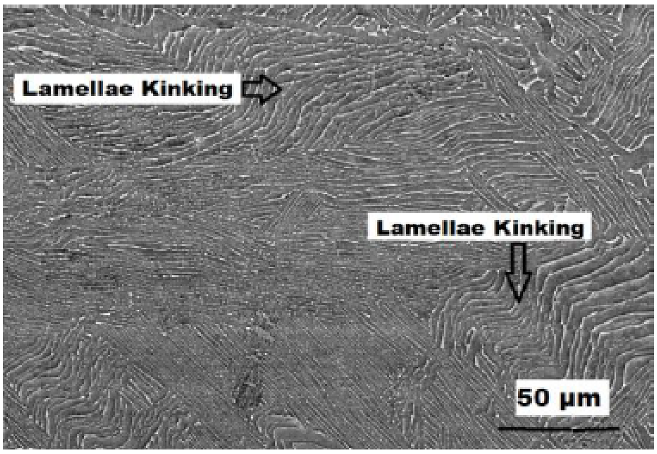

Figure 2.16: Illustration of the kinking of laths during hot deformation of a Ti-6Al-4V specimen[90].

When combining hot working with post-deformation annealing, similar

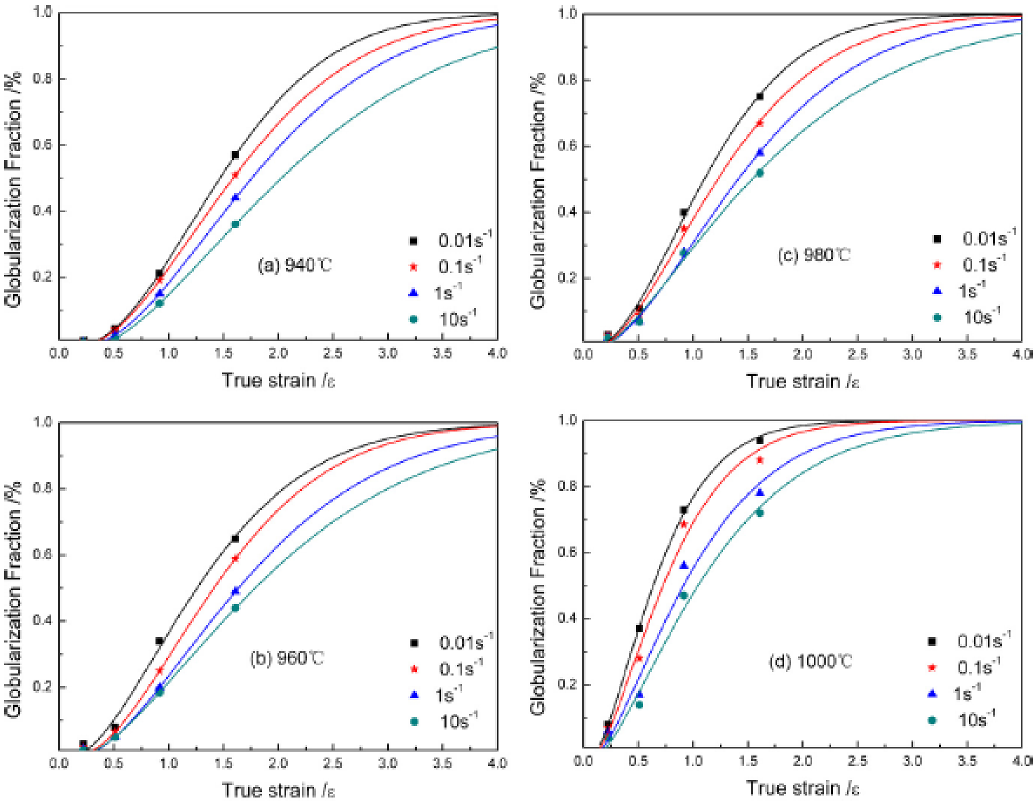

Figure 2.17: Fraction of dynamic globularisation in BT25 titanium alloy as functions of strain and strain rate at 940°C (a), 960°C (b), 980°C (c), 1000°C (d)[51].

observations were made. It was reported that increasing pre-strain leads to an increase in spheroidised fraction after heat treatment [108]. The level of strain required to obtain fully equiaxed structure is lower for dynamic globularisation due to mechanisms such as boundary splitting and termination migration being active during annealing to complete the separation of alpha grains. Annealing however generates coarser microstructure.

2.4.2.3 Effect of strain rate

Microstructural evolution is also affected by the deformation rate. Under high strain rates, strain localisation and heterogeneous deformation is observed within the material; for instance, the development of adiabatic shear [86]. These are described as a localised plastic instability phenomena resulting from dynamic impact and high speed loading [39]. Seshacharyulu et al. [86] observed kinking of lamellae after a strain of 0.7 at a strain rate higher than $0.1s^{-1}$ in Ti-6Al-4V alloy, whereas globularisation of α particles were noticed at lower strain rates. Hence, it can be deduced that the higher the strain rate the lower the spheroidisation kinetics. Such a behaviour is visible in Figure 2.17 where full globularisation is reached at lower strains for low strain rates.

At lower strain rates, homogeneous deformation is dominant that leads to higher fraction of globularisation. Zhao et al. [114] explained this based on the fact that recrystallisation does not occur at higher strain rates and as a result α laths stay in a deformed condition and globularisation is omitted. Low strain rates at elevated temperatures promotes recovery and diffusion processes which are essential for the development of α/α boundaries, for penetration of β phase along these boundaries and hence completion of termination migration [61]. The enhancement of diffusion process at lower strain rates however leads to grain growth and a microstructure with larger grains [93].

Fan et al. [18] found that strain rate has no significant impact on microstructural evolution in TA15 alloy after pre-strain and post-deformation annealing. Strain rate only affects those mechanisms that are active during the deformation process, and thus the generated substructures which in turn affects boundary splitting. This mechanism however occurs only during the first stage of annealing and plays a relatively insignificant role in the process of globularisation [96]. The evolution of substructure hence has an indirect effect on spheroidisation. Similarly, Semiatin et al. [80] showed that although deformation rate has an effect on dynamic spheroidisation rate in titanium alloys, it is of second order importance compared to the strain effect.

2.4.2.4 Effect of deformation temperature

The hot working temperature can have a significant effect on microstructural evolution in titanium alloys. For instance, the fraction of α phase and the thickness of α laths can be influenced by the hot working temperature [95]. Yet, Song et al. [93] found that the temperature effect on globularisation rate is complex, and smaller when compared to that of the strain level. Likewise, Stefansson et al. [96] concluded that the deformation temperature does not have a significant influence on the final globularisation fractions, after conducting annealing on Ti-6Al-4V over a temperature range between 900°C and 955°C. On the other hand, Wang et al. [99] and Ma et al. [51] reported an increase in the dynamic spheroidisation kinetics with increased temperatures. This trend was related to the higher diffusion rate and thus the ease of intraphase boundary migration at higher temperatures [105]. Song et al. [94] also detected an increase in globularisation rates with increased temperatures. Nevertheless, relationships for their prediction models were derived from the Zener-Hollomon parameter which describes both strain rate and temperature simultaneously, and it is rather difficult to decouple the effect of each parameter separately.

Temperature also affects the deformation mechanisms observed in the α laths. Indeed, the applied stress required to generate shear banding and lamella buckling evolves with temperature. Below a critical temperature, the required stress to generate lamella buckling is higher and hence shear bands are observed in the material, whereas above this critical temperature, the opposite is observed [113] (see Figure 2.18). Since shear bands develop locally and at low temperature, globularisation occurs only in these zones, and lower kinetics of microstructural evolution tend to be observed.

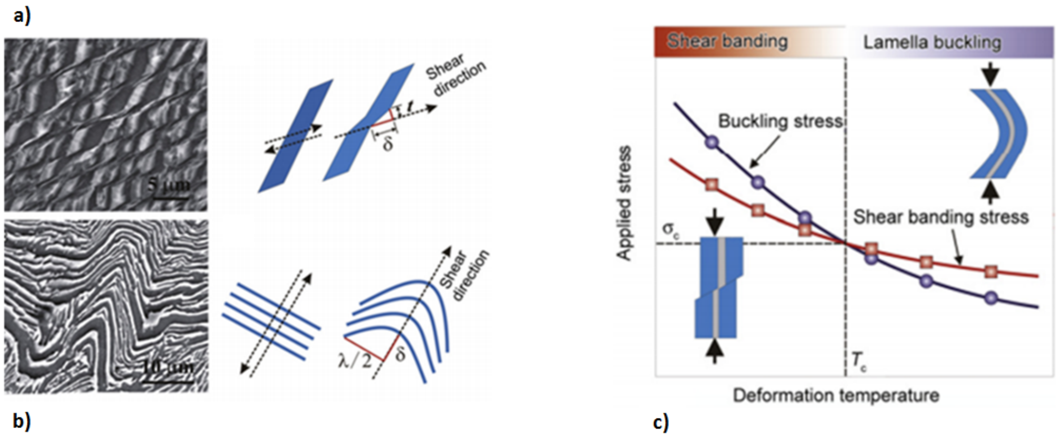

Figure 2.18: Influence of temperature on active deformation mechanisms of α laths partitioning, (a) illustration of shear band formation, (b) illustration of lammela buckling, and (c) competition mechanism between the stress required for shear band formation and lamella buckling [113].

For fine martensitic structures, unlike lamellar structures, increasing the deformation temperature leads to a decrease in globularisation kinetics. This is due to the coarsening of the α laths during pre-heating step [91]. Nevertheless, the spheroidisation kinetics for this type of microstructures is still faster than that for coarse lamellar microstructures.

During deformation at lower temperatures, heterogeneous strain localisation may occur that leads to initiation of defects such as cracks [86]. Even so, these working conditions may be desirable to produce ultra-fine ($\leq$ 1 μm) equiaxed grain structure since higher temperatures leads to significant grain growth that compromises the production of microstructures with grain size below a certain size.

2.4.2.5 Effect of post-deformation annealing

Achieving a fully equiaxed structure typically requires a post-deformation annealing process. During this heat treatment, only diffusion based mechanisms such as boundary splitting or termination migration occur. It is thus logical to find a temperature that has a maximised impact on globularisation kinetics. Stefansson and Semiatin [95] for instance have reported a tenfold decrease in kinetics when the heat treatment temperature increased from 900°C to 955°C for Ti-6Al-4V alloy (see Figure 2.19). Similar behaviour was observed by Sheed et al. [90] as well. Although higher temperatures yield improved spheroidisation kinetics, temperatures closer to the β-transus (e.g. $\geq$970°C for Ti-6Al-4V) are avoided. This is because the volume fraction of alpha phase decreases sharply and the post heat treatment microstructure is similar to a β-transformed microstructure.

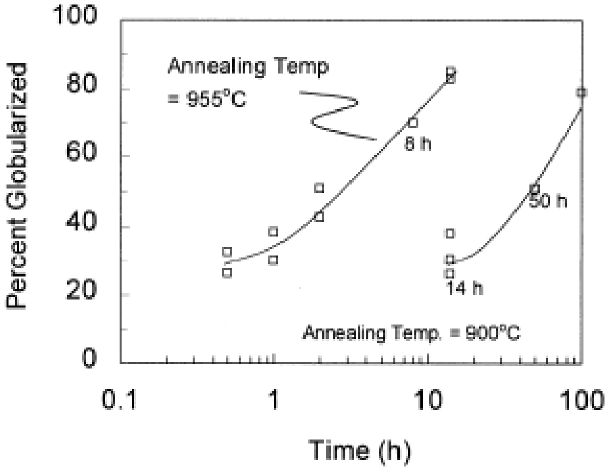

Figure 2.19: Effect of annealing time and temperature on the fraction of globularised α [96].

The fraction of globularised α also increases with annealing time, as shown in Figure 2.20. The aspect ratio of α grains decreases sharply after a short annealing time and become more sluggish afterwards. Despite that, longer annealing is still performed to enhance globularisation [62]. Nevertheless, the fraction of globularised α as a function of time follows an asymptotic trend [18], thus after a certain annealing period the kinetics of spheroidisation approaches a plateau. Furthermore, the effect of annealing duration on grain growth should carefully be taken into consideration as obtaining higher fractions of spheroidisation with larger grain size is not of interest for most applications.

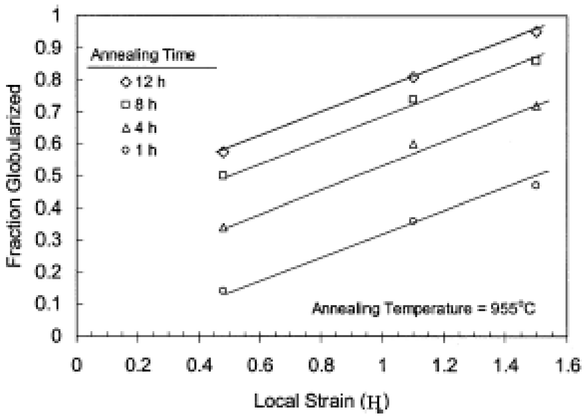

Figure 2.20: Effect of annealing time and pre-strain on the fraction of globularised α [95].

2.4.2.6 Effect of strain path

It was reported that strain levels of 2-3 were required to reach a fully globular structure [72]. The use of processes such as uniaxial compression or extrusion to apply such high level of deformation leads to significant changes in shape and dimensions of the material. Also, strong texture usually develops during these types of deformation which is undesirable. Furthermore, large strains may lead to the initiation of various defects such as cracks and cavities in the material. Hence non-monotonic deformation processes such as cogging are used to manufacture industrial products. The frequent changes in strain path included in these processes affect microstructural evolution in a number of metals. For instance, a change in rolling direction enables activation of a higher number of slip systems in CP titanium which leads to higher levels of interactions between dislocations, a lower intragranular misorientation and as a consequence a higher number of high angle grain boundaries [26]. Likewise, globularisation in α+β titanium alloys is affected by strain path and it has been the subject of numerous studies [36, 37, 67, 72, 81]. For example, Figure 2.21 shows the difference in microstructures between torsion and reversed torsion when a similar level of deformation is applied. It clearly appears that reversed torsion yields lower globularisation kinetics. Figure 2.22 further illustrates the effect of strain path on globularisation kinetics during other processes.

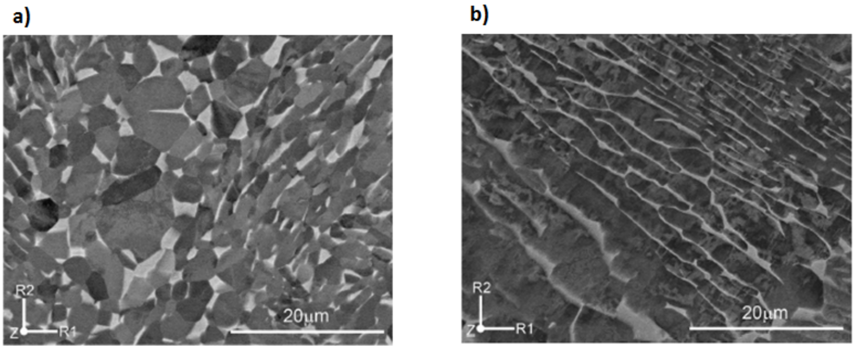

Figure 2.21: Microstructures achieved after applying a strain of 0.5 in torsion (a) and reversed torsion (b) [56].

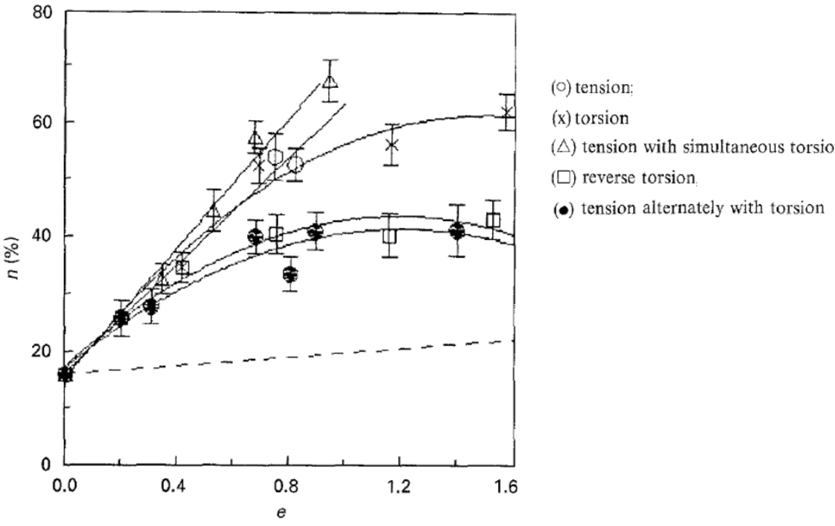

Figure 2.22: Fractions of equiaxed particles vs accumulated strain for different strain paths [37].

Multiaxial forging along three orthogonal directions was investigated to create a globular sub-micron crystalline structure in titanium alloys [72, 115]. Experiments were performed at lower temperatures (450-800°C) with a strain increment of 0.4 and the samples were quenched and machined between each forging to keep all the edges straight. Globularisation was observed after strain of about 3 in a material with initial martensitic structure, while in the material with a coarse lamellar structure, heterogeneous transformation was observed and ≈30% of laths remained at the end of the process. Microstructural evolution was linked to the formation of high angle boundaries and incoherent inter-phase boundaries whose fraction increased more significantly with strain magnitude when a change in strain path was introduced (see Table 2.1). The change in strain path was found to be advantageous in activating more slip systems. This confirmed the findings previously reported by Bieler and Semiatin [8] and Mironov et al. [54] where it was concluded that due to the presence of laths with ”stable orientation” with respect to the loading direction, a change in strain path would enhance the globularisation process.

Table 2.1: Effect of cumulative strain for monotonic and multiaxial deformation process on the fraction of different types of boundaries [72].

type of boundary	fraction (%)				
	one deformation step (30%)	one deformation step (60%)	three deformation steps	five deformation steps	twelve deformation steps
low angle boundary (2° to 15°)	90	90.3	81.1	54.2	31.1
high angle boundary (¿15°)	10	9.7	18.9	45.8	68.9

Other studies focused on the cogging/side pressing process of titanium alloys. For instance, Song et al. [94] found that this procedure improved the globularisation kinetics in TC11 alloy compared to uniaxial compression. This is also in agreement with the findings reported by Bieler and Semiatin [8] and Mironov et al. [54]. Nevertheless, very little information is provided on the process parameters used for the cogging operation; quantitative analysis or comparison with other studies is thus complicated.

Kim et al. [36] also examined multi-axial forging of Ti-6Al-4V alloy and observed that the globularisation rate was strongly dependant on the instantaneous microstructural evolution (i.e. thickness of α laths and fraction of α phase) during each compression step that stems from the non-isothermal conditions as well as the deformation and reheating cycles. Both forging temperature and initial α lath thickness were found to be influential on the kinetics of globularisation. Full globularisation was only achieved in a thin structure at high forging temperatures. During the entire forging process, a dual phase titanium alloy experiences an effective strain of around 2.4; however, the localised strain at microstructure scale, which is different due to the non-isothermal conditions and the changes in strain path, can be varied. Quantitative comparison of the kinetics of globularisation between a forged material and that resulted from other processes such as uniaxial compression is thus difficult. Even so, it clearly appears that when deformation is performed at lower temperatures (e.g 900°C), spheroidisation kinetics are much lower than that of monotonic deformation (e.g. compression testing).

Sheed et al. [90] did not notice any globularisation after a strain of 1.5 applied by multi-directional forging. Instead, the observed material microstructure consisted of mainly non-deformed, kinked and fragmented α lamellae. These microstructural features were interpreted as a presence of large amount of strain energy stored in the material as a result of the deformation process. This might have been the case, as α globularisation took place after a 2hrs post-deformation annealing at elevated temperature.

The aforementioned reviews demonstrated that globularisation can be achieved with multi-axial cogging, even though discrepancies were noted regarding the kinetics compared with monotonic deformations. Also, restrictions are indicated concerning the initial structure, that should be fine lamellar or martensitic. These studies however explored the cogging operations as a whole rather than investigating individual steps involved to provide an insight into the evolution of microstructure throughout the process. For instance, the effect of reheating frequency and duration or the strain at each increment were not investigated. Besides, the reported works were mostly on the kinetics of globularisation and little emphasis are made on the mechanisms underpinning the variations in kinetics.

Some studies were focused on microstructural evolution in titanium alloys during torsion tests [56, 67]. Strain reversal led to a decrease in globularisation kinetics compared to monotonous torsion for the level of applied strain [67]. Additional strain reversal was observed not to increase the kinetics but rather made the progress of globularisation sluggish (see Figure 2.23). The lower rate of globularisation observed was attributed to a reduction in the rate of dislocation multiplication by strain reversal, which decreases the rate of recovery, and thus the formation of sub-boundaries. Furthermore, the formation of shear bands was delayed during strain reversal and the fraction of kinking in lamellae was also decreased. Muszka et al. [56] further examined the impact of strain reversal on microstructural evolution during torsion in Ti-6Al-4V alloy. It was reported that the strain reversal led to the rearrangement of the dislocation structure, manifested by a lower peak stress during reversal of the direction of straining, which consequently lowered the dislocation density. Under this condition lower frequency of micro-band formation was expected to occur within α laths making it more difficult to kink lamellae and therefore led to a smaller rate of dynamic globularisation. Strain reversal also lowered the magnitude of strain energy induced during deformation compared to monotonic torsion, which led to lower driving forces for static globularisation [56]. Additionally, forward torsion produced more dynamically globularised grains that continue to coarsen during the heat treatment, leading to a higher globularisation rate compared to strain reversal. The strain increment was also considered during reversed torsion and it was observed that if a certain amount of monotonic strain (i.e. ≈0.6 in this case) is exceeded, then satisfying globularisation rate can still be achieved.

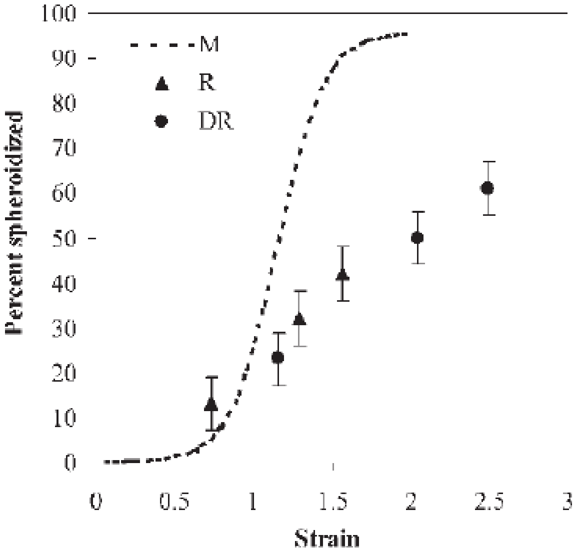

Figure 2.23: Fraction of equiaxed grains as a function of accumulated strain for different strain path in torsion: monotonic (M), reversed (R), and double-reversed (DR) [67].

Korshunov et al. [37] reported microstructural evolution in titanium alloy VT9 under different loading conditions. Monotonic deformations (i.e. tension, torsion, tension with simultaneous torsion) were found more efficient than non-monotonic methods (i.e. reverse torsion, tension alternately with torsion, multi-axial forging) for globularisation. The measured kinetics of globularisation as a function of strain level for these deformation modes are shown in Figure 2.22. Similar reasons as those suggested by Muszka et al. [56] were proposed for the difference in globularisation rates between monotonic and non-monotonic deformations. The multi-modal deformation tests (i.e. tension with simultaneous torsion) resulted in the highest rate of dynamic spheroidisation. This was interpreted on the basis of the availability of higher number of deformation mechanisms and slip systems during these methods of deformation, which helped breaking the structure.

The impact of prior-β processing on microstructural evolution during α + β forging was also investigated [38]. Lamellar structures obtained through cooling of heat treated β phase was found to have homogeneous morphology and crystallographic orientation distributions. On the other hand, after deformation in β stability temperature range, elongated β grains were resulted which affect the nucleation and growth of α phase upon cooling, modifying the morphology and orientation distribution of the lamellae [38, 114]. This in turn has been shown to affect the globularisation process. Because of the shorter and non-randomly orientated lamellae present in the deformed prior-β grains, higher spheroidisation rates were observed. Furthermore, the direction of α + β forging compared to that of the β upsetting was found to be important [114]. It was reported that when the two directions were perpendicular, higher globularisation rates were achieved.

Several studies have been reported in literature in which different deformation processes such as cross rolling, reversed torsion or cogging have been used to examine the effect of strain path on globularisation. The implemented deformation procedures reported in these studies allowed homogeneous deformation to be achieved even for high levels of strain. However, these deformation methods do not apply the same loading conditions, and as a consequence, different deformation mechanisms might be activated leading to discrepancies in the observed globularisation kinetics.

During multi-pass rolling or cogging, reheating steps are often required in order to maintain the desired temperature throughout the sample. In the reviewed papers, since the specimens studied were small, short reheating times were used. For example, Ari-Gur and Semiatin [2] and Kim et al. [36] used 3 minutes and 10 minutes respectively for annealing between different forming steps. These short annealing times were not enough to affect the microstructure significantly, although a slight grain coarsening was somewhat observed after several deformation and reheating cycles [36]. On the other hand, during industrial cogging operations, the time required to reheat a bar is much longer (i.e. in excess of a few hours). This may lead to microstructural changes and affect the following steps of the process, however these potential effects have not been investigated.

2.4.2.7 Effect of cooling rate

Thermo-mechanical processes, consisting of sequential mechanical deformation and thermal treatments lead to major microstructural evolutions in titanium alloys. These processes include heating and cooling rates under which the material is heated or cooled to a certain temperature. In titanium alloys, the morphology of primary α is also affected by the cooling conditions. During slow cooling from temperatures in the α+β range, primary α grows in every spatial direction [82]. Both the size and volume fraction of primary α increase with decreasing temperature under slow cooling, and only a small fraction of secondary α can be formed. On the other hand, under fast cooling condition, the growth of primary α has only been observed down to temperatures around 840°C when secondary alpha platelets were formed within the β matrix. This strongly decreases the supersaturation level of the matrix which drives the growth of primary α during continuous cooling and thus hinders the growth of primary α [82]. As a result, in a material that undergoes slow cooling, primary α with lower aspect ratios are observed compared to that of a material subjected to water quenching from the same elevated temperature. This difference is even more pronounced for higher temperatures, as rapid cooling from elevated temperature results in an increased aspect ratio and decreased volume fraction of α phase decreases. For example, Stefansson et al. [96] observed a significant reduction in aspect ratio in a material that was slow cooled from 955°C compared to that of a material cooled from 900°C. However, as the aspect ratio of primary α grains decrease towards 2 (i.e. the grains become globular) due to deformation and annealing at elevated temperature, the effect of the cooling rate become less significant.

2.4.3 Prediction of globularisation

Process modelling has become increasingly important for industry, as the need for improved productivity and product quality at reduced cost is growing. Finite element analysis (FEA) provides the likely occurrence of thermal and mechanical process that a material experiences during manufacturing, to a reasonable accuracy. However, prediction of microstructural evolution and the development of various microstructural features that determine the mechanical properties of the final component is still not well developed to the same extent. Prediction of microstructural evolution is nonetheless crucial to control the final properties of a component, optimise process parameters, and understand material behaviour during multi-stage processes [25]. Hence extensive research has been carried out to develop microstructural predictive models and a wide range of approaches have been adopted [34, 48, 100, 107].

Using empirical equations to estimate microstructural changes is a common and practical method that has been undertaken extensively. For example, power law functions are used to describe recrystallisation during hot working, and continuous cooling transformation (CCT) diagrams to depict microstructural evolution during cooling of steels from elevated temperatures [25]. To capture the evolution of dynamic globularisation in titanium alloys, an Avrami type equation (eq.2.2) is most often used [51, 93, 99, 105]. It is a phenomenological model describing the kinetics of isothermal phase transitions which proceed through nucleation and growth [20]. Transformations described by this model are found to follow a s-shape profile where the kinetics are slow at the beginning and the end of the transformation but rapid in between. The model's constants are determined as a function of the process parameters such as strain rate and temperature. This type of model fits well with the dynamic globularisation process during monotonic deformation trials. However, its sigmoid shape appears to be insufficient for trials with a change in strain path changes (i.e. deformation direction) (see Figures 2.22 and 2.23). Nonetheless it was successfully used to predict spheroidisation during a cogging procedure [94].

$$f_g = 1 - exp(-k(\varepsilon - \varepsilon_c)^n) \tag{2.2}$$

Semiatin and Furrer [76] developed an equation (2.3) for the estimation of the fraction of α grains that undergo static globularisation as a function of process parameters such as strain, annealing time and temperature. Experimental data from Stefansson and Semiatin [95] were used as a basis for this phenomenological model.

$$f_{sg} = (a\varepsilon + f)logt + b\varepsilon + cT + d \tag{2.3}$$

These types of models are easy to use and require low computational power, however their development requires extensive experimental data. Further, they are limited to special conditions specific to process parameters range used during a certain deformation process on a material with specific alloying elements.

Another approach to describe microstructural evolution is by the aid of advanced statistical methods such as artificial neural networks. Such tools allow evaluation of a large number of input parameters and are able to solve problems with highly complex and non-linear relationships between variables without a need for hypothesised mathematical model [45]. This method was used to predict both static and dynamic globularisation in titanium alloys with a reasonable accuracy [34, 100, 107]. Note that the capabilities of this method depends greatly on the amount of available data as well as the type of neural network chosen. Also, this method does not provide any physical insight into the process, although it may reveal trends in data-sets with multiple inputs [25].

A physically based approach has also been developed to describe the metallurgical changes happening during material processing. In this approach, basic phenomena underpinning the microstructural changes are characterised, and a number of material features (i.e. internal-state variables) such as the dislocation density are used as inputs. This method is capable of capturing some of the inherent complexity in the process, and achieving acceptable accuracy, while expending an acceptable computational effort and cost [25]. The first step in this method is to derive the occurring phenomena such as restoration and work hardening and represent them with a set of equations using the internal-state variables. Genetic algorithm based method is then used along with experimental tests to solve these equations. This method was successfully used to predict material flow stress, recrystallisation and grain growth [16, 44, 97] but only few reported on the globularisation process. Yang et al. [109] and Gao et al. [24] took into consideration the dynamic globularisation in their equation set and achieved a reasonable match with experimental data, whereas Babu and Lindgren [3] achieved the same result by considering both dynamic and static globularisation in their model.

Theoretical approaches were proposed to predict the time required for boundary splitting mechanism and also for termination migration mechanism during heat treatment. Using the thermal grooving theory developed by Mullins [55], Stefansson and Semiatin [95] established the time required for penetration of the β phase along α/α interface according to equation 2.4.

$$t_p = \frac{0.2 * {d_\alpha}^3}{A * m^3} \tag{2.4}$$

In equation 2.4, d_α is the average thickness of α lath, m is the slope of the groove and A is defined in equation 2.5.

$$A = \frac{C_F \gamma_{\alpha\beta} V_M D_\beta}{RT} \tag{2.5}$$

In equation 2.5, $\gamma_{\alpha\beta}$ is the interface energy, V_M is the molar volume of the matrix, D_β is the diffusivity of the solute atoms through the matrix, R is the gas constant, T is the temperature and C_F is the composition factor. The composition factor is used instead of the diffusion rate of solute atoms in the matrix to correct for the fact that neither the α nor the β phase is a thermodynamically stable solid solution in Ti-6Al-4V alloy [76]. This model was applied to the experimental data from Stefansson and Semiatin [95] and the prediction time were consistent with the observations.

At longer annealing times, termination migration mechanism occurs where attempt has been taken by Semiatin et al. [83] to establish the kinetics of the process on the basis of Fick's diffusion law. They proposed equation 2.6a for the time τ required for the completion of spheroidisation, considering a round remnant α phase of average diameter d_α and average thickness w.

$$\frac{\tau}{\tau'} = \frac{\xi^3 - [0.328\xi^{7/3}(1 + \sqrt{1 - 0.763\xi^{-4/3}})^2]}{4[\frac{2(1+\xi)}{3(0.5-0.572\xi^{-1/3})} + \frac{0.5\xi^{1-3}+0.665\xi^{2/3}}{3(0.143+0.934\xi^{-1/3})}]} \tag{2.6a}$$

$$\xi = (w/d_\alpha) + 0.5 \tag{2.6b}$$

$$\tau' = d_\alpha^3 RT / C_F \gamma_{\alpha\beta} V_M D_\beta \tag{2.6c}$$

Time required for the completion of spheroidisation predicted by equation 2.6a were in a good agreement with experimental observations [83]. Based on the same approach, other studies adapted the equation to take into consideration the geometry of remnant α grains. For example, Park et al. [60] looked at the termination migration kinetics of rod shaped α phase, while Park et al. [62] examined the case of elliptical α phase, and both achieved a reasonable convergence.

These physically based models enabled a reasonable estimation of the fraction of globularised α after a specific annealing period. For instance, for the conditions tested in [62], it was found that 75% of globularisation was achieved after an annealing of 8hrs and that to reach full globularisation an annealing in excess of 39hrs was required which is much longer than the durations in industrial processes. Besides, no indication on the morphology of the non-globularised α after 8hrs annealing was provided by the model. Thus it is not practical for industrial use.

2.5 Summary

Microstructural evolution in titanium alloys during hot deformation and heat treatment was studied extensively in the last decades. A large body of works have been carried out to provide mechanistic understanding of the phenomenon. Studies focused on the mechanisms involved in the globularisation process [23], the kinetics of microstructural changes [51], and on the applications of such a process (e.g., the production of submicron crystalline structures) [115]. The most common approach was to carry out hot compression or rolling tests and analyse the microstructure of the deformed samples. This led in particular to the development of various predictive models both empirical and physically based.

Although studies provided knowledge on the mechanisms and kinetics of globularisation, understanding of certain aspects of the process is still lacking. For instance, capability to predict microstructural evolution during industrial cogging process is limited. A few research works investigated the effect of the change in strain path during various manufacturing processes on globularisation [37, 67], others concentrated particularly with the cogging operation [36, 90, 94]. However, the effect of each stage of the manufacturing process (deformation step, heat treatments) as well as the influence of parameters such as strain increment and the duration of annealing steps was mostly overlooked. As a result, a simple empirical model that takes into consideration both dynamic and static parts of globularisation during cogging has not been produced.

This work is thus intended to shed light on the effect of process parameters (e.g. strain increment, direction of loading, annealing frequency, annealing duration) during cogging operation on microstructural evolution of Ti-6Al-4V alloy. The proposed approach is to replicate the cogging process on laboratory scaled samples followed by a quantitative analysis of the microstructural evolution.

Chapter 3

Experimental methodologies

This chapter summarises the experimental procedures undertaken and the equipment used throughout the course of this EngD study on the evolution of microstructure during thermo-mechanical processing of titanium alloy Ti-6Al-4V with a particular focus on globularisation. The thermo-mechanical processes implemented are resembling the secondary α/β hot working stage of the manufacturing processes of Ti-6Al-4V for microstructure modification. This chapter starts with an overview of the study, followed by a thorough review of different methodologies utilised. The material studied in this EngD thesis, the forging trials, their corresponding simulations using FEA, and the metallographic inspections are successively described.

3.1 Overview

Globularisation in titanium alloys has been extensively studied by different groups of researchers using laboratory facilities and small scale standard samples, often standard compression testing. Both the mechanisms and kinetics of globularisation have, to some extent, been understood for small scale samples. However, a satisfactory explanation for the effect of strain path, particularly the change in loading direction during cogging operations, on spheroidisation has not yet been proposed. Furthermore, the effect of process parameters such as the number of side pressing between annealing steps and the strain increment at each step on microstructural evolution during side pressing operations, is not well understood. The main aim of this EngD thesis is to enhance current knowledge of the globularisation process in Ti-6Al-4V alloy during cogging process, particularly the effect of strain paths on large industrial scale sample size. Multi-axial compression tests have been carried out to replicate the industrial cogging operations. Particular attention has been paid to material characterisation, to consistently and accurately assess the kinetics of globularisation. Comparisons are made between the obtained data and the results of established predictive models, and a new augmented model that has been proven to be more efficient for microstructure prediction during complex industrial processes, is proposed. An overall summary of different sections of this study are shown in a form of a flowchart in Figure 3.1.

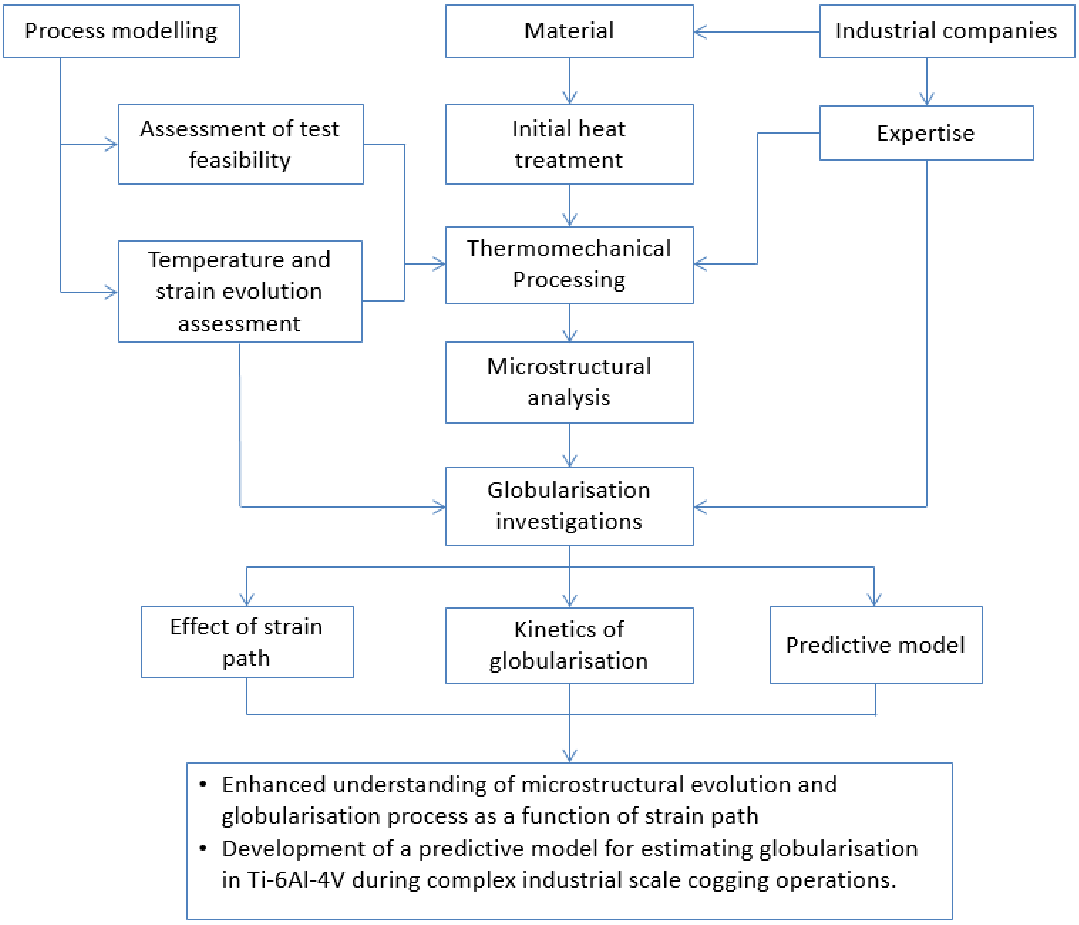

Figure 3.1: A flow chart depicting the general approach to this work.

3.2 Material

Almost all reported studies in literature have been conducted on standard laboratory scaled samples [58, 99, 105]. The size of these test pieces was in the range of 5-20 mm in height and diameter, with only few investigations using larger samples with a length/width up to 100 mm [94, 115]. The size of some microstructural features such as β grains is in the order of hundreds of micrometres to a few millimetres. Hence, small laboratory scale samples have a limited number of such microstructural features that may not be representative of a broad range of grain orientations present in a large industrial billet. Due to the dependency of materials thermo-mechanical properties and microstructural evolutionary mechanisms on crystallographic orientation, a limited number of grains may not be a good representative of larger orientation spectrum in a large billet, and hence may lead to biased results. Larger samples would prevent such an issue and allow obtaining a statistically relevant data. Also, larger samples would provide experimental data that is more relevant to industrial scale forging equipment and operations. Thus, in agreement with the industrial sponsors, a relatively large cubic sample geometry with 100mm edge dimension (i.e. 1 dm^3) was chosen for this EngD thesis. This geometry satisfies the size requirement of being comparable with industrial scale forging, and suitable for both uni-axial and multi-axial compression testing.

The material used in this study was a Ti-6Al-4V alloy supplied by Aubert & Duval®, as one of the industrial sponsor for this EngD thesis. The material was received in a form of sections from a round $\alpha + \beta$ forged billet, with a diameter of 240 mm. This type of billet is typically supplied for further manufacturing processes such as forging into critical components used in a jet engine (e.g. forged discs and compressor blades) or structural component in aircraft. The cubic samples used for the forging trials in this study were machined from the supplied billet sections. The orientations of the samples with respect to the original billet axis were recorded and traced throughout all stages of the experimental studies (see Figure 3.2). This was to ensure that all compression tests, conducted throughout this work, were performed along the cogging direction which is representative of the industrial process, and not along the upsetting axis.

In order to obtain a fully lamellar and homogeneous microstructure in all

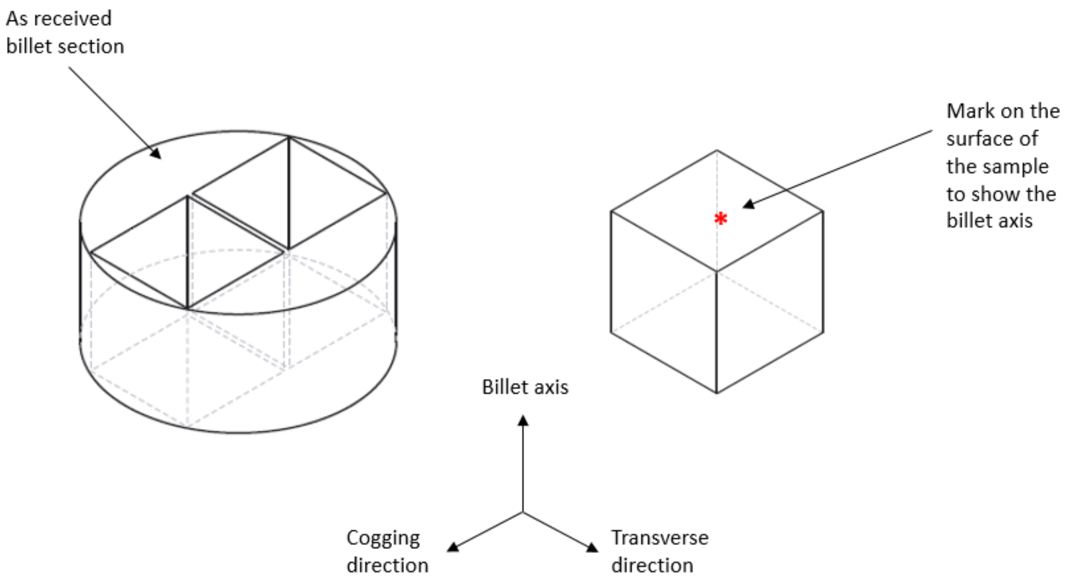

Figure 3.2: Machining of the cubic samples out of billet sections and marking of the billet axis.

specimens, a heat treatment was carried out above the β-transus at 1050°C for one hour followed by a controlled cooling to room temperature at 5°C/min in a VFE/TAV TPH 25/25/35 horizontal vacuum furnace. The one hour soaking time above the β-transus temperature was long enough to dissolve all primary α and produce a fully lamellar structure on cooling; but it is also short enough to prevent substantial β grain growth. The applied slow cooling rate is in a range of what is typically experienced by industrially manufactured bars, during air cooling.

3.3 Forging trials

A broad range of conditions including combinations of deformation levels, forging directions and annealing time, were considered for these investigations. These conditions, including the post forging cooling methods, are summarised in Tables 3.1 and 3.2. Note that few of the samples were subjected to two cycles of forging and heat treatments. For uniaxial forging, all the forging steps were carried out in a single direction, one after another, whereas for multi-axial forging the sample was rotated 90° clockwise after each cycle, unless noted in Table 3.2 otherwise. The plot of experimental trials is schematically shown in Figure 3.3 and 3.4. The temperature was kept constant at 950°C except for a couple of tests for which the deformation was carried out at 900°C, which is in the range of industrial practice, and also the press ram speed was kept constant at 5 mm.s^{-1} which delivers a nominal strain rate of 0.05 s^{-1} to the samples.

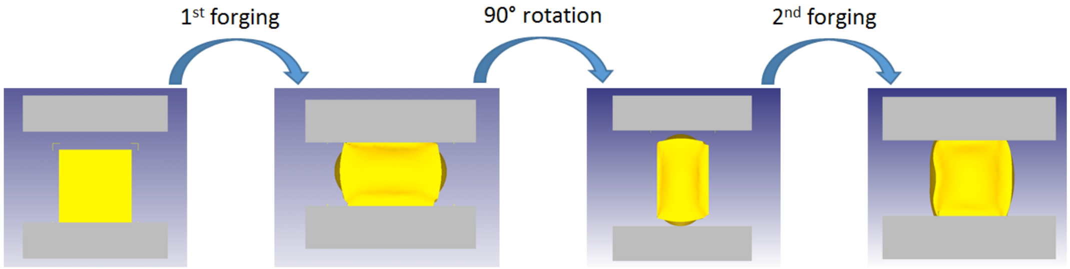

Figure 3.3: Schematic representation of a multi-axial forging represented by screen shots from the FE simulation carried out in DEFORM.

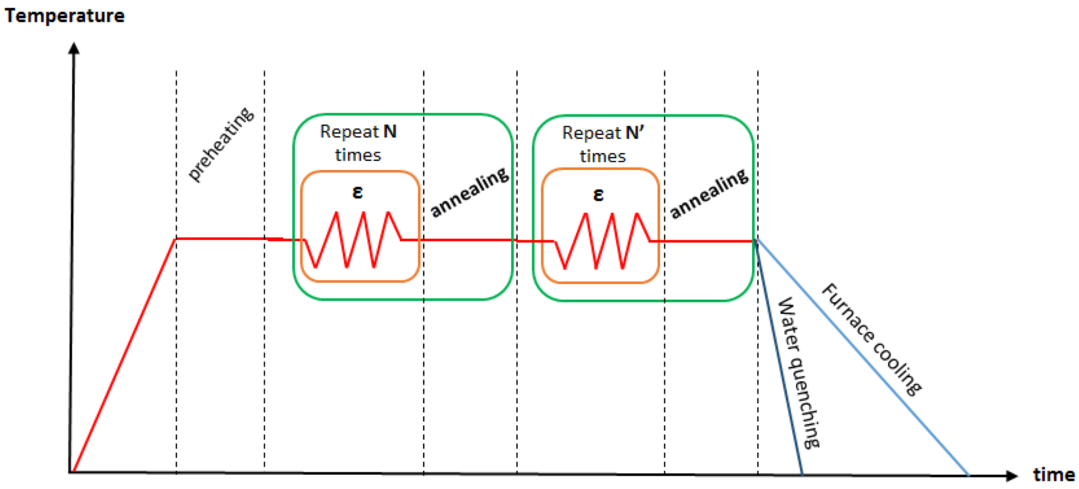

Figure 3.4: Schematic plot of thermo-mechanical trials carried out throughout the course of this study.

To easily identify and refer to different tests in this study, a naming system is adopted. An example of this naming convention is 5_0.1M_5h_FC. The first number (i.e., 5) is the number of deformation steps in the forging cycle. The second number (i.e., 0.1) is the deformation increment applied for each forging step; it is associated with a letter (U or M) to specify whether the deformation was carried out in a uniaxial or multiaxial manner. Then duration of the post-deformation heat treatment is defined

('5h' in this example); finally, the cooling method is indicatedas either of water quenched (WQ), air cooled (AC) or furnace cooled (FC). In some cases, brackets are used for simplification (e.g, 2_(0.25U-1h)_FC), but the naming convention remains unchanged; the brackets only indicates that each deformation step is followed by a heat treatment. In this example, the test consists of a first forging step (with a strain of 0.25) followed by an annealing of 1 hour, then a second forging step along the same direction as the first one (and also with a strain of 0.25) equally followed by an annealing of 1 hour, and finally a furnace cooling is applied. Each trial carried out in this project is listed in Tables 3.1, 3.2 and 3.3 along with their test conditions and naming reference.

3.3.1 Uniaxial compression

To understand the effect that each processing stage has on microstructural evolution, several uniaxial compression tests were performed with interrupted tests carried out along the process, as is detailed in Table 3.1. This included the status of microstructure at high temperature by quenching a sample after 1 hr annealing at 950°C, and also after forging and different post-deformation annealing. Forging was completed in one or several stages with intermediate annealing steps. For the sake of consistency, a nominal cumulative strain of 0.5 was chosen for all samples, disregarding the number of steps. This provides knowledge on the effect of uniaxial compression on globularisation, but also serves as a base for comparison with other testing conditions such as changes in loading direction (i.e., strain path).

3.3.2 Effect of strain path

To uncover the effect of strain path on globularisation, a set of multiaxial forgings were carried out with and without intermediate annealing step. These series of experiments comprised tests with a cumulative strain of 0.5 and a total annealing time of 5hrs. The magnitude of deformation applied prior to each annealing step was varied and the number and duration of annealing steps were changed to evaluate the effect of these process parameters on globularisation kinetics. One interrupted test was also taken as is detailed in Table 3.2. Additionally, two tests consisting of one and two cycles of deformation ($\varepsilon = 3*0.1$) and annealing of 1h were performed.

Table 3.1: Thermo-mechanical conditions investigated throughout this study.

test name	forging cycle 1				forging cycle 2				cooling rate
	number of cycles N	strain increment	annealing time	forging direction	number of cycles N’	strain increment	annealing time	forging direction	
SA+1h	-	-	1h	-	-	-	-	-	water quench
1_0.5U_WQ	1	0.5	-	uniaxial	-	-	-	-	water quench
1_0.5U_1h_WQ	1	0.5	1h	uniaxial	-	-	-	-	water quench
1_0.5U_1h_FC	1	0.5	1h	uniaxial	-	-	-	-	furnace cooling
1_0.5U_4h_FC	1	0.5	4h	uniaxial	-	-	-	-	furnace cooling
2_(0.25U-1h)_WQ	1	0.25	1h	uniaxial	1	0.25	1h	uniaxial	water quench
2_(0.25U-1h)_FC	1	0.25	1h	uniaxial	1	0.25	1h	uniaxial	furnace cooling
5_(0.1U-1h)_FC	5	0.1	1h between each pass	uniaxial	-	-	-	-	furnace cooling
2_(0.25M-1h)_WQ	1	0.25	1h	multiaxial	1	0.25	1h	multiaxial	water quench
2_(0.25M-1h)_FC	1	0.25	1h	multiaxial	1	0.25	1h	multiaxial	furnace cooling
2_0.25M _1h_FC	1	0.25	-	multiaxial	1	0.25	1h	multiaxial	furnace cooling
5_(0.1M-1h)_FC	5	0.1	1h between each pass	multiaxial	-	-	-	-	furnace cooling
5_0.1M_5h_FC	5	0.1	5h	multiaxial	-	-	-	-	furnace cooling
3_0.1M_3h_WQ	3	0.1	3h	multiaxial	-	-	-	-	water quench
3_0.1M_3h_2_0.1M_2h_FC	3	0.1	3h	multiaxial	2	0.1	2h	multiaxial	furnace cooling
3_0.1M_1h_WQ	3	0.1	1h	multiaxial	-	-	-	-	water quench
3_0.1M_1h_3_0.1M_1h_WQ	3	0.1	1h	multiaxial	3	0.1	1h	multiaxial	water quench
4_0.25M_WQ	4	0.25	-	multiaxial	-	-	-	-	water quench
10_0.1M_WQ	10	0.1	-	multiaxial	-	-	-	-	water quench
upset	3	0.2	0h	2 cogging and 1 upsetting)	-	-	-	-	furnace cooling
45°	3	0.15	1h	2 strokes at 90°, then 1 stroke at 45°	-	-	-	-	furnace cooling

Strain increment during non-monotonic deformation was found to have an effect on microstructural evolution during multi-axial forging of zirconium alloy [1] and reversed torsion of titanium alloy [56]. In this study, to evaluate its effect on the globularisation process, two tests were performed to a cumulative nominal strain of 1 with a strain increment of 0.1 and 0.25.

Because of the influence of the angle between the α lath and the loading direction on the globularisation kinetics, it was deduced that a change in strain path would be helpful to reach a globular structure [8]. To investigate the effect of a change in forging direction on the globularisation kinetics, two tests were performed with specific loading directions. One test comprised of upsetting (i.e. forging in a third orthogonal direction) and another with a rotation of 45° around the billet axis.

3.3.3 Effect of forging temperature

The industrial transformation of ingots into mill products is typically performed through non-isothermal processes. Due to temperature gradient in the billet, varying microstructural responses are expected depending on the location. To evaluate the effect of temperature on microstructural changes, a couple of tests were carried out at lower temperatures (i.e. 900°C) in this work (see last two tests in Table 3.2). One test was a uniaxial compression to a nominal strain 0.5. The other test comprised of three multiaxial forging strokes with 0.1 strain increment followed by a 3h annealing at 950°C for comparison with similar test carried out at higher temperature.

Table 3.2: Thermo-mechanical conditions investigated throughout this study.

test name	forging cycle				cooling rate
	number of cycles N	strain increment	annealing time	forging direction	
1_0.5U_WQ(900°C)_WQ	1	0.5	-	uniaxial (900°C)	water quench
3_0.1M(900°C)_3h(950°C)_WQ	3	0.1	3h	multiaxial (900°C)	water quench

3.3.4 Effect of post-deformation annealing duration

It is known that annealing duration has an impact on the globularisation process through diffusion based mechanisms [95]. The kinetics of static globularisation is somewhat influenced by the deformation stage (level of strain, strain path) [37]. To evaluate the effect of annealing duration on globularisation kinetics during non-monotonic deformation routes, annealing at 950°C for 1hr and 4hrs were performed as detailed in Table 3.3. Also, the influence of the annealing duration after deformation at lower temperature was evaluated by conducting heat treatment on the sample uniaxially compressed at 900°C and at 950°C.

Table 3.3: Heat treatment conditions studied in this work.

test name	Forging cycle				heat treatment
	number of cycle N	strain increment	forging direction	cooling rate	
10_0.1M_1h_AC	10	0.1	multiaxial	water quench	1h
10_0.1M_4h_AC					4h
4_0.25M_1h_AC	4	0.25	multiaxial	water quench	1h
4_0.25M_4h_AC					4h
1_0.5U(900°C)_1h(950°C)_AC	1	0.5	uniaxial at 900°C	water quench	1h
1_0.5U(900°C)_4h(950°C)_AC					4h

3.3.5 Forging trials

A 500T hydraulic press was used for the forging trials. The machine was controllable over the ram speed range of up to 6mm.s^{-1}. The press is equipped with heating dies capable of applying and maintaining up to a maximum of 400°C during operation. To minimise the friction between the dies at 400°C and the samples, graphite based lubricant was applied to the surface of the dies. Rotation of specimens during multi-axial forging tests was always executed around the billet axis. Heat treatments including pre-heating, inter-pass reheating and annealing were carried out in a Carbolite furnace GPC 12/131. In order to protect the test pieces from oxidation at elevated temperatures as well as to decrease friction during deformation, a *Prince ForgeOx 872207 Pinkglass* coating was applied. After trials, the deformed samples were subjected to either water quenching or controlled cooling. The controlled cooling was performed in a *Severn thermal solution EC 2112* furnace. The applied temperature profile consisted of a hold at 600°C for 10 minutes followed by cooling at 10°C/min to 300°C temperature, which resulted in an average cooling rate of about 15°C/min which is similar to that experienced during forging of industrial bars. All operations such as the transfer of the specimens from the furnace to the press and the rotation of samples between compressions was performed manually by an operator.

Once the experiment was completed, a slice is extracted from the middle of the sample for microstructural analysis.

Figure 3.5: Hydraulic press used for the forging experiments.

The cubic samples were subjected to hot forging trials in one direction or in multiple directions depending on the testing requirements. Ideally, for cubic samples flat faces should be reserved throughout all uni- or multi-directional forging processes, however, this is not the case in practice as barrelling occurs during deformation as a result of friction and also heat transfer between the hot sample and the dies at lower temperatures. Consequently, heterogeneities were observed in the deformation in a form of forging cross effect. This resulted in lower effective strain near the surfaces of the cubic samples and higher effective strain in the core of the samples, by a factor of 2, compared to the nominal applied strain. This phenomenon has been taken into consideration during the microstructural observations and assessments. By taking into an account the number of rotations and forging trials per orientation for each sample, high levels of strain can be achieved. For instance, an effective strain of up to 3.2 were reached for some cases in this work.

3.4 Process modelling of the forging trials

The barrelling effect observed due to the heat transfer (i.e. temperature drop in the sample) and friction between the dies and the sample increases with an increase in the level of strain. Although the bulged samples can be flattened during the subsequent orthogonal compression, it can potentially lead to an instability in the sample resulting in buckling. As a result, no additional deformation can be carried out on the sample in a desirable direction. One way to compensate for this effect would be to quench the sample immediately after each forging step and machine the bulged sections away to obtain a parallelepiped shape. However, this was not carried out in this work as the quenching and reheating processes between each forging trial may affect microstructural evolution, compared to industrial processes, and alter the results. Consequently, strain increments in this work could not exceed 0.25, since higher values would have produced buckling in the parts (see Figure 3.6).

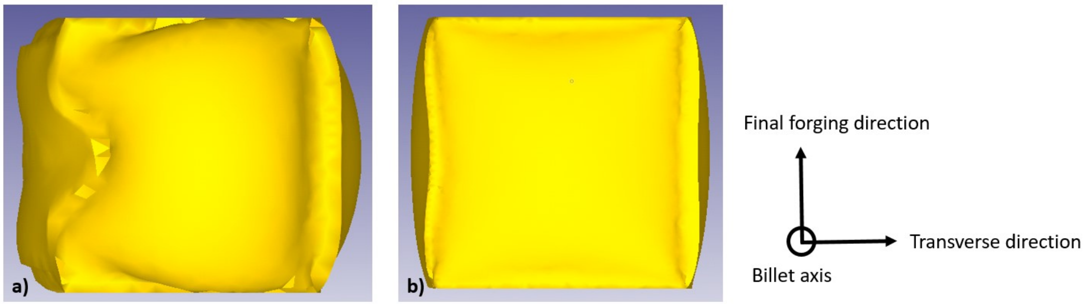

Figure 3.6: Impact of the strain increment on the forgeability of cubic samples: strain increment of 0.4 (a) and 0.25 (b).

Finite element (FE) simulation of the forging trials planned for this work was to ensure that appropriate conditions, comparable to industrial practices, are chosen. One of the major disadvantageous of non-isothermal forging trials is the heterogeneous deformation caused mainly by a drop in temperature profile across the specimens. Modelling the forging trials by the aid of FE provides an insight into the strain and temperature distributions in the sample under each testing condition. This allows microstructural evaluations to be carried out at correct locations where specific strain and strain rate levels are of interest.

Forging trials were thus modelled using FE in DEFORM (DEFORM$^{\mathrm{TM}}$ v11.0) software package. This software platform is able to model all stages of the experiments such as annealing, sample transfer from the furnace to the hydraulic press, forging and cooling to the room temperature to be simulated. The samples were modelled with tetrahedral elements of size about 2 mm. To solve the heating and deformation processes, Newton-Raphson method was used. Material properties data for Ti-6Al-4V alloy including thermo-mechanical (e.g. flow stress) and thermo-physical (e.g. heat capacity) were taken from the softwares library. Heat transfer coefficient for hot forging of titanium alloys varies depending on the coating of the test piece, lubrication and the applied pressure. It ranges from 200 to $700\ W.m^{-2}.K^{-1}$ when the part is resting on the dies and from 1,500 to $15,000\ W.m^{-2}.K^{-1}$ during forging operations [28, 47]. The coefficient of friction for hot forging is also dependant on the lubrication and coating conditions and was found to be between 0.3 (with lubrication) and 0.8 (dry condition) [87, 117]. The coefficients (i.e. friction and heat transfer) used in the model were iteratively modified until a satisfactory match between the predicted and measured geometries of the test pieces was reached. The final and acceptable values for these parameters are listed below.

- convection coefficient (for transfer operations and annealing): 20 W/m^2K
- heat transfer coefficient between sample and die when resting on the bottom die: 400 W/m^2K
- heat transfer coefficient between sample and the dies during forging: 2,500 W/m^2K
- friction coefficient: 0.3

Figure 3.7 shows an example of the results of forging trial simulation for both temperature and deformation distributions.

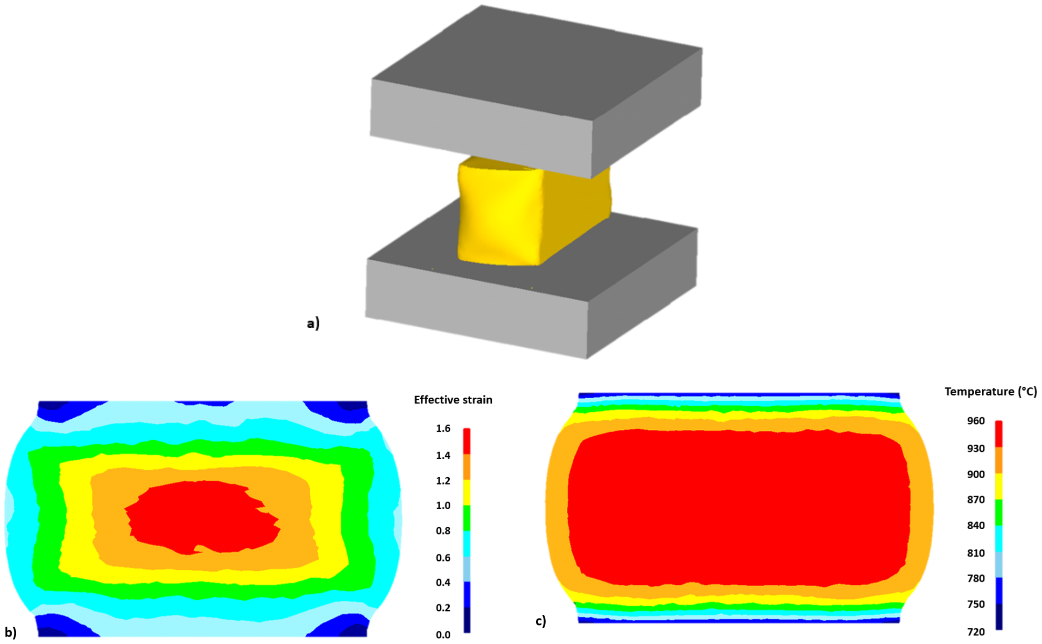

Figure 3.7: FE simulation of the forging trials (a), predicted strain distribution (b), and predicted temperature distribution(c).

3.5 Metallographic Inspection

3.5.1 Sample preparation

In this section, the procedures of sample preparation undertaken for materials characterisations are described. These include cutting, grinding, polishing and chemical etching. A suitable preparation was essential in order to obtain high quality images of microstructure using optical microscopy.

Following the forging and heat treatment stages, the samples were subjected to sand blasting to remove the glass coat layer, which was introduced to the samples prior to forging to minimise friction and heat loss, from the surface. Then, for each sample, a section (slice of 10 mm thickness) was machined from the centre of the forged sample by Electrical-Discharge Machining (EDM). The inspected plane of the extracted rectangular section contains the last forging axis and the original billet axis, as schematically illustrated in Figure 3.8.

The sections were then prepared using a Buehler EcoMet 300 grinding/polishing

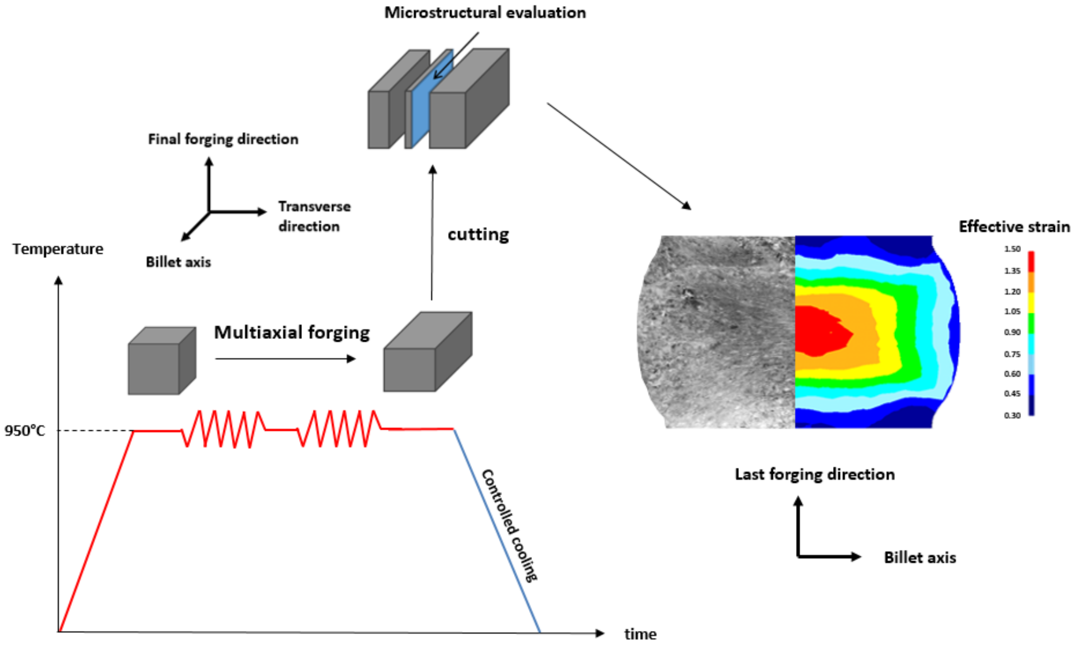

Figure 3.8: Sample extraction for material characterization.

machine. A series of grinding steps using silicon carbide paper with a grit size varying from 80 to 2500 were performed with water as lubricant/coolant; the aim being to make the samples flat and gradually remove scratches from the surface. A final step using colloidal silica suspension and a polishing cloth was carried out to obtain specimens with a mirror finish surface.

Finally, an etching operation is completed in order to reveal the microstructure of the material. The etchant used in this work was Kroll's reagent with a chemical composition of 92% of distilled water, 6% of HNO3 and 2% of HF. This procedure revealed the microstructure as the α phase appeared white and the β phase in dark after the etching.

3.5.2 Material characterisation

The etched surfaces of the samples were inspected with a Leica DM12000M optical microscope in bright field mode. For each sample, micrographs were recorded in three different strain zones, including high, medium and low strain levels. Because of the various conditions tested in this study, different levels of strain were achieved in each sample. This means that, for example, the three zones investigated in sample ’1_0.5U_WQ’ underwent a deformation of 1.7, 1.25, and 0.8 whereas in sample ’4_0.25M_WQ’ they underwent a deformation of 3.0, 2.2 and 1.4 as shown in Figure 3.9. In any case, the investigated strain zones included the highest strain level for each sample and two zones with lower strain levels that allowed covering most of the experienced strain spectrum for each case. For each strain zone, 5 micrographs, covering a typical scan area of 1.3 mm^2 were taken.

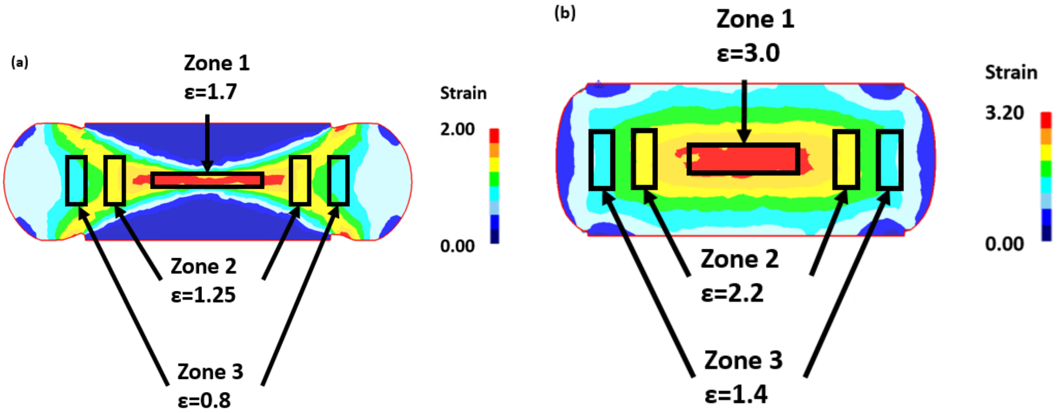

Figure 3.9: The various strain zones investigated in sample ’1_0.5U_WQ’ (a) and ’4_0.25M_WQ’ (b).

Since measuring globularisation and the fraction of globularised grains can be strongly dependant on the approach taken for the measurements, care needs to be taken in choosing an appropriate method. Generally, this measurement is done either manually or automatically. For the former, the grains are detected and measured manually following standard procedures such as line intercept method for the measurement of grain size, and the latter is based on automatic detection and measurements of grains.

In this project, manual point counting method (i.e., following ASTM E562) has been used for the measurement of globularisation. In this procedure, a rectangular grid with 100 points was applied to five images obtained for each strain zone. Then, the length and thickness of the laths intersecting the distributed points on the rectangular grid were measured using *ImageJ* software, as shown in Figure 3.10, and the aspect ratios were calculated from these data. In the event of water quenched or air cooled samples in which the fraction of α phase is much lower than in the furnace cooled samples, when a point of the grid falls in β phase the measurements are taken in the nearest α grain. This is to guarantee that a total of 100 measurements are taken from each image and 500 grains are indeed analysed for each deformation zone to ensure decent relative accuracy of globularised fraction measurements. The plot of measured aspect ratios for each condition was then produced and the globularised fractions were calculated from the plot of aspect ratio distribution by considering the grains with aspect ratio lower than 2 (see Figure 3.11).

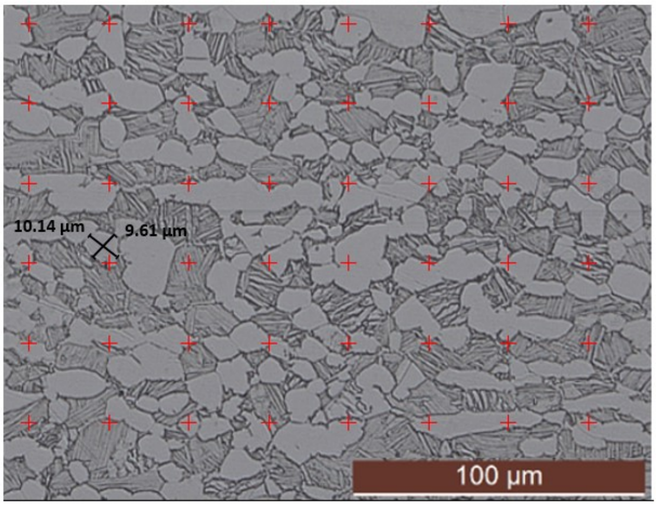

Figure 3.10: Microstructure with superimposed grid for point count procedure with a measurement highlighted.

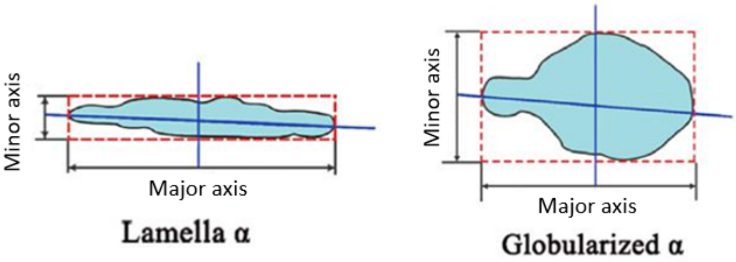

Figure 3.11: Schematic highlighting the measurements of the aspect ratio of α grains.

For ease of comparison between process routes/testing conditions in the Results chapter, globularised fractions are plotted into graphs as a function of effective strain. For each testing condition, three data points are displayed showing the globularised fraction observed in the three analysed deformation zones as shown in Figure 3.12.

The values of globularisation volume fraction, their confidence interval, and the level of strain in each investigated zones are detailed for every sample in Appendix B.

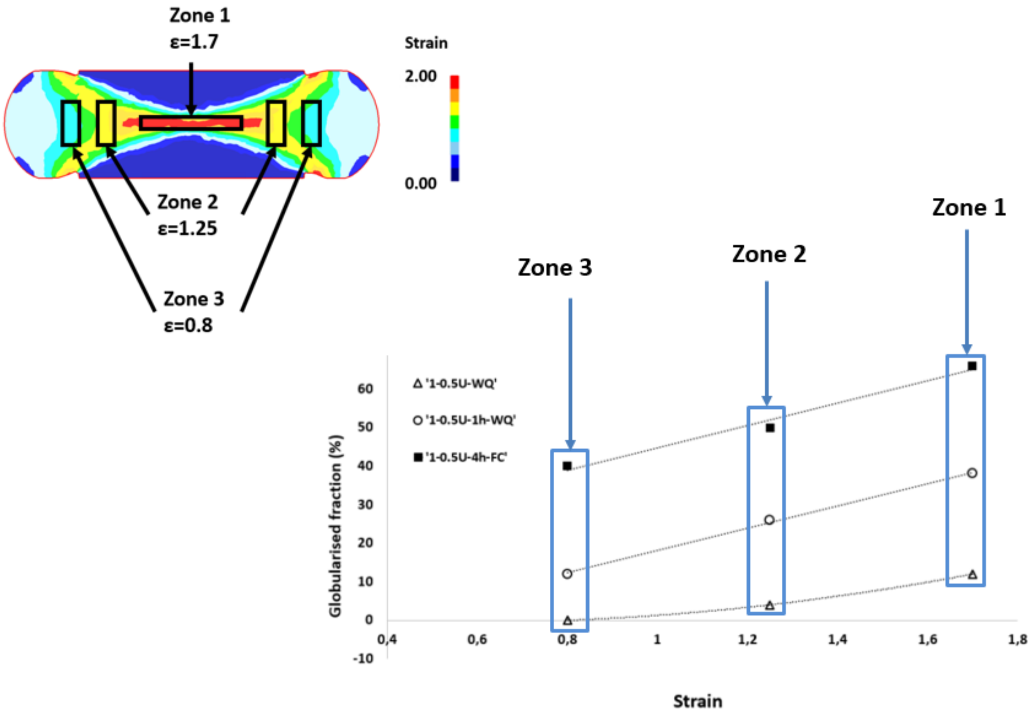

Figure 3.12: Schematic highlighting the representation of globularisation volume fraction with respect to strain for various process conditions.

3.5.3 Texture characterisation

Electron backscattered diffraction (EBSD) was used for microstructure and crystallographic texture analyses. For these analysis, samples with 15 mm x 25 mm dimensions were cut from the high strain zones of some of the forged cubic billets (see Table 3.5 for details). The samples were cut from the plane containing the billet axis and the final forging direction, and mechanically ground and polished to mirror finished condition following the same procedure described for the samples prepared for metallography earlier. The mirror finished samples were then electro-polished to remove approximately 2030 µm material from the mechanically polished surface using Struers electrolyte A2 at ambient temperature for 15 s at 35 V.

The acquisition of EBSD maps was carried out using a fully automated

NordlysNano EBSD system interfaced to a FEI Quanta-250 field-emission gun scanning electron microscope, with an accelerating voltage of 20 kV and a 100 µm diameter aperture. The acquisition time was set to 40 ms, collecting at least 2 frames for each point. Orientation mapping was performed with 5 µm step size covering an area of 12 mm 2.5 mm. In all cases, a minimum of 30% of the scanned areas were indexed.

Data acquired from EBSD is then used to create crystallographic orientation maps, revealing information about grain morphology, orientation and boundaries with *HKL Channel 5* software (Figure 3.13). Parameters used to define grains in these maps were 15° for the misorientation angle for high angle grain boundaries, and 5° for the misorientation angle for low angle grain boundaries. To represent the position and intensity of specific crystallographic orientations of the grains with regard to the specimen's orientation, pole figures are constructed (Figure 3.14). Settings shown in Table 3.4 are used to produce these pole figures.

Table 3.4: Settings used to generate the pole figures.

half width	cluster size	projection type	projection hemisphere	planes
10°	5°	stereographic	upper	{0001}, {11-20},{10-10}

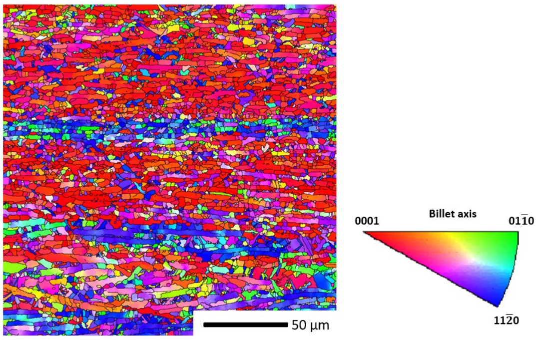

Figure 3.13: An example of an acquired EBSD map displaying the grain boundaries and the grain crystallographic orientation using inverse pole figure (IPF) colouring with respect to the loading direction.

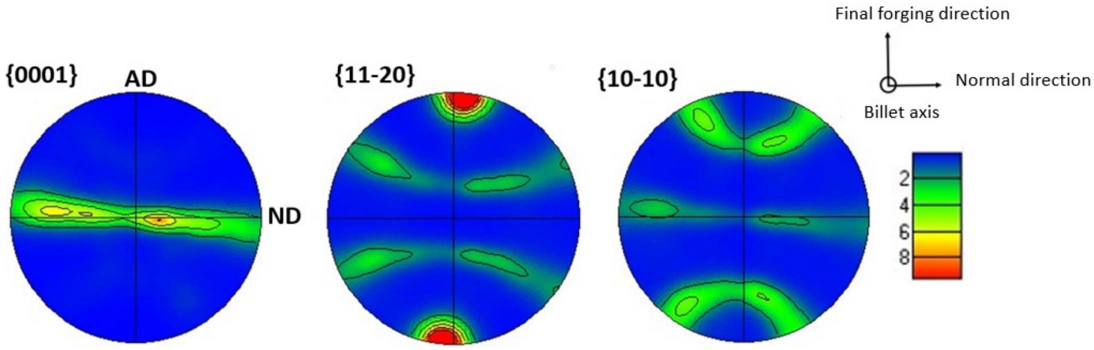

Figure 3.14: An example of pole figure for a uniaxially compressed sample (i.e., '1-0.5U-WQ').

Table 3.5: Thermo-mechanical conditions investigated by EBSD.

forging cycle 1				forging cycle 2				cooling rate
number of cycles N	strain increment	annealing time	forging direction	number of cycles N’	strain increment	annealing time	forging direction	
-	-	1h	-	-	-	-	-	water quenched
1	0.5	-	uniaxial	-	-	-	-	water quenched
1	0.5	1h	uniaxial	-	-	-	-	water quenched
1	0.5	4h	uniaxial	-	-	-	-	furnace cooled
1	0.25	1h	uniaxial	1	0.25	1h	uniaxial	water quenched
1	0.25	1h	multiaxial	1	0.25	1h	multiaxial	water quenched
1	0.25	-	multiaxial	1	0.25	1h	multiaxial	furnace cooled
5	0.1	1h between each pass	multiaxial	-	-	-	-	furnace cooled
4	0.25	0h	multiaxial	-	-	-	-	water quenched
1	0.5	-	uniaxial at 900°C	-	-	-	-	water quenched

3.6 Summary

An experimental methodology has been developed to investigate the evolution of globularisation in Ti-6Al-4V during cogging process. The use of large cubic samples, a 500T hydraulic press and furnaces allow the compression of the sample along more than one axis and combinations of forging and heat treatment steps. A slice containing the direction of the last compression and the billet axis is extracted from each sample for material characterisation. Material preparation is performed and etching with HF is carried out to reveal the different phases in the material. Evolution of globularisation is assessed by manual point counting method (i.e., following ASTM E562) on 500 α grains yielding aspect ratio distributions for different strain zones in each sample. Crystallographic texture was also assessed via EBSD on several selected samples.

Chapter 4

Results

This chapter summarises the results of experimental observations and microstructural evolutions in samples tested under different conditions, replicating industrial open die forging (i.e. cogging) process for globularisation in Ti64. The effects of strain path and process parameters are investigated. The observed microstructures are evaluated and characteristics of microstructural features, e.g. distribution of α -lath aspect ratio and grain size, are presented. Also, the evolution of crystallographic texture during cogging operations for globularisation has been explored selectively and the results are presented.

4.1 Preliminary FE simulation

For the purpose of determination and validation of heat transfer coefficient (HTC) and friction coefficient (COP) in FE modelling of the hot forging process, several modelling trials of the uniaxial forging were carried out. For each parameter, a limit was defined; these were between 500 and 8000 $W.m^{-2}.K^{-1}$ for the heat transfer coefficient, and 0.08 to 0.6 for the friction coefficient. Subsequently, the final dimensions of the model predictions were compared with the geometry of the actual forging trials as shown in Figure 4.1. The measured dimensions of a formed sample along with the results of prediction models with different coefficients are listed in Table 4.1. Models using the lowest value for HTC or COP display very little barrelling effect during the uniaxial compression unlike in the physical experiment;

hence, the predicted dimension of the specimens are quite far from the ones of the physical part. These values are not appropriate for accurate modelling of the forging experiments carried out in this work. On the other hand, at higher values of COP and HTC, the predicted dimensions are much closer to the actual ones. Also, the choice of modelling coefficients in that range of values does not seem to affect significantly the geometry, the deformation and the temperature distributions (see Figures 4.2 and 4.3). This is due to the large cooling effect from the dies occurring during the physical experiments and that is captured in models when a HTC value of 2500 $W.m^{-2}.K^{-1}$ or more is used. Indeed, the contact of the part with the low temperature of the dies, i.e. 400°C, generates dead zones and results in a bulged forged geometry regardless of the COF used (0.3 or 0.6).

Consequently, based on previous studies reported in literature [28, 47, 87, 117] and also values used by industry (i.e., the forging companies involved in this project: Aubert & Duval and Timet), 2500 $W.m^{-2}.K^{-1}$ and 0.3 were chosen for heat transfer and friction coefficients, respectively. To ensure that these parameters are as close as possible to their actual values, comparisons have been made between all the forged samples and the results of FE simulations.

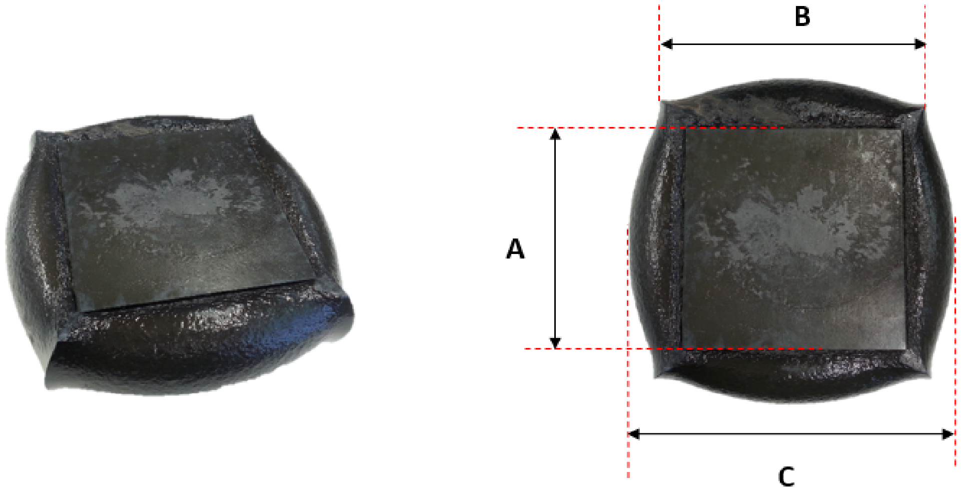

Figure 4.1: Photographs of one of the samples in the as forged conditions, (a) side view, and (b) top-view with the sides used for dimensional measurements highlighted.

Table 4.1: Summary of the measured dimensions and the results of prediction models with different heat transfer coefficient (HTC) and coefficient of friction (COF).

test conditions		measurements (mm)		
Heat transfer coefficient (W/m 2 K)	Coefficient of friction	a	b	c
physical part		102	135	163
500	0.08	130	141	155
	0.3	112	137	157
	0.6	106	134	158
2500	0.08	107	137	159
	0.3	101	133	163
	0.6	101	133	163
8000	0.08	101	137	163
	0.3	100	134	164
	0.6	100	134	164

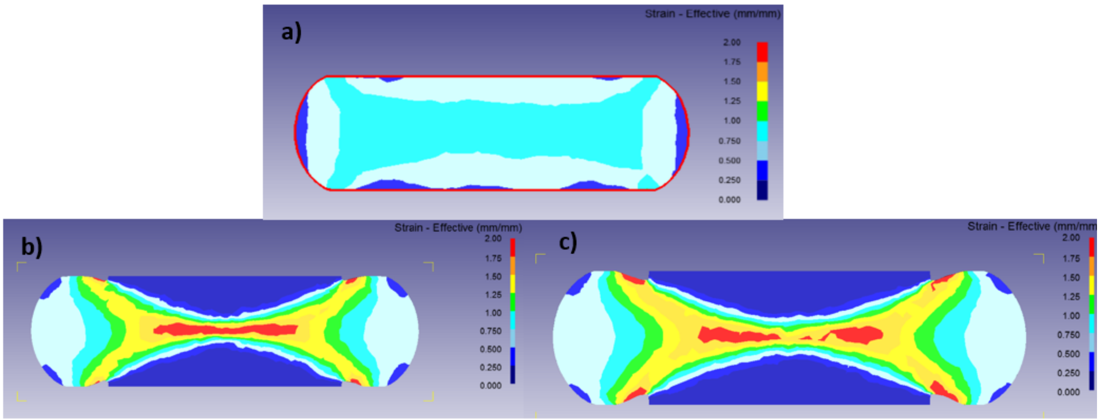

Figure 4.2: Simulated strain distributions predicted under different conditions: (a) HTC 500 - COF 0.08, (b) HTC 2500 - COF 0.3, (c) HTC 8000 - COF 0.6. The scale is between 0 and 2.

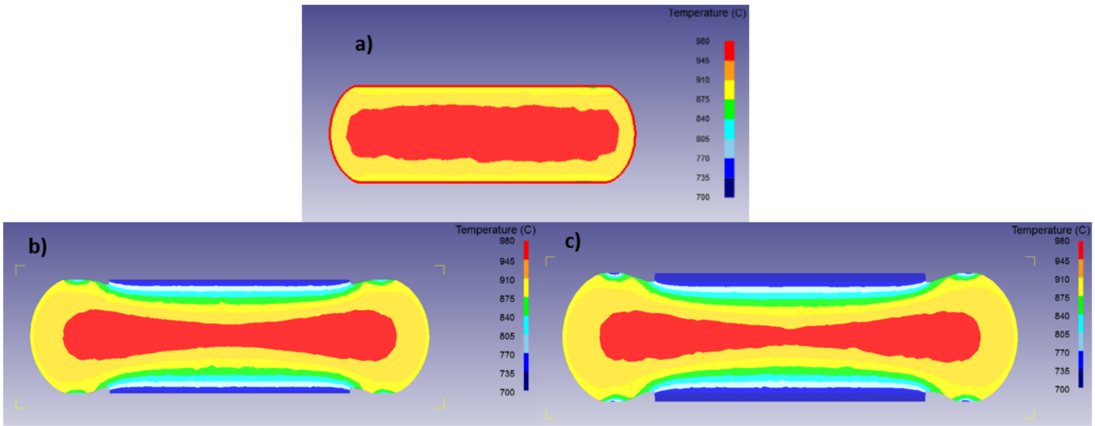

Figure 4.3: Simulated temperature distributions predicted under different conditions: (a) HTC 500 - COF 0.08, (b) HTC 2500 - COF 0.3, (c) HTC 8000 - COF 0.6. The scale is between 700°C and 980°C.

4.2 Initial microstructure

The as-received material was solution annealed at 1050°C for 1 hour, for a purpose of homogenisation, and then furnace cooled to room temperature at 5°C/min to obtain the desired initial microstructure. Figure 4.4 shows the temperature profile as a function of time for this heat treatment. The microstructure is characterised by colonies of α plates with an average thickness of 4.2 µm within prior-β grains whose boundaries are decorated with a 7.2 µm thick layer of α. The average prior β grain size was measured to be 890 µm. Figure 4.5 displays an optical micrograph of the initial material.

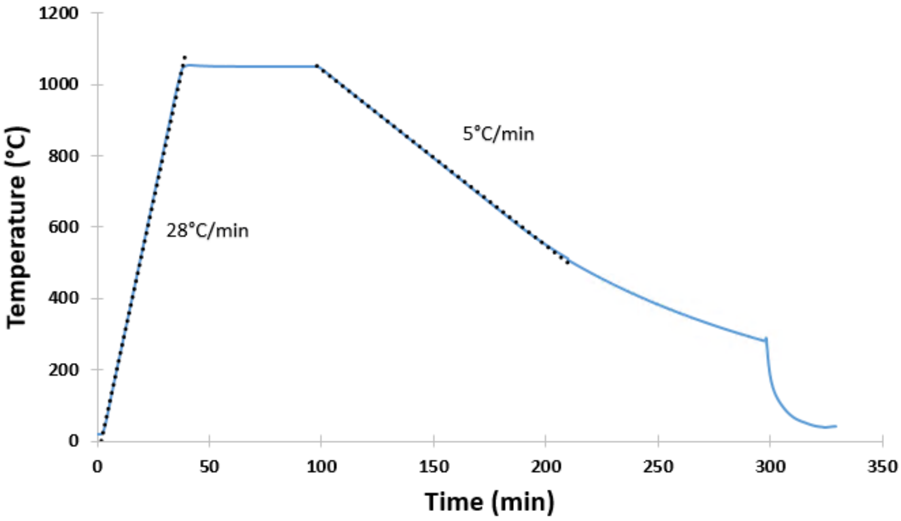

Figure 4.4: Plot of temperature evolution as a function of time for the solution heat treatment.

To assess the initial microstructure at the forging temperature, a separate sample was heated to 950°C, held for 1 hour and then water quenched immediately. Figure 4.6 shows the assessed microstructure. The obtained microstructure is similar to the one that was furnace cooled to the room temperature with slightly thinner α laths (i.e. average thickness of 3.1 µm) and also thinner grain boundary α layer (i.e. average thickness of 5.6µm). Also, the volume fraction of α phase was significantly lower, around 30%, compared to the furnace cooled microstructure, which contains around 90% of α phase.

Figure 4.5: Optical microscopy appearance of the initial microstructure that was heat treated at 1050°C for 1 hour followed by furnace cooling at 5°C/min.

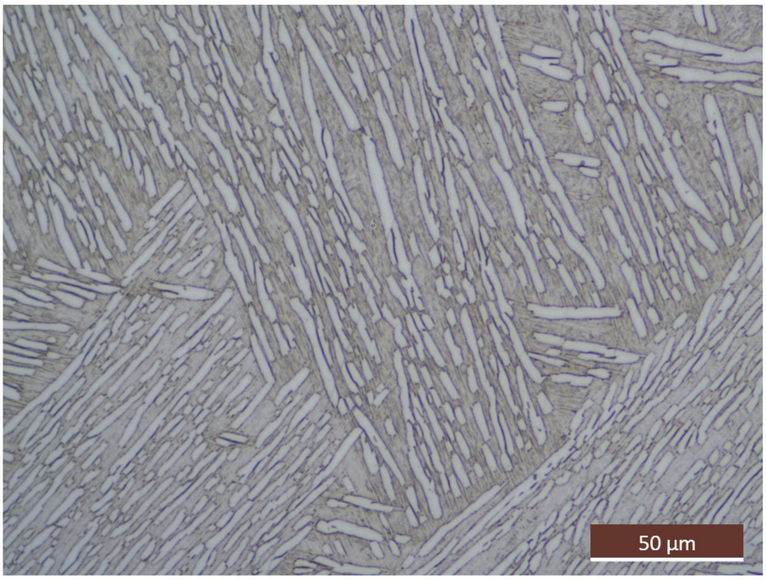

Figure 4.6: Optical microscopy appearance of the initial microstructure that was heat treated at 950°C for 1 hour followed by water quenching.

4.3 Effect of uniaxial compression on globularisation

For all samples subjected to a uniaxial compression, microstructural changes become more significant with increasing effective (local) strain. In regions that underwent small deformations (e.g., ε=0.8), the microstructure appears to be almost unchanged compared to 'SA+1h' with only a few buckled laths (see Figure 4.7). On the other hand, at locations where higher levels of deformation are induced (e.g., ε=1.7), the initial α colony structure has almost entirely disappeared, and only traces of grain boundary α layer remained with bent and broken α laths (see Figure 4.8). As a result of this lath fragmentation, the evaluated aspect ratio distributions shown in Figure 4.9a display an evolution towards lower values with increased strain. In addition to lath fragmentation, α lamellae tend to rotate and become aligned with a direction perpendicular to the loading axis (see Figure 4.8).

Additional annealing of the strained samples leads to further fragmentation of α laths and therefore higher fraction of globularised grains (see Figure 4.10). The fraction of globularised α is seen to be increased with longer annealing time at 950°C (see Figure 4.9 and 4.11). However, the additional heat treatments at 950°C produces a coarser microstructure compared to the as-forged condition (see Figure 4.10). Indeed, the thickness of α laths grows from 2.7 ± 0.5 µm after forging to 7.3 ± 1.4 µm after 1 hour of annealing and 9.1 ± 1.7 µm after 4 hour of annealing.

It is noted that performing two steps forging with a 1 hour annealing at 950°C in between, leads to a lower level of strain in the sample. This is due to a lower temperature gradient occurring within the test piece after the annealing step in between the forgings, leading to lower barrelling effect and consequently a smaller strain level at the centre of the sample. As can be seen from the results of simulation shown in Figure 4.12, strain level of 1.3 is achieved with two steps forging and annealing in between compared to 1.7 strain obtained for a one step forging. However, this has barely affected the microstructure evolution and the globularisation rate compared to samples '1-0.5U-1h-WQ' and '1-0.5U-1h-FC' (see Figure 4.13 and 4.14). In fact, for both cases the alignment of α laths with a direction perpendicular to the loading direction is noticed. Though, due to the additional annealing between the two forging steps, the structure appears coarser than that of the sample underwent a single forging step followed by a 1 hour annealing (see Figure 4.15).

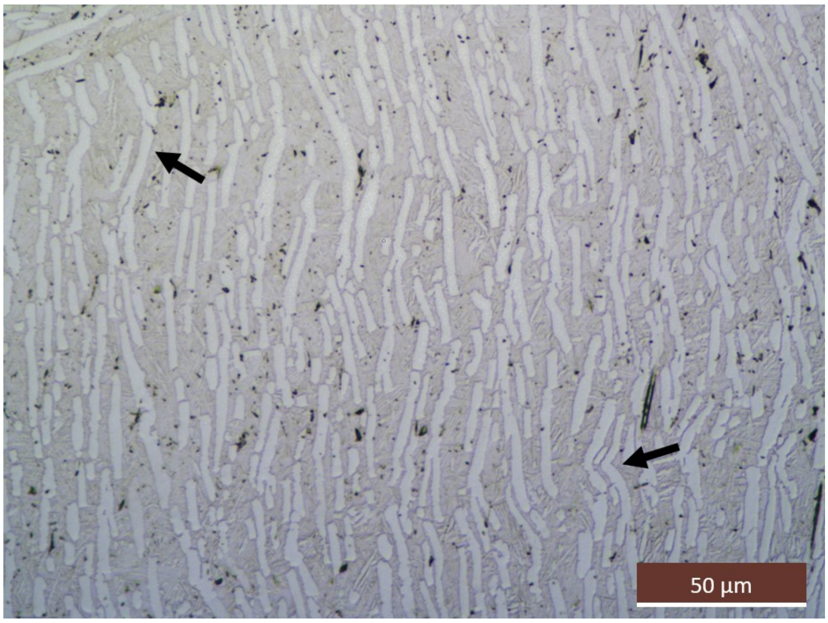

Figure 4.7: Optical micrographs of the sample '1-0.5U-WQ' in the low strain zone (ε= 0.8). Arrows point at buckled α laths.

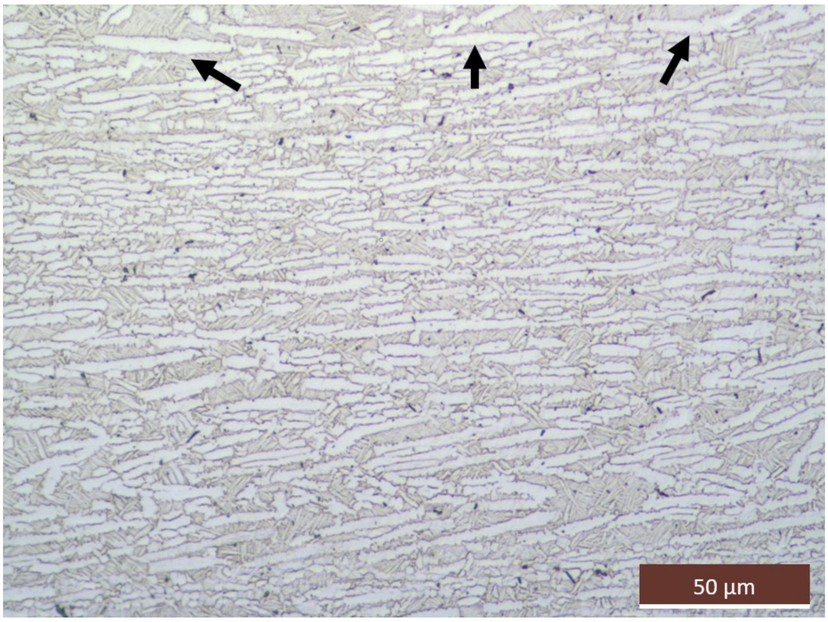

Figure 4.8: Optical micrographs of the sample '1-0.5U-WQ' in the high strain zone (ε= 1.7). Arrows indicates remnants of grain boundary α layer.

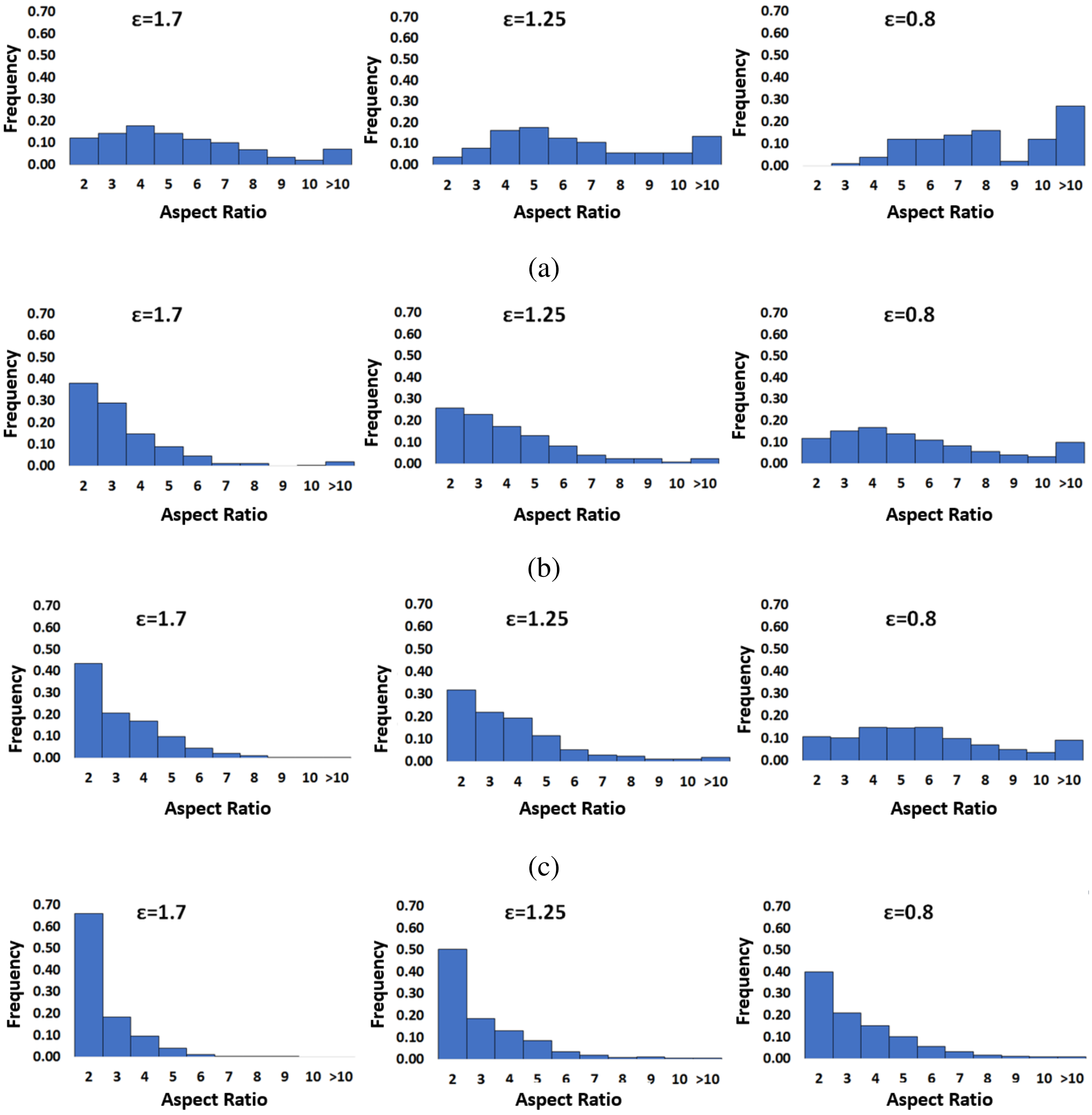

(a)

(b)

(c)

(d)

Figure 4.9: Plots of α lath aspect ratio distributions for the uniaxially forged samples, (a) '1-0.5U-WQ', (b) '1-0.5U-1h-WQ', (c) '1-0.5U-1h-FC', (d) '1-0.5U-4h-FC'.

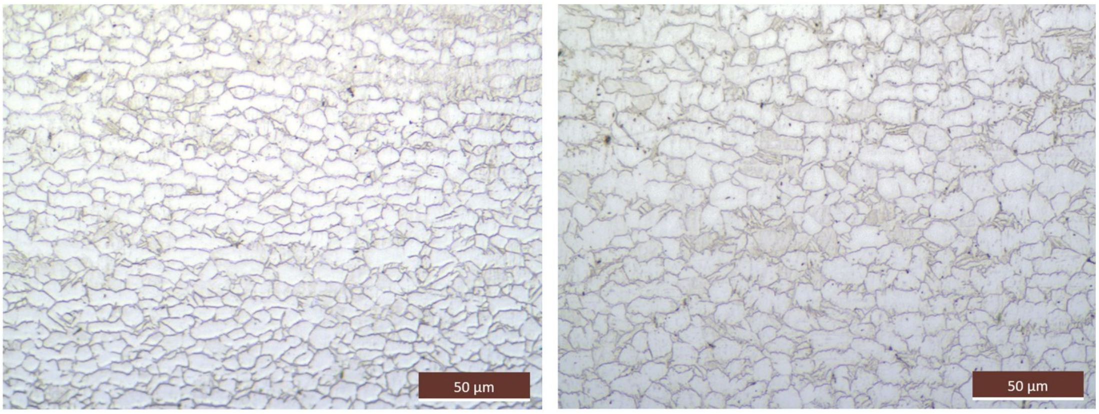

Figure 4.10: Optical micrographs of the sample '1-0.5U-WQ' in the high strain zone (ε= 1.7) after: (left) 1 hour annealing, and (right) 4 hours annealing).

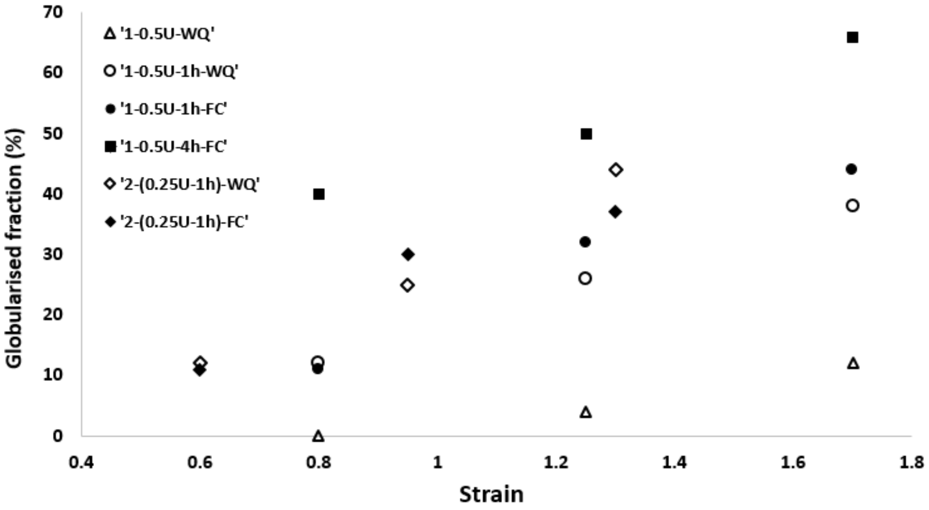

Figure 4.11: Plots of globularised fraction as a function of local strain for the uniaxially forged samples followed by various annealing.

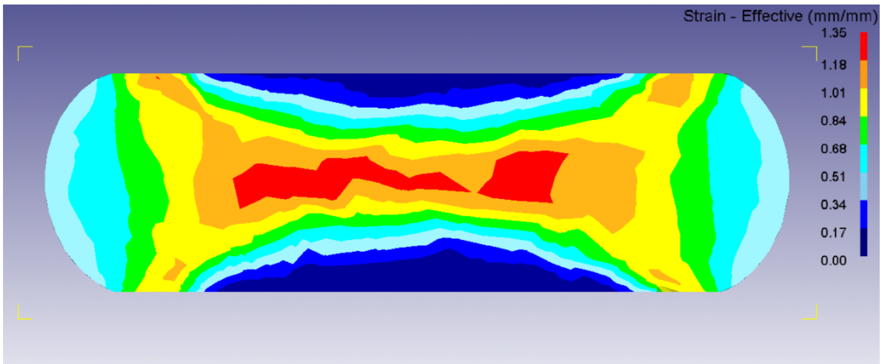

Figure 4.12: Predicted strain distribution for the test '2-(0.25U-1h)-WQ'.

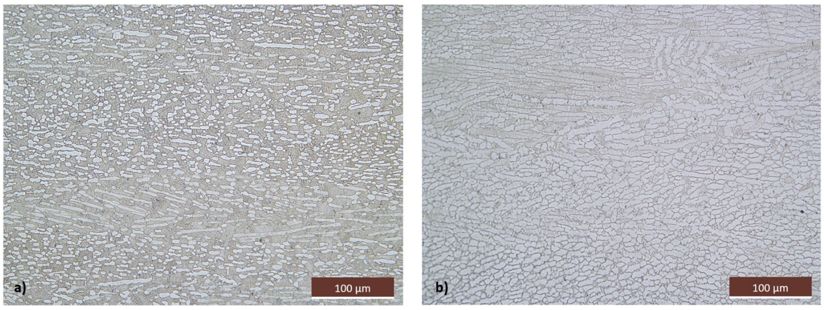

Figure 4.13: Optical micrographs of the sample: (left) '2-(0.25U-1h)-WQ', and (right) '2-(0.25U-1h)-FC' in the high strain zone (ε= 1.3).

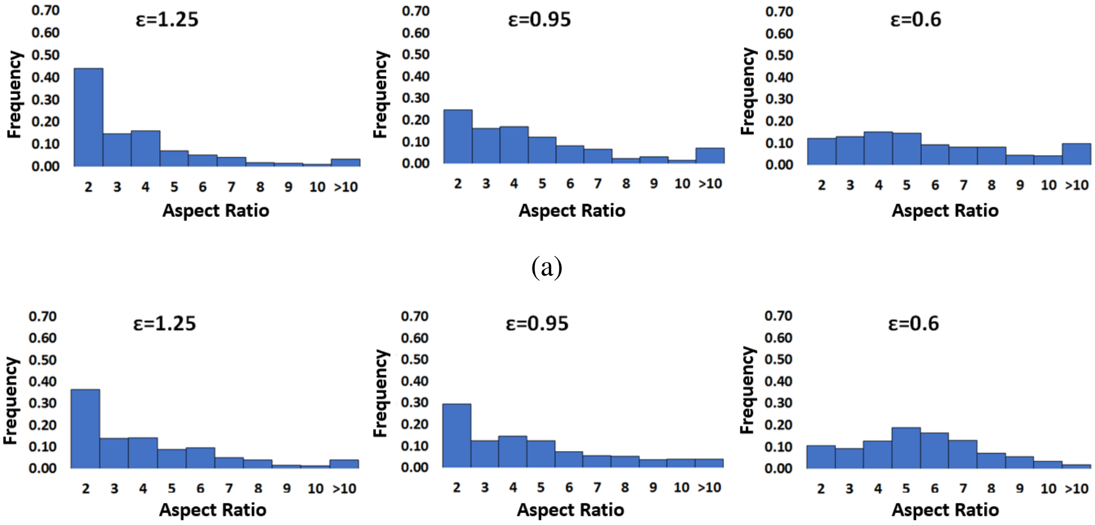

(a)

(b)

Figure 4.14: Plots of α lath aspect ratio distributions for the uniaxially forged samples, (a) '2-(0.25U-1h)-WQ', and (b) '2-(0.25U-1h)-FC'.

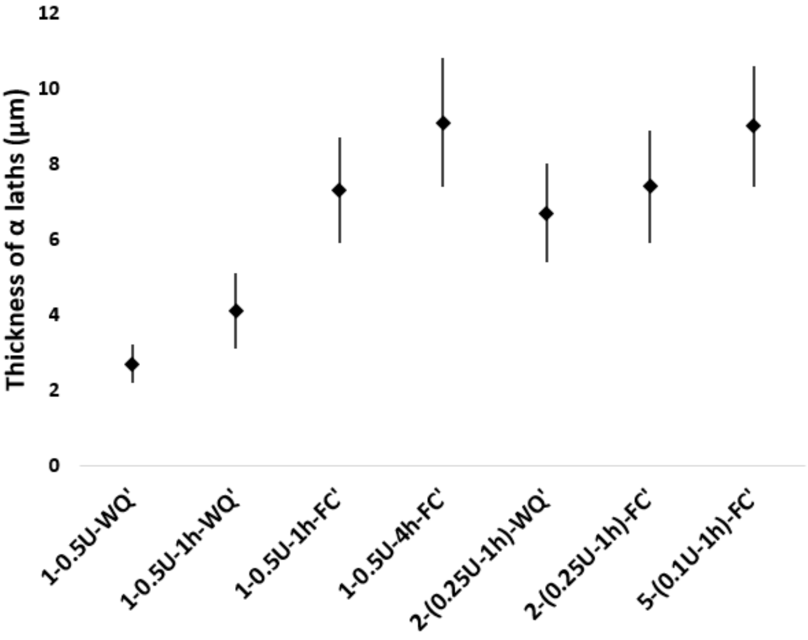

Figure 4.15: Plots of the thickness of α *laths of samples forged uniaxially and annealed under different conditions.*

In the sample subjected to 5 steps of 0.1 strain along the same axis followed by 1 hour annealing after each step (i.e. sample '5-(0.1-1h)-FC'), the observed changes in microstructure evolution are not as advanced as those of samples subjected to uniaxial tests in one or two steps (see Figure 4.16). Traces of prior-β grains and α colonies were still visible (highlighted in Figure 4.16a), and the rotation of α laths towards the loading direction was not as pronounced. However, this may be due to the lower magnitude of local strain observed in this test piece (e_max = 0.85). Indeed, when comparing with a zone of similar level of deformation in sample '1-0.5U-4h-FC', the microstructure and globularised fraction are very much alike (see Figure 4.17).

It appears that during uniaxial compression tests under the conditions tested in this work, the combination of deformation and annealing steps does not affect substantially the microstructural evolution. Only the total magnitude of deformation and annealing time have a major impact on globularisation.

The cooling rate applied after each forging trial affects the final appearance of microstructure. For instance, furnace cooling promotes primary α growth whereas water quenching leads to the formation of secondary α. Therefore, the volume fraction of primary α is much higher in the samples subjected to controlled cooling, $\approx 90\%$,

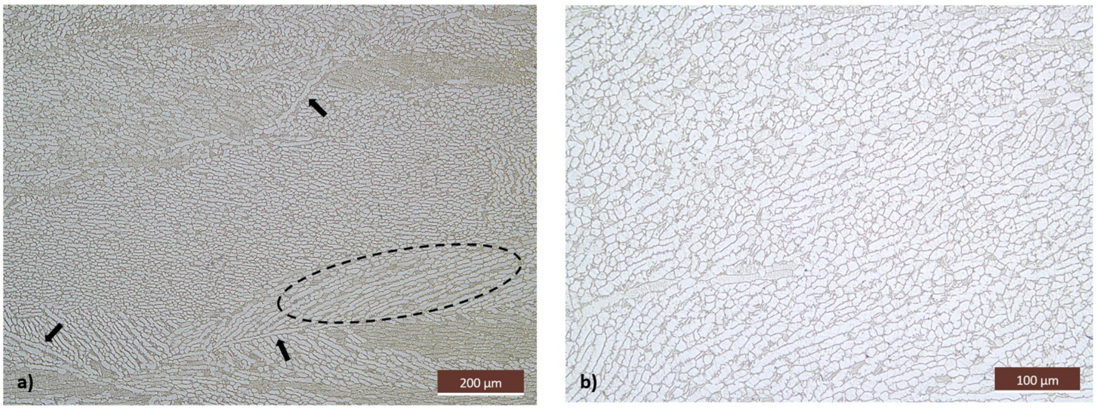

Figure 4.16: Optical micrographs of the sample '5-(0.1U-1h)-FC' in the high strain zone (ε= 0.85): a) 100x magnification, and b) 200x magnification.

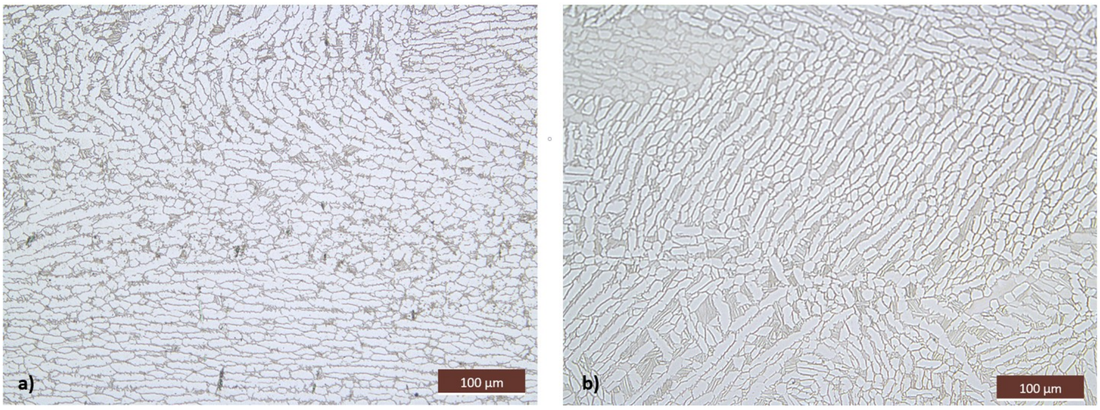

Figure 4.17: Optical micrographs of the sample: a) '5-(0.1U-1h)-FC' in the high strain zone (ε= 0.85), and b)'1-0.5U-4h-FC' in the low strain zone (ε= 0.8).

as opposed to $\approx 30\%$ in those water quenched. However, the cooling rate from the forging temperature does not seem to have an effect on the overall microstructural evolution; no additional fragmentation of laths is observed. Thus no effect is seen on the kinetics of globularisation, in fact the aspect ratio distributions are similar for water quenched and furnace cooled samples subjected to identical forging and heat treatment processes (see Figures 4.14, 4.9, 4.11).

4.4 Effect of strain path on globularisation

Figure 4.18 displays micrographs of the samples subjected to 50% of strain in two steps, 25% along two orthogonal directions by rotating the sample after the first step. The observed microstructure is substantially different from those of the samples forged along one axis (see Figure 4.13). Prior-β grains and α colonies are clearly visible (see Figure 4.19), and no preferred lath orientation with respect to the loading direction is observed (i.e. laths do not rotate towards a direction perpendicular to loading axis). The break-up of α laths is also highly heterogeneous, with some colonies displaying deformed, kinked or fragmented lamellae whereas others remain unaffected (see Figure 4.19). Therefore, the overall level of α lath fragmentation is lower (see Figure 4.20) and the globularised fraction is inferior (i.e. 10% less). The resulting microstructure is slightly coarser (α lath thickness of 7.5 ± 1.8µm and 9.7 ± 2.1µm after water quench and furnace cooling, respectively) than those subject to uniaxial forging (α lath thickness of 6.7 ± 1.3µm and 7.4 ± 1.5µm after water quench and furnace cooling, respectively). The change in strain path performed on these samples has found to be not effective in enhancing globularisation.

The removal of the annealing process at 950°C in between the two deformation steps was not seen effective in changing the microstructure and globularisation kinetics. A small fraction of fragmented laths was observed when no annealing was performed (see Figure 4.21). Also, the α lamellae in '2-0.25M-1h-FC' are not as coarse as that of '2-(0.25M-1h)-FC' (8.4 ± 1.7µm compared to 9.7 ± 2.1µm) due to shorter annealing time spent at high temperatures (i.e. 1hr at 950°C instead of 2hrs) where lath growth by diffusion mechanisms is possible [95].

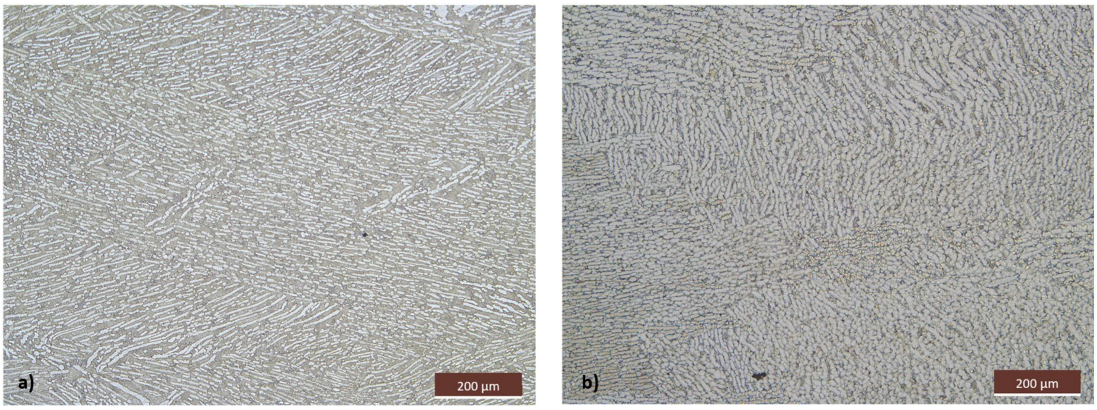

Figure 4.18: Optical micrographs of the high strain zone (ε= 1.4) of the samples: a) '2-(0.25M-1h)-WQ' , and b) '2-(0.25M-1h)-FC'.

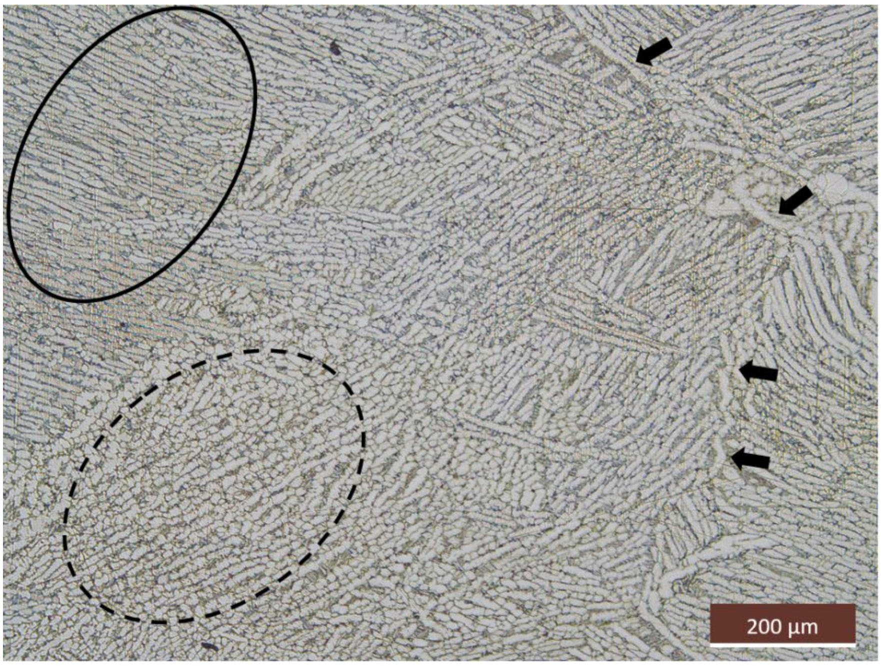

Figure 4.19: Optical micrographs of the sample '2-(0.25M-1h)-FC' highlighting unaffected α colonies (solid circle), fragmented α laths (dashed circle), and remnant of Prior-β grain boundaries (arrows).

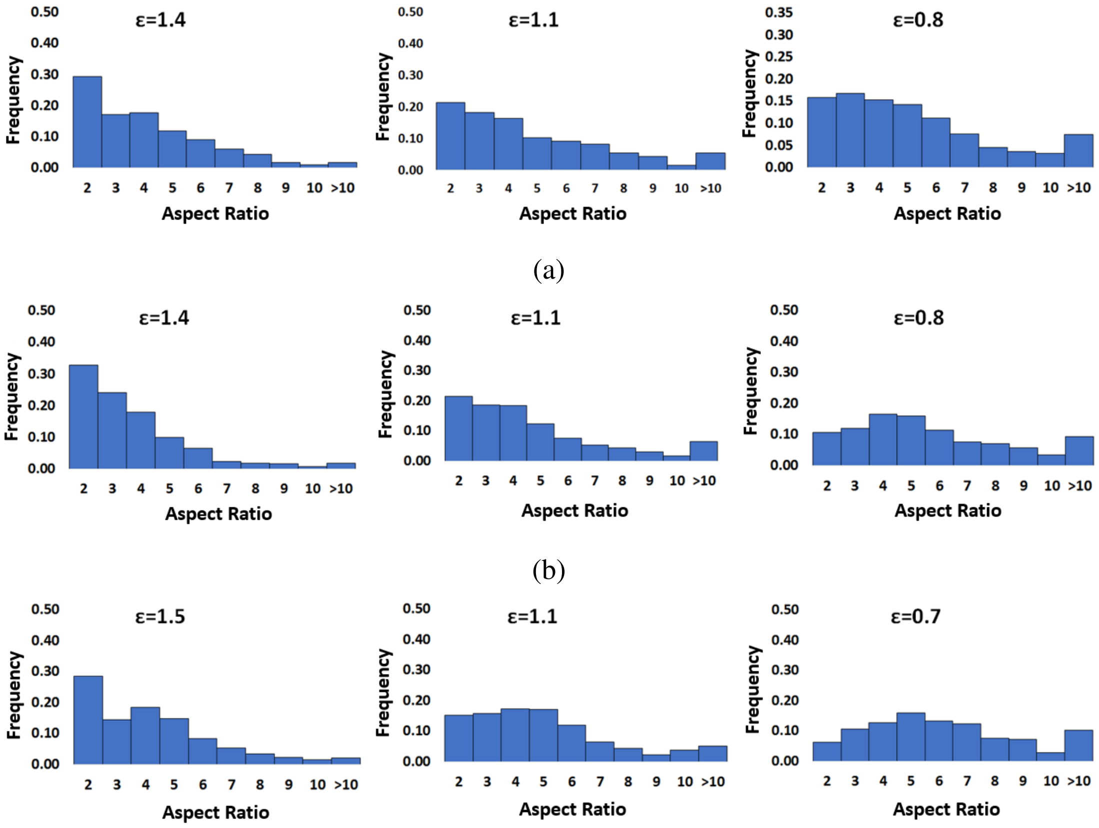

(a)

(b)

(c)

Figure 4.20: Plots of α lath aspect ratio distributions for the biaxially forged samples, (a) '2-(0.25M-1h)-WQ', (b) '2-(0.25M-1h)-FC', and (c) '2-0.25M-1h-FC'.

Figure 4.21: Optical micrographs of the sample forged biaxially with no annealing between the two steps '2-0.25M-1h-FC'.

Figure 4.22 to 4.25 show the evolution of microstructure and globularisation following different thermo-mechanical testing conditions. For all these test conditions, a total strain level of 0.5 was applied in 5 increments of 0.1, with different annealing steps (i.e. total annealing duration of 5 hours) throughout the deformation steps as detailed below:

- '5-(0.1M-1h)-FC'
- '5-0.1M-5h-FC'
- '3-0.1M-3h-2-0.1M-2h-FC'

The applied iterative thermo-mechanical processes do not have significant effect on the final α lath size and morphology. The average measured α lath thickness is ≈ 9.5 µm for all samples tested under these conditions.

Also, the change in strain path appears not to affect microstructural evolution or the globularisation kinetics significantly. Indeed, in every sample, the initial colony structure within prior-β grain boundaries remain visible (see Figure 4.22) with varying level of fragmented and bent α lamellae in the highly strained zone (centre of sample) depending on the condition. The fragmented and bent laths are heterogeneously distributed within the highly strained zone. Typically, the microstructure in the areas that underwent lower strains (towards edge of sample)

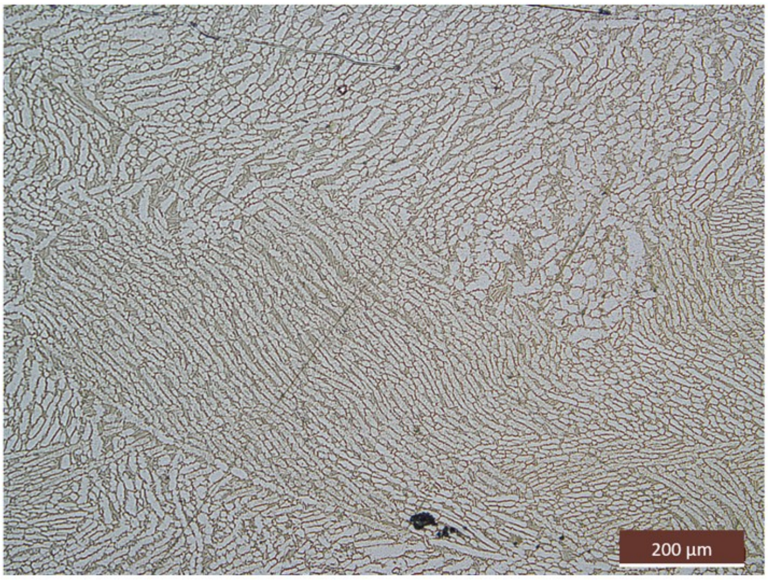

Figure 4.22: Optical micrographs of the high strain zone (ε= 1.5) of '5-(0.1M-1h)-FC' sample.

appears almost unaffected, only slightly coarsened, and no measurable globularisation has occurred (see Figure 4.24b).

Similarly to the uniaxial compression tests, the combination of deformation and annealing steps does not have a large effect on globularisation, as is illustrated in Figure 4.26 where comparable globularisation kinetics are observed. Even though no quantitative difference is observed between test conditions regarding globularised fraction; it appears that microstructural change is more advanced for the case of '5-0.1M-5h-FC' test which suggests that a higher level of deformation prior to an annealing stage is beneficial for microstructural evolution. Overall, these testing conditions are found not to be ideal for globularisation though since a maximum of 39% globularised fraction was achieved for '5-0.1M-5h-FC' sample, which is much lower than that achieved during uniaxial testing (e.g. 66% in test '1-0.5U-4h-FC'). These observations confirm that a change in forging direction is not beneficial for globularisation.

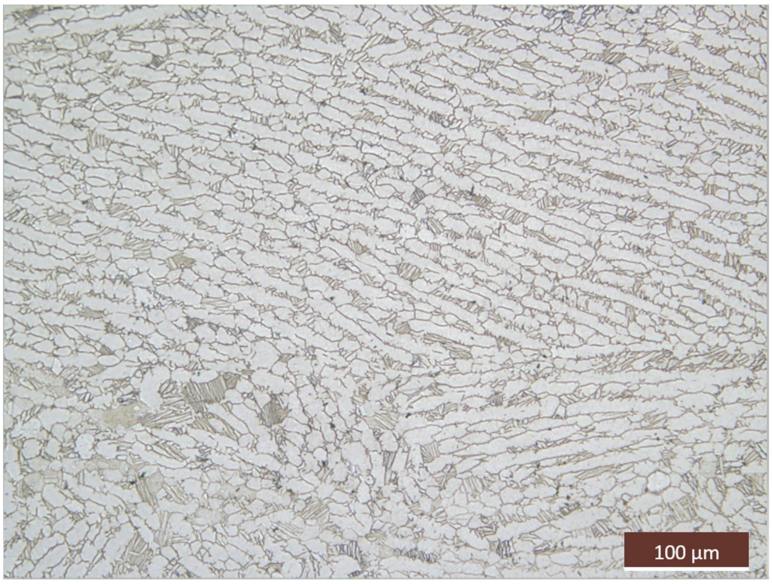

Figure 4.23: Optical micrographs of the high strain zone (ε= 1.7) of '5-0.1M-5h-FC' sample.

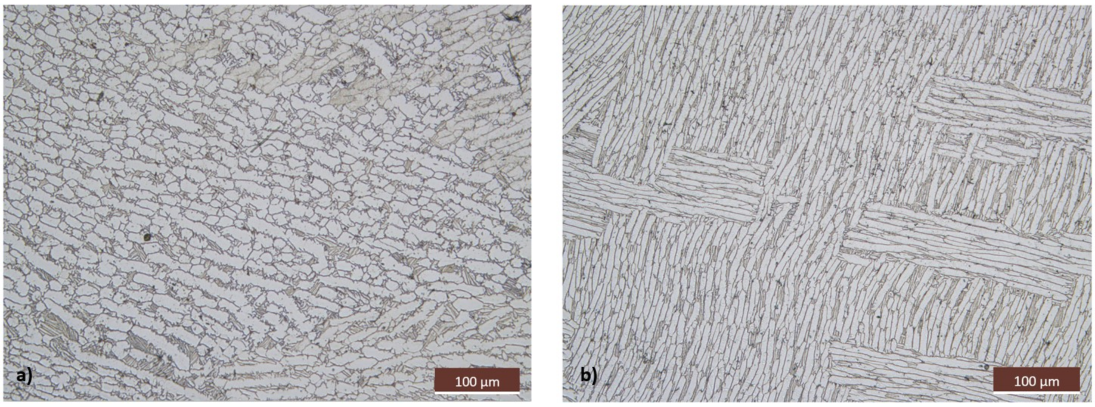

Figure 4.24: Optical micrographs of '3-0.1M-3h-2-0.1M-2h-FC' sample in two different strain zones: (a) ε= 1.5, and (b) ε= 0.7 .

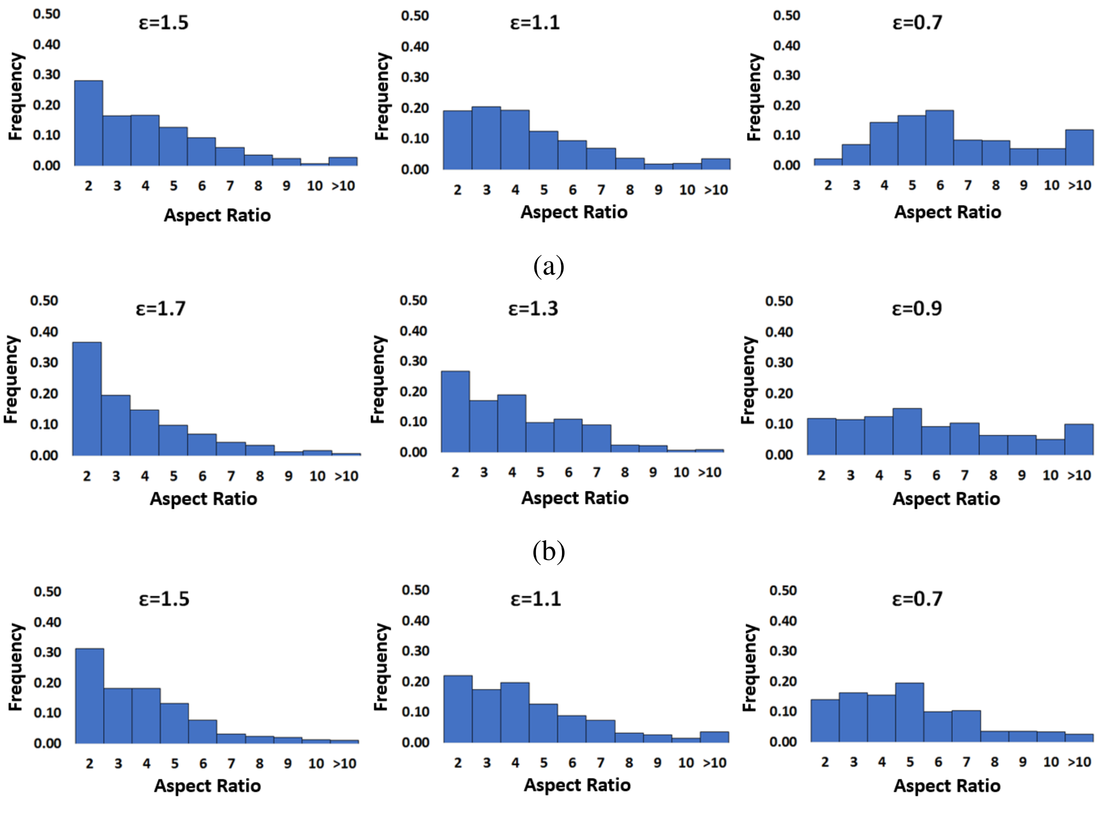

(a)

(b)

(c)

Figure 4.25: Plots of α lath aspect ratio distributions for samples: (a) '5-(0.1M-1h)-FC', (b) '5-0.1M-5h-FC', and (c) '3-0.1M-3h-2-0.1M-2h-FC'.

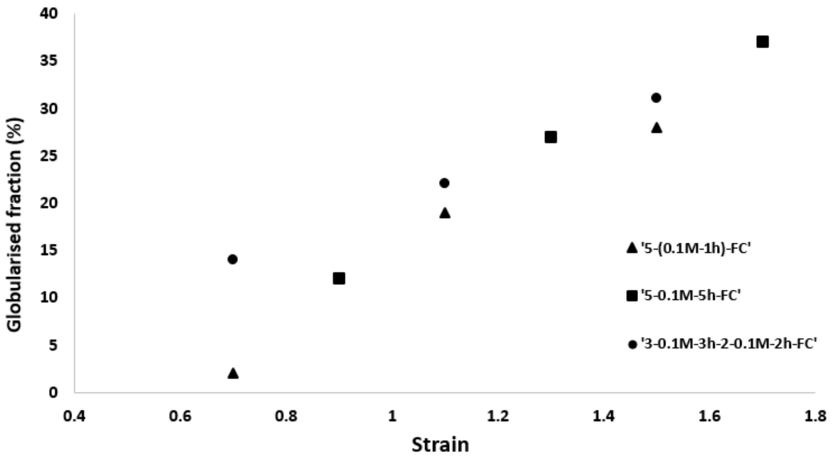

Figure 4.26: Plots of globularised fraction as a function of local strain for the multi-axially forged samples followed by various annealing.

Sample ’3-0.1M-1h-WQ’ and sample ’3-0.1M-1h-3-0.1M-1h-WQ’ were respectively subjected to one and two cycles of 3 multiaxial compressions with 0.1 strain along each axis followed by a 1 hour annealing. The optical microscopy appearances of their microstructures are shown in Figure 4.27 and their associated α lath aspect ratio distributions are provided in Figure 4.28. Similarly to samples deformed to a total strain of 0.5 and annealed for a total duration of 5 hours, the microstructure in these samples is hardly deformed (i.e. the α colonies are still visible). However, the α laths are measured to be thinner (4.1 ± 0.8 µm) and no difference in coarsening is observed between the two thermo-mechanical cycles.

One sample was subjected to a cycle of 3 multiaxial compressions with 0.1 strain along each axis followed by a 1 hour annealing (i.e. ’3-0.1M-1h-WQ’). Its microstructure also contains remnant of α colonies, but the α laths display a lower aspect ratio than in sample ’3-0.1M-3h-WQ’ (see Figures 4.29 and 4.30). The microstructure is actually close to that of sample ’3-0.1M-1h-3-0.1M-1h-WQ’, but with a little coarser grains(5.0 ± 1.0 µm).

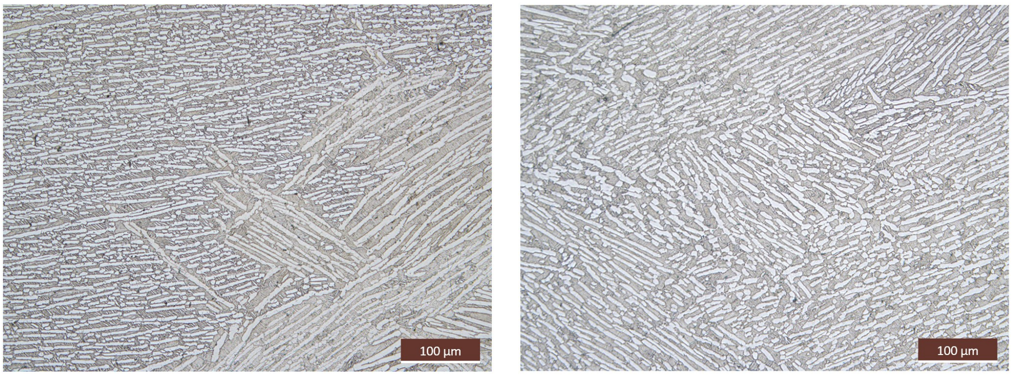

Figure 4.27: Optical micrographs of the samples '3-0.1M-1h-WQ' (left) and '3-0.1M-1h-3-0.1M-1h-WQ' (right).

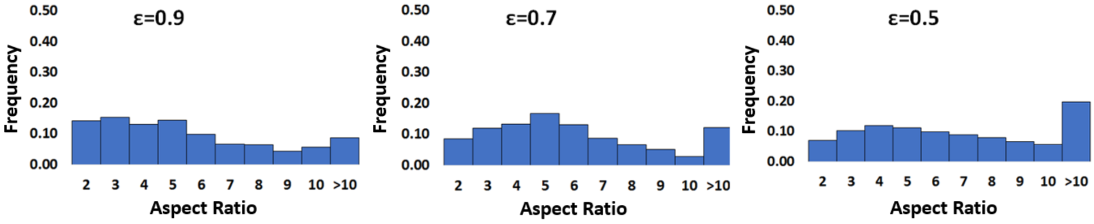

(a) ε=3*0.1 - 1h annealing - WQ

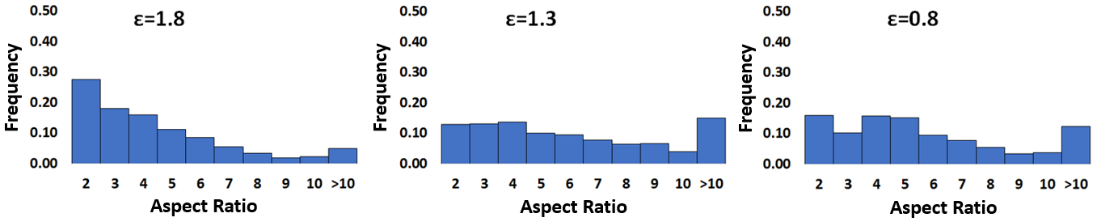

(b) ε=3*0.1 - 1h annealing - ε=3*0.1 - 1h annealing - WQ

Figure 4.28: Plots of α lath aspect ratio distributions for samples: (a) '3-0.1M-1h-WQ', and (b) '3-0.1M-1h-3-0.1M-1h-WQ'.

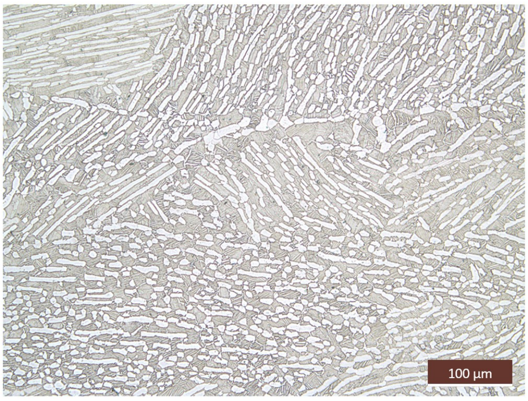

*Figure 4.29: Optical microscopy appearance of the interrupted test: ε= 3*0.1 - 3h annealing - WQ.*

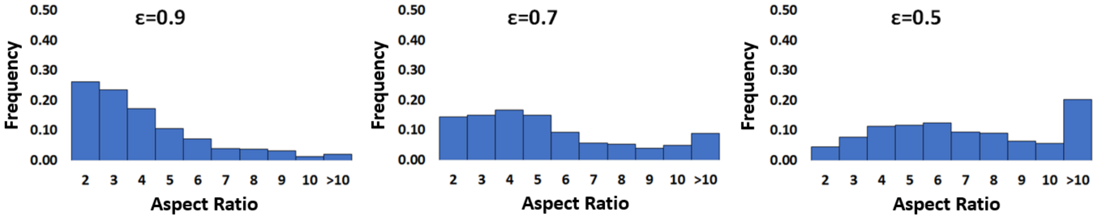

Figure 4.30: Plots of α lath aspect ratio distributions for '3-0.1M-3h-WQ' sample.

Figures 4.31 and 4.32 show optical micrographs of the samples subjected to a total strain of 1 through different multistep processing routes of ten steps of 0.1 strain and four steps of 0.25 strain, respectively, with 90° rotation in between each increment. The distribution of α lath aspect ratio in both microstructures are displayed in Figure 4.33.

The microstructures of both samples appears to be affected by the level of local strain in a heterogeneous way such that in some areas bent and fragmented α lamellae are observed (see Figure 4.31.a), while other areas appear to be less deformed (see Figure 4.31.b). Though, the initial prior-β grains and hence α colony structure are still apparent in the regions underwent high strains (see Figure 4.32.a). In the regions subjected to lower levels of strain, the resulting microstructure (Figure 4.32.b) looks similar to that of the as received material (Figure 4.6), with only few bent lamellae. The aspect ratio distribution of α laths shifts slightly towards smaller values with increasing local strain in both samples, however, the fraction of globularised α remains below 14%.

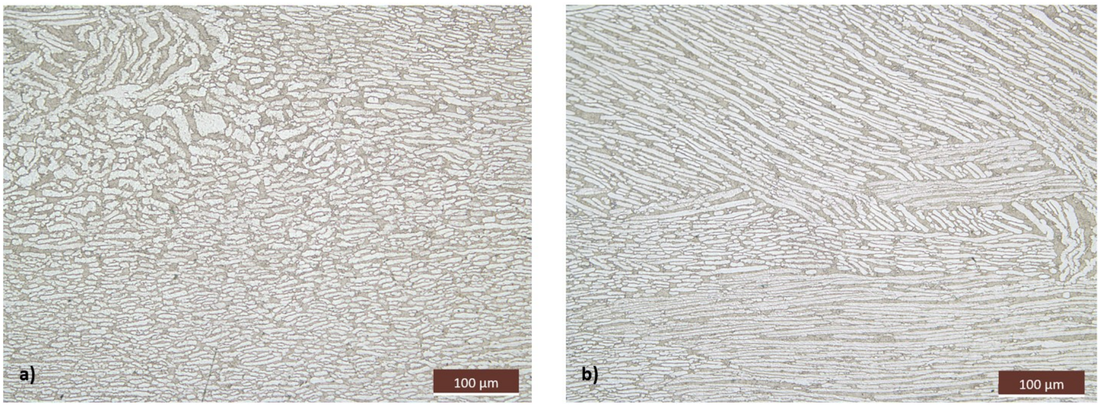

Figure 4.31: Optical micrographs of sample '4-0.25M-WQ' in the zone: (a) ε= *3.1, and (b)* ε= *1.5 .*

The results obtained for these two experiments are similar which indicate that applying the same overall strain level through different strain increment scenarios does not have a significant effect on microstructural evolution. Also, it is worth noting that the maximum local strain reached in both samples is around 3.2 which did not lead to significant globularisation, whereas in uniaxially compressed samples the same amount of globularisation is reached after a strain of 1.8 (see Figure 4.8); also under similar level of overall strain (i.e. ε =3.1) almost the entire microstructure is observed to be globularised [93]. This suggests that a change in loading direction (i.e. strain path) with small level of strain at each increment is not enhancing globularisation kinetics under the conditions tested in this work. It is worth noting however that after a 4 hrs annealing, the sample forged with 0.25 strain increments exhibited higher globularised fraction (i.e. 41%) than the sample forged with 0.1 strain increments (i.e. 26%). This suggests that slightly larger strain increment leads to higher stored energy that is used for static globularisation.

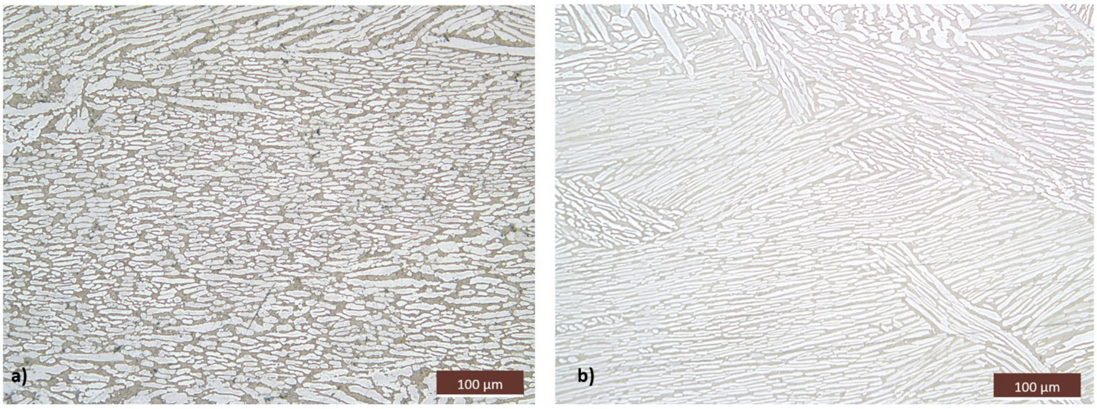

Figure 4.32: Optical micrographs of sample '10-0.1M-WQ'in the strain zone: (a) ε= 3.1, and (b) ε= 1.5 .

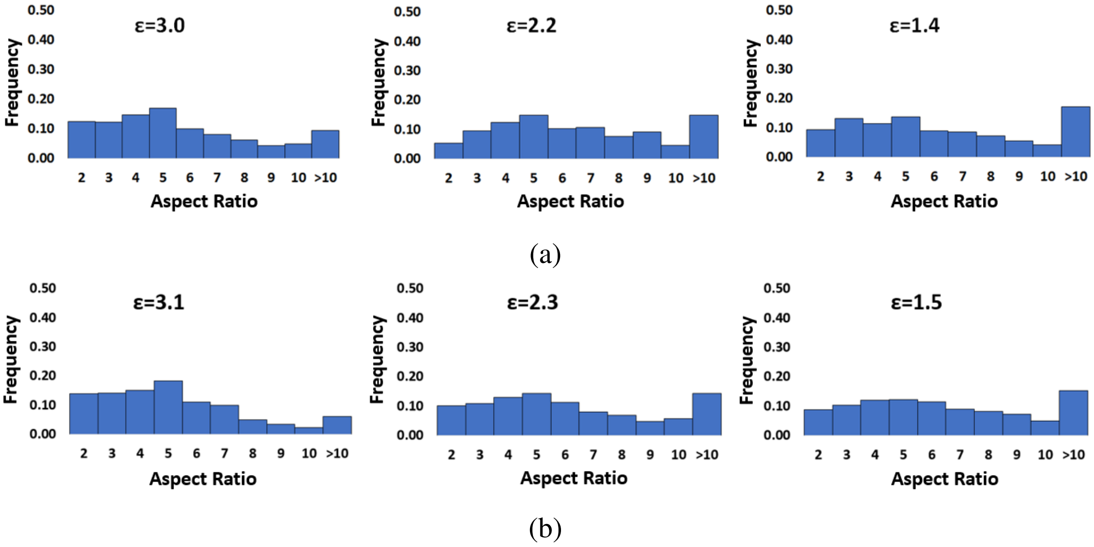

(a)

(b)

Figure 4.33: Plots of α lath aspect ratio distributions for samples: (a) '4-0.25M-WQ', and (b) '10-0.1M-WQ'.

The microstructural changes achieved after compression of a sample ('upset') to overall strain of 60% along three directions (i.e., 20% strain along each) are presented in Figure 4.35a. The α lath aspect ratio distributions for these microstructures are shown in Figure 4.36a.

Performing compressions along three orthogonal directions with a strain increment of 0.2, does not yield high globularisation rates. The initial α colonies and β grains were still evident after these processes; the α laths were not fragmented but mostly buckled (see Figure) 4.35a. Although some changes were observed in the aspect ratio distribution of α grains with increased strain level, no significant fraction of grains were globularised (less than 10%) (see figure 4.36a). The levels of globularisation achieved in these tests are similar to those obtained during uniaxial compression (e.g., '1-0.5U-WQ')(see Figure 4.34); however the microstructure does not appear as deformed. Additional deformation cycles would be required to reveal whether this deformation path is effective in comparison to uniaxial compressions. Also, post-deformation heat treatments would help with the understanding of the effect of this strain path on the kinetics of static globularisation.

The introduction of an additional deformation axis in between the two orthogonal directions, i.e., 45° rotation between compressions axes, during the test with similar level of strains at each step did not improve the kinetics of globularisation (see Figure 4.36b). The initial β grains and α colonies were still visible after the test (see Figure 4.35b) despite of being slightly deformed, and hence only small fraction of globularisation is observed (21%). When compared to a test conducted along two orthogonal directions, i.e., 90 rotation was applied between each forging steps (sample '3-0.1M-1h-WQ') (see Figure 4.27 and 4.34), no significant difference was observed. This corroborates the observation that additional deformation along an axis at 45° rotation to the other deformation axes does not affect microstructural changes significantly.

Overall, these specific deformation conditions did not have a significant effect on microstructural evolution and α lath globularisation. However, because of the limited number of tests performed in this work, it is difficult to conclude its efficiency compared to the other loading conditions for industrial applications. Indeed, the effect of these specific loading conditions have not been investigated for larger levels of strains and strain increments.

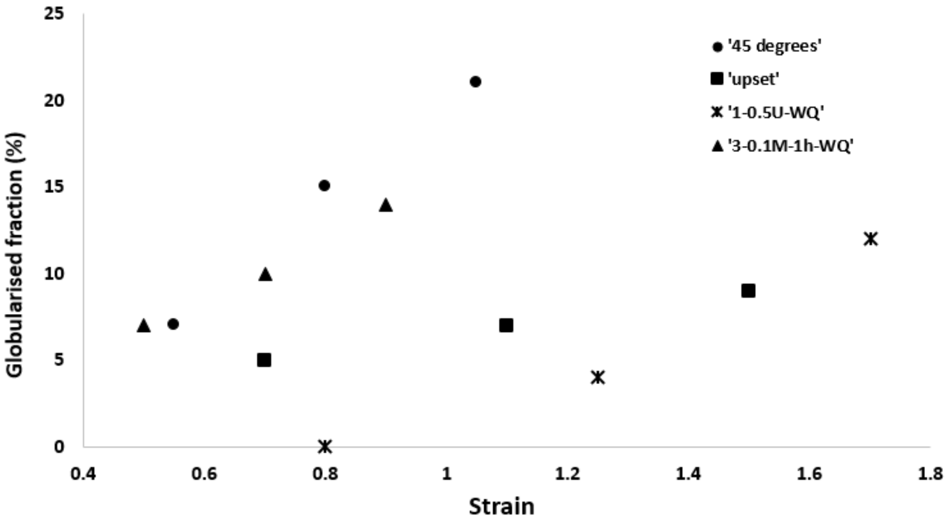

Figure 4.34: Plots of globularised fraction as a function of local strain for tests 'upset' and '45 degree' as well as for tests '3-0.1M-1h-WQ' and '1-0.5U-WQ' for comparison.

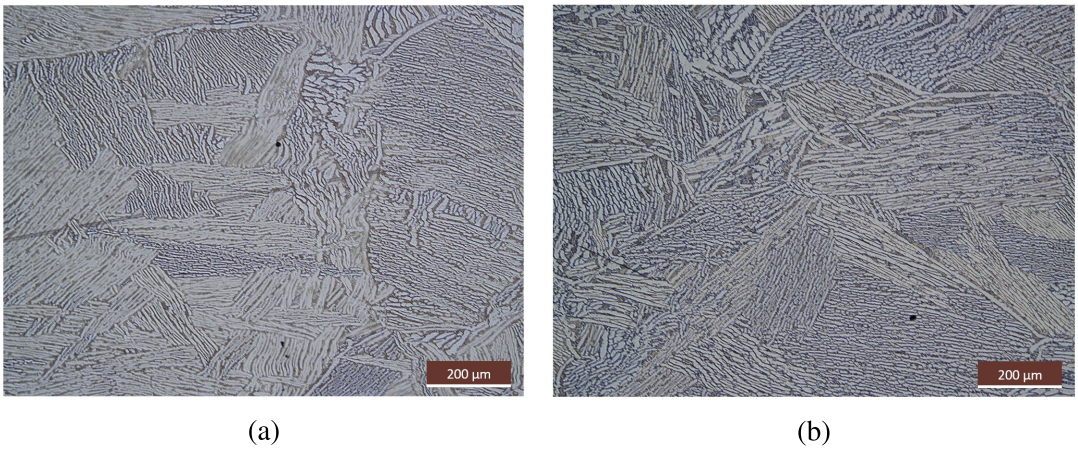

(a) (b)

Figure 4.35: Optical micrographs of samples: (a) 'upset', and (b) '45°'.

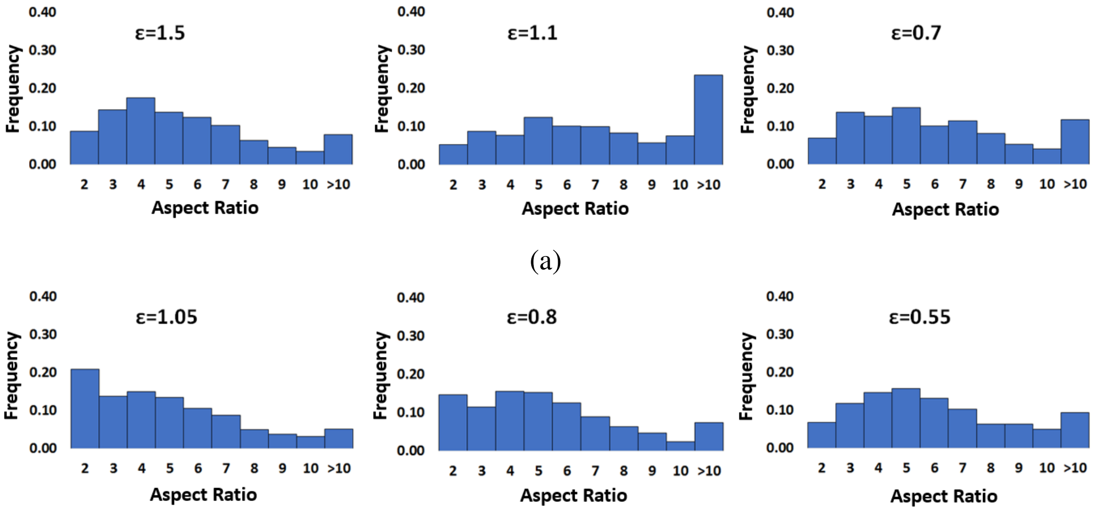

(a)

(b)

Figure 4.36: Plots of α lath aspect ratio distributions for samples: (a) 'upset', and (b) '45°'.

4.5 Effect of forging temperature on globularisation

For this investigation, two samples (i.e., '1-0.5U(900°C)-WQ' and '3-0.1M(900°C)-3h(950°C)-WQ') were forged at 900°C, one uniaxially to a total strain of 0.5 in one step, and the other multi-axially along two orthogonal axes to a strain of 0.3 by applying 0.1 at each step. Both samples were then subjected to annealing up to 4 hours at a higher temperature of 950°C. Their optical microscopy appearances are displayed in Figures 4.37 and 4.39, respectively, with their associated analysed α lath aspect ratio distributions in Figures 4.38 and 4.40, respectively.

Uniaxial forging at lower temperature of 900°C has resulted in a noticeably higher fraction of α phase, $\approx 75\%$ compared to 30% for that of a similar test conducted at 950°C. The microstructure appears to be influenced by this process, although α colonies and prior grain-boundary α layers are still visible after deformation. No rotation of the α laths towards a direction perpendicular to the loading axis is noticed. Though, shear bands across α colonies are observed in multiple locations (see Figure 4.37a), which were not noticed in the samples deformed at 950°C. Additionally, the deformation of α lamellae is not as homogeneous; the laths are only fragmented in locations where shear bands occurred, otherwise they are mostly bent. These results are manifested in the plots of aspect ratio distributions with a high fraction of elongated α laths having an aspect ratio of 10 or more (see Figure 4.38a).

The negative effect of the lower forging temperature on microstructural evolution is still visible after an annealing at higher temperature of 950°C (see Figure 4.37c and 4.37e). In fact, annealing at 950°C enhances the globularisation of the lamellae that were sheared and buckled during forging at 900°C, however, the rest of α remain elongated even after 4 hours of heat treatment (see figures 4.37d and 4.37e). This has resulted in lower fractions of globularised α grains compared to those of the tests that underwent deformation at higher temperature of 950°C (see Figure 4.9).

When deformation is carried out in a multi-axial manner followed by an annealing at 950C, the lower forging temperature leads to a slight increase in the fraction of α phase but a decrease in the thickness of α laths. The kinetics of globularisation are also reduced in comparison to the counterpart forged at higher temperature (see Figure 4.27).

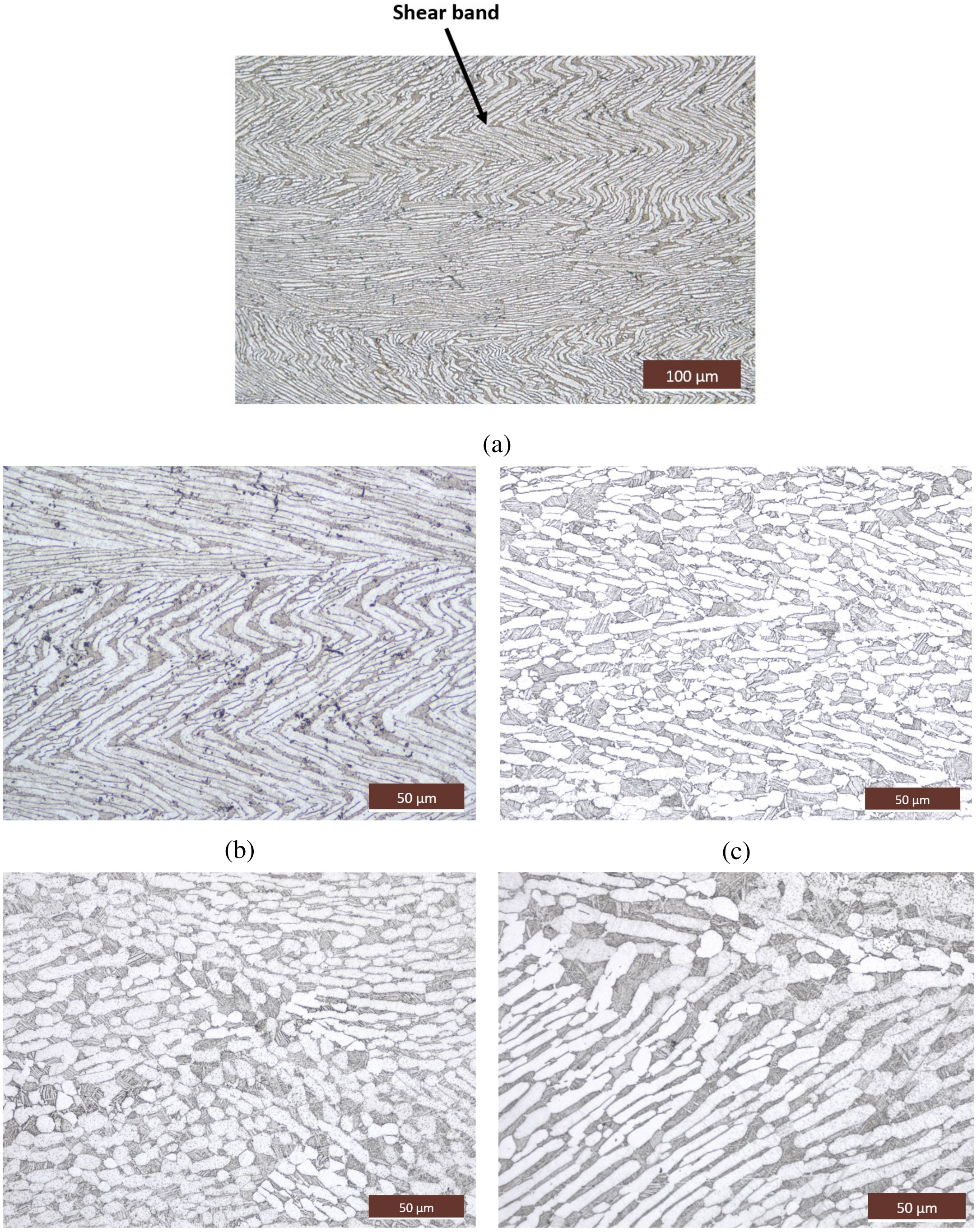

(a)

(b) (c)

(d) (e)

Figure 4.37: Optical micrographs of sample '1-0.5U(900°C)-WQ': (a-b) as forged, (c) after 1 hr annealing, and (d-e) after 4 hrs annealing.

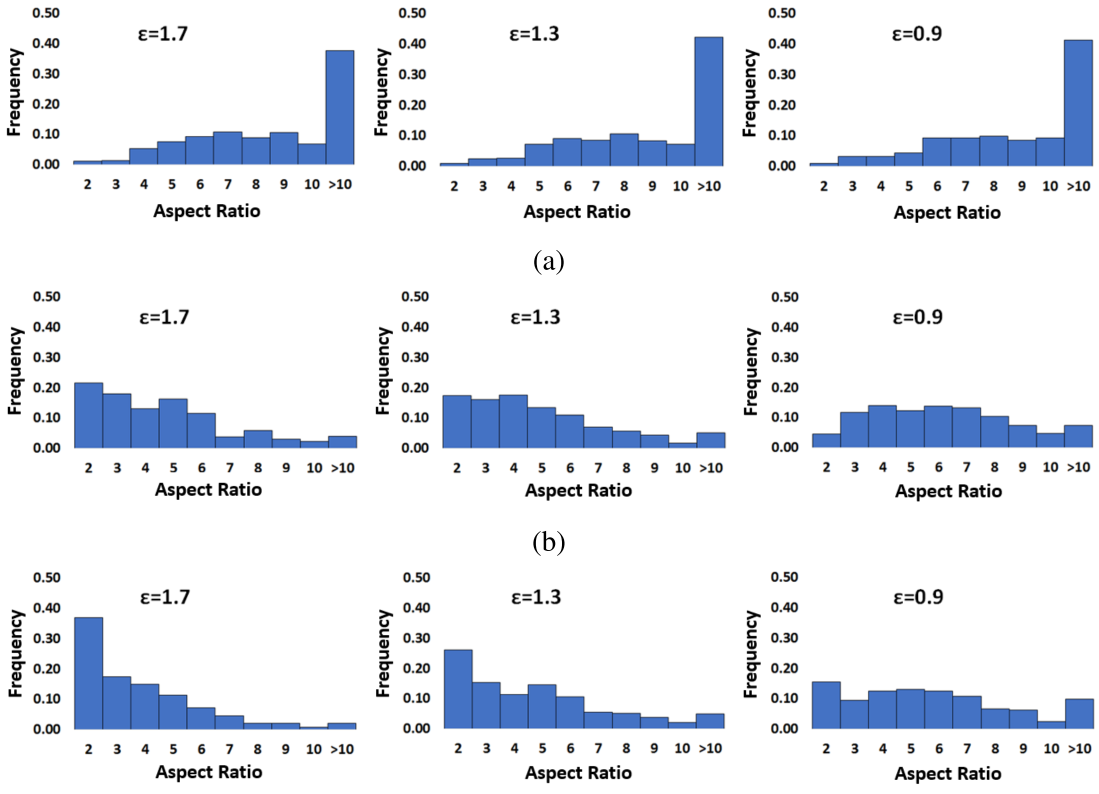

(a)

(b)

(c)

Figure 4.38: Plots of α lath aspect ratio distributions for sample '1-0.5U(900°C)-WQ': (a) as forged, (b) after 1 hr annealing, and (c) after 4 hrs annealing.

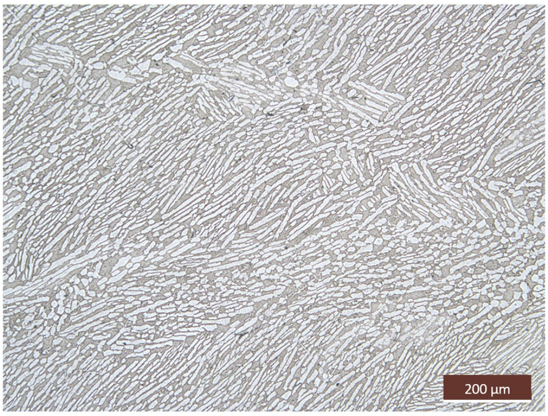

Figure 4.39: An optical micrograph of sample '3-0.1M(900°C)-3h(950°C)-WQ'.

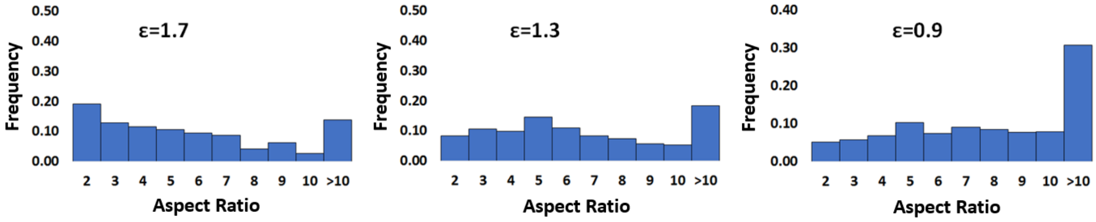

Figure 4.40: Plots of α lath aspect ratio distributions for sample '3-0.1M(900°C)-3h(950°C)-WQ'.

4.6 Effect of post-forging annealing duration on globularisation

It was observed that annealing duration at 950°C has a positive impact on the globularisation rate regardless of the pre heat treatment forging conditions. For both cases where samples were forged uniaxially (e.g. '1-0.5U-WQ') and multi-axially (e.g. '4-0.25M-WQ'), the fraction of globularised α grains has been seen to increase with longer annealing time (see Figures 4.9, 4.10, 4.41, and 4.42). The kinetics of globularisation however is seen to be dependent on the forging conditions where samples compressed uniaxially were displaying faster kinetics than those forged multi-axially (see Figure 4.43). The underlying globularisation mechanisms, e.g. boundary splitting (A) and edge spheroidisation (B), are highlighted in the micrographs of the annealed samples shown in Figure 4.44. At the areas of lower local strains (relative to each test conditions), most α laths did not appear to be fragmented during annealing at 950°C. Instead they appear to be slightly shorter and thicker (see Figure 4.45) while retaining a higher aspect ratio, even though the globularised fraction of α grains increased (see Figure 4.9). Grain coarsening is also observed with increased heat treatment duration (see Figure 4.41). This was seen for every annealed sample regardless of the forging conditions, although the extent of grain coarsening is observed to be dependent on deformation condition (see Figure 4.46).

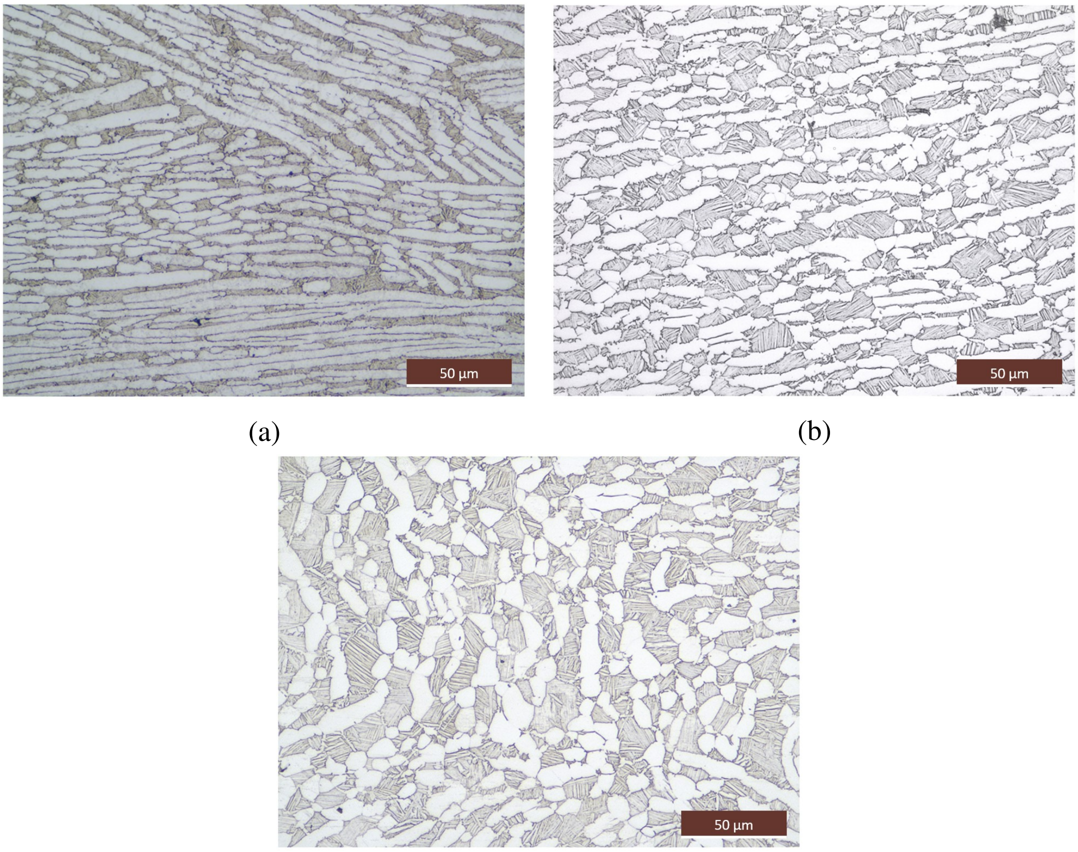

(a) (b)

(c)

Figure 4.41: Optical micrographs of sample '4-0.25M-WQ': (a) as forged, (b) after 1 hr annealing, and (c) after 4 hrs annealing.

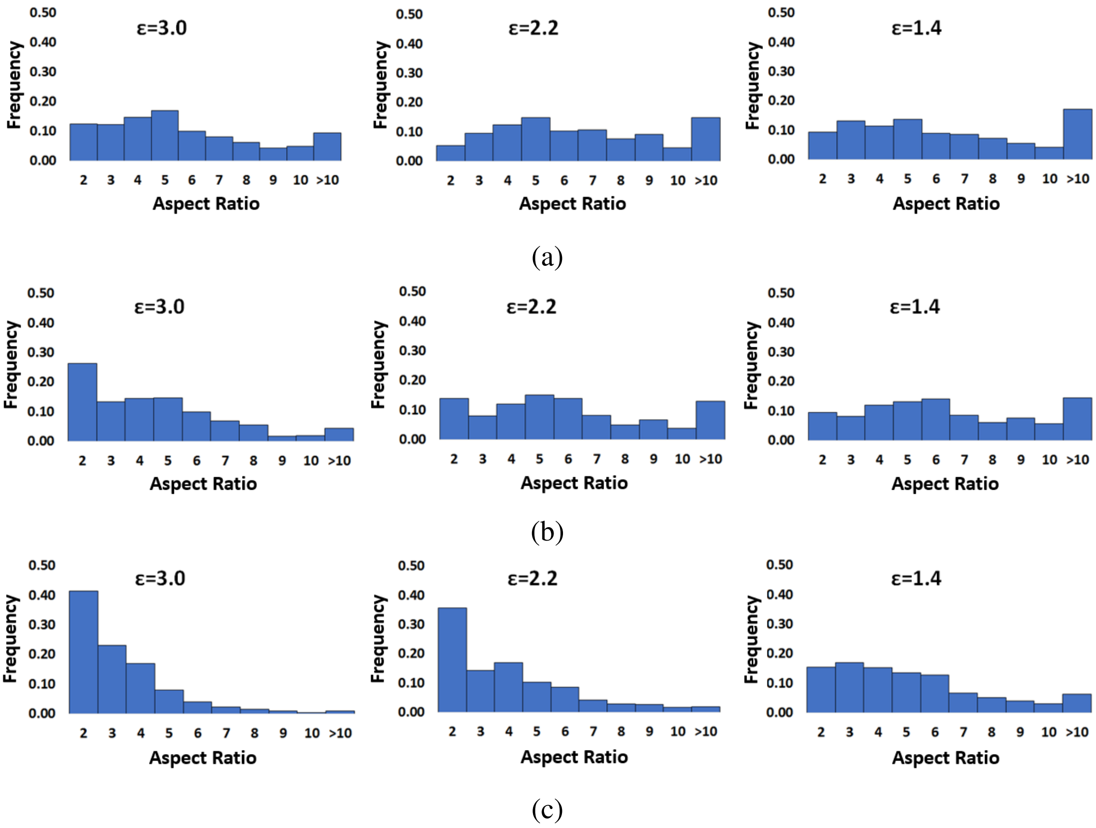

(a)

(b)

(c)

Figure 4.42: Plots of α lath aspect ratio distributions for sample '4-0.25M-WQ': (a) as forged, (b) after 1 hr annealing, and (c) after 4 hrs annealing.

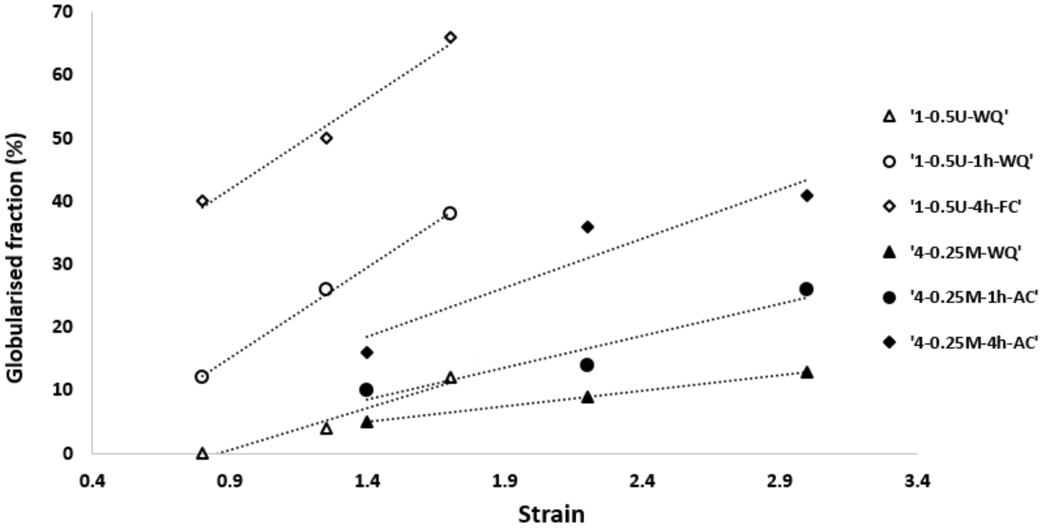

Figure 4.43: Plots of globularised fraction as a function of local strain for uniaxially and multiaxially forged samples followed by various annealing.

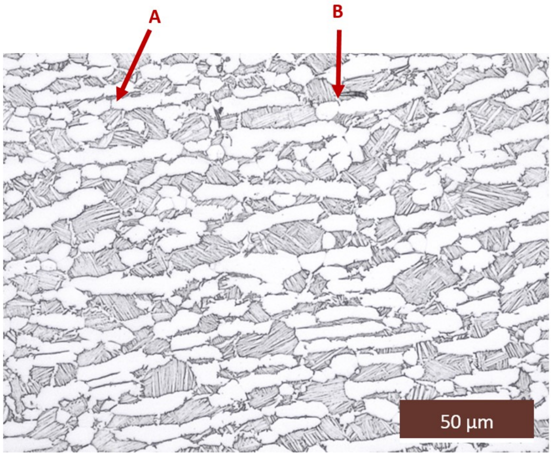

Figure 4.44: Optical micrograph of sample '4-0.25M-1h-WQ' displaying different mechanisms of globularisation.

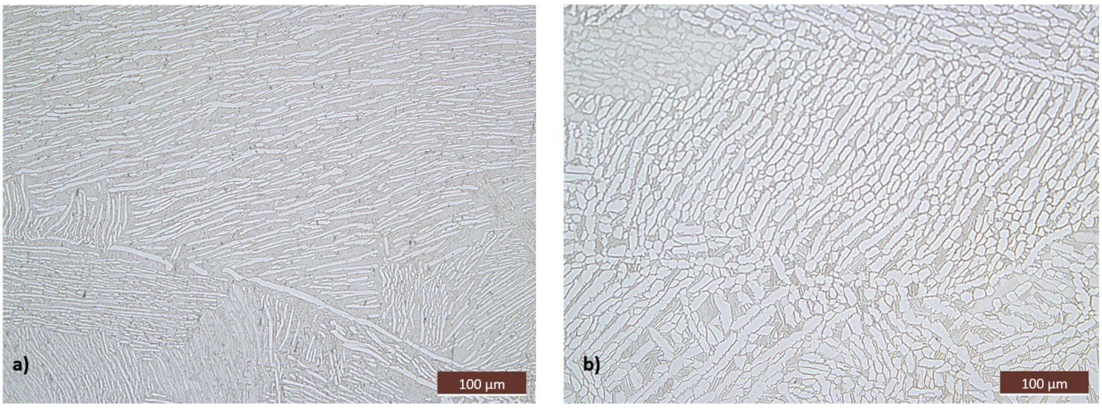

Figure 4.45: Optical micrographs of sample '1-0.5U-1h-WQ' in the low strain zone (ε = 0.8): (a) as forged, and (b) after 4 hrs annealing.

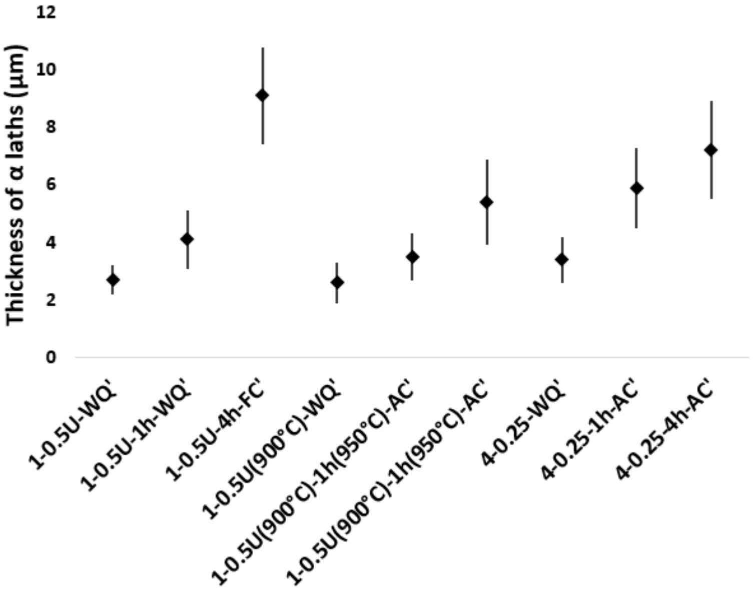

Figure 4.46: Plot of α laths thickness for uniaxially and multiaxially forged samples followed by various annealings.

4.7 Texture evolution

Figure 4.47 shows the texture in the material after the initial heat treatment (i.e., 1hr annealing at 1050°) and after annealing for 1 hr at 950° (i.e., sample 'SA+1h'). It appears that the material after initial heat treatment has a texture with a preferential alignement of $\{0001\}$ poles, i.e., c axis of HCP α unit cell, towards the direction of the billet axis. This was previously observed [65] and was attributed to preferential transformation from β to certain α variants (i.e., variant selection) upon cooling from heat treatment temperature during previous processes. This variant selection could be due to a few factors such as local stresses or the presence of nearly parallel $\{110\}$ planes at β grain boundaries due to prior hot working conditions.

In the material heated up to 950°C and water quenched, the texture changed such that the $\{0001\}$ poles rotated to 60° from the billet axis. The texture is also a little weaker which may be due to the water quench that reduces variant selection [84].

Figure 4.48 displays the texture in samples after uniaxial compression and different heat treatments conditions. Uniaxial forging reveals a transverse texture with a strong tendency of the axis to rotate in an orientation perpendicular to the loading

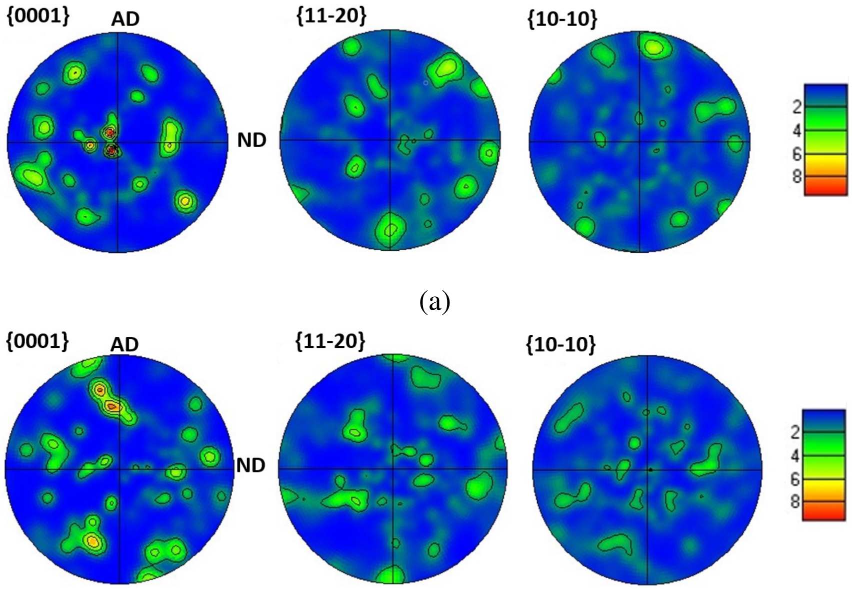

(a)

(b)

Figure 4.47: $\{0001\}$, $\left\{11\bar{2}0\right\}$, $\left\{10\bar{1}0\right\}$ *pole figures of the material: (a) after initial heat treatment and (b) 'SA+1h'.*

direction and an alignment of the $\left\{11\bar{2}0\right\}$ poles in the compression plane. This type of texture evolution is common during compression tests [43, 108]. Texture remains unchanged during post-deformation annealing and its intensity increases to some extent. This has been ascribed to the grain coarsening along the orientation of original deformation textures [40, 101] and to recovery processes that reduce defect density and the orientation variation within the lamellae [43].

Figure 4.49 displays the texture in the sample that underwent two orthogonal compressions. The $\langle c\rangle$ poles are either aligned with the billet axis or in the plane formed by the two compression directions. Also, the texture is much weaker than in the case of uniaxial compression. Finally, a slight alignment of the $\left\{11\bar{2}0\right\}$ poles with the final compression direction can be seen. The same deformation mechanisms operate during the second compression as that of the first one with a tendency to rotate the $\langle c\rangle$ poles in a direction perpendicular to the compression.

The introduction of a 1h annealing before the second compression does not affect the final texture mode and barely alter its intensity as is shown in Figure 4.50. This is similar to the findings after a single compression.

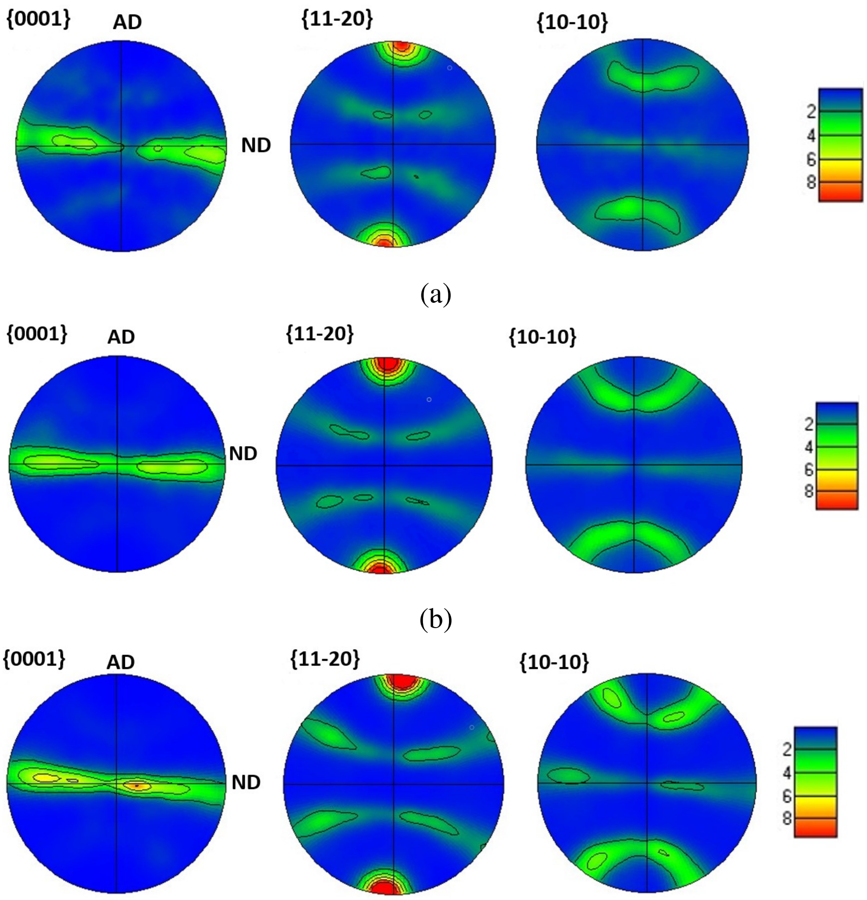

(a)

(b)

(c)

Figure 4.48: $\{0001\}$, $\{11\bar{2}0\}$, $\{10\bar{1}0\}$ *pole figures of the material after uniaxial compression test: (a) water quenched (b) annealed for 1hr then water quenched and (c) annealed for 4hrs then slow cooled.*

After four orthogonal compressions, the texture is quite weak (i.e., by almost 3 times) and the $\langle c \rangle$ poles are spread in the plane perpendicular to the billet axis (see Figure 4.51). Furthermore, a symmetry around the billet axis can be observed in all the pole figures. These findings are common during cogging process and are linked to the fact that whatever the strain path used to deform the part, it always tends to reduce the diameter of the sample and increase its length. As a results the overall strain path can be compared to extrusion which typically leads to a partial fibre texture with the fibre axis parallel to the extrusion direction [65].

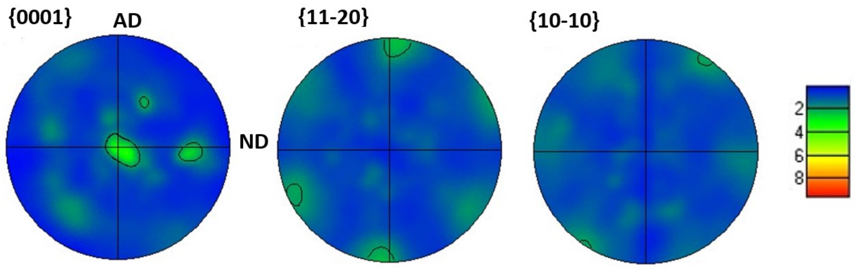

Figure 4.49: $\{0001\}$, $\{11\bar{2}0\}$, $\{10\bar{1}0\}$ *pole figures of the material after test ’2_0.25M _1h_FC’.*

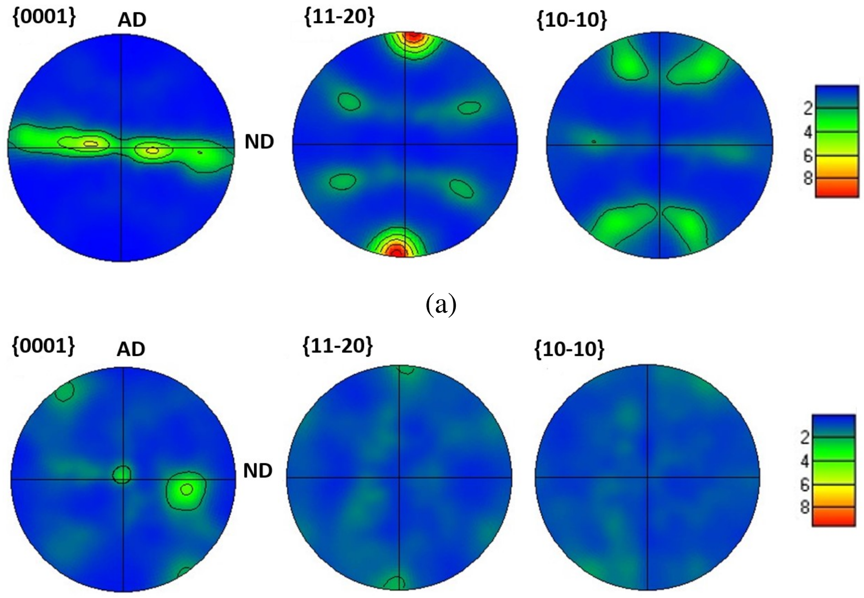

(a)

(b)

Figure 4.50: $\{0001\}$, $\{11\bar{2}0\}$, $\{10\bar{1}0\}$ *pole figures of the material from tests including an annealing between compressions: (a) uniaxial and (b) orthogonal compressions.*

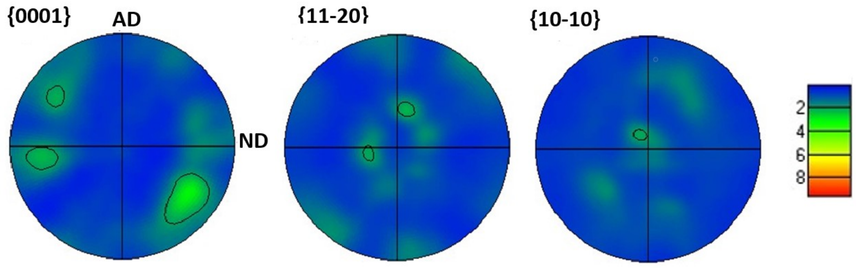

Figure 4.51: $\{0001\}$, $\{11\bar{2}0\}$, $\{10\bar{1}0\}$ *pole figures of the material from test ’4_0.25M_WQ’.*

The compression temperature does not seem to have a significant effect on the texture mode during uniaxial compression. Indeed, after compression at 900°C, the same pole figure as for compression at 950°C is observed but with a weaker intensity (see Figure 4.52).

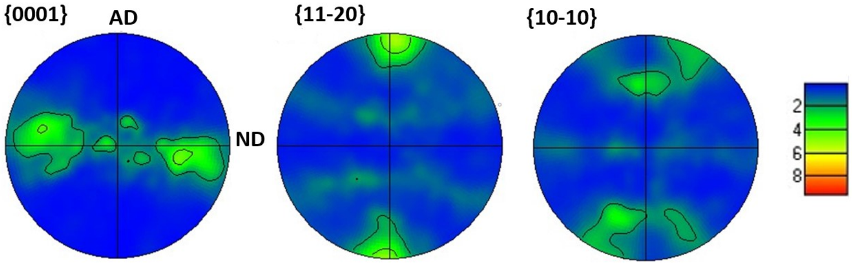

Figure 4.52: $\{0001\}$, $\{11\bar{2}0\}$, $\{10\bar{1}0\}$ *pole figures of the material from test '1_0.5U_WQ(900°C)_WQ'.*

4.8 Summary

A set of tests have been performed to investigate the evolution of globularisation during cogging operations of Ti-6Al-4V. The experimental set up was benchmarked against literature using uniaxial compressions and heat treatments. The kinetics increase with increasing strain and annealing time in a similar fashion as found in literature; and this provides a reference base for multiaxial tests in this work. Interrupting the uniaxial deformation with heat treatment did not modify the kinetics of globularisation significantly. Introducing a 90° rotation between two deformation steps decreased the kinetics of microstructural evolution; and the effect of the reheating schedule was also found to be negligible. The deformation increment during multiaxial forging did not have a significant effect on the kinetics of globularisation either. The forging temperature was found to have an effect on the microstructural evolution, with the higher temperature (viz.950C) yielding higher kinetics of globularisation while the lower temperature (viz.900C) was observed to be very unfavourable.

Chapter 5

Microstructure modelling

In this chapter, various models for the prediction of microstructural evolution during α/β forging of titanium alloys are assessed. Initially, the validity of the existing models for the experimental data produced throughout this work is evaluated. Then, an augmented model is proposed to describe the microstructural evolution observed in this EngD project.

5.1 Application of existing models

The literature survey carried out for this project (see section 2.4.3) found previous studies describing different steps of the globularisation process. The data produced in this work are input in these models to assess the accuracy of their estimation of microstructural evolution (i.e. progress of globularisation) during single- and multi-axial forging.

5.1.1 Avrami based model

Avramis based equations have often been used to successfully describe the progress of dynamic globularisation in titanium alloys [93, 94, 99, 105]. However, the suitability of this class of models for multi-axial forging, carried out during this project, is difficult to be verified, as the maximum level of dynamic globularisation

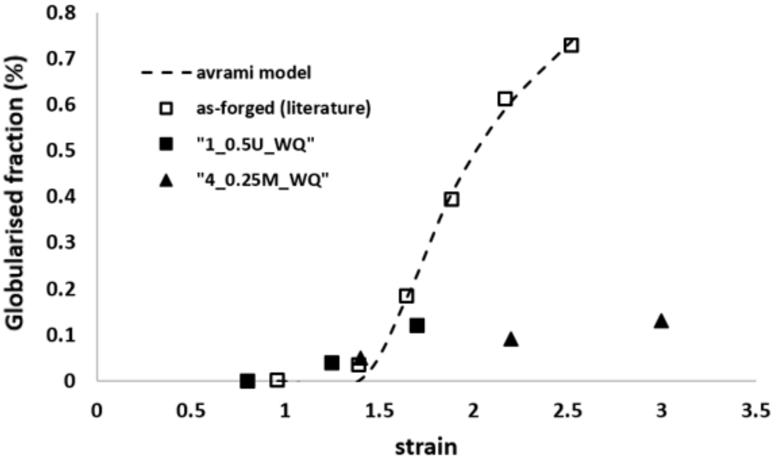

Figure 5.1: Plot of the globularised fractions as a function of local strain; predicted using Avrami model from literature and experimentally determined in this study.

achieved is not significantly high. Indeed, a maximum of 15% globularised α is achieved (see chapter 4). Figure 5.1 displays globularised fractions as a function of local strain for tests ”1_0.5U_WQ”, ”4_0.25M_WQ” in this study and from Shell and Semiatin [91]. For the case of uniaxial compression, it appears that the experimental data from this study matches those from the literature, and with the results of the Avrami model. However, more experimental data do not exist to confirm for the higher levels of strain. Same observation is made for the case of multi-axial forging. A different set of parameters would be required for the model, but Avrami model could be suitable to describe globularisation during multi-axial forging. Additional tests would be needed to verify whether a sigmoidal evolution of globularised fraction will be reached at higher strains.

5.1.2 Boundary splitting model

A model based on boundary splitting has been proposed, following classic analyses (Lifshitz-Slyozov-Wagner theory) [55], in which the time required for the penetration of β phase in α laths is estimated (see eqation 2.4). This model does not yield a fraction of globularised α, rather a time after which termination migration becomes the dominant mechanism for globularisation (see Section 2.4.3 for further details).

The constants in this model are taken from Semiatin and Pilchak [77] and are listed in Table 5.1

Table 5.1: List of constants for boundary splitting model.

m	C_f	D ($\mu m^2.s^{-1}$)	$V_m(mm^3)$	$\gamma J.m^{-2}$
0.4	61.3	0.05	10,440	0.4

This model was used for microstructures with different lath thickness distributions that were produced under different conditions. The output statistics are then compared with the measured experimental observations to evaluate the compatibility between the model predictions and the data produced in this work.

The results of model prediction agree well with the microstructure obtained during uniaxial compressions at 950°C. Indeed, the predicted time for boundary splitting mechanism is about 2 hrs (see Figure 5.2), while in practice this is measured to be $\approx$ 1 hr. Actually after a 1 hr annealing at 950°C, most laths are observed to be segmented and begin to coarsen at a faster rate (see Figure 4.10) due to the termination migration becoming the dominant mechanism for microstructural change [95]. When the compression test is conducted at lower temperatures (i.e. 900°C) but the post forging annealing was performed at 950°C, same correlation is observed between the predicted and experimentally observed time for boundary splitting.

For the case of multi-axial compression test, (i.e., '4_0.25M_WQ'), the predictions of the model do not match well with the experimental data. As can be seen in Figure 5.2, the predicted time for boundary splitting is $\approx$ 5hrs whereas experimental observations show that globularisation and to some extend coarsening have taken place after 4hrs at 950°C. This implies that termination migration takes place more rapidly than boundary splitting. Also, the model takes the deformation level into an account through the slope of the groove parameter (see section 2.4.3 for details). This parameter can vary for different test conditions (i.e. uniaxial vs multiaxial), and even for areas with different localised strain level in a sample. In this work, the slope of the groove has not been assessed experimentally and thus the value used is taken from the literature [77] which might contribute in the discrepancy between the model predictions and the experimental results.

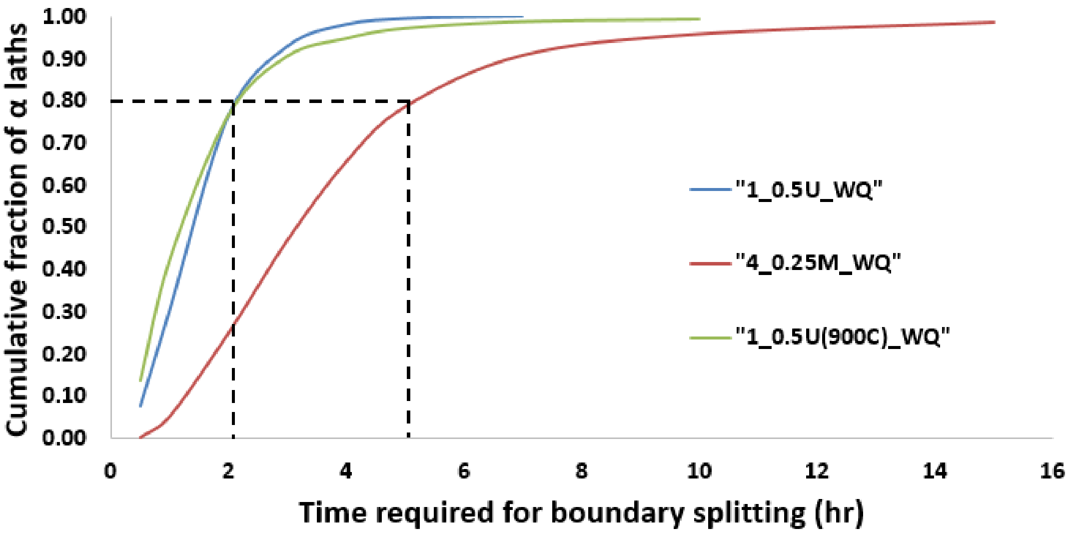

Figure 5.2: Predicted time for boundary splitting mechanism in Ti-6Al-4V subjected to different deformation conditions.

5.1.3 Termination migration model

The microstructural evolution due to termination migration is predicted based on Ficks diffusion law [83] (see section 2.4.3). The efficiency of the model is assessed in this project for samples that underwent both uniaxial and multiaxial forging. The results are provided in Table 5.2.

Table 5.2: Comparison between the experimentally measured globularised fractions and the results of model prediction based on the termination migration mechanism.

Input data	Data used for comparison	Experimental globularised fraction (%)	Predicted globularised fraction (%)
1_0.5U_1h_WQ	1_0.5U_4h_FC	66	71
3_0.1M_1h_WQ	3_0.1M_3h_WQ	26	25
4_0.25M_WQ	4_0.25M_4h_AC	41	38
1_0.5U(900°C)_1h(950°C)_AC	1_0.5U(900°C)_4h(950°C)_AC	37	49

The lath thickness data used as an input in the model were taken from the forged samples (i.e. both uni- and multi-axilally forged) that were annealed at 950°C for 1hr, since this condition was considered to be an ideal case for the activation of the termination migration mechanism. However, for multi-axially forged (i.e. ε= 4*0.25) and annealed samples, it was observed that termination migration and grain coarsening occurred simultaneously from the start of the heat treatment. Hence, input information for the model was taken from the as-forged condition.

The predicted globularised fractions by this model are in a good agreement with the experimentally measured data for both uni- and multi-axially compressed samples (see Table 5.2). This is likely to be due to the fact that this model is solely based on diffusion mechanisms [83] and does not take into account the deformation history of the material.

The highest inconsistency between the measured data and the results of model prediction was observed for the forging experiments that were carried out at lower temperatures (900°C). The observed difference in the globularised fraction can be explained on the basis that after 4 hrs annealing at higher temperature (i.e. 950°C), a higher fraction of α phase is present in the microstructure; which affect the diffusion process and consequently the evolution of globularisation (i.e. aspect ratio). Also, the deformation at lower temperature was observed to be quite heterogeneous, leading to some areas with higher rates of globularisation (i.e. up to 50%) as predicted, whereas in other areas almost no globularisation occurred. This yielded an overall α globularised fraction lower than the predicted value.

The applicability of these prediction models have been shown in previous studies [95, 116] where good agreements were observed with the experimental data. A reasonably good agreement between the experimental data and the prediction results is also achieved in this project. Using these predictive tools allow the determination of the fraction of globularised alpha particles in a manufactured part taking into considerations the applied thermo-mechanical process parameters. The shortfall of these models is that the dimension of the α laths at the beginning of the thermo-mechanical treatment is needed which is not always straightforward. Also, no information regarding the quantitative evolution of these dimensions is accessible. The models do not take the process parameters directly as inputs, rather they use a framework of variables that are somehow dependant on the process parameters. These deficiencies make these equations less practical for implementation in industrial applications. The mismatch between experimental observations and the results of these predictions can be indicative of the activation of a certain microstructural evolutionary mechanism such as recovery that has not been taken into consideration.

5.1.4 Empirical models

For simple implementation in production practice, phenomenological models are also developed. For example, a model was proposed based on the data from Stefansson and Semiatin [95] (Equation in section 2.4.3). This empirical equation takes process parameters such as strain, annealing temperature and annealing duration, as inputs and evaluates the volume fraction of spheroidised α grains.

The proposed empirical relationship in Equation 2.3 is used to predict microstructural evolution (i.e. globularisation) during the forging operations conducted in this project. The parameters applied during the trials are used as input parameters for the prediction of globularisation, and the results are compared with the experimentally measured fraction of globularised grains. The material constants are determined using an optimisation solver in Microsoft Excel with the objective function provided in Equation 5.1. The constants that resulted in a minimum objective function are presented in Table 5.3. These are then used in the model for the evaluation of the globularised fractions.

$$S = \sum_{i=1}^{n} (f_c - f_e)^2 \tag{5.1}$$

In Equation 5.1, n is the number of data points, f_c and f_e are the calculated and experimental globularised fractions respectively.

Table 5.3: List of constants from the empirical model predicting globularised fraction.

	model's constants				
	a	b	c	d	f
uniaxial experiments	1.27	30.15	0.927	-1209.8	36.64
multiaxial experiments	0.48	24.18	0.915	-1125.0	2.15

Separate parameters were evaluated for both uniaxial and multiaxial test procedures, due to their different approaches that might affect the kinetics of globularisation. Upon using only one set of parameters to predict microstructural evolution during all test procedures, no reasonable convergence was reached, and the

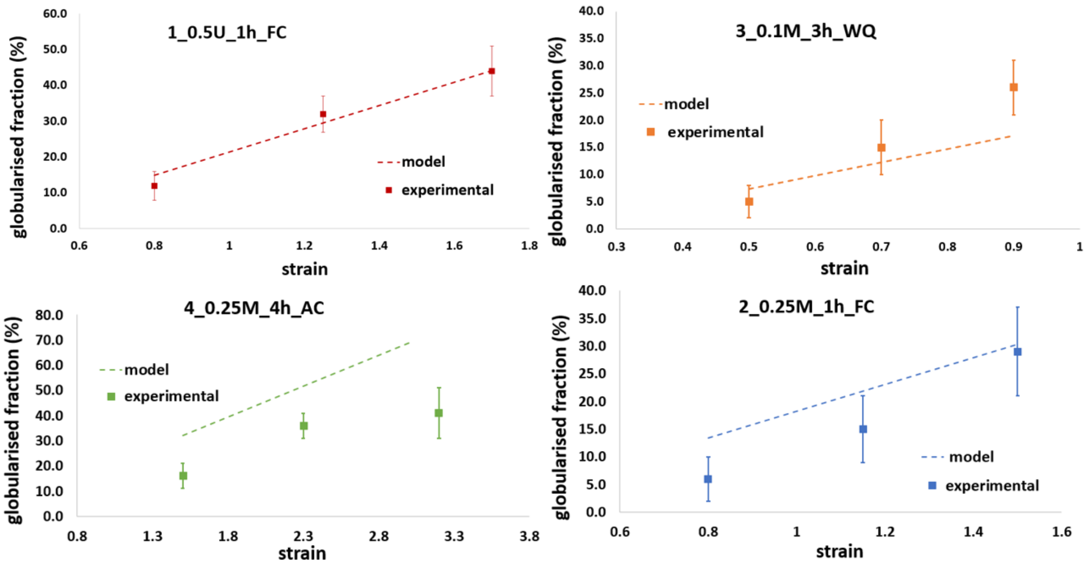

Figure 5.3: Comparison between the experimentally measured fractions of globularisations with the results of predictions using empirical model in Eq.2.3.

model is not able to predict globularisation accurately. When separate sets of parameters are used, acceptable predictions are obtained for uniaxial compressions followed by annealing as is shown in Figure 5.3.

For the case of multiaxial compression tests, using separate materials constant has resulted in better convergence, however a significant level of uncertainty is still observed (see Figure 5.3). The model is not capable of considering changes in the strain path in the calculation, and this might be the reason for the high uncertainty compared to the experimental results. Otherwise, the model is able to predict the trend of globularisation as a function of strain for all cases. This model could thus be used as a tool for a rough estimation of microstructural evolution, while a more suitable model is needed to precisely predict spheroidisation during cogging process.

5.2 A new model for globularisation

The predictive models reviewed and applied in the preceding section and in the literature survey, often describe microstructural evolution in Ti-6Al-4V through a certain mechanism. Only few models take into consideration both dynamic and static globularisation throughout the forging process. Accurate prediction of microstructural evolution during cogging operation necessitates both dynamic and static phenomena to be considered concurrently. With this aim in mind, a global model has been proposed to address this requirement. Despite the difference in the kinetics of globularisation between samples subjected to uniaxial and multiaxial forging, the exhibited trends are similar; thus the same equations are examined. Modifications have been applied to the parameters to include the effects of changes in strain path, as well as the intermediate reheating and heat treatment. Therefore, the proposed global model is composed of different sub-models to address both dynamic and static globularisation phenomena. In this section these sub-models are briefly described, and a new methodology, integrating these sub-models, is proposed subsequently. Accordingly, the total fraction of globularised α can be decomposed into the fraction of grains globularised through dynamic globularisation (f_{dg}) and those through static globularisation (f_{sg}) as described in in Equation 5.2.

$$f_{glob} = f_{dg} + (1 - f_{dg})f_{sg} \tag{5.2}$$

5.2.1 Dynamic globularisation

Due to a similarity between dynamic globularisation and recrystallisation, an Avrami based relationship, presented in Equation 5.3, is often used to predict evolution of α grains [93, 94, 99].

$$f_{dg} = 1 - exp(-ln(2) * (\frac{\varepsilon - \varepsilon_c}{\varepsilon_{0.5} - \varepsilon_c})^n) \tag{5.3}$$

Where ε_c and $\varepsilon_{0.5}$ represent levels of deformation at which the transformation (i.e. globularisation in this case) starts and reach 50%, respectively.

Liu et al. [46] has used a similar relationship (Eq.5.4) to describe dynamic recrystallisation in magnesium alloy.

$$f_{dg} = [1 + k^{(1-(\varepsilon-\varepsilon_c/\varepsilon_{0.5}-\varepsilon_c))}]^{-1} \tag{5.4}$$

The model predicts a sigmoid shape curve for recrystallisation as a function of strain with a slow kinetics at the beginning and the end of the transformation and fast kinetics in between. ε_c and $\varepsilon_{0.5}$ also represent levels of deformation at which the transformation starts and reach 50%, respectively. The authors claim that this model has more physical meaning than the Avrami equation, and that it better represents microstructural evolution over a broader range of strains. Furthermore, they provide strain values for the limits of each domain of slow, fast and slow kinetics; this is important to determine effective processes in industrial production. Hence this model is also considered in this work.

5.2.2 Static globularisation

A few models are proposed in literature for the prediction of static globularisation, such as constitutive Johnson-Mehl-Avrami-Kolmogorov (JMAK) model (Eq.5.5a) [18, 30, 92, 107].

$$f_{sg} = 1 - exp(-ln(2) * (\frac{t}{t_{0.5}})^n) \tag{5.5a}$$

$$t_{0.5} = K\epsilon^a exp(\frac{Q}{RT}) \tag{5.5b}$$

An alternative approach proposed for the prediction of static globularisation is an asymptotic relationship provided in Eq.5.6 [18], which is used to describe non-nucleation type processes. Termination migration and grain coarsening are the two main microstructural mechanisms occurring during annealing and do not involve nucleation. Fan et al. [18] thus argue that an asymptotic model is more adequate to predict static globularisation. In fact, both JMAK and asymptotic models are found to be accurate as is shown in Figure 5.4.

$$f_{sg} = 1 - (1 + k't)^{-1/m} \tag{5.6}$$

A third approach proposed for the prediction of static globularisation is a physically based model that takes into consideration the dislocation density [3]. This relationship (Eq.5.7a) is based on an assumption that the driving force for static

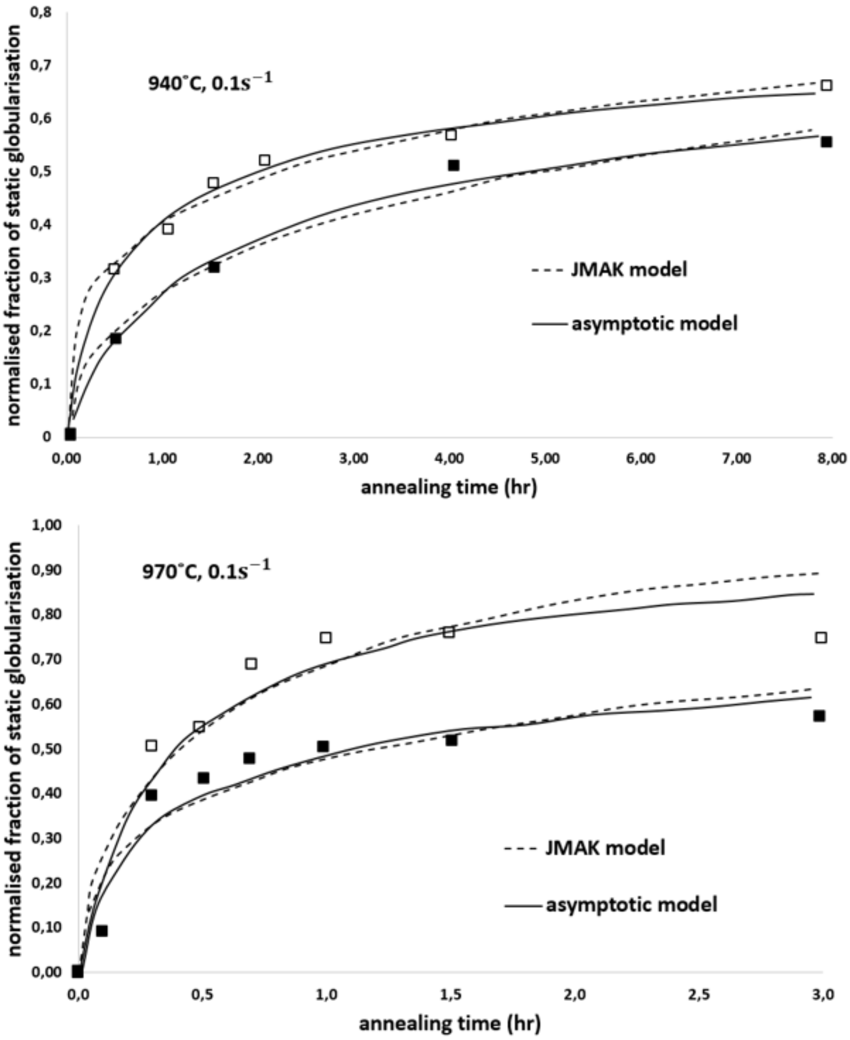

Figure 5.4: Predicted globularised fraction by JMAK model and asymptotic model for different deformation conditions [18].

globularisation is the same as that for grain growth. This model is also considered in the global model.

$$\dot{X}_s = M\frac{\dot{g}}{g} \tag{5.7a}$$

where *M* is a constant and *g* is the grain size defined as:

$$g^n - {g_0}^n = Kt \tag{5.7b}$$

where g_0 is the initial grain size, *t* is the annealing time, *K* and *n* are constants.

5.2.3 Effect of changes in strain path

In every work in the literature, models for predicting dynamic globularisation take the effective strain as an input for the level of deformation [93, 94, 99]. The effective strain is defined here as a monotonically increasing scalar value which is calculated incrementally. This may be appropriate to use for uniaxial compression tests such as the ones performed in these studies, however, it may not be the most adequate way of representing the state of deformation of a part during multi-axial forging. Indeed, during cogging, deformation sometimes happens in a direction opposite to that of the previous stroke; hence the monotonically increasing value of effective strain may not be the most suitable way of characterising the state of deformation. Most of the trials carried out in this work do not include a compression along the billet axis of the samples. So the strain value along that direction is continually increasing; and the increments vary depending on the strain path. Taking this scalar as an input for the new developed model is thus considered. Another option to represent the level of deformation of an object is the VonMises strain which reflects the current state of deformation of the material rather than a cumulative value. The evolution of these three strain representations during a multi-axial forging test, ”4_0.25M_WQ”, is illustrated in Figure 5.5 to highlight their differences.

During multiaxial forging tests, samples were held for 2 minutes in a furnace between each forging hit, to resemble actual industrial operations. This holding time can potentially affect the kinetics of globularisation. Fan et al. [17, 19], Vo et al. [98]

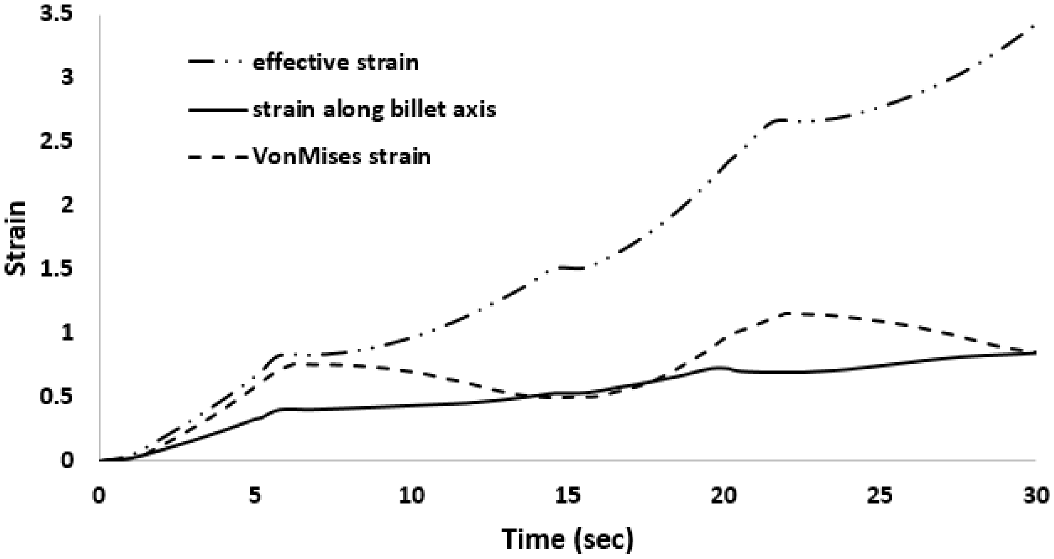

Figure 5.5: Plot of the strain as a function of time for test '4_0.25M_WQ'.

suggested that dislocation annihilation occurred during inter-pass annealing through static recovery, most of which was happening within the first few minutes of intermediate annealing. Part of this dislocation annihilation was found not to be used efficiently for microstructural changes [98]. Besides, the data acquired in this work suggest that the change in loading direction (i.e. strain path) does not favourably influence globularisation (see section 4.4). To take these phenomena into an account in the new global model, alterations to the strain input is applied throughout the process, as a function of forging steps, by proposing the relationship in Equation 5.8. Although the recovered fraction is found to vary with interrupted time and strain level [19], the recovery factor is considered as a constant in this work.

$$\varepsilon^* = \varepsilon * (1 - \eta)^{n-1} \tag{5.8}$$

where η is the recovery factor estimating the fraction of strain recovery, and *n* is the number of forging hits during a test.

5.2.4 Creation of the new model for globularisation

A Design Of Experiment (DoE) is created for the formation of the new global model proposed in this work. Table 5.4 summarises the factors and levels of this DoE including the dynamic and static models and their characteristics. Each combination is tested and for each ”sub-model”, the associated constants are optimised using a procedure described earlier (see section 5.1.4) in form of Eq.5.1, utilising Microsoft Excel. The sub-model with the lowest objective function (Eq.5.1) is considered as suitable for the prediction of globularisation during multi-axial forging.

Table 5.4: Combinations of options for the new model.

Factor	Level		
Dynamic model	Avrami	model from *(Liu, 2011)*	
Static model	JMAK	asymptotic	model from *(Babu, 2012)*
strain	effective	component along billet axis	VonMises
recovery	no	yes	

Figure 5.6 shows the effect of each factor on the accuracy of the new global model. It appears that the choice of equation for dynamic globularisation does not affect the accuracy of the global model significantly. The Avrami model is thus chosen as it is more common and it has exhibited a slightly higher accuracy. On the other hand, selecting the correct equation for the static globularisation is essential, as an important difference in accuracy of the global model is noted. The asymptotic approach is not recognised as suitable due to a high objective function meaning that the level of fitting with the experimental data obtained in this work is not adequate. Instead, JMAK equation (see Eq.5.5a) is chosen, as it yields closer predictions to the results of experiments. The nature of the strain used as input in the model is also critical. For instance, the results of predictions are improved when VonMises strain is used as an input since it better captures the deformation state of material during multi-axial forging. Using the formula developed for static recovery during inter-passs reheating (see Eq.5.8) also enhances the performance of the model, as is illustrated in Figure 5.7.

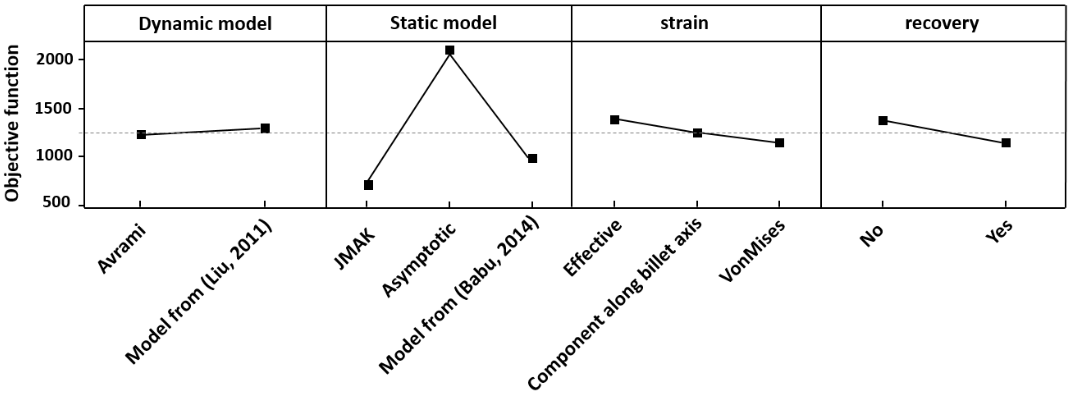

Figure 5.6: Effect of different factors on the accuracy of the global model.

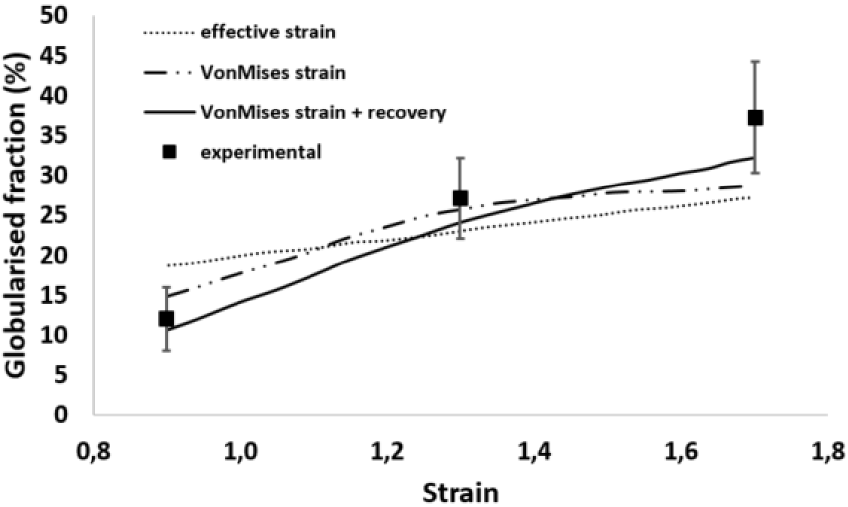

Figure 5.7: Plot of the globularised fraction as a function of strain for test ”5_0.1M_5h_FC” along with the predicted values from the new model.

Consequently, the model for globularisation in this work is formulated with these criteria:

$$\begin{cases} \varepsilon^* = \varepsilon * (1-\eta)^{n-1} \\ f_{dg} = 1 - exp(-ln(2) * (\frac{\varepsilon^* - \varepsilon_c}{\varepsilon_{0.5} - \varepsilon_c})^n) \\ f_{sg} = 1 - exp(-ln(2) * (\frac{t}{t_{0.5}})^m) \\ t_{0.5} = K(\epsilon^*)^a exp(\frac{Q}{RT}) \\ f_{glob} = f_{dg} + (1 - f_{dg}) f_{sg} \end{cases}$$

And the associated optimised constants are:

$$\begin{cases} \varepsilon_c = 0.117 \\ \varepsilon_{0.5} = 21.389 \\ n = 0.448 \\ K = 5.168 \\ a = -1.610 \\ m = 0.838 \\ \eta = 0.051 \end{cases}$$

The proposed model has successfully predicted fractions of globularised alpha grains for the conditions tested in this work; with a standard deviation of ≈ 0.04 from the experimental data. However, it is limited to providing a single globularisation fraction value for each set of the input parameters (i.e. strain, number of forging hits, and annealing time). To assess globularisation fraction at several locations in a part, the level of strains need to be determined at the desired locations, using FE analysis. Implementing the model directly into a FE software would make analysis more straightforward as it would allow access to the distribution of globularised fraction inside the whole work piece, not only at one specific time but throughout the entire process. In addition, building the model into the FE software package would make data examination faster and easier as there would be no need for transfer of information between different software when running the model.

This new global model has been integrated into a commercially available FE software, DEFORM. There are different ways of introducing a microstructural evolution model in DEFORM FEM software. One method is to use the built-in models for recrystallisation and grain growth from the pre-processor environment, that includes Avrami, mesoscale, and texture controlled model. The equations are built in, and only proper constants need to be provided. Nevertheless, the existing Avrami description in DEFORM is not adequate for the model developed in this project, as it needs to be amended. This requires a custom built user subroutine that needed to be developed. There are two types of subroutines in DEFORM environment, including (i) the post-processor, and (ii) the FEM, with the main difference being in the interaction with the software. These are schematically shown in Figure 5.8. The post-processor subroutine is applied after the completion of FEM simulation where the outcome of the simulation is used as inputs for the prediction of globularisation using the new global model. On the other hand, the FEM subroutine interacts with the DEFORM FEM engine and that is able to modify internal variables and properties during the simulations. This is particularly useful as the flow behaviour of the material is dependent on the changes in microstructure during the process. The model generated in this work is not coupled in a sense that it does not modify the flow behaviour of the material as a function of the predicted microstructural changes; so there is no required interaction with the internal variables during the forging simulation. Hence, it is decided to implement the new global model for globularisation using the post-processor subroutine. The subroutine and its implementation into the FE software are detailed in Appendix A.

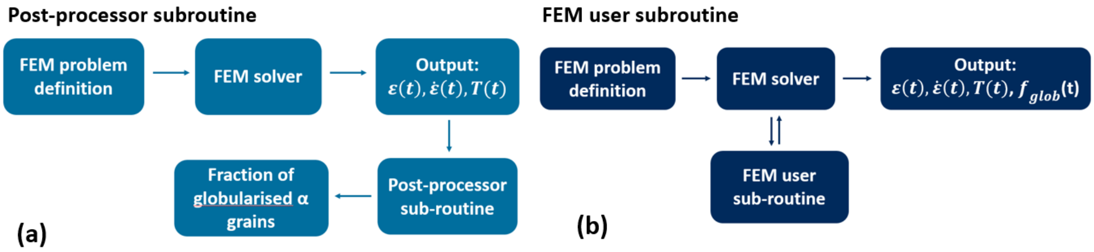

Figure 5.8: Two methods fo of subroutine implementation in DEFORM FE package (a)post-processor subroutine, and (b) embedded FEM subroutine.

Figures 5.9 and 5.10 show examples of the evaluated distribution of globularised fraction for two test conditions. In both cases, comparisons have been made between the predicted values and the experimentally measured fractions along the centre line of the samples. It can be seen that the results of predictions, obtained using the modified user-subroutine, agree well with the experimental data (i.e. within ≈ 0.04 uncertainties).

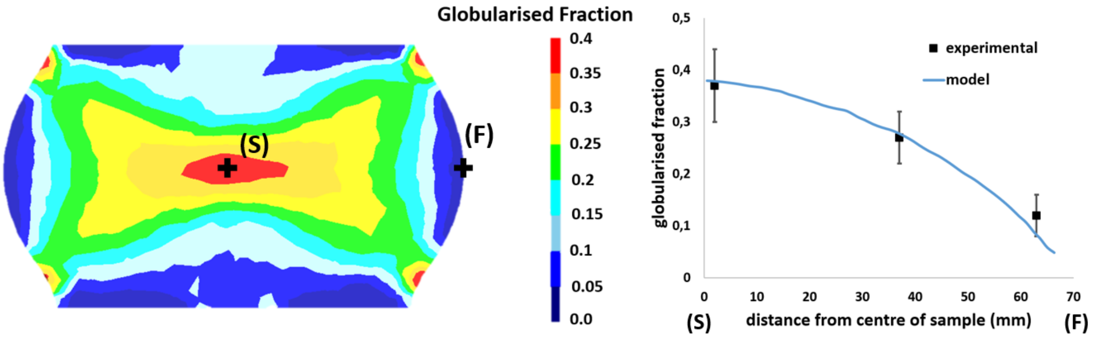

Figure 5.9: Distribution of globularised fraction obtained with the subroutine for test '5_0.1M_5h_FC'.

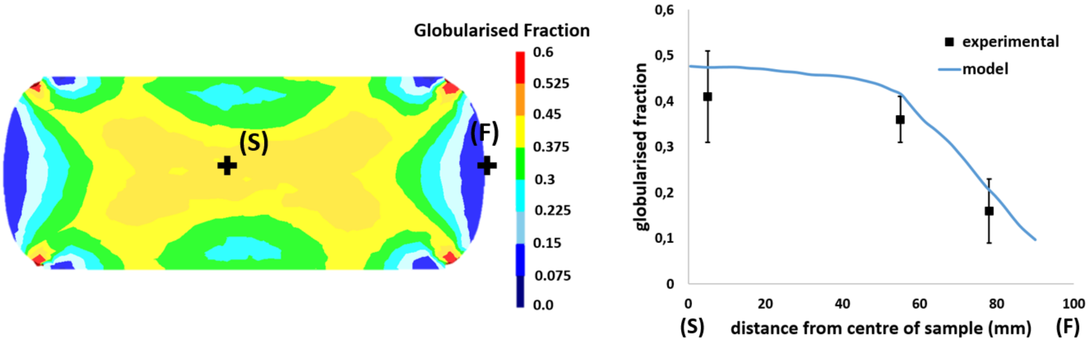

Figure 5.10: Distribution of globularised fraction obtained with the subroutine for test '4_0.25M_4h_AC'.

5.3 Summary

Various models for prediction of evolution of globularisation are available in the literature. A couple of models focusing on microstructural mechanisms like boundary splitting and termination migration were implemented in this work and accurate predictions were reached. Though, their use was not convenient due to specific requirement of knowledge of dimensions of α grains throughout the process. A novel model was developed to better capture the evolution of globularisation during cogging operations. It takes into account both dynamic and static globularisation using Avrami's equations. The effect of strain path is also considered through the use of the Von Mises strain. And the effect of inter-step reheating is factored in through the use of a recovery factor. Finally, this model has been integrated into a subroutine for Deform FEM software.

Chapter 6

Discussion

The results of experimental observations and predictive tools described in Chapters 4 and 5 show that deformation level, temperature and annealing time affect the globularisation behaviour in Ti-6Al-4V during open die forging. Additionally, the strain path, percentage of deformation at each incremental forging step, number of heat treatment stages and deformation magnitude also contributes to the kinetics of microstructural evolution during cogging operations. The degree of contribution of each of these parameters on the globularisation mechanism is discussed in more details in this chapter, and connections are made with the results of predictive models.

6.1 Globularisation during forging and annealing

In this project, the choice is made to use test specimens larger than the traditional lab scale experiments. The broader size is mainly selected for practical reasons to allow multiaxial forging to be carried out on a 500T hydraulic press easily. That way, experimental conditions seen in this work resemble somewhat the ones witnessed in industrial practice. Also, the wide samples allow microstructural characterisation of big areas that are subjected to the same thermo-mechanical conditions. Indeed, for each sample, the deformation zones investigated are roughly $240mm^2$. Hence these areas include more than 250 prior-β grains. In comparison, a traditional ∅ 12mm x 18 length compression sample has an area that can be analysed in the order of $20mm^2$

which is more than 10 times smaller. This means that the larger scale samples provides a better representation of the spectrum of crystallographic orientations of grains and this is important as grain orientation affects the kinetics of microstructural evolution. As deformation occurs, different behaviours are detected in grains depending on their crystallographic orientation, which leads to substantial variations in the final globularised fraction observed. These variations in globularised fraction are observed in this work but may be missed when smaller scale samples are used. The statistical variations are gathered for all samples in Appendix B, and Figures 6.1 and 6.2 show the incertitude on globularised fraction measurements for some uniaxial and multiaxial tests. In some instances, the incertitude on the value of globularised fraction is so large that it becomes difficult to compare processing routes and conclude regarding their relative efficiency for microstructural evolution.

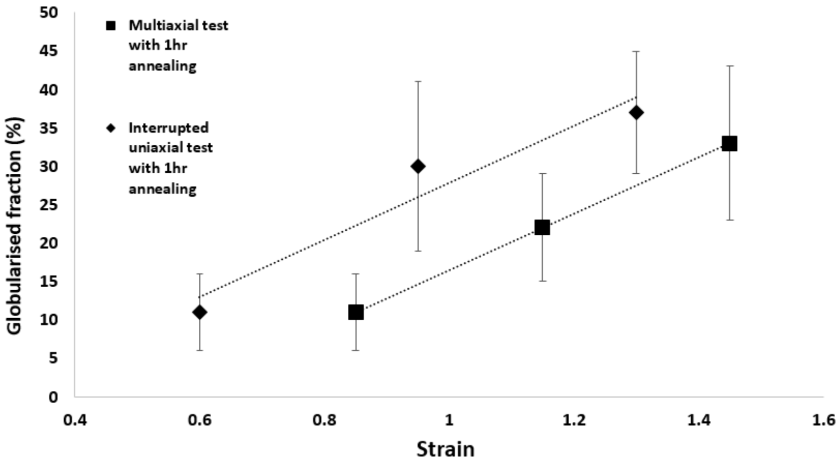

Figure 6.1: Plots of globularised fraction as a function of local strain for interrupted tests with 2 steps of deformation.

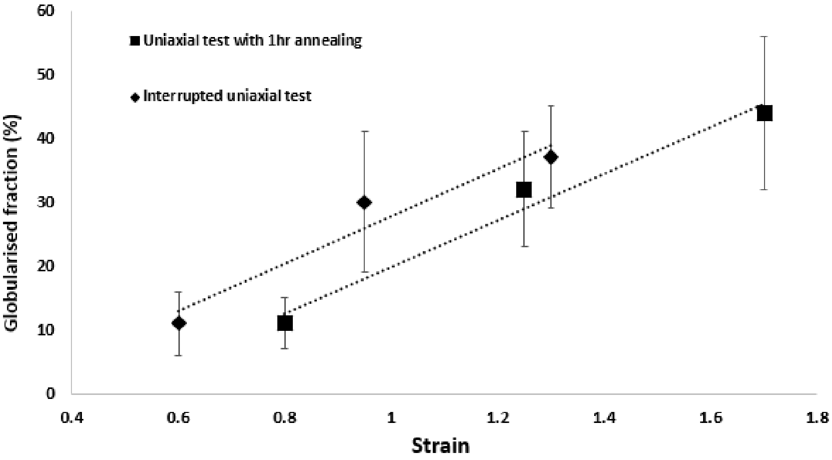

Figure 6.2: Plots of globularised fraction as a function of local strain for uniaxial compressions tests with and without interruption of deformation.

Due to the large scale of the samples used in this work and the non-isothermal environment of the forging trials, the deformation conditions are not ideal. ”Dead zones”, where almost no deformation occurs, are observed and samples also appear to bulge during forging. Hence, it is important to verify that the deformation conditions are not too far from the ones experienced during ideal compression. To this end, the strain tensor related to each compression is assessed at a few locations within a sample. Three locations (P1, P2 and P3) are chosen for each forging conditions as shown in Figure 6.3.

The strain tensors for locations P1, P2 and P3 during uniaxial compression are respectively $\begin{bmatrix} 0.9 & 0 & -0.03 \\ 0 & 0.9 & 0.03 \\ -0.03 & 0.03 & -1.84 \end{bmatrix}$, $\begin{bmatrix} 0.74 & 0 & 0.01 \\ 0 & 0.62 & -0.08 \\ 0.01 & -0.08 & -1.35 \end{bmatrix}$, and $\begin{bmatrix} 0.48 & 0 & 0 \\ 0 & 0.36 & -0.04 \\ 0 & -0.04 & -0.84 \end{bmatrix}$.

At the centre of the sample, the strain conditions resemble the ones from ideal compression. The shear components are almost null, a large component is observed on the direction of deformation and two equal smaller components on the other directions. In locations closer to the edge of the sample, deviation from ideal conditions is noticed. Components ϵ_x and ϵ_y are no longer equal; however, it is still close to the optimal case.

The strain tensors for location P1, P2 and P3 after two orthogonal compressions are respectively $\begin{bmatrix} 0.55 & 0 & -0.02 \\ 0 & -0.30 & 0 \\ -0.02 & 0 & -0.25 \end{bmatrix}$, $\begin{bmatrix} 0.43 & -0.08 & 0 \\ -0.08 & -0.20 & 0 \\ 0 & 0 & -0.22 \end{bmatrix}$, and $\begin{bmatrix} 0.27 & -0.05 & 0 \\ -0.05 & -0.14 & 0 \\ 0 & 0 & -0.13 \end{bmatrix}$.

Ideally, after two orthogonal compressions, the originally cubic sample should become an elongated bar with a square section. So the strain tensor in the three examined locations should have no shear component, and the components ϵ_y and ϵ_z

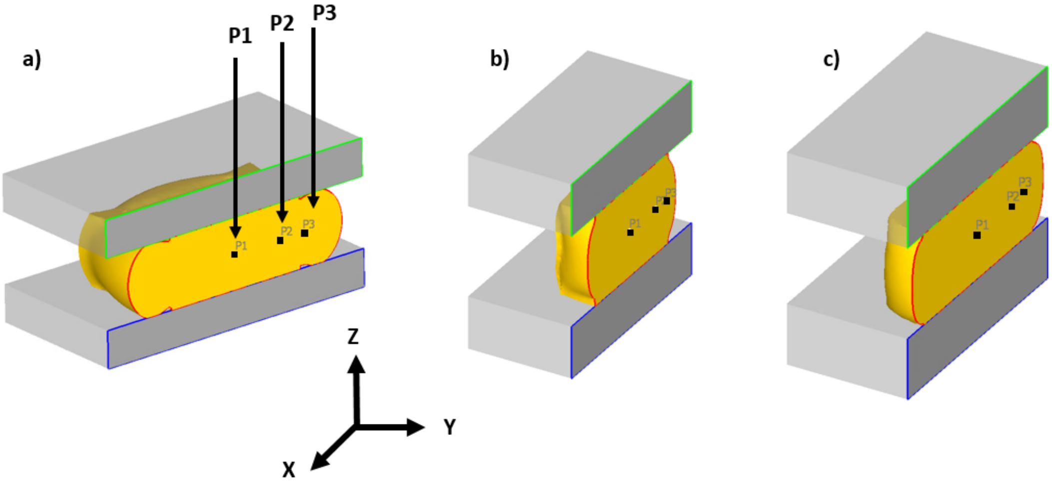

Figure 6.3: Locations in samples where the strain tensors is evaluated for the conditions: (a) uniaxial compression to 50% reduction, (b) two orthogonal compressions of 25% reduction each, and (c) four orthogonal compressions of 25% reduction each.

should be equal while ϵ_x represents the elongation in the direction of the billet. This is approximatively observed here, meaning that the experimental conditions for the areas analysed in this work are close to a perfect scenario. Also, the shear components are negligible meaning that indeed the the material in the areas investigated in this work underwent mainly compressive deformation.

The strain tensors for location P1, P2 and P3 after four orthogonal compressions are respectively $\begin{bmatrix} 0.83 & 0.01 & -0.02 \\ 0.01 & -0.53 & 0 \\ -0.02 & 0 & -0.33 \end{bmatrix}$, $\begin{bmatrix} 0.79 & 0.1 & 0 \\ 0.1 & -0.47 & 0 \\ 0 & 0 & -0.32 \end{bmatrix}$, and $\begin{bmatrix} 0.48 & 0.08 & 0 \\ 0.08 & -0.28 & 0 \\ 0 & 0 & -0.20 \end{bmatrix}$.

In this case, the strain tensors should be similar to the ones of the sample experiencing two orthogonal forging. And in this instance too, the shear components are fairly negligible. However, the components ϵ_y and ϵ_z are not equal, which is aligned with the observation of a forged sample not having a perfect square section. Nevertheless, the experimental conditions are somewhat close to pure compression.

In the case of multi-axial forging, the amplitude of the change in strain path can be measured by the parameter θ (Equation 6.1) [69].

$$\theta = \frac{\epsilon_p : \epsilon}{\sqrt{\epsilon_p : \epsilon_p}\sqrt{\epsilon : \epsilon}} \tag{6.1}$$

where ϵ_p is the strain tensor during the pre-strain and ϵ is the strain tensor during the second loading.

In an ideal scenario of two orthogonal compressions under isothermal conditions and no friction, the parameter θ would be equal to -0.5. For the experiments carried out in this work θ is calculated between -0.70 and -0.83 depending on the number of passes, the deformation increment, and the location in the sample. This difference is due to samples presenting bulged surfaces rather than flat which affects the deformation behaviour. This could be improved by quenching the samples after each forging steps to machine flat surfaces for the following compressions; but these series of quench and reheat would not be representative of the industrial process and may also affect microstructural evolution making analysis difficult. Creating isothermal and low friction experimental conditions could also help. Nevertheless, the conditions achieved in this work are adequate to investigate evolution of globularisation during multi-axial forging replicating industrial practice.

Globularisation can occur dynamically during forging and statically during post-deformation heat treatments. In this work, the uniaxially compressed samples exhibited an increasing trend in the fraction of globularisation with higher levels of strain. Many theoretical explanations on the mechanisms of dynamic globularisation at high temperature, viz. 950°C, are available in the literature [14, 23, 42, 95, 102] and are generally based on a series of microstructural changes in the material that are commonly found (see Section 2.4.1). Dislocations introduced during deformation re-arrange to create α/α low angle boundaries and sub-grains. These boundaries gradually evolve into high angle boundaries with increasing strain separating α laths into smaller grains. In line with these proposed mechanisms, the orientation of α laths with respect to the loading axis were observed to be increased with the applied strain; this evolution can be seen in Figures 4.7 and 4.8. Depending upon the magnitude of local strain, about $\varepsilon = 1.3$ in this work, most α laths are aligned perpendicularly to the loading axis; and this is in line with the strong transverse texture observed in the highly deformed zone with $\varepsilon > 1.4$ (see Figure 4.48). α laths further deform by elongating or breaking up into smaller grains, as shown in Figure 6.4, and their fragmentation further continues with increasing deformation level, driven by basal slip [8].

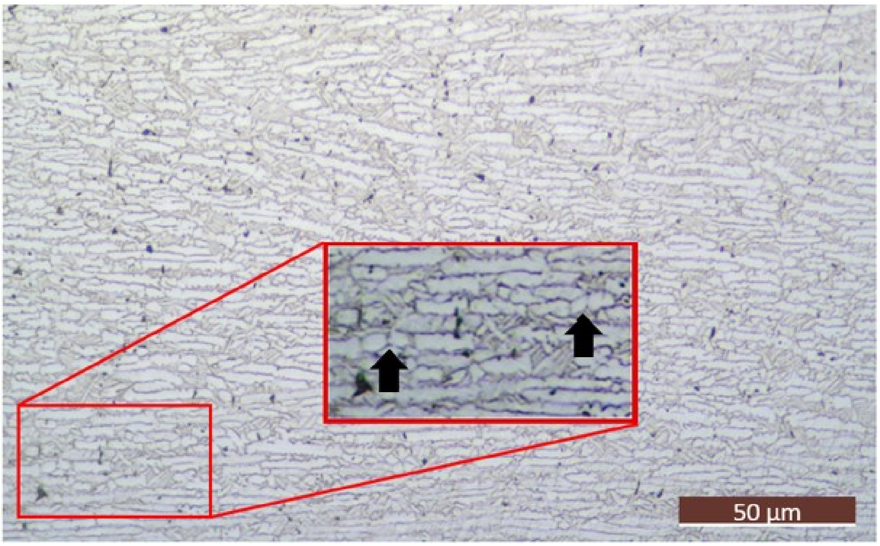

Figure 6.4: Optical microscopy appearance of a region in the high strain zone (ε= 1.7) taken from sample '1-0.5U-WQ'. Arrows show the α laths fragmentation by different mechanisms.

Similarly, the microstructural evolution occurring by static globularisation mechanisms can be distinguished via a range of characteristic microstructural features [89, 95, 116]. During the initial stage of post-forging annealing, rearrangements of dislocations into sub-grains (i.e., low angle grain boundaries) occur in α laths, which then leads to further breaking up in α lamellae due to the penetration of the β phase along these boundaries. Fragmentation of α grains that is likely to be based on this mechanism was observed in this study, as illustrated in Figure 6.5. After longer annealing periods, termination migration, edge spheroidisation and Ostwald ripening mechanisms appear to take place, reducing the aspect ratio of elongated α lath, yielding a higher globularised fractions. Figure 4.44 shows observations of such microstructural changes. These mechanisms are diffusion based processes and consequently their extent increases with time at high temperatures. This corroborates the increase in globularised fraction with post-deformation annealing time, as illustrated in Figure 4.11.

During uniaxial compression, interruption of deformation with a 1 hour inter-pass annealing did not lead to a significant difference in microstructural evolution, as shown in Figure 4.13. The most important parameters affecting globularisation and significant microstructural changes are clearly apparent to be the level of deformation and the total annealing time. This is because interruption in the

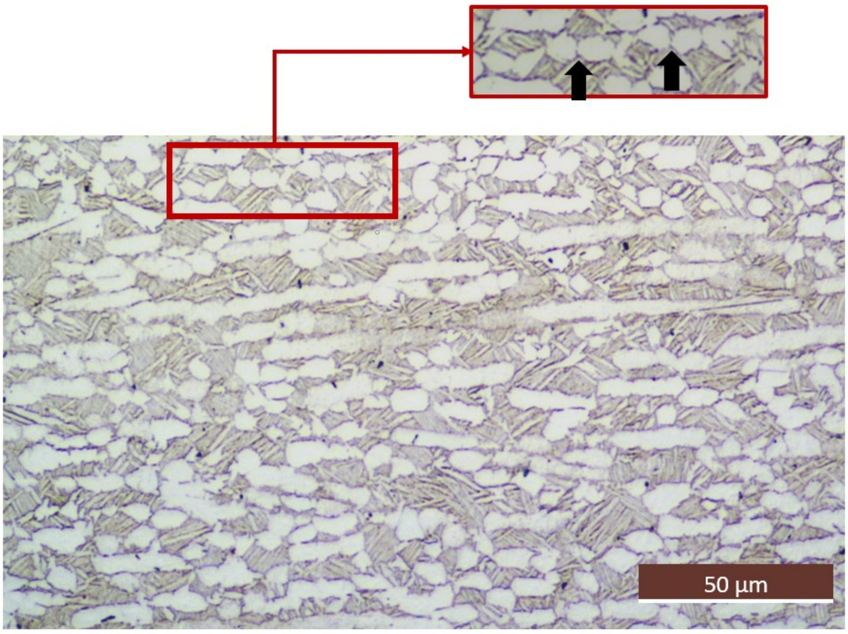

Figure 6.5: Optical microscopy appearance of the high strain level (ie., ε= 1.7) zone from sample '1-0.5U-WQ' after 1hr annealing. Arrows indicate α laths fragmented by β phase penetration.

deformation (i.e., forging) followed by inter-pass annealing affects the substructure modification and boundary splitting mechanisms that only have a moderate impact on the overall globularisation process based on previous observations [95]. This is unlike the findings of Fan et al. [19] where acceleration of globularisation was observed during interrupted compression tests. This was linked to the formation of transverse α/α boundaries through recovery and the break-down of Burgers orientation relationship by β recrystallisation. The difference in this behaviour reported in various studies may be explained by the difference in the alloy chemistry (i.e. near-α alloy TA15) and the fact that the finer initial microstructure (lath thickness of 1.2 µm) used in those studies requires lower levels of strain and shorter annealing time to break down.

A body of literature is reported on the effects of both crystallographic orientation and physical orientation of α lamellae on the kinetics (i.e., rate) of globularisation [8, 70]. The majority of the α laths that are favourably oriented, i.e. with the c-axis tilted between 15 and 75° from the compression axis are deformed, fragmented or bent;

while the laths that are in less favourable orientation (i.e. with a c-axis within 15° to the loading axis) undergo little deformation. Finally, laths that are nearly perpendicular to the compression axis can undergo large amount of deformation, but they are difficult to fragment due to the limited number of available slips systems (i.e., only prismatic slip). This strong dependency of the globularisation behaviour on local microstructure (i.e., grain morphology and crystallographic orientation) results in a heterogeneous microstructure after forging.

During uniaxial compression of titanium alloys with a lamellar structure, laths progressively rotate, aligning their longer axes and consequently the c-axis, perpendicular to the loading axis [64, 80]. This was observed in [64] and is in line with the findings in this work where similar texture was noticed after uniaxial compression to 50% in reduction (see Figures 4.48 and 4.8). This means that under low strains, α laths deform and fragment in a heterogeneous manner depending on their crystallographic orientation with respect to the compression axis. At higher strain (i.e. $\varepsilon > 1$) deformation occurs more homogeneously, as most laths are aligned perpendicularly to the loading axis, however, this orientation is not the most favourable for their fragmentation and dynamic globularisation.

Introduction of a 90° rotation of the sample in between two compressions steps of 25% in reduction does not improve kinetics of dynamic globularisation. Laths that were in a hard orientation (i.e. parallel to the first loading axis) and thus barely deformed during initial forging step become perpendicular to the second compression axis after rotation, so undergo further deformation but their fragmentation remains limited. Laths that were perpendicular to the first loading axis (either initially or due to rotation during hot working) become parallel to the second compression axis so they will remain mostly unaffected during the second deformation step. α laths that were in a favourable orientation, continue to deform further towards more globularised structure. These heterogeneities due to laths orientation are even exacerbated by strain localisation in the area of deformed lamellae (see Figure 4.19). The introduction of the 90° rotation also stops the alignment of α laths perpendicularly to the first loading axis; instead they start rotating to a direction orthogonal to the second compression axis leading to a much weaker texture (see Figure 4.49). In addition, it is known that a certain level of dislocation density is required to initiate recrystallisation or in this case globularisation [56, 97]. The change in the direction of deformation after a limited level of deformation (i.e., strain) causes a decrease in the number of geometrically necessary dislocations, and leads to the generation of the dislocations with opposite sign, promoting annihilation of dislocations. This produces a lower efficiency of microstructural changes compared to that of the uniaxial deformation case, as can be observed in Figures 6.6 and 6.7.

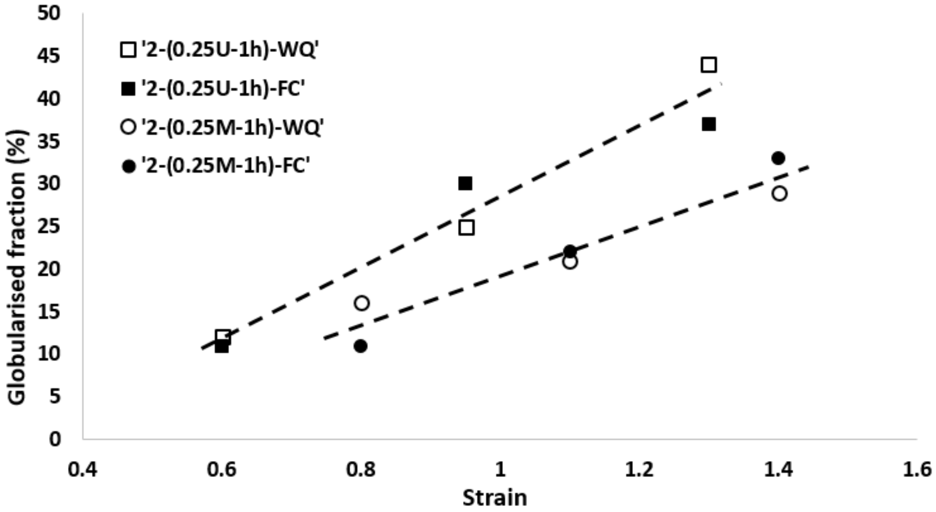

Figure 6.6: Plots of globularised fraction as a function of local strain for interrupted tests with 2 steps of deformation.

Similarly to the tests carried out uniaxially, the experimental trials performed multi-axially with various reheating schedules in between different steps (i.e., samples 5-0.1M-5h-FC, 5-(0.1M-1h)-FC, ...) did not exhibit significant difference in microstructural changes (see Figure 4.26). Indeed, the interruption in the deformation process with reheating stages do not affect the final microstructure considerably (see Figures 4.22, 4.23 and 4.24). This is because the overall level of deformation and the total annealing time are the most important parameters for fast globularisation. In this case also, a lower amount of microstructural changes is noticed in the samples deformed multiaxially compared to those deformed uniaxially. A maximum of 39% globularised fraction was achieved for 5-0.1M-5h-FC sample which is much lower than the 66% achieved during uniaxial testing in test 1-0.5U-4h-FC under equivalent effective strain. This is due to a partial recovery of the microstructure and a reduced rate of α/α sub-boundary formation when a change in strain path occurs [56].

Very little difference in microstructural changes are observed in samples

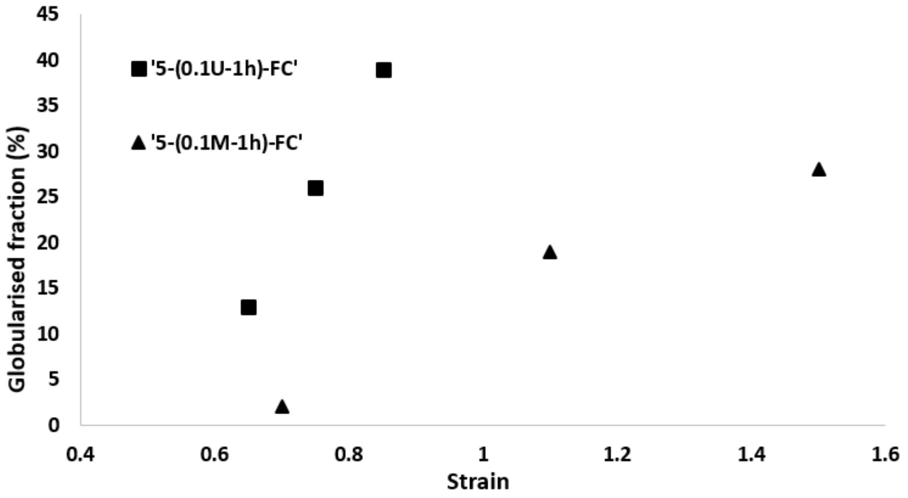

Figure 6.7: Plots of globularised fraction as a function of local strain for interrupted tests with 5 steps of deformation.

deformed multiaxially with low strain increments of 0.1 and 0.25, as is shown in Figure 4.33. It can be deduced that the strain increment has a limited effect on the globularisation rate during cogging operations of titanium alloys. However, the range of strain increment studied in this work, which is very close to those practiced by industry, is quite narrow and higher strains may produce different results. Indeed, recovery of the deformation is observed with lower dislocation density when deformation direction (i.e., strain path) is changed before a local strain of 0.6 is reached; whereas local strains higher than 0.6 during the first deformation step lead to unrecoverable changes such as loss of the Burgers orientation relationships between α and β phase, and the formation of incoherent α and β interphase boundaries [33, 56]. Although no significant microstructural transformations are observed with a change in strain increment from 0.1 to 0.25, the rates of globularisation during post-deformation heat treatments differs slightly. This marginally higher globularisation fraction is observed in heat treated samples 4-0.25M-1h-AC and 4-0.25M-4h-AC (see Figure 6.8) which may be linked to a greater quantity of stored energy during deformation due to lower level of recovery occurring during the change in loading direction (i.e., sample rotation).

At lower forging temperatures (i.e. 900°C), a higher fraction of α phase is present (see Figure 6.9) which changes the flow behaviour of the material due to the

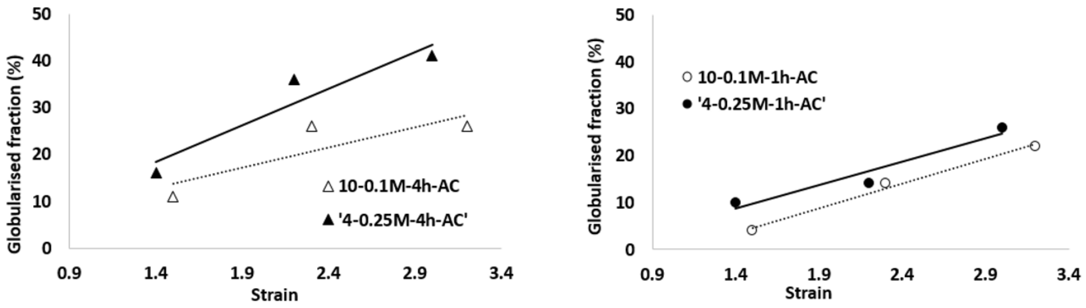

Figure 6.8: Plots of globularised fraction as a function of local strain for trials to a strain of 1 with annealing of 1 hr (left) and 4 hrs (right).

activation of various deformation mechanisms, i.e. shear bands vs lamellae buckling at higher forging temperature (see Figure 4.37a) [113]. This results in more localised microstructural evolution and thus lower globularisation rate than those deformed at higher forging temperature (i.e. 950°C) as shown in Figures 4.37a, 4.8, 4.38a, and 4.9a. Similar trends were also observed by [51, 99]. These different microstructures are affected differently by dissolution and diffusion during post-deformation heat treatment at 950C and reach distinct conditions in terms of volume fraction of α phase and thickness of α lamellae. This leads to various globularisation rates throughout the microstructure with the smallest fraction measured in samples forged at lower temperature (see Figure 6.10). Similar behaviour was observed in [36], but this is in contrary to the results from [96] where they found no relationship between the deformation and the final globularised fraction after annealing at the same temperature.

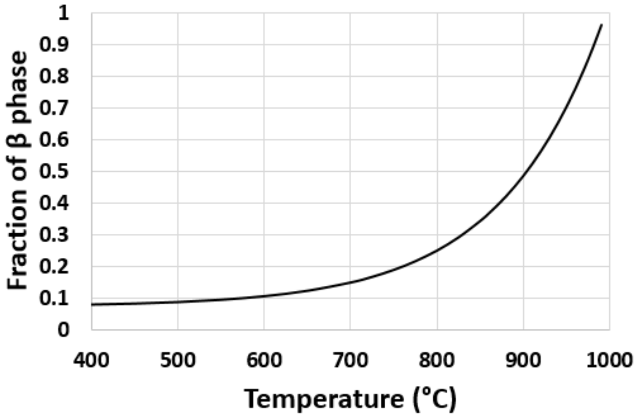

Figure 6.9: Plot of β phase volume fraction as a function of temperature [52].

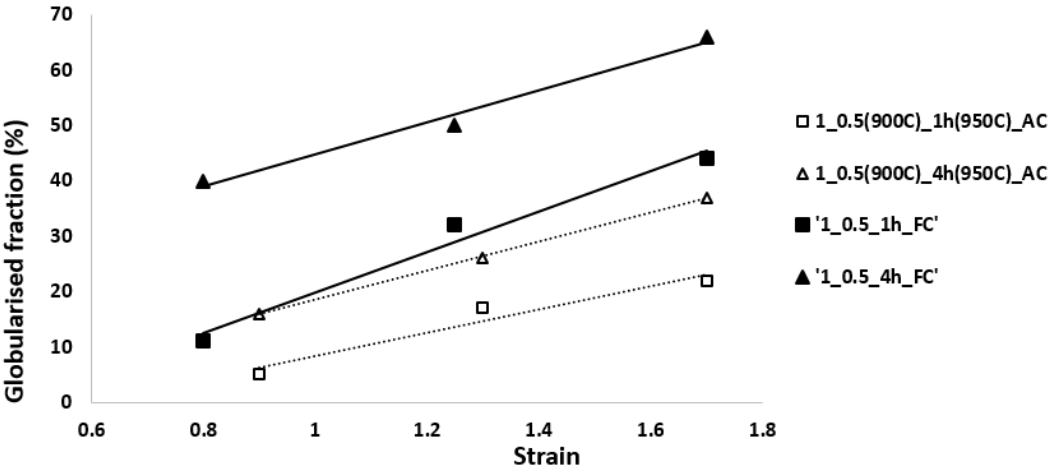

Figure 6.10: Plot of globularised fraction as a function of local strain for the uniaxially forged samples at 900°*C and* 950°*C followed by various annealing.*

6.2 Microstructural modelling

The static globularisation phenomenon during post-forging heat treatments is well documented, and several physics based models have been developed based on diffusion and particle coarsening theories [55]. For instance, the proposed model for predicting time for boundary splitting mechanism (equation 2.4) is a robust approach for the case of uniaxial compression [95]. However, it is not able to accurately predict globularisation during non-monotonic deformation routes (i.e., multi-axial forging). This deficiency implies that other phenomena are involved in the microstructural evolution, concurrently with the boundary splitting mechanism. Indeed, termination migration, edge spheroidisation and particle coarsening are observed in samples after multiaxial forging and annealing for 1hr and 4hrs, as seen in Figure 4.41. This could limit the applications of the equation 2.4 for prediction purposes as most often deformation is carried out in a non-monotonic manner in industrial practice. Furthermore, the model requires a distribution or at least an average value for both length and thickness of α laths after deformation; this is not readily available. Besides, boundary splitting plays a minor role in the overall globularisation process and a model for termination migration mechanism may be more adequate to predict the overall globularisation process.

Semiatin et al. [83] developed an equation (i.e., equation 2.6a) to predict microstructural evolution during prolonged annealing, taking into consideration termination migration mechanism. Since the model is solely based on diffusion based mechanisms, the effect of strain path is not well captured. Even though, the obtained prediction results for the experiments conducted in this work were fairly reasonable, as shown in Table 5.2. The only discrepancy noticed was for the sample deformed uniaxially at 900°C (i.e. '1-0.5U(900°C)-WQ'); and this is attributed to the higher volume fraction of α phase present in that sample, which affects the diffusion coefficient [82]. This model can be useful for designing heat treatments for industrial process routes. However, it also requires knowledge of morphological dimensions of α laths after deformation whose acquisition is experimentally time consuming and is not currently predictable. Besides the model forecasts the time required for globularisation (i.e., for a grain to have an aspect ratio below 2), although it does not predict the aspect ratio of the grains after a given annealing duration. This makes the model difficult to use during industrial process routes which often include several steps of deformation and annealing.

The empirical model mentioned in [76] (equation 2.3) was based on the data from [95] which include uniaxial compressions of Ti-6Al-4V samples followed by annealing at high temperature (955°C) on samples with a thin lamellar ($\approx$ 2.5 µm) initial microstructure. The model does not have any physical meaning; it is a mathematical equation that best fit the experimental data. It is adequate to predict globularisation during uniaxial compression tests, though requires a different set of constants for this study compared to those used for the data in [95]. This is expected because the trials are similar with only slightly different conditions such as strain rate, and initial α lath thickness. When the experimental conditions are far from those in [95], the model is not able to predict microstructural evolution accurately as is the case for the multiaxial forging trials in this work (see Figure 5.3). Thus it has limited applications and does not look promising for industrial practices which includes cogging operations.

The model chosen in this work for dynamic globularisation (Section 5.2.4) relies on the Avrami equation (equation 5.3). This is not unusual as it has been used in a number of studies for uniaxial compressions [51, 93, 99, 105]; and even though kinetics of dynamic globularisation are different during multiaxial deformation this equation was still successfully applied to a cogging operation [94]. In this project, the constants $\varepsilon_c = 0.117$ and $\varepsilon_{0.5} = 21.389$ imply that although globularisation can happen at low strain, a huge level of deformation is required to increase that fraction above 50%. The value of $\varepsilon_{0.5}$ may appear unrealistically high and may indicate that despite the decent fit to experimental data in this project, Avrami equation may not be able to adequately predict dynamic globularisation during cogging process. On the other hand, multiaxial forging at high temperature was found very inefficient; Korshunov et al. [37] did not reach 50% globularisation even after effective strains of up to 10 were applied in their experimental work with α/β titanium alloy VT9. Therefore, the $\varepsilon_{0.5}$ value in this work is not unreasonable.

To predict static globularisation in this work, JMAK model (equation 5.5a) is selected. It has been used in many instances to predict recrystallisation during heat treatments and has also been used successfully for prediction of static globularisation [18, 107]. Usually, the parameter *n* in the JMAK model (equation 5.5a) is between 1 and 4 and affects the shape of the static globularisation curve as is shown in Figure 6.11. Also, it hints at the nature of the described transformation; a value of 3 or 4 indicates a random nucleation and an unhindered growth whereas a value of 1 or 2 rather indicates a non-random nucleation or a restricted growth of the nuclei. Here, the value is less than 1 which removes the nucleation part of the model and take away the physical meaning of the equation. Babu and Lindgren [3] based their model for static globularisation on grain growth (equation 5.7a); and this may seem more appropriate since termination migration is a mechanism similar to grain growth and is also diffusion based; however, this equation gives a lower accuracy in its predictions for experimental conditions in this work.

A change in strain path has an effect on the kinetics of globularisation, as seen in Section 4.4; thus it is important to take it into consideration when developing a predictive model. A few options are considered (see Section 5.2.3) and the use of Von Mises strain is the most relevant approach to take into account the geometric effect of sample rotations during the forging procedure, producing the most accurate predictions for dynamic globularisation. The introduction of a recovery factor in the model (equation 5.8) also leads to a closer convergence, confirming that some strain recovery does happen during the small laps between forging hits. Nevertheless, its

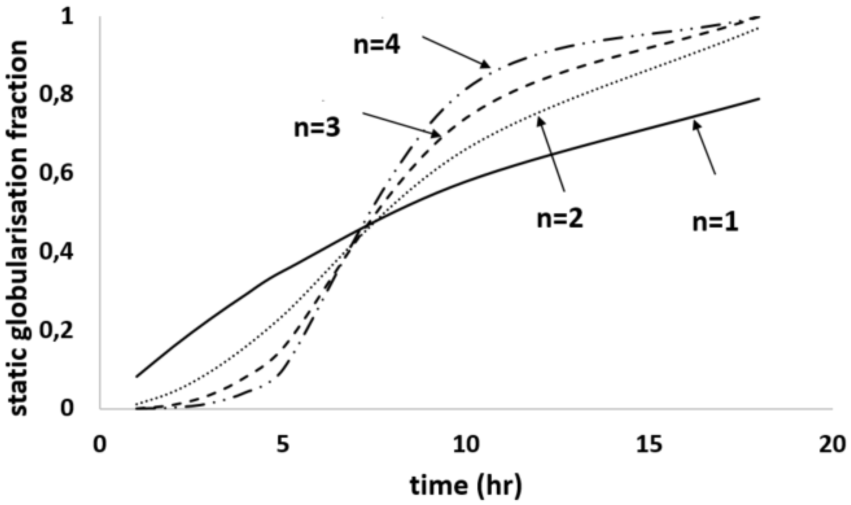

Figure 6.11: Predictions of static globularisation fraction as a function of annealing time with JMAK model for different values of exponent n.

value of η= *0.051* indicates that this phenomenon is rather limited.

The implementation of the model into a post-processor subroutine for DEFORM modelling software allows visualisation of the distribution of globularised fraction. This could be useful for forging industry to design new process routes, as it removes the material and time consuming elements that experimental trials usually pose. Currently, to assess the globularised fraction, the user has to utilise the subroutine after the FEM solver has run all the operations. However, the process can be made even faster by integrating the model into a runtime FEM subroutine, instead of a post-processor subroutine. That way, the globularised fraction is calculated at the same as the FEM solver is running, rather than a separate post-processing task. This was not done here because all the simulations for experimental conditions in this work were already carried out prior to the work on globularised fraction prediction. So it was more time efficient to use the post-processor subroutine than to run all the simulations again with a runtime FEM subroutine.

The proposed model in this work can find applications in the design of process routes; but it remains as an empirical model and therefore with limitations. For instance, the effect of forging temperature, strain rate or initial microstructure are not taken into consideration here and the model may have a restricted range of conditions over which it is valid. To improve the prediction ability for globularisation, a physically based model can be created such as dislocation density model, that would take into account all the process parameters. It was successfully used to predict dynamic globularisation during uniaxial compression of forming [3, 4, 24, 106, 109]. But no studies have investigated the effect of strain path on the kinetics of globularisation; therefore, work remains to be done to fit such model to cogging operations.

6.3 Summary and outcome for the forging industry

The kinetics and mechanisms of globularisation in Ti-6Al-4V alloy as well as their modelling were discussed in this chapter.

Globularisation occurred through the formation of α/α boundaries, boundary splitting, termination migration and edge spheroidisation during uniaxial compression and annealing. The introduction of a $90°$ rotation between two deformation steps resulted in heterogeneous deformation with areas of fragmented α laths and areas of non-deformed α laths because of their hard orientation with regards to the compression directions. Overall, this leads to lower levels of globularisation. During either uniaxial or multiaxial forging, the reheating schedule does not affect the kinetics of globularisation, as it is mostly influenced by the total applied strain and annealing time. Larger deformation increments during multiaxial forging may generate microstructural changes in the material and may be beneficial to the kinetics of globularisation; however, that effect is not observed in the range of strain increments studied in this work. When forging occurs at lower temperature (viz.900°C), different mechanisms for microstructural evolution take place. A more heterogeneous deformation with shear bands is observed; and this negatively affect the kinetics of globularisation.

A few models from the literature based on physical mechanisms (i.e., boundary splitting and termination migration) were successfully used in this work. Accurate predictions were achieved, but these models were disregarded due to their lack of practicality for industrial operations. Other available models did not yield satisfactory predictions, so a novel approach was taken to model the evolution of globularisation.

This model is based on Avrami's equation but includes modifications such as a recovery factors and the Von Mises strain as an input to better consider the impact of the processing route on globularisation. Its implementation into a FEM software can help improving current processing routes and exploring new ones for production of Ti-6Al-4V alloy.

The methodology created in this thesis was shown to be adequate to study the effect of strain path on globularisation in Ti-6Al-4V; the forging industry can rely on it for future investigations as it provides more complete information regarding globularisation heterogeneity than traditional uniaxial compression tests and it does not require the large amount of material that full industrial scale testing need.

This work shows that a larger strain before a change in strain path is more efficient for rapid globularisation which hints that a critical monotonic strain is required to reach fast microstructural changes during multiaxial forging; and this is in line with findings from literature. However, the 25% reduction increment tested in this study was found not to be enough to reach this critical monotonic strain; and microstructural evolution is highly heterogeneous. In industrial practice, forging increments are usually lower than 25%, which means that in the current situation of forging along orthogonal directions, a substantial amount of deformation and redundant work is necessary to reach full globularisation in final billets. Besides the heterogeneity in microstructural behaviour is high regardless of the process route tested in this work; this also translates in to necessary additional redundant forging to reach full globularisation.

The lower forging temperature produces a finer structure but lower amount of globularisation in the samples tested in this work both during uniaxial and multiaxial forging. The lower kinetics of microstructural changes remain even after annealing at higher temperature. For the forging industry, this means that higher forging temperature (viz.950°C) should be favoured to generate higher kinetics of globularisation; whereas lower temperatures can be used when finer grain size is essential.

The model designed in this thesis proved more adequate than the empirical ones currently available in the literature to predict microstructural evolution during multiaxial forging. The forging industry could use it to test production-like conditions and explore new processing routes. This could help avoid the cost of unnecessary physical trials.

Chapter 7

Conclusions and further work

This work has used an original methodology based on large samples and a 500T hydraulic press to replicate industrial cogging process and investigated the effect of strain path and the mechanisms involved on the kinetics of globularisation in Ti-6Al-4V alloy. Predictions of microstructural evolution during these thermo-mechanical processes have also been investigated and an innovative model has been developed to consider the effects of various processing routes on globularisation. First, the conclusions from this body of work are presented; then, possible further work is discussed.

7.1 Conclusions

The following conclusions can be drawn from this EngD thesis.

A large amount of literature is available on the mechanisms and kinetics of both dynamics and static globularisation. The mechanisms involved in this microstructural transformation are shearing of α laths, creation of dislocation walls, boundary splitting, termination migration [42, 95, 102]. he kinetics of this transformation are favourably affected by deformation level, temperature and annealing time, however, faster strain rates or coarser initial microstructure leads to slower kinetics. Changes in strain path make the kinetics of both dynamic and static globularisation sluggish [36, 37, 56, 67, 81], but a systematic study focusing on industrial scale cogging operations is still remaining to be investigated.

The experimental methodology developed in this work has proven to be a successful procedure to evaluate the effect of forging routes on globularisation. Benchmarking against results from standard compression tests in previous studies [95], analysis of deformation conditions allowed validation of this methodology. Furthermore, the globularisation heterogeneity is captured in this type of test thanks to the larger scale of samples that contain significantly more grains than traditional laboratory scale ones. Hence, this procedure can be used in the future to assess the effect of strain path and reheating schedule on globularisation.

The experiments carried out in this work showed that the mechanisms of globularisation are the same during uniaxial and multiaxial compression (i.e. creation of α/α boundaries, termination migration and edge spheroidisation) and that the kinetics of globularisation are mostly governed by the level of strain and the total annealing time. Hence, interruption of deformation by inter-step reheating does not affect significantly microstructural evolution. Also, the introduction of a $90°$ rotation between two deformation steps has a negative impact on globularisation because deformation mechanisms then occur in reverse or in new directions, decreasing the transformation kinetics. It is critical to take this into consideration for the design of wrought processes to reach microstructural uniformity.

The deformation increment during multiaxial forging had limited effect on microstructural evolution in the tested range; but indications that larger increment may have a more positive effect on kinetics of globularisation were found and linked to a higher level of stored energy in the work piece and possible loss of Burgers relationship between α and β phase. However large deformation increments are not practical due to bulging of sample during forging and are not used in industrial forging.

Processing routes involving lower forging temperatures should be avoided to reach efficient globularisation, unless small grain size is a major requirement. Indeed, trials in this work show that forging at lower temperature (viz.900°C) involves deformation mechanisms such as the generation of hear bands instead of lath buckling and rotation at higher forging temperature (viz.950°C); and it results in more heterogeneous deformation and overall lower kinetics of dynamic globularisation. However, grain growth remains limited at lower temperature; which can be desired for instance for applications in superplastic forming.

Modelling the microstructural evolution is of great technical significance to the microstructure tailoring and optimization of thermo-mechanical processing. However, very few models for globularisation available in the literature are practically useful for industrial purposes. Models based on mechanisms such as boundary splitting and termination migration (equations 2.4 and 2.6a respectively) provides accurate predictions; but they require knowledge of morphological dimensions of α laths after deformation stages which cannot be easily obtained, so they have limited use in industrial processes. Avramis empirical relationship (5.3) that is commonly used to forecast recrystallisation and globularisation in titanium alloys during uniaxial compression [51, 93, 99, 105], is not adequate to include the effect of strain path that is inherent to the industrial cogging process.

The model developed in this work has been successfully implemented into a FEM subroutine and it has been demonstrated that it can be helpful for forging industries to explore new processing routes without the need for expensive and time consuming physical trials. The model is based on Avrami's equation and includes the Von Mises strain as an input instead of the effective strain usually used, and a recovery factor to consider the microstructural recovery occurring during each reheating. This allows precise prediction of kinetics of globularisation during complex thermo-mechanical processing routes.

7.2 Further work

This thesis is a step forward in the effort to generate deeper understanding of globularisation in Ti-6Al-4V alloy; and it produces knowledge on microstructural evolution and its kinetics during forging under industrial-like conditions. However, some challenges remain and further research could be conducted to follow up on this work.

The methodology developed in this work is adequate to evaluate the effect of strain path on microstructural evolution; it could be used to investigate other forging process conditions to further uncover the effect of microstructure morphology, texture and strain path on globularisation and its heterogeneous kinetics. Also, this procedure could be used to examine other titanium alloys.

This work exploits the larger scale of the samples to analyse more grains and get insight into globularisation heterogeneity. However, this method is time consuming and still examine a limited amount of microstructural features. Further development in characterization methods could help gather deeper knowledge of the varied kinetics of globularisation. Additionally, it would be interesting to perform EBSD analysis on forged sample as it may reveal and confirm the underlying mechanisms of globularisation heterogeneity and the interactions between crystallographic texture and globularisation kinetics during complex strain paths.

The model formulated in this thesis provides an improvement on the empirical ones available in the literature and allows for more accurate prediction of microstructural evolution during forging under non-monotonic strain paths. Nonetheless, it remains an empirical model with limitations in terms of applicability over a broad process parameters. It would be useful to complete further research exploring the globularisation mechanisms and establishing physical-based models to predict microstructural evolution in a more robust manner.

References

[1] Y. B. Ammar. *Traitements thermomécaniques des colonies de lamelles parallèles du Zircaloy-4 trempé-β.* PhD thesis, Ecole Nationale Supérieure des Mines de Saint-Etienne, 2012.

[2] P. Ari-Gur and S. Semiatin. Evolution of microstructure, macrotexture and microtexture during hot rolling of ti-6a1-4v. *Materials Science and Engineering: A*, 257(1):118–127, 1998.

[3] B. Babu and L.-E. Lindgren. Dislocation density based model for plastic deformation and globularization of ti-6al-4v. *International Journal of Plasticity*, 50:94–108, 2013.

[4] Q. Bai, J. Lin, T. Dean, D. Balint, T. Gao, and Z. Zhang. Modelling of dominant softening mechanisms for ti-6al-4v in steady state hot forming conditions. *Materials Science and Engineering: A*, 559:352–358, 2013.

[5] S. Balasubramanian and L. Anand. Plasticity of initially textured hexagonal polycrystals at high homologous temperatures: application to titanium. *Acta materialia*, 50(1):133–148, 2002.

[6] I. Balasundar, T. Raghu, and B. Kashyap. Modeling the hot working behavior of near-α titanium alloy imi 834. *Progress in Natural Science: Materials International*, 23(6):598–607, 2013.

[7] S. Barrabes, M. Kassner, M. T. Pérez-Prado, and E. Evangelista. Geometric dynamic recrystallization in α-zirconium at elevated temperatures. In *Materials Science Forum*, volume 467, pages 1145–1150. Trans Tech Publ, 2004.

[8] T. R. Bieler and S. Semiatin. The origins of heterogeneous deformation during primary hot working of ti–6al–4v. *International Journal of Plasticity*, 18(9): 1165–1189, 2002.

[9] R. Boyer. An overview on the use of titanium in the aerospace industry. *Materials Science and Engineering: A*, 213(1-2):103–114, 1996.

[10] F. Bridier, P. Villechaise, and J. Mendez. Analysis of the different slip systems activated by tension in a α/β titanium alloy in relation with local crystallographic orientation. *Acta Materialia*, 53(3):555–567, 2005.

[11] G. Z. Chen, D. J. Fray, and T. W. Farthing. Direct electrochemical reduction of titanium dioxide to titanium in molten calcium chloride. *Nature*, 407(6802): 361, 2000.

[12] H. Chen and C. Cao. Static globularization of tc11 alloy during hot working process. *Rare Metal Materials and Engineering*, 40(6):946–950, 2011.

[13] C. Cui, B. Hu, L. Zhao, and S. Liu. Titanium alloy production technology, market prospects and industry development. *Materials & Design*, 32(3):1684–1691, 2011.

[14] M. Darrieulat, F. Montheillet, D. Piot, G. Kermouche, and C. Desrayaud. Transformation par forgeage à chaud des microstructures lamellaires dalliages hexagonaux. *Matériaux & Techniques*, 103(5):504, 2015.

[15] M. J. Donachie. *Titanium: a technical guide*. ASM international, 2000.

[16] X. Fan and H. Yang. Internal-state-variable based self-consistent constitutive modeling for hot working of two-phase titanium alloys coupling microstructure evolution. *International Journal of Plasticity*, 27(11):1833–1852, 2011.

[17] X. Fan, H. Yang, and P. Gao. Deformation behavior and microstructure evolution in multistage hot working of ta15 titanium alloy: on the role of recrystallization. *Journal of materials science*, 46(18):6018–6028, 2011.

[18] X. Fan, H. Yang, S. Yan, P. Gao, and J. Zhou. Mechanism and kinetics of static globularization in ta15 titanium alloy with transformed structure. *Journal of Alloys and Compounds*, 533:1–8, 2012.

[19] X. Fan, H. Zheng, Y. Zhang, Z. Zhang, P. Gao, M. Zhan, and J. Liu. Acceleration of globularization during interrupted compression of a two-phase titanium alloy. *Materials Science and Engineering: A*, 720:214–224, 2018.

[20] M. Fanfoni and M. Tomellini. The johnson-mehl-avrami-kohnogorov model: a brief review. *Il Nuovo Cimento D*, 20(7-8):1171–1182, 1998.

[21] H. Flower. Microstructural development in relation to hot working of titanium alloys. *Materials Science and Technology*, 6(11):1082–1092, 1990.

[22] F. Froes. *Titanium: physical metallurgy, processing, and applications*. ASM International, 2015.

[23] T. Furuhara, B. Poorganji, H. Abe, and T. Maki. Dynamic recovery and recrystallization in titanium alloys by hot deformation. *JOM Journal of the Minerals, Metals and Materials Society*, 59(1):64–67, 2007.

[24] P. Gao, H. Yang, X. Fan, and S. Zhu. Unified modeling of flow softening and globularization for hot working of two-phase titanium alloy with a lamellar colony microstructure. *Journal of Alloys and Compounds*, 600:78–83, 2014.

[25] Ø. Grong and H. Shercliff. Microstructural modelling in metals processing. *Progress in Materials Science*, 47(2):163–282, 2002.

[26] N. Gurao, S. Sethuraman, and S. Suwas. Evolution of texture and microstructure in commercially pure titanium with change in strain path during rolling. *Metallurgical and Materials Transactions A*, 44(3):1497–1507, 2013.

[27] A. D. Hartman, S. J. Gerdemann, and J. S. Hansen. Producing lower-cost titanium for automotive applications. *Jom*, 50(9):16–19, 1998.

[28] Z. Hu, J. Brooks, and T. Dean. The interfacial heat transfer coefficient in hot die forging of titanium alloy. *Proceedings of the Institution of Mechanical Engineers, Part C: Journal of Mechanical Engineering Science*, 212(6):485–496, 1998.

[29] F. J. Humphreys and M. Hatherly. *Recrystallization and related annealing phenomena*. Elsevier, 2012.

[30] H. Jiang, L. Yang, J. Dong, M. Zhang, and Z. Yao. The recrystallization model and microstructure prediction of alloy 690 during hot deformation. *Materials & Design*, 104:162–173, 2016.

[31] V. A. Joshi. *Titanium alloys: an atlas of structures and fracture features*. Crc Press, 2006.

[32] W. Kasprzak, D. Emadi, M. Sahoo, and M. Aniolek. Development of aluminium alloys for high temperature applications in diesel engines. In *Materials Science Forum*, volume 618, pages 595–600. Trans Tech Publ, 2009.

[33] B. Kedia, I. Balasundar, and T. Raghu. Globularisation of α lamellae in titanium alloy: Effect of strain, strain path and starting microstructure. *Transactions of the Indian Institute of Metals*, 71(7):1791–1801, 2018.

[34] J. H. Kim, N. Reddy, J. T. Yeom, J. K. Hong, C. S. Lee, and N.-K. Park. Microstructure prediction of two-phase titanium alloy during hot forging using artificial neural networks and fe simulation. *Metals and Materials International*, 15(3):427–437, 2009.

[35] J. Y. Kim, I. O. Shim, and S. H. Hong. Effect of initial lamellar structure on globularization of hot multi-forged eli grade ti-6al-4v alloy. In *Materials Science Forum*, volume 558, pages 529–532. Trans Tech Publ, 2007.

[36] J. Y. Kim, K.-T. Park, I. O. Shim, and S. H. Hong. Globularization behavior of eli grade ti-6al-4v alloy during non-isothermal multi-step forging. *Materials transactions*, 49(1):215–223, 2008.

[37] A. Korshunov, F. Enikeev, M. Mazurski, G. Salishchev, O. Dmitriev, A. Muravlev, and P. Chistyakov. Grain-structure refinement in titanium alloy under different loading schedules. *Journal of materials science*, 31(17):4635–4639, 1996.

[38] I. Lahiri, D. Lahiri, and S. Bhargava. Effect of prior β processing on superplasticity of (α+ β) thermomechanically treated ti–6al–4v alloy. *Materials and manufacturing processes*, 18(4):621–635, 2003.

[39] W. Lee and C. Lin. Adiabatic shear fracture of titanium alloy subjected to high strain rate and high temperature loadings. *Le Journal de Physique IV*, 7(C3): C3–855, 1997.

[40] X. Lei, L. Dong, Z. Zhang, Y. Liu, Y. Hao, R. Yang, and L.-C. Zhang. Microstructure, texture evolution and mechanical properties of vt3-1 titanium alloy processed by multi-pass drawing and subsequent isothermal annealing. *Metals*, 7(4):131, 2017.

[41] C. Leyens and M. Peters. *Titanium and titanium alloys: fundamentals and applications*. John Wiley & Sons, 2003.

[42] C. Li, X.-y. Zhang, K.-c. Zhou, and C.-q. Peng. Relationship between lamellar α evolution and flow behavior during isothermal deformation of ti–5al–5mo–5v–1cr–1fe near β titanium alloy. *Materials Science and Engineering: A*, 558: 668–674, 2012.

[43] S. Lim, K. Yang, Y. Yang, Y. Cheng, A. Huang, X. Wu, and C. Davies. Tracking microstructure, texture and boundary misorientation evolution of hot deformed and post-deformation annealed ti–6al–4v alloy. *Materials Science and Engineering: A*, 651:524–534, 2016.

[44] J. Lin and T. Dean. Modelling of microstructure evolution in hot forming using unified constitutive equations. *Journal of Materials Processing Technology*, 167 (2-3):354–362, 2005.

[45] Y. Lin and X.-M. Chen. A critical review of experimental results and constitutive descriptions for metals and alloys in hot working. *Materials & Design*, 32(4): 1733–1759, 2011.

[46] J. Liu, Z.-s. Cui, and L.-q. Ruan. A new kinetics model of dynamic recrystallization for magnesium alloy az31b. *Materials Science and Engineering: A*, 529:300–310, 2011.

[47] B. Lu, L. Wang, Z. Geng, and Y. Huang. Determination of interfacial heat transfer coefficient for tc11 titanium alloy hot forging. *Heat and Mass Transfer*, 53(10):3049–3058, 2017.

[48] J. Luo, M. Li, and X. Li. Internal state variable models for microstructure in high temperature deformation of titanium alloys. *Science in China Series E: Technological Sciences*, 51(11):1921–1929, 2008.

[49] G. Lütjering. Influence of processing on microstructure and mechanical properties of (α+ β) titanium alloys. *Materials Science and Engineering: A*, 243(1):32–45, 1998.

[50] G. Lütjering and J. C. Williams. *Titanium*. Springer, 2007.

[51] X. Ma, W. Zeng, F. Tian, and Y. Zhou. The kinetics of dynamic globularization during hot working of a two phase titanium alloy with starting lamellar microstructure. *Materials Science and Engineering: A*, 548:6–11, 2012.

[52] J.-G. Malcor. *Comportement mécanique et évolution structurale de l'alliage de titane Ti-6% Al-4% V dans le domaine du forgeage à chaud*. PhD thesis, 1983.

[53] S. Mannepalli and K. S. Mangalampalli. Indentation plasticity and fracture studies of organic crystals. *Crystals*, 7(11):324, 2017.

[54] S. Mironov, M. Murzinova, S. Zherebtsov, G. Salishchev, and S. Semiatin. Microstructure evolution during warm working of ti–6al–4v with a colony-α microstructure. *Acta Materialia*, 57(8):2470–2481, 2009.

[55] W. W. Mullins. Theory of thermal grooving. *Journal of Applied Physics*, 28(3): 333–339, 1957.

[56] K. Muszka, M. Lopez-Pedrosa, K. Raszka, M. Thomas, W. Rainforth, and B. Wynne. The impact of strain reversal on microstructure evolution and orientation relationships in ti-6al-4v with an initial alpha colony microstructure. *Metallurgical and Materials Transactions A*, 45(13):5997–6007, 2014.

[57] K. Muszka, L. Madej, and B. Wynne. Application of the digital material representation to strain localization prediction in the two phase titanium alloys for aerospace applications. *Archives of Civil and Mechanical Engineering*, 16 (2):224–234, 2016.

[58] K. Mutombo, C. Siyasiya, and W. Stumpf. Dynamic globularization of α-phase in ti6al4v alloy during hot compression. In *Materials Science Forum*, volume 783, pages 584–590. Trans Tech Publ, 2014.

[59] Y. Okazaki, Y. Ito, A. Ito, and T. Tateishi. Effect of alloying elements on mechanical properties of titanium alloys for medical implants. *Materials Transactions, JIM*, 34(12):1217–1222, 1993.

[60] C. Park, S. Kim, C. Oh, Y. Hyun, J. Hong, and J. Yeom. Prediction of termination migration of a rod-type particle in ti–6al–4fe alloy. *Philosophical Magazine Letters*, 92(12):701–709, 2012.

[61] C. H. Park, K.-T. Park, D. H. Shin, and C. S. Lee. Microstructural mechanisms during dynamic globularization of ti-6al-4v alloy. *Materials transactions*, 49 (10):2196–2200, 2008.

[62] C. H. Park, J. W. Won, J.-W. Park, S. Semiatin, and C. S. Lee. Mechanisms and kinetics of static spheroidization of hot-worked ti-6al-2sn-4zr-2mo-0.1 si with a lamellar microstructure. *Metallurgical and Materials Transactions A*, 43(3): 977–985, 2012.

[63] N. E. Paton and M. Mahoney. Creep of titanium-silicon alloys. *Metallurgical Transactions A*, 7(11):1685–1694, 1976.

[64] B. Perumal, M. A. Rist, S. Gungor, J. W. Brooks, and M. E. Fitzpatrick. The effect of hot deformation parameters on microstructure evolution of the α-phase in ti-6al-4v. *Metallurgical and Materials Transactions A*, 47(8):4128–4136, 2016.

[65] A. Pilchak, C. Szczepanski, J. Shaffer, A. Salem, and S. Semiatin. Characterization of microstructure, texture, and microtexture in near-alpha titanium mill products. *Metallurgical and Materials Transactions A*, 44(11): 4881–4890, 2013.

[66] I. Polmear, D. StJohn, J.-F. Nie, and M. Qian. *Light alloys: metallurgy of the light metals*. Butterworth-Heinemann, 2017.

[67] R. Poths, B. Wynne, W. Rainforth, J. Beynon, G. Angella, and S. Semiatin. Effect of strain reversal on the dynamic spheroidization of ti-6al-4v during hot deformation. *Metallurgical and Materials Transactions A*, 35(9):2993–3001, 2004.

[68] Y. Prasad, T. Seshacharyulu, S. Medeiros, and W. Frazier. Effect of prior β-grain size on the hot deformation behavior of ti-6al-4v: Coarse vs coarser. *Journal of materials engineering and performance*, 9(2):153–160, 2000.

[69] E. Rauch, J. Gracio, F. Barlat, and G. Vincze. Modelling the plastic behaviour of metals under complex loading conditions. *Modelling and Simulation in Materials Science and Engineering*, 19(3):035009, 2011.

[70] S. Roy and S. Suwas. Orientation dependent spheroidization response and macro-zone formation during sub β-transus processing of ti-6al-4v alloy. *Acta Materialia*, 2017.

[71] A. Salem and S. Semiatin. Anisotropy of the hot plastic deformation of ti–6al–4v single-colony samples. *Materials Science and Engineering: A*, 508(1): 114–120, 2009.

[72] G. Salishchev, S. Y. Mironov, and S. Zherebtsov. Mechanisms of submicrocrystalline structure formation in titanium and two-phase titanium alloy during warm severe processing. *Rev. Adv. Mater. Sci*, 11:152–158, 2006.

[73] G. A. Salishchev, S. Zerebtsov, S. Y. Mironov, and S. L. Semiatin. Formation of grain boundary misorientation spectrum in alpha-beta titanium alloys with lamellar structure under warm and hot working. In *Materials Science Forum*, volume 467, pages 501–506. Trans Tech Publ, 2004.

[74] R. Schutz and H. Watkins. Recent developments in titanium alloy application in the energy industry. *Materials Science and Engineering: A*, 243(1):305–315, 1998.

[75] S. Semiatin and T. Bieler. The effect of alpha platelet thickness on plastic flow during hot working of ti–6al–4v with a transformed microstructure. *Acta materialia*, 49(17):3565–3573, 2001.

[76] S. Semiatin and D. Furrer. Modeling of microstructure evolution during the thermomechanical processing of titanium alloys. *ASM Handbook*, 22:522–535, 2009.

[77] S. Semiatin and A. Pilchak. Advances in the development of processing-microstructure relations for titanium alloys. In *Proceedings of the 13th World Conference on Titanium*, pages 187–202. Wiley Online Library, 2016.

[78] S. Semiatin, V. Seetharaman, and I. Weiss. The thermomechanical processing of alpha/beta titanium alloys. *JOM Journal of the Minerals, Metals and Materials Society*, 49(6):33–39, 1997.

[79] S. Semiatin, V. Seetharaman, and A. Ghosh. Plastic flow, microstructure evolution, and defect formation during primary hot working of titanium and titanium aluminide alloys with lamellar colony microstructures. *Philosophical Transactions of the Royal Society of London A: Mathematical, Physical and Engineering Sciences*, 357(1756):1487–1512, 1999.

[80] S. Semiatin, V. Seetharaman, and I. Weiss. Flow behavior and globularization kinetics during hot working of ti–6al–4v with a colony alpha microstructure. *Materials Science and Engineering: A*, 263(2):257–271, 1999.

[81] S. Semiatin, J. Brown, T. Brown, D. DeLo, T. Bieler, and J. Beynon. Strain-path effects during hot working of ti-6al-4v with a colony-alpha microstructure. *Metallurgical and Materials Transactions A*, 32(6):1556–1559, 2001.

[82] S. Semiatin, S. Knisley, P. Fagin, D. Barker, and F. Zhang. Microstructure evolution during alpha-beta heat treatment of ti-6al-4v. *Metallurgical and Materials Transactions A*, 34(10):2377–2386, 2003.

[83] S. Semiatin, N. Stefansson, and R. Doherty. Prediction of the kinetics of static globularization of ti-6al-4v. *Metallurgical and Materials Transactions A*, 36(5): 1372–1376, 2005.

[84] S. Semiatin, K. Kinsel, A. Pilchak, and G. Sargent. Effect of process variables on transformation-texture development in ti-6al-4v sheet following beta heat treatment. *Metallurgical and Materials Transactions A*, 44(8):3852–3865, 2013.

[85] T. Seshacharyulu, S. Medeiros, J. Morgan, J. Malas, W. Frazier, and Y. Prasad. Hot deformation and microstructural damage mechanisms in extra-low interstitial (eli) grade ti–6al–4v. *Materials Science and Engineering: A*, 279 (1):289–299, 2000.

[86] T. Seshacharyulu, S. Medeiros, W. Frazier, and Y. Prasad. Microstructural mechanisms during hot working of commercial grade ti–6al–4v with lamellar starting structure. *Materials Science and Engineering: A*, 325(1):112–125, 2002.

[87] R. Sethy, L. Galdos, J. Mendiguren, and E. Sáenz de Argandoña. Friction and heat transfer coefficient determination of titanium alloys during hot forging conditions. *Advanced Engineering Materials*, 19(6):1600060, 2017.

[88] G. Shakhanova and M. Y. Brun. Structure of titanium alloys and methods used for its control. *Metal Science and Heat Treatment*, 24(7):467–471, 1982.

[89] G. Sharma, R. Ramanujan, and G. Tiwari. Instability mechanisms in lamellar microstructures. *Acta materialia*, 48(4):875–889, 2000.

[90] D. Sheed, B. Kashyap, and R. Singh. Study of globularization in ti-6al-4v alloy during non-isothermal forging and annealing process. In *Proceedings of 22nd The IIER International Conference, London, United Kingdom, April 2015*, 2015.

[91] E. Shell and S. Semiatin. Effect of initial microstructure on plastic flow and dynamic globularization during hot working of ti-6al-4v. *Metallurgical and Materials Transactions A*, 30(12):3219–3229, 1999.

[92] C. Sommitsch, D. Huber, F. Ingelman-Sundberg, S. Mitsche, M. Stockinger, and B. Buchmayr. Recrystallization and grain growth in the nickel-based superalloy allvac 718plus. *International Journal of Materials Research*, 100(8):1088–1098, 2009.

[93] H.-W. Song, S.-H. Zhang, and M. Cheng. Dynamic globularization kinetics during hot working of a two phase titanium alloy with a colony alpha microstructure. *Journal of Alloys and Compounds*, 480(2):922–927, 2009.

[94] H.-w. Song, S.-h. Zhang, and M. Cheng. Dynamic globularization prediction during cogging process of large size tc11 titanium alloy billet with lamellar structure. *Defence Technology*, 10(1):40–46, 2014.

[95] N. Stefansson and S. Semiatin. Mechanisms of globularization of ti-6al-4v during static heat treatment. *Metallurgical and Materials Transactions A*, 34 (3):691–698, 2003.

[96] N. Stefansson, S. Semiatin, and D. Eylon. The kinetics of static globularization of ti-6al-4v. *Metallurgical and Materials Transactions A*, 33(11):3527–3534, 2002.

[97] Z. Sun, H. Yang, G. Han, and X. Fan. A numerical model based on internal-state-variable method for the microstructure evolution during hot-working process of ta15 titanium alloy. *Materials Science and Engineering: A*, 527 (15):3464–3471, 2010.

[98] P. Vo, M. Jahazi, and S. Yue. Recrystallization during thermomechanical processing of imi834. *Metallurgical and Materials Transactions A*, 39(12): 2965, 2008.

[99] K. Wang, W. Zeng, Y. Zhao, Y. Lai, and Y. Zhou. Dynamic globularization kinetics during hot working of ti-17 alloy with initial lamellar microstructure. *Materials Science and Engineering: A*, 527(10):2559–2566, 2010.

[100] K.-x. Wang, W.-d. Zeng, Y.-q. Zhao, Y.-t. Shao, and Y.-g. Zhou. Prediction of dynamic globularization of ti-17 titanium alloy with initial lamellar microstructure during hot compression. *Materials Science and Engineering: A*, 527(23):6193–6199, 2010.

[101] J. L. Warwick, N. G. Jones, I. Bantounas, M. Preuss, and D. Dye. In situ observation of texture and microstructure evolution during rolling and globularization of ti–6al–4v. *Acta Materialia*, 61(5):1603–1615, 2013.

[102] I. Weiss, F. Froes, D. Eylon, and G. Welsch. Modification of alpha morphology in ti-6al-4v by thermomechanical processing. *Metallurgical and Materials Transactions A*, 17(11):1935–1947, 1986.

[103] G. Welsch, R. Boyer, and E. Collings. *Materials properties handbook: titanium alloys*. ASM international, 1993.

[104] J. Williams, R. Baggerly, and N. Paton. Deformation behavior of hcp ti-al alloy single crystals. *Metallurgical and Materials Transactions A*, 33(3):837–850, 2002.

[105] C.-B. Wu, Y. He, X.-G. Fan, and Z.-C. Sun. Dynamic globularization kinetics during hot working of ta15 titanium alloy with colony microstructure. *Transactions of Nonferrous Metals Society of China*, 21(9):1963–1969, 2011.

[106] Y. Wu, D. Wang, Z. Liu, and G. Liu. A unified internal state variable material model for ti2alnb-alloy and its applications in hot gas forming. *International Journal of Mechanical Sciences*, 164:105126, 2019.

[107] J. Xu, W. Zeng, Z. Jia, X. Sun, and J. Zhou. Prediction of static globularization of ti-17 alloy with starting lamellar microstructure during heat treatment. *Computational Materials Science*, 92:224–230, 2014.

[108] K. V. Yang, C. V. S. Lim, K. Zhang, J. Sun, X. Yang, A. Huang, X. Wu, and C. H. Davies. Microstructure and texture evolution in double-cone samples of ti-6al-4v alloy with colony preform microstructure. *Metallurgical and Materials Transactions A*, 46(12):5989–6002, 2015.

[109] L. Yang, N. Li, B. Wang, J. Lin, H. Zhao, and W. Ma. Unified constitutive modelling for two-phase lamellar titanium alloys at hot forming conditions. *Manufacturing Review*, 3:14, 2016.

[110] J. T. Yeom, J. H. Kim, N. Y. Kim, N. K. Park, and C. S. Lee. Characterization of dynamic globularization behavior during hot working of ti-6al-4v alloy. In *Advanced Materials Research*, volume 26, pages 1033–1036. Trans Tech Publ, 2007.

[111] M. Yoo, S. Agnew, J. Morris, and K. Ho. Non-basal slip systems in hcp metals and alloys: source mechanisms. *Materials Science and Engineering: A*, 319: 87–92, 2001.

[112] S. Zaefferer. A study of active deformation systems in titanium alloys: dependence on alloy composition and correlation with deformation texture. *Materials Science and Engineering: A*, 344(1-2):20–30, 2003.

[113] B. Zhang, L. Lei, X. Jiang, Z. Song, X. Huang, and G. Zhang. On temperature and strain rate dependent strain localization behavior in ti–6.5 al–3.5 mo–1.5 zr–0.3 si alloy. *Journal of Materials Science & Technology*, 29(3):273–278, 2013.

[114] A. Zhao, H. Yang, X. Fan, P. Gao, R. Zuo, and M. Meng. The flow behavior and microstructure evolution during (α+ β) deformation of β wrought ta15 titanium alloy. *Materials & Design*, 109:112–122, 2016.

[115] S. Zherebtsov, G. Salishchev, R. Galeyev, O. Valiakhmetov, S. Y. Mironov, and S. Semiatin. Production of submicrocrystalline structure in large-scale ti–6al–4v billet by warm severe deformation processing. *Scripta materialia*, 51(12): 1147–1151, 2004.

[116] S. Zherebtsov, M. Murzinova, G. Salishchev, and S. Semiatin. Spheroidization of the lamellar microstructure in ti–6al–4v alloy during warm deformation and annealing. *Acta Materialia*, 59(10):4138–4150, 2011.

[117] Y. Zhu, W. Zeng, X. Ma, Q. Tai, Z. Li, and X. Li. Determination of the friction factor of ti-6al-4v titanium alloy in hot forging by means of ring-compression test using fem. *Tribology International*, 44(12):2074–2080, 2011.

Appendix A

Appendix A gives more detail on the innovative model presented in Chapter 5. The associated subroutine is provided; and the implementation into DEFORM FEM software is also explained.

The subroutine shown below is written in Fortran language within a template file provided by DEFORM. It is then compiled to create a Dynamic Link Library (.dll) file that will be called during post-processing operations. Figures 1 and 2 illustrate that process. Once a forging model has been created in the pre-processor and run, it can be opened in the post-processor. The icon showed with arrow *1* in Figure 1 opens the interface for subroutines (numbered *2*). The *.dll* file can be loaded there and the desired variables can be acccesed. Calculations are the performed to obtain values for these variables throughout the whole modeled process (shown in interface number *3*). Visualisation of the desired variables can be reached via the icon with arrow *1* in Figure 2. This opens the corresponding interface (numbered *2*) where display options can be chosen.

```
****************************************************************

SUBROUTINE USRPS1_2(TNOW,DTMAX,RZ,TEMP,EFEPS,TEPS,EFSTS,
DAMG,RDTY, STS,EPS,TSR,ATOM,WEAR,VF,VFN, VAR1, VAR2, VNAME,
ISTEP,INIT, IOBJ,NUMNP,NUMEL,NTMATR,ICURNE)

****************************************************************

                          *** INPUT ***

TNOW : Current time
```

DTMAX : Max time step when set in simulation controls
RZ : Element center coord.
TEMP : Temperature
EFEPS : Effective strain rate
TEPS : Total accumulated strain
EFSTS : Effective stress
DAMGE : Damge factor
RDTY : Relative density
STS : Stress tensor
EPS : Strain rate tensor
TSR : Strain tensor
WEAR(5) : Interface temperature, sliding velocity, and interface pressure on master object nodes
ATOM : Dominating Atom Contents
NTMATR : Number of Material Phases
VF : Volume Fraction
VFN : Transformation Starting Volume Fraction
VAR1(1-95) : Initial state variables
VAR2(1-95) : Updated state variables
VNAME(1-95) : Name for each variables
ISTEP : Step number
INIT : Flag for Different Operations
0 - Define characteristic of the subroutine
1 - Initialize User Defined Variables (Initial Step)
2 - Calculate User Defined Variables (Subsequent Steps)
IOBJ : Object number in current object
NUMNP : Number of nodes in current object (when INIT=1,2)
NUMEL : Number of elements in current object (when INIT=1,2)
ICURNE : Current node/element number in object (when INIT=1,2)

****

This routine will be executed in three phases. In the second and third phases, this subroutine will be called for each element.
PHASE 1 : ”INIT” will be set to ”0”. Variables names (VNAME) should be defined at this stage so that the variables can be displayed on the screen. The variables with

```
defined ”VNAME” are tracked. For easier identification purpose, it is recommended
that proper name or descriptions to be assigned under ”VNAME”.
PHASE 2 : In the second phase (ISTEP equals to the starting step), ”INIT” will be set
to ”1”. At this stage, you should initialize the state variables VAR2. Up to five state
variables can be stored and used.
PHASE 3 : In the third phase, ”INIT” will be set to ”2” . The porgram expects new
”VAR2” from this routine. The variable ”VAR1” is an INPUT in this case. The
variables ”VAR2” will be interpolated automatically across the remeshing.

******************************************************************

IMPLICIT DOUBLE PRECISION (A-H,O-Z), INTEGER (I-N)
CHARACTER*24 VNAME(95)
REAL EPS_CRI, EPS_50, N_D, K_S, A_S, M_S, eta
REAL fract_t, dyna, dyna_2
REAL t_ini, t_hold
REAL Ex, Ey, Ez, Gx, Gy, Gz

DIMENSION RZ(3),STS(6),EPS(6),TSR(6),VAR1(95),VAR2(95),WEAR(5)
DIMENSION VF(NTMATR),VFN(NTMATR)

Phase 1

Initialize the Variable Names

IF(INIT.EQ.0) THEN
VNAME(1) = ’Time’
VNAME(2) = ’effective strain’
VNAME(3) = ’effective strain rate’
VNAME(4) = ’dynamic globularisation’
VNAME(5) = ’static globularisation’
VNAME(6) = ’total globularisation’
VNAME(7) = ’modified strain’          ! this for calculation of globularised fraction
VNAME(8) = ’start strain’          ! strain at the start of the forging step
VNAME(9) = ’end strain’          ! strain at the end of the forging step
VNAME(10)= ’vonMisesStrain’
```

```
Set of constants for the equations of globularised fraction

EPS_CRI = 0.117
N_D = 0.448
K_S = 5.168
A_S = -1.610
EPS_50 = 15
M_S = 0.838
eta = 0.051

t_ini = 0.0
t_hold = 0.0

RETURN
ENDIF

Phase 2

Initialize the state Variable

IF (INIT.EQ.1) THEN
VAR2(1)= TNOW
VAR2(2)=TEPS
VAR2(3)=EFEPS
VAR2(4)=0.0
VAR2(5)=0.0
VAR2(6)=0.0
VAR2(7)=0.0
VAR2(8)=0.0
VAR2(13)=0.0
VAR2(10)=0.0
RETURN
ENDIF

Phase 3

Update The State Variables

IF (INIT.EQ.2) THEN
```

```
useful variables

VAR2(1)=TNOW
VAR2(2)=TEPS
VAR2(3)=EFEPS


Calculation of the VonMises strain
Ex=(2*TSR(1)-TSR(2)-TSR(3))/3
Ey=(2*TSR(2)-TSR(1)-TSR(3))/3
Ez=(2*TSR(3)-TSR(2)-TSR(1))/3
Gx=TSR(4)
Gy=TSR(5)
Gz=TSR(6)

VAR2(10)=(2.0/3.0)*
sqrt((3.0/2.0)*(Ex*Ex+Ey*Ey+Ez*Ez)+3*(Gx*Gx+Gy*Gy+Gz*Gz))


                    Calculation of globularised fraction

starting time for recovery

IF (EFEPS.EQ.0.0.AND.t_ini.EQ.0.0) THEN
t_ini=TNOW
ELSE IF (EFEPS.GT.0.0) THEN
t_ini=0.0
ENDIF

calculation of the revovery time

IF (t_ini.GT.0.0) THEN
t_hold=TNOW-t_ini
ENDIF

IF (EFEPS.GT.0.0) THEN
t_hold=0.0
ENDIF
```

```
calculation of recovered fraction

IF (t_hold.LE.120) THEN
fract_t=eta*(t_hold)/120
ENDIF

IF (t_hold.GT.120) THEN
fract_t=eta
ENDIF

starting strain for increment measurement

IF (EFEPS.GT.0.0.AND.VAR1(3).EQ.0.0) THEN
VAR2(8)=VAR1(10)
ENDIF

calculation of the strain including increment and recovery

IF (EFEPS.GT.0.0) THEN
VAR2(7)=VAR1(7)+VAR2(10)-VAR1(10)
VAR2(9)=VAR1(7)+VAR2(10)-VAR1(10)
ELSE
VAR2(7)= VAR1(9)-(fract_t)*(VAR2(10)-VAR2(8))
VAR2(9)=VAR1(9)
ENDIF

Calculations of the globularised fractions

IF (VAR2(7).GT.EPS_CRI) THEN
dyna=1-EXP(-0.693*((VAR2(7)-EPS_CRI)/EPS_50)**N_D)
dyna_2=VAR1(4)
VAR2(4)=MAX(dyna, dyna_2)
ELSE
VAR2(4)=VAR1(4)
ENDIF

IF ((VAR2(7).GT.0.0)) THEN
```

```
T_50=3600*EXP(160000/(8.314*TEMP))*K_S*VAR2(7)**A_S
VAR2(5)=1-EXP(-0.693D0*(TNOW/T_50)**M_S))
ELSE
VAR2(5)=VAR1(5)
ENDIF

VAR2(6)=VAR2(4)+(1-VAR2(4))*VAR2(5)
```

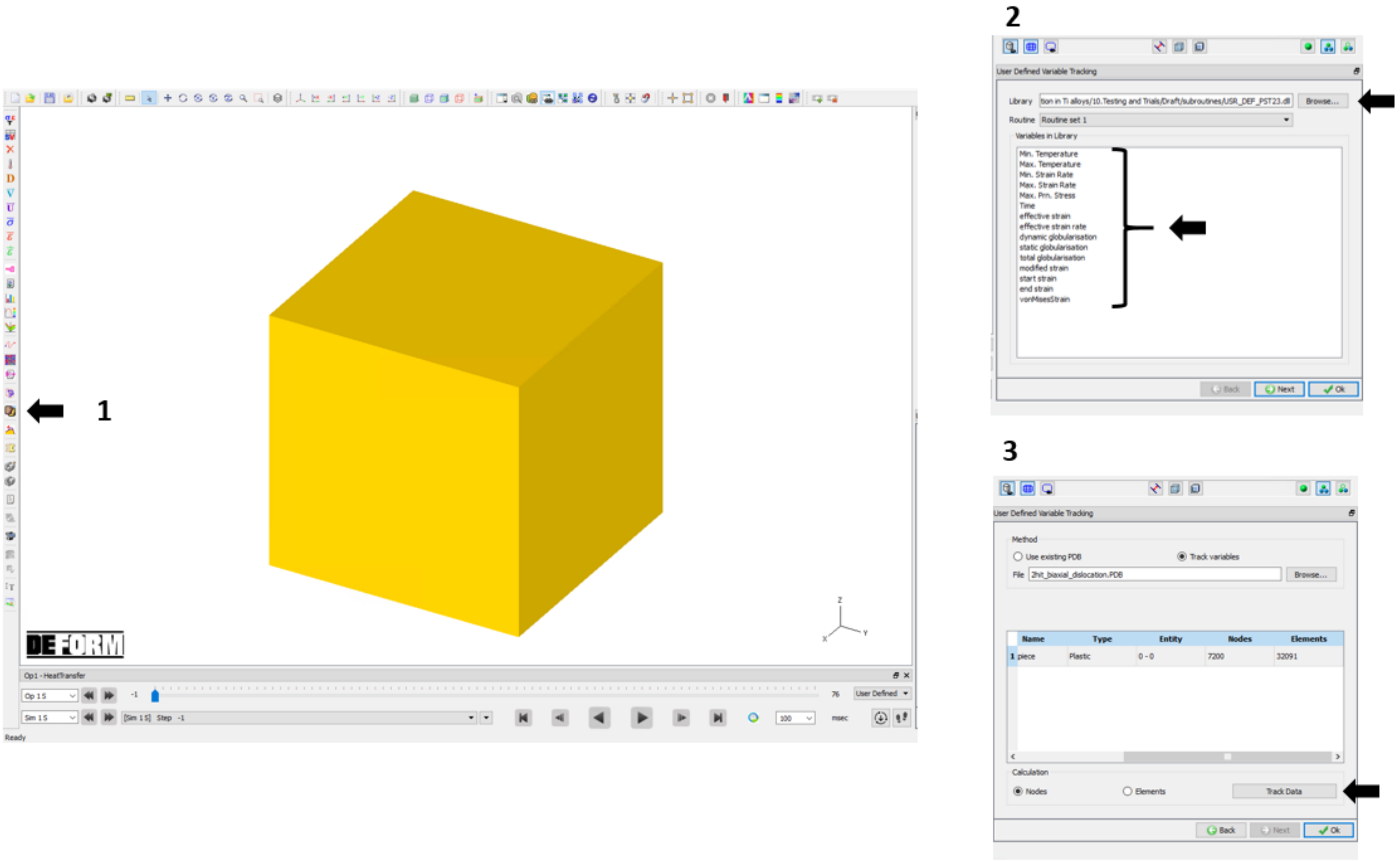

Library: tion in Ti alloys/10.Testing and Trials/Draft/subroutines/USR_DEF_PST23.dll

Routine: Routine set 1

Variables in Library

- Min. Temperature
- Max. Temperature
- Min. Strain Rate
- Max. Strain Rate
- Max. Prn. Stress
- Time
- effective strain
- effective strain rate
- dynamic globularisation
- static globularisation
- total globularisation
- modified strain
- start strain
- end strain
- vonMisesStrain

Method

○ Use existing PDB ● Track variables

File: 2hit_biaxial_dislocation.PDB

	Name	Type	Entity	Nodes	Elements
1	piece	Plastic	0 - 0	7200	32091

Calculation

● Nodes ○ Elements

Figure 1: Post-processing environment in DEFORM software showing how to integrate the created subroutine.

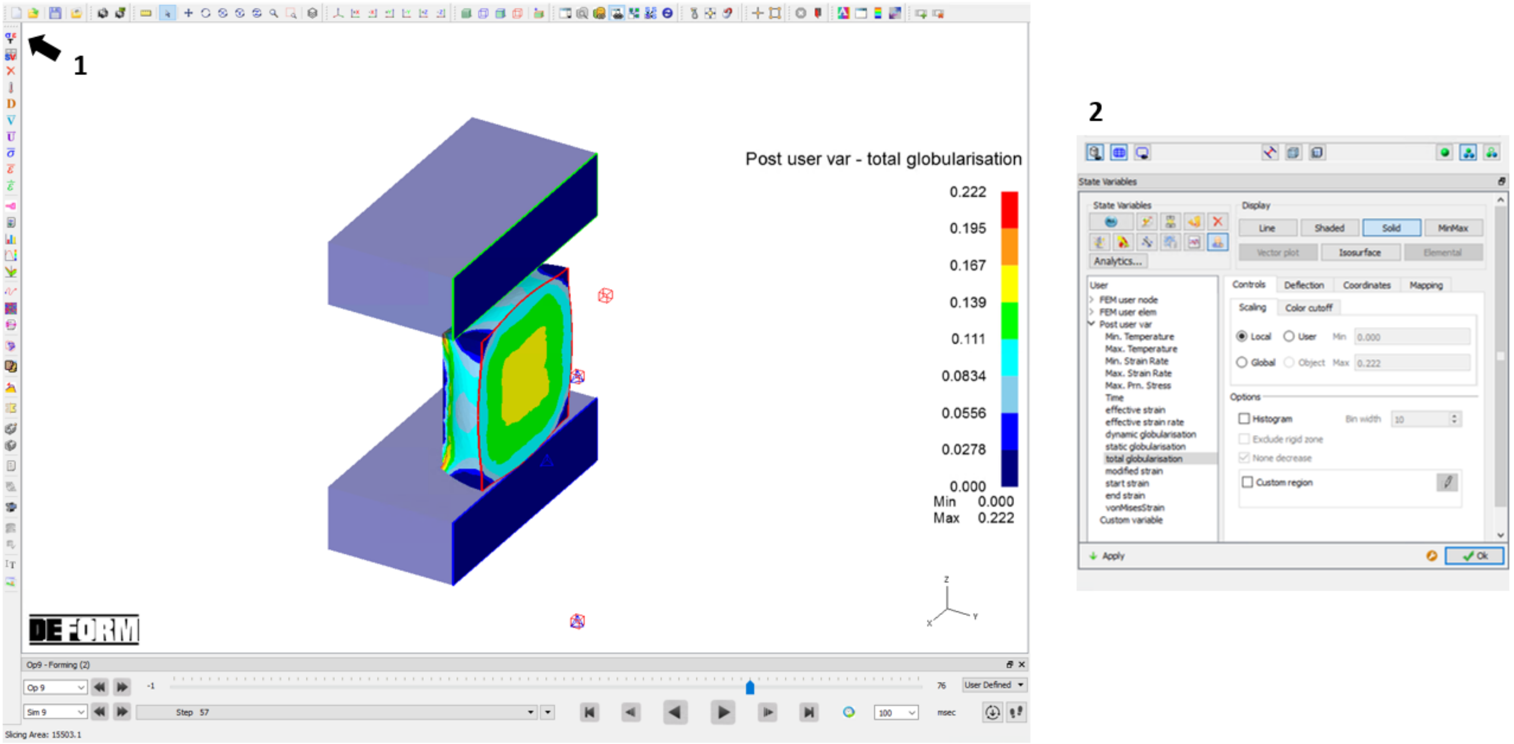

Figure 2: Post-processing environment in DEFORM software showing how to display the predicted globularised fraction in a model of a multiaxial forging.

Appendix B

Appendix B gives more details on the results from each test conducted in this work. For each experimental condition, the strain distribution in the sample as well as the level of globularisation in each studied deformation zone are displayed. Also, micrographs representative of the microstructural evolution in each deformation zone are included.

Test - “0.5U_WQ”

Strain level	Globularised fraction
0.8	0.0±0.0
1.25	0.04±0.02
1.7	0.12±0.07

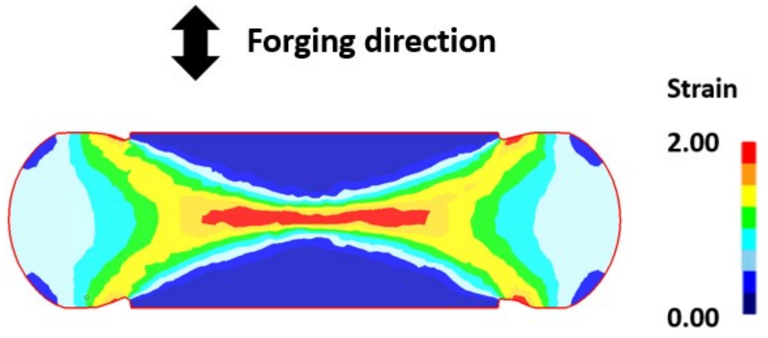

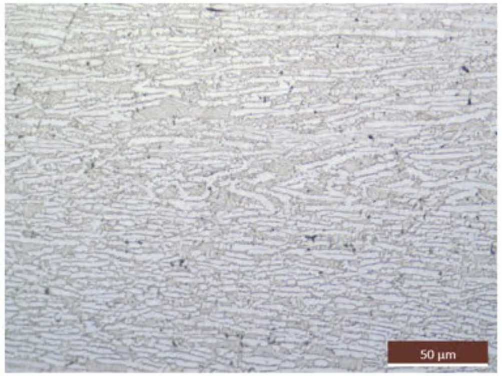

ε = 1.7

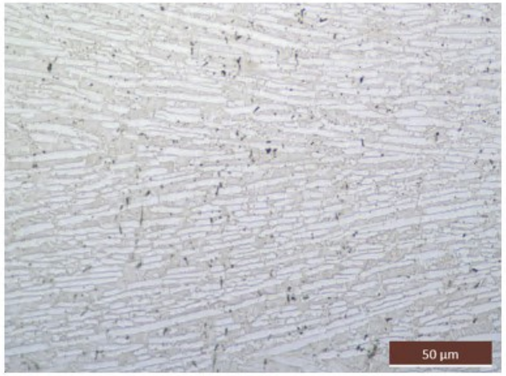

ε = 1.25

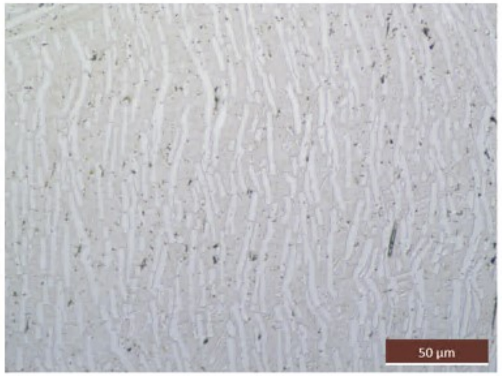

ε = 0.8

Test - "0.5U_1h_WQ"

Strain level	Globularised fraction
0.8	0.12±0.05
1.25	0.26±0.09
1.7	0.38±0.04

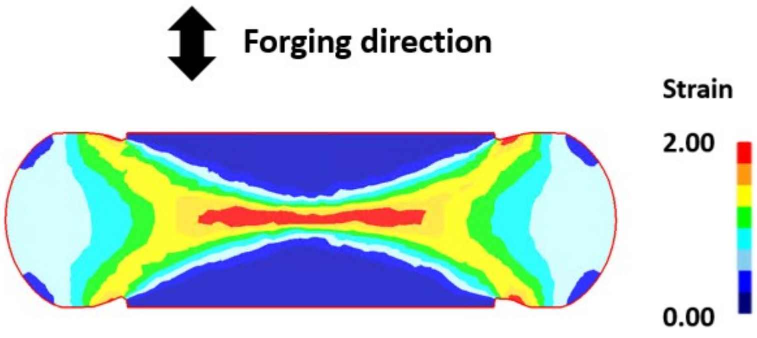

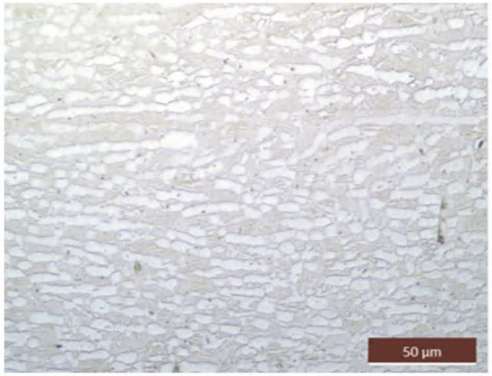

$\varepsilon = 1.7$

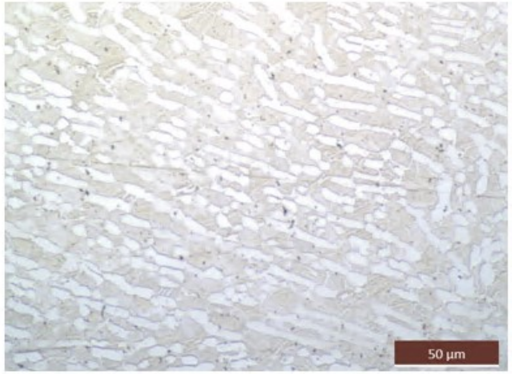

$\varepsilon = 1.25$

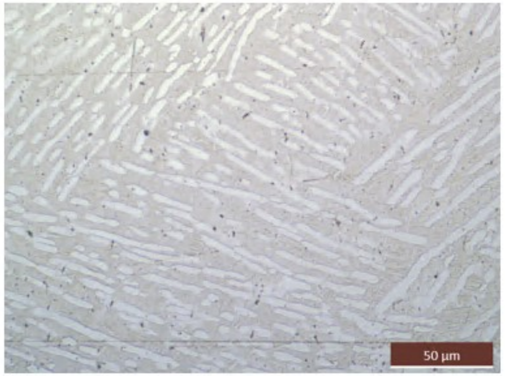

$\varepsilon = 0.8$

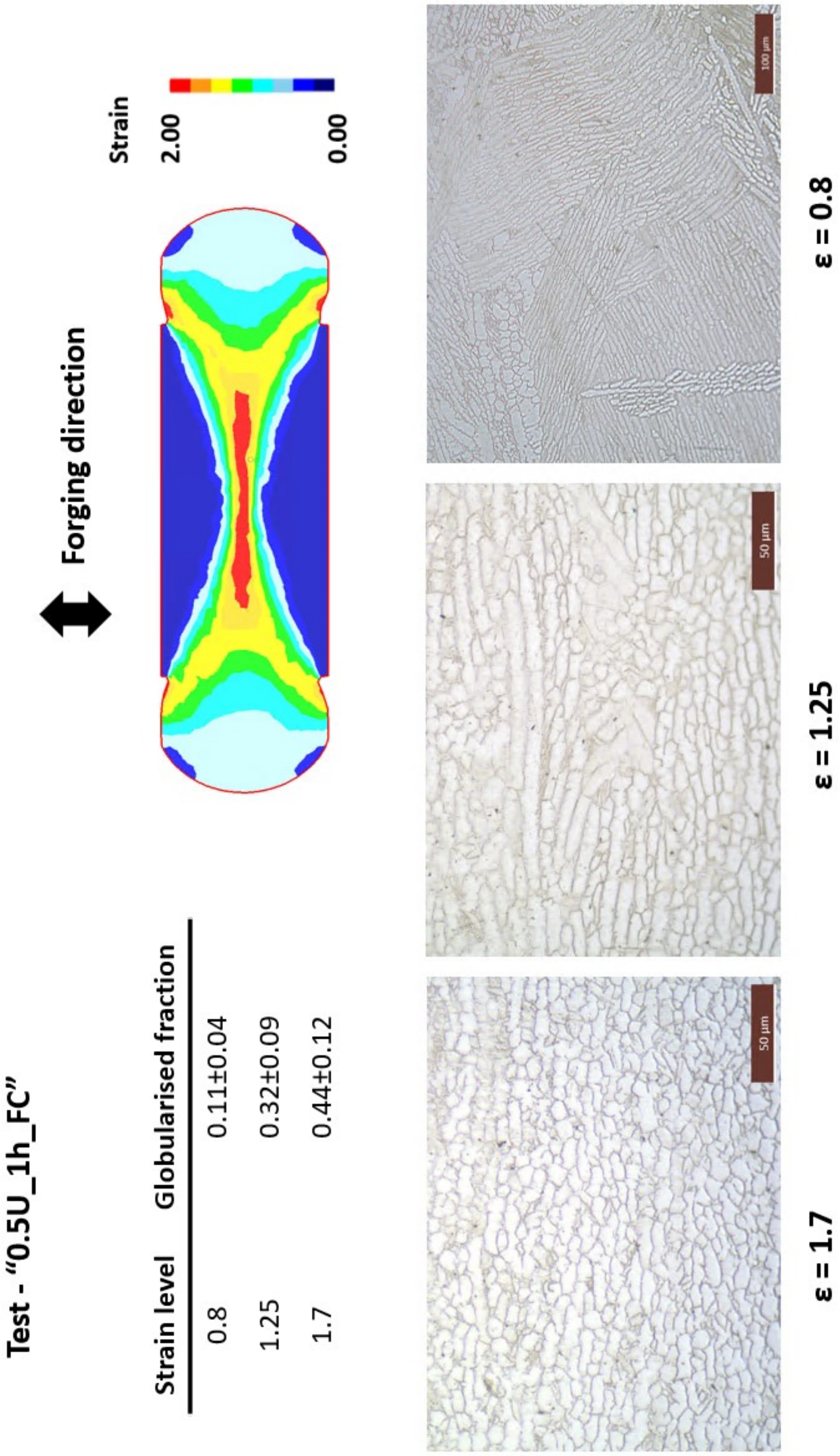

Test - "0.5U_1h_FC"

Strain level	Globularised fraction
0.8	0.11±0.04
1.25	0.32±0.09
1.7	0.44±0.12

Test - “0.5U_4h_FC”

Strain level	Globularised fraction
0.8	0.11±0.04
1.25	0.50±0.07
1.7	0.66±0.06

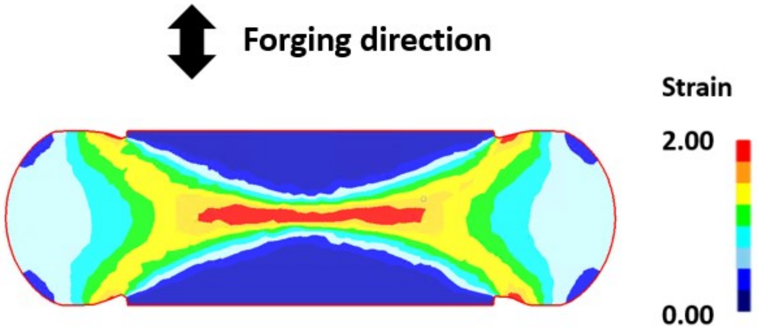

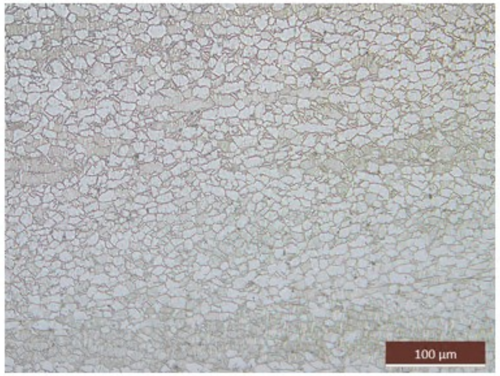

ε = 1.7

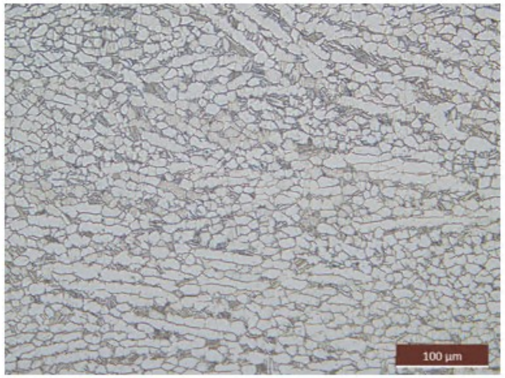

ε = 1.25

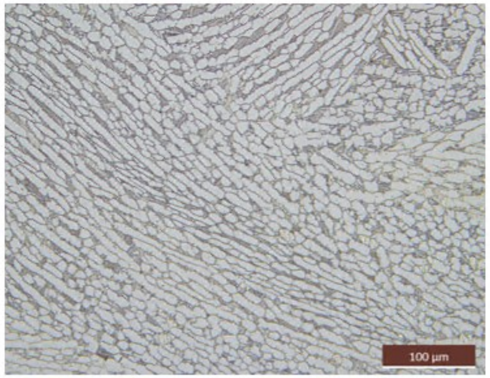

ε = 0.8

Test - “2_(0.25U_1h)_WQ”

Strain level	Globularised fraction
0.65	0.12±0.05
0.95	0.25±0.06
1.30	0.44±0.07

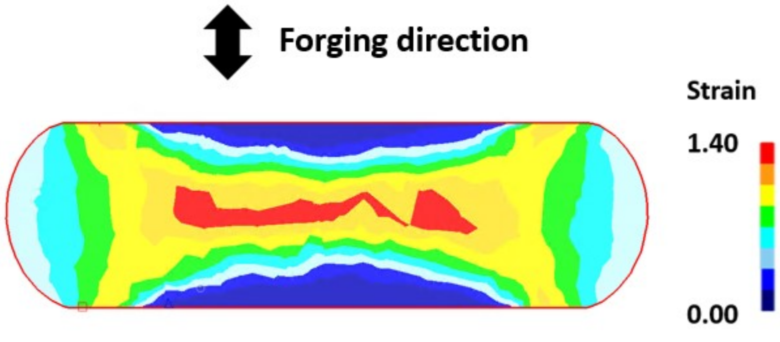

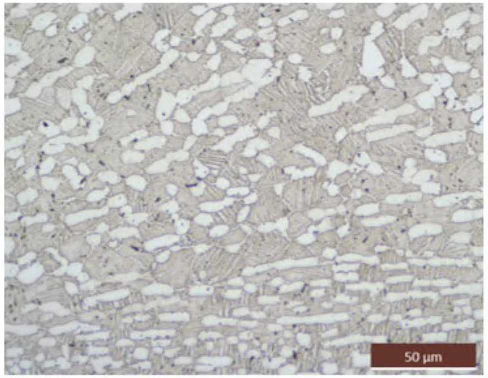

ε = 1.3

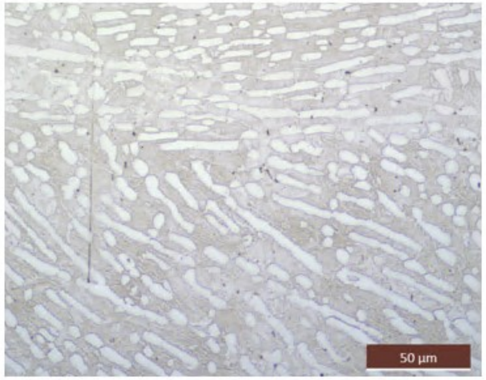

ε = 0.95

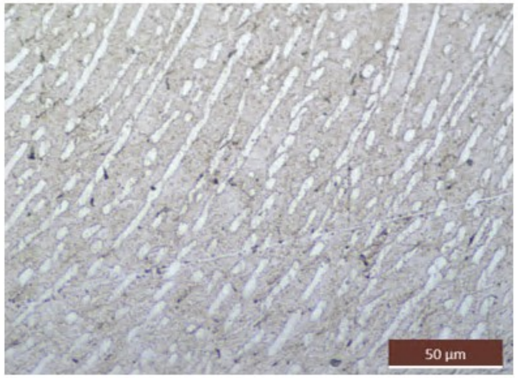

ε = 0.65

Test - “2_(0.25U_1h)_FC”

Strain level	Globularised fraction
0.65	0.11±0.05
0.95	0.30±0.11
1.30	0.37±0.08

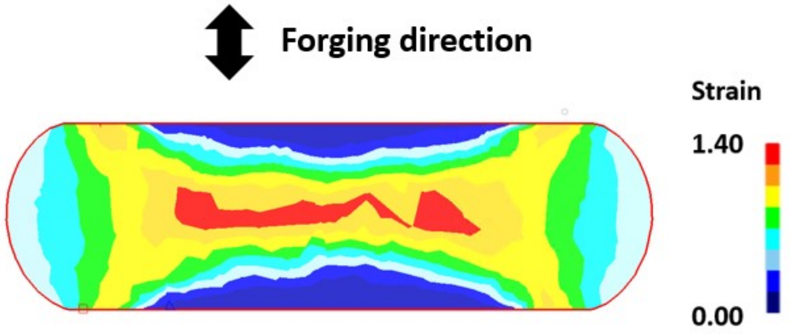

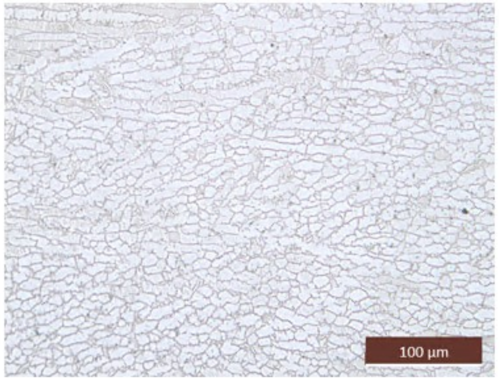

$\varepsilon = 1.3$

$\varepsilon = 0.95$

$\varepsilon = 0.65$

Test - “2_(0.25M_1h)_WQ”

Strain level	Globularised fraction
0.85	0.16±0.05
1.15	0.21±0.08
1.45	0.29±0.05

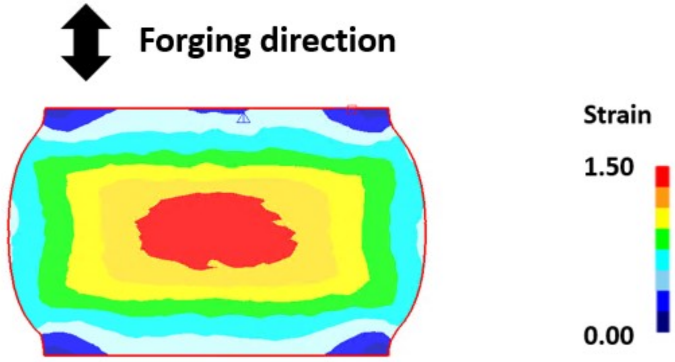

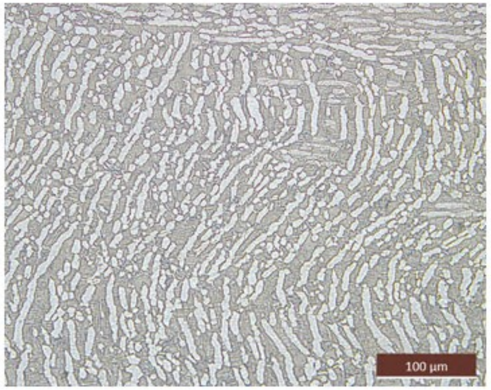

ε = 1.45

ε = 1.15

ε = 0.85

Test - “2_(0.25M_1h)_FC”

Strain level	Globularised fraction
0.85	0.11±0.05
1.15	0.22±0.07
1.45	0.33±0.10

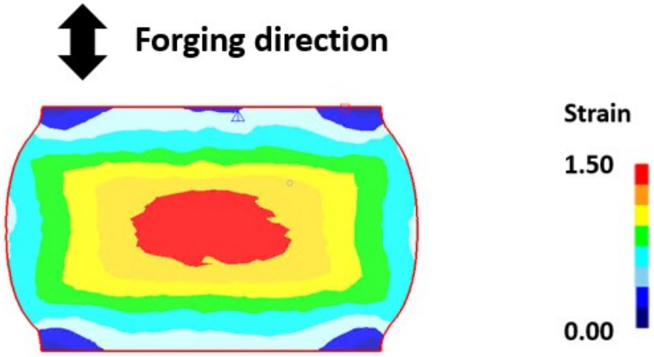

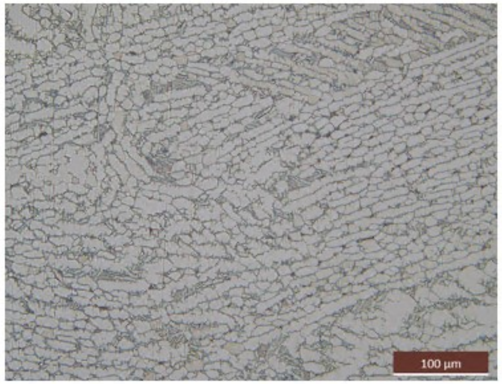

$\varepsilon = 1.45$

$\varepsilon = 1.15$

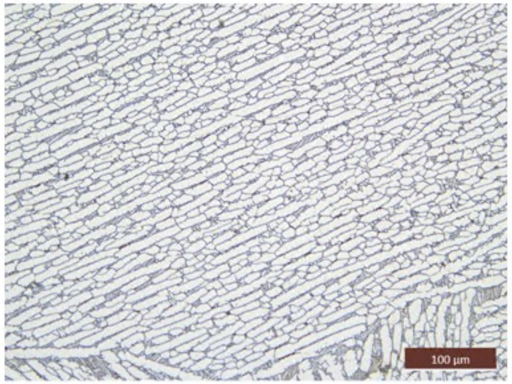

$\varepsilon = 0.85$

Test - “2_0.25M_1h_FC”

Strain level	Globularised fraction
0.65	0.06±0.04
0.95	0.15±0.06
1.30	0.29±0.08

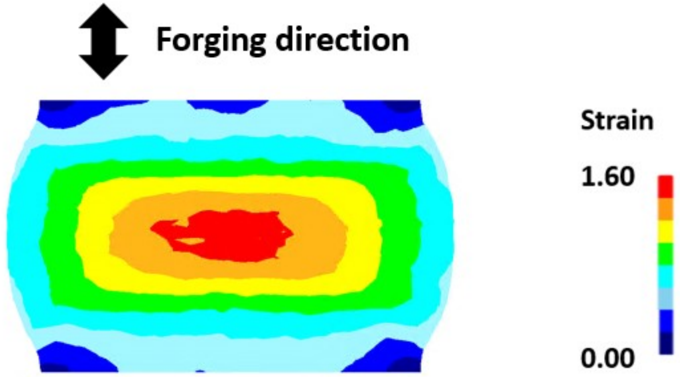

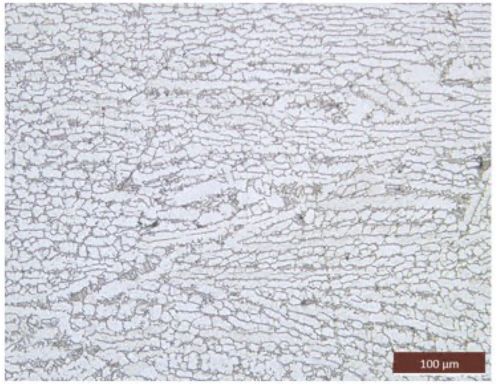

ε = 1.5

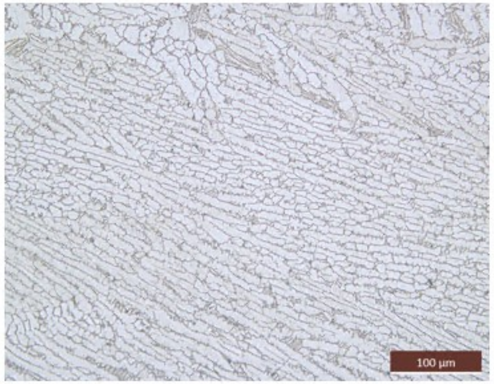

ε = 1.1

ε = 0.7

Test - "5_(0.1U_1h)_FC"

Strain level	Globularised fraction
0.5	0.13±0.07
0.7	0.26±0.09
0.90	0.39±0.06

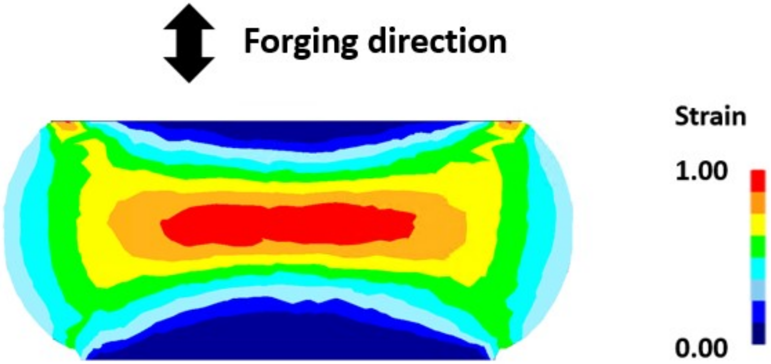

$\varepsilon = 0.9$

$\varepsilon = 0.7$

$\varepsilon = 0.5$

Test - “5_(0.1M_1h)_FC”

Strain level	Globularised fraction
0.65	0.02±0.03
0.95	0.19±0.07
1.30	0.28±0.07

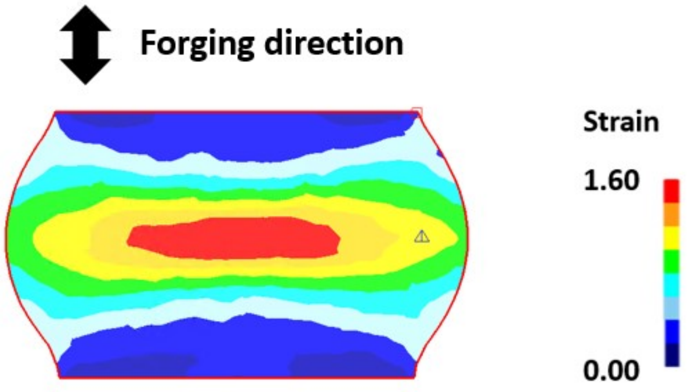

ε = 1.5

ε = 1.1

ε = 0.7

Test - “4_0.25M_WQ”

Strain level	Globularised fraction
1.4	0.05±0.02
2.2	0.09±0.03
3.0	0.13±0.06

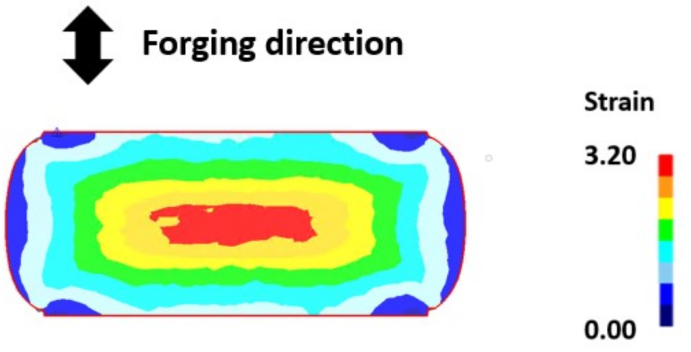

ε = 3.0

ε = 2.2

ε = 1.4

Test - “4_0.25M_1h_AC”

Strain level	Globularised fraction
1.4	0.10±0.04
2.2	0.14±0.06
3.0	0.26±0.04

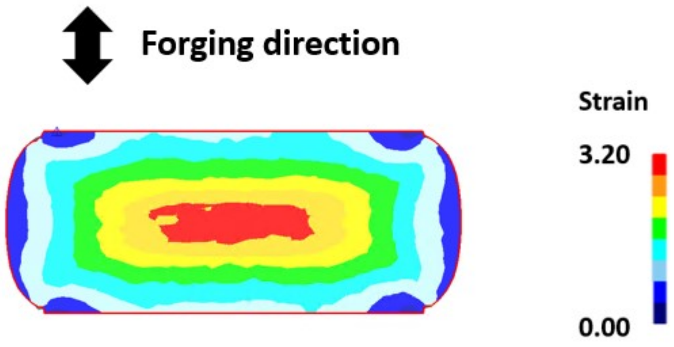

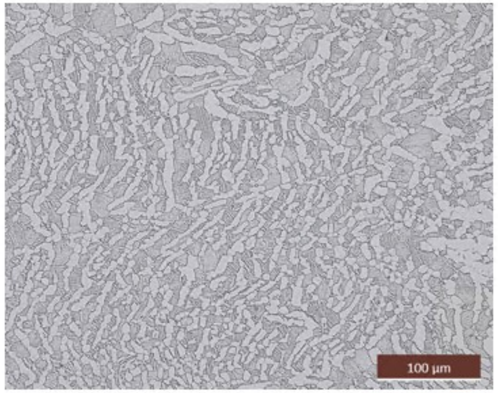

ε = 3.0

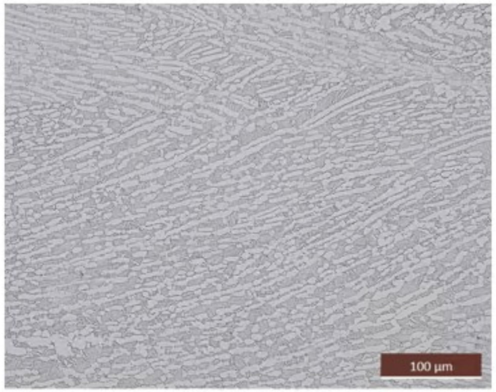

ε = 2.2

ε = 1.4

Test - “4_0.25M_4h_AC”

Strain level	Globularised fraction
1.4	0.16±0.05
2.2	0.36±0.06
3.0	0.41±0.10

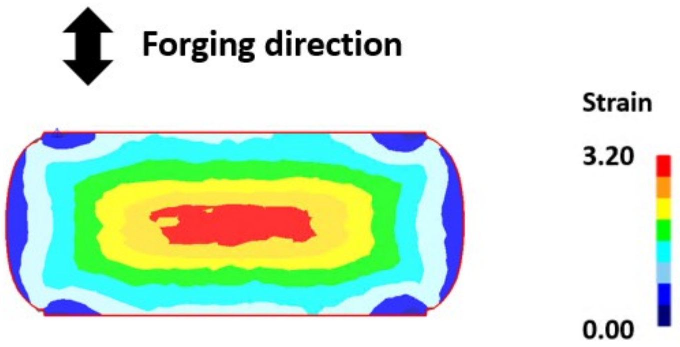

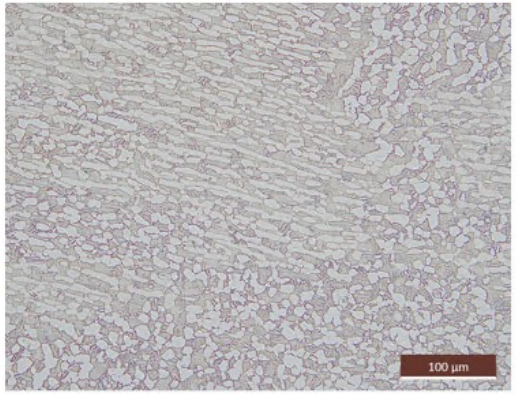

$\varepsilon = 3.0$

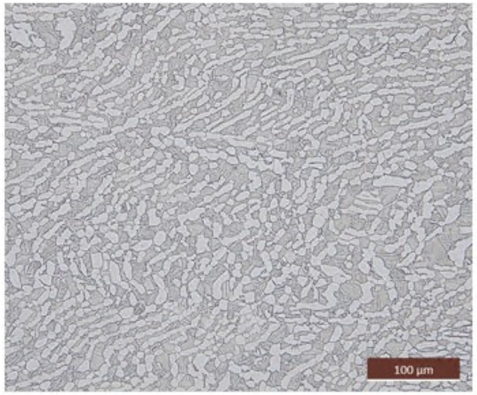

$\varepsilon = 2.2$

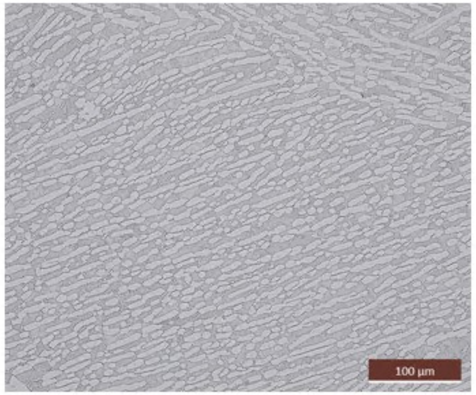

$\varepsilon = 1.4$

Test - “10_0.1M_WQ”

Strain level	Globularised fraction
1.4	0.09±0.12
2.2	0.10±0.06
3.0	0.14±0.07

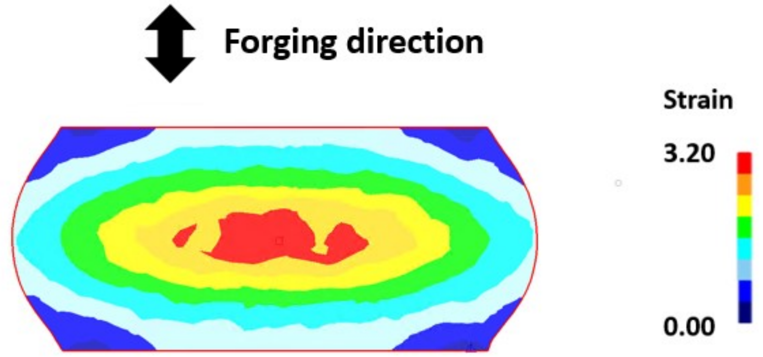

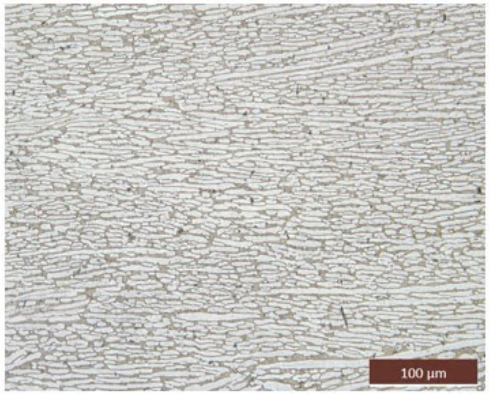

ε = 3.0

ε = 2.2

ε = 1.4

Test - "10_0.1M_1h_AC"

Strain level	Globularised fraction
1.4	0.04±0.03
2.2	0.14±0.06
3.0	0.22±0.10

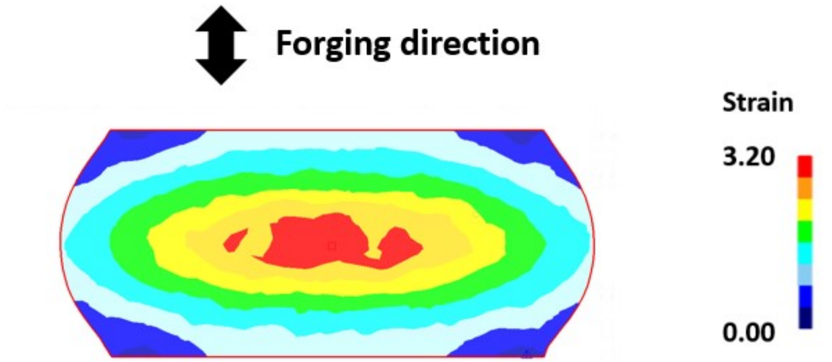

$\varepsilon = 3.0$

$\varepsilon = 2.2$

$\varepsilon = 1.4$

Test - “10_0.1M_4h_AC”

Strain level	Globularised fraction
1.4	0.11±0.07
2.2	0.26±0.09
3.0	0.26±0.11

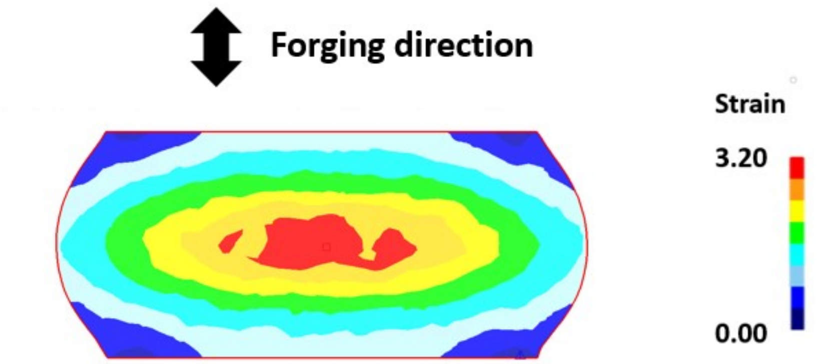

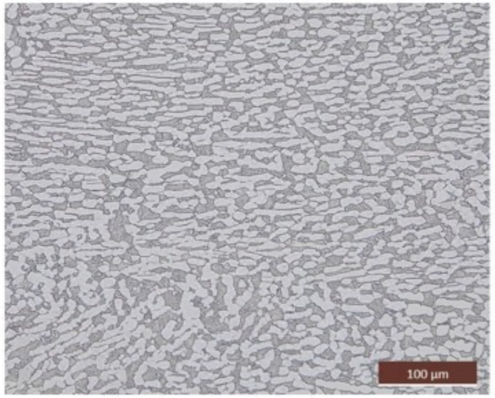

ε = 3.0

ε = 2.2

ε = 1.4

Test - “5_0.1M_5h_FC”

Strain level	Globularised fraction
0.8	0.12±0.04
1.2	0.27±0.05
1.6	0.37±0.07

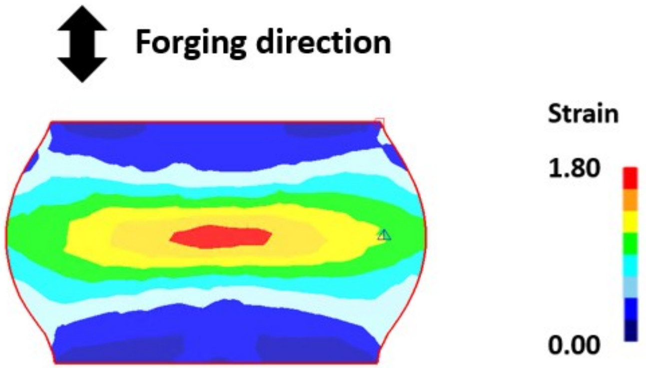

ε = 1.6

ε = 1.2

ε = 0.8

Test - “3_0.1M_3h_WQ”

Strain level	Globularised fraction
0.5	0.05±0.03
0.7	0.15±0.05
0.9	0.26±0.05

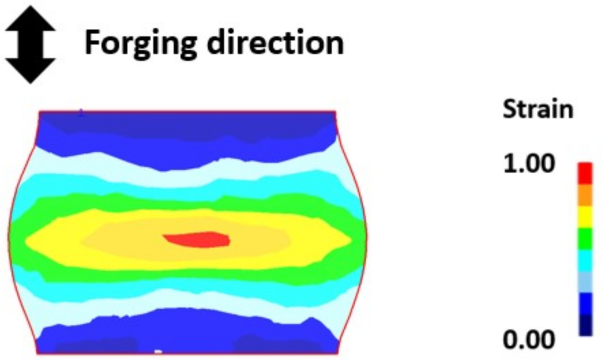

ε = 0.9 ε = 0.7 ε = 0.5

Test - “3_0.1M_3h_2_0.1M_2h_FC”

Strain level	Globularised fraction
0.7	0.14±0.05
1.1	0.22±0.06
1.5	0.31±0.05

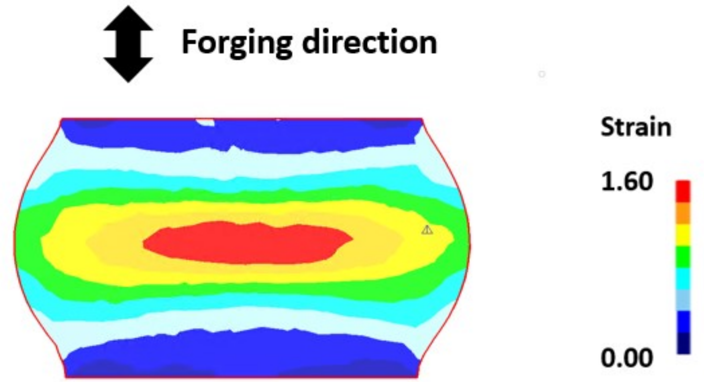

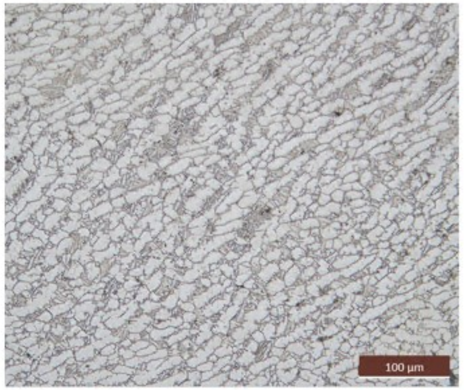

ε = 1.5

ε = 1.1

ε = 0.7

Test - “3_0.1M_1h_WQ”

Strain level	Globularised fraction
0.5	0.07±0.05
0.7	0.09±0.06
0.9	0.14±0.10

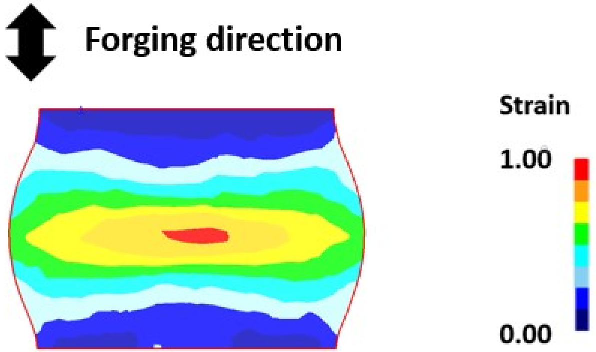

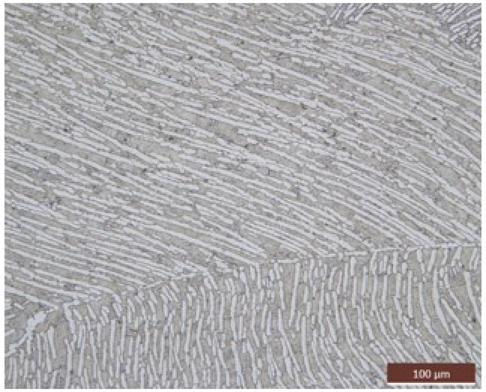

ε = 0.9

ε = 0.7

ε = 0.5

Test - “3_0.1M_1h_3_0.1M_1h_WQ”

Strain level	Globularised fraction
0.8	0.13±0.05
1.3	0.16±0.07
1.8	0.28±0.09

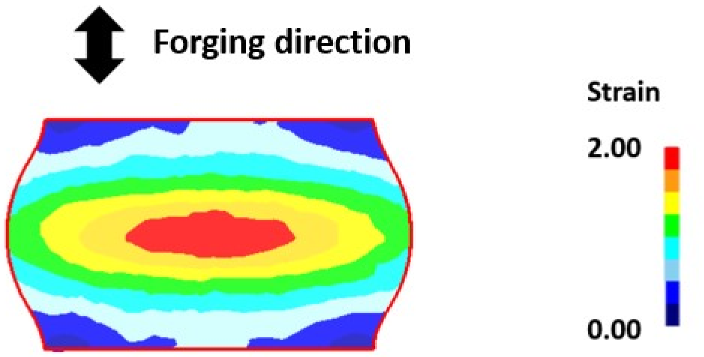

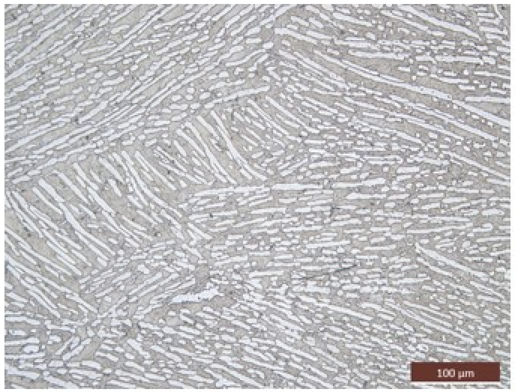

ε = 1.8

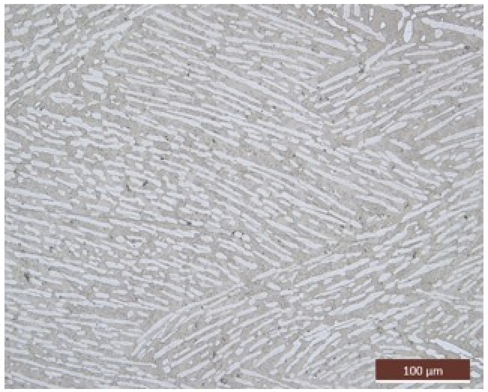

ε = 1.3

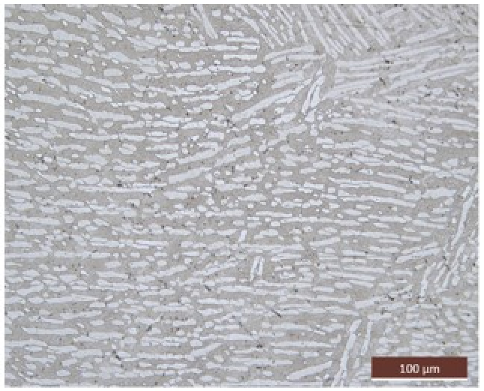

ε = 0.8

Test - "3_0.2M_WQ" (upsetting)

Strain level	Globularised fraction
0.7	0.07±0.06
1.1	0.05±0.04
1.5	0.09±0.05

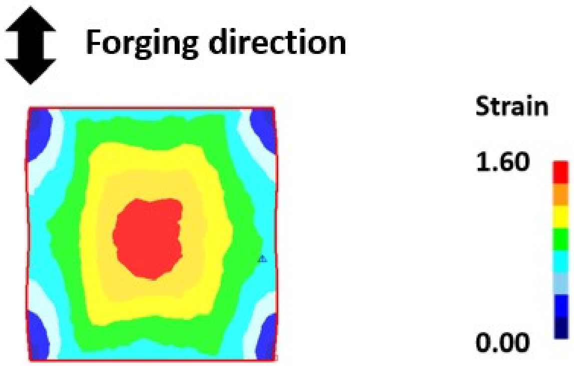

ε = 1.5 ε = 1.1 ε = 0.7

Test - "3_0.15M_1h_FC" (45° rotation)

Strain level	Globularised fraction
0.6	0.07±0.03
0.8	0.15±0.11
1.0	0.21±0.10

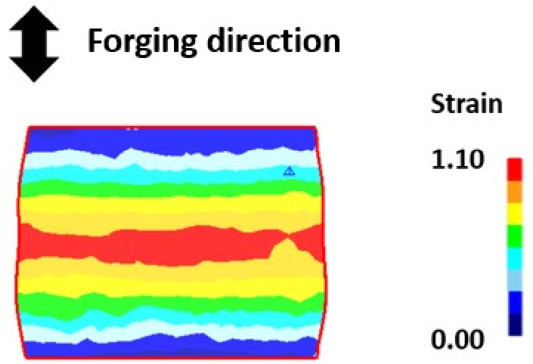

ε = 1.0

ε = 0.8

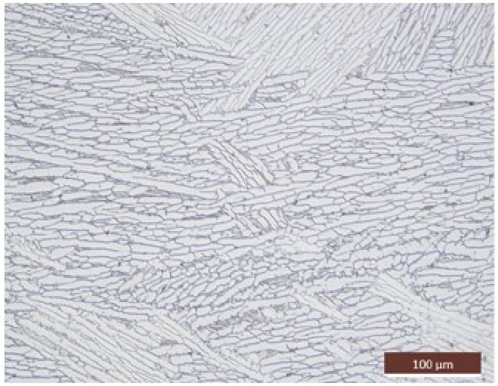

ε = 0.6

Test - “0.5U(900°C)_WQ”

Strain level	Globularised fraction
0.6	0.01±0.01
1.0	0.01±0.01
1.4	0.01±0.01

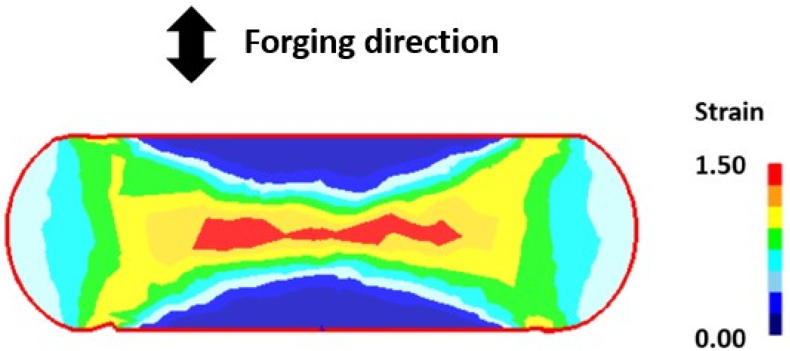

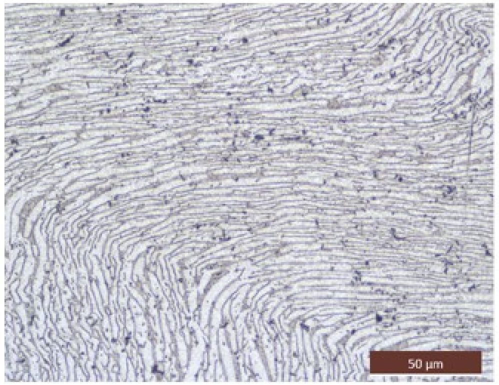

ε = 1.4

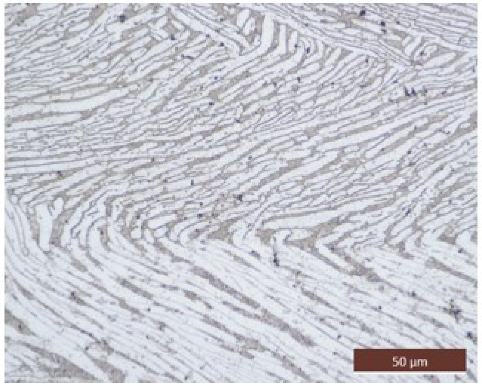

ε = 1.0

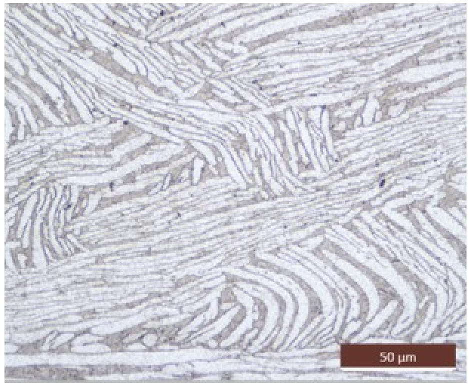

ε = 0.6

Test - “0.5U(900°C)_1h_AC”

Strain level	Globularised fraction
0.6	0.05±0.02
1.0	0.17±0.06
1.4	0.22±0.07

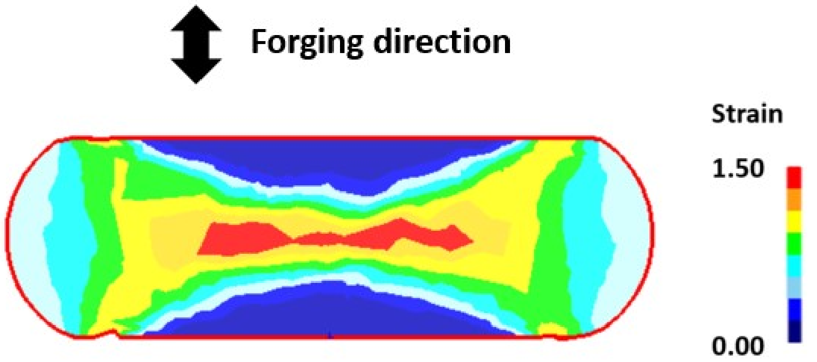

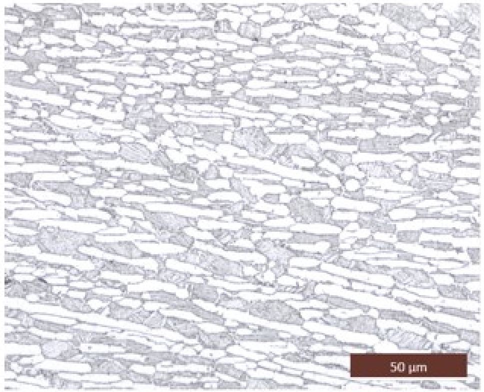

ε = 1.4

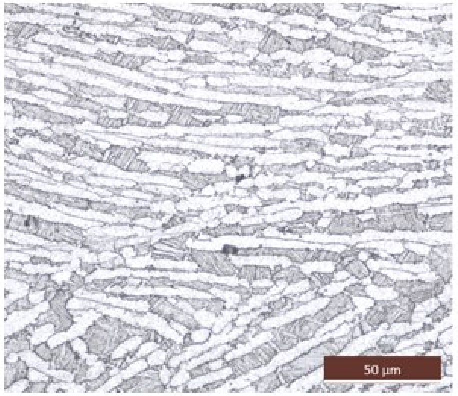

ε = 1.0

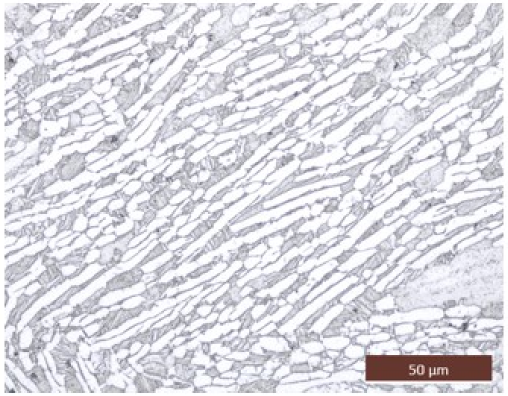

ε = 0.6

Test - "0.5U(900°C)_4h_AC"

Strain level	Globularised fraction
0.6	0.16±0.08
1.0	0.26±0.07
1.4	0.37±0.09

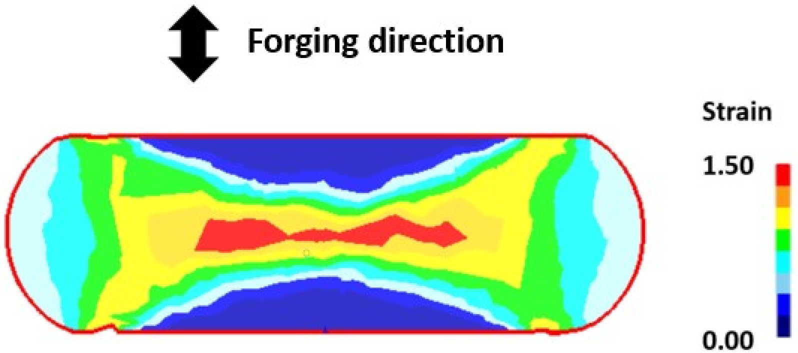

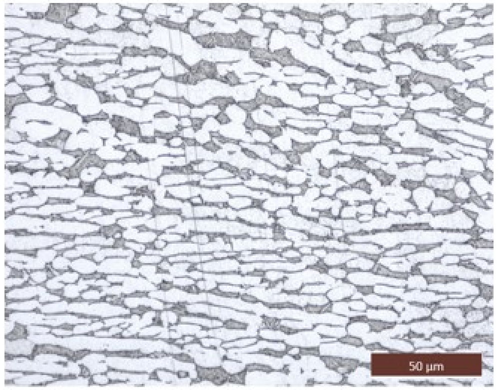

ε = 1.4

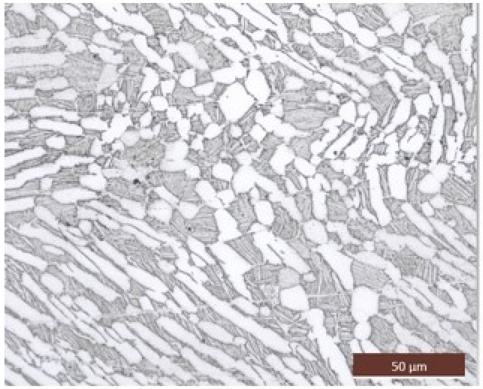

ε = 1.0

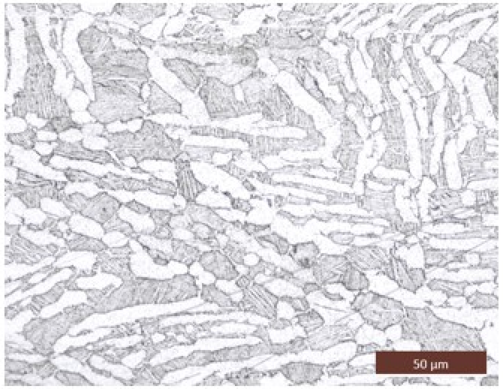

ε = 0.6

Test - "3 0.1M(900°C)_3h(950°C)_WQ"

Strain level	Globularised fraction
0.4	0.05±0.05
0.6	0.08±0.05
0.8	0.19±0.08

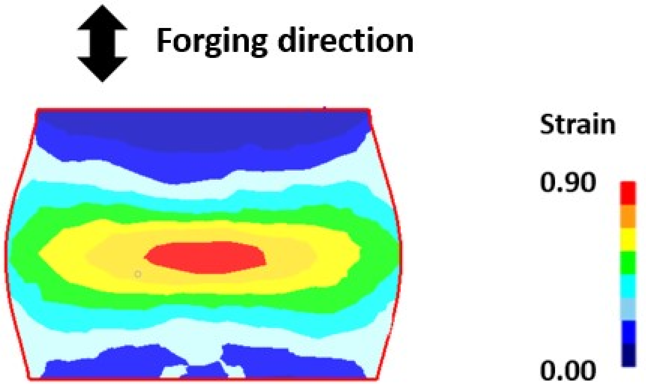

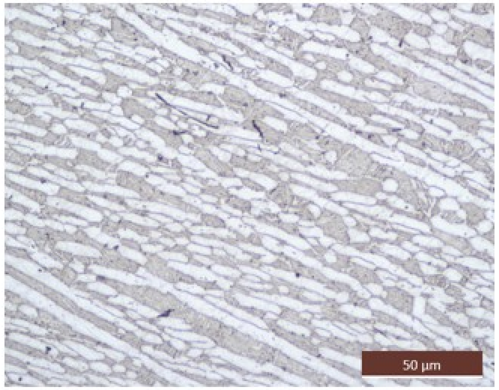

ε = 0.8

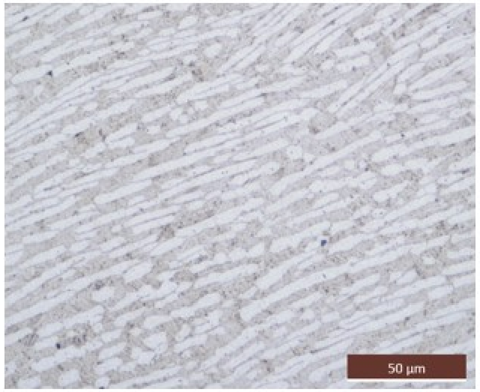

ε = 0.6

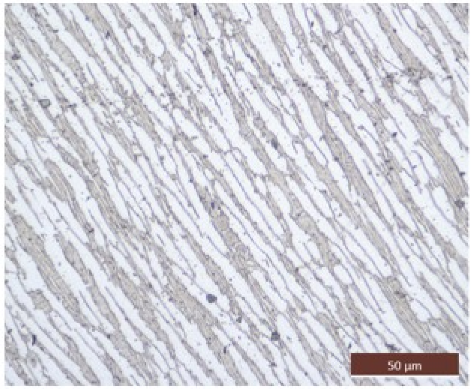

ε = 0.4